Fragmentation in Interstellar Filaments

Stefan Martin Heigl

München 2019

Fragmentation in Interstellar Filaments

Stefan Martin Heigl

Dissertation
an der Fakultät für Physik
der Ludwig–Maximilians–Universität
München

vorgelegt von
Stefan Martin Heigl
geb. in München

München, den 22.10.2019

Erstgutachter: Prof. Dr. Andreas Burkert
Zweitgutachter: Prof. Dr. Paola Caselli
Tag der mündlichen Prüfung: 09.12.2019

Zusammenfassung

Interstellare Filamente sind ein wesentlicher Schritt der Sternentstehung. In den letzten Jahren haben Beobachtungen die analytischen und numerischen Studien aus mehreren Jahrzehnten bewiesen, die gezeigt haben, dass Molekülwolken im interstellaren Medium hochgradig filamentär und Entstehungsorte massearmer Sterne sind. Es gibt jedoch noch viele ungelöste Fragen im Zusammenhang mit den physikalischen Bedingungen in Filamenten und dem genauen Prozess, wie das Gas in einzelne Sternentstehungskerne fragmentiert. Die vorliegende Arbeit trägt zum Verständnis dieser Kernbildung bei. Viele physikalische Prozesse beeinflussen und prägen die Entstehung der Geburtsorte von zukünftigen Sternen. In mehreren Studien untersuchen wir Modelle idealisierter Filamente unter verschiedenen Bedingungen mittels numerischer Simulationen mit dem adaptive-mesh-refinement code RAMSES.

Wir wenden das theoretische Modell der Fragmentierung durch schlichte Gravitationskräfte auf Beobachtungsdaten der L1517-Region des Taurus Sternentstehungsgebietes an, in der auch ein konsistentes Muster in der Geschwindigkeit gemessen wurde. Wir können nicht nur die beobachteten Messwerte der Dichte und der Geschwindigkeit in der Sichtlinie zu einem hinreichendem Maße reproduzieren, sondern darüber hinaus zeigen, dass das Abgleichen von Beobachtungsgrössen es uns ermöglicht, die Inklination der Filamente und den Umgebungsdruck des umgebenden Mediums zu bestimmen.

Darüber hinaus verwenden wir das Modell der Gravitationsfragmentierung zur Vorhersage der beobachteten Morphologie der Dichtestruktur von Kernen. Die beobachtete Form eines Kernes hängt direkt von der Linienmasse eines Filamentes ab und kann von Beobachtern verwendet werden, um Filamente mit niedriger von Filamenten mit hoher Linienmasse zu unterscheiden. Die entsprechenden Zeitskalen auf denen Kerne anwachsen, legen ebenfalls nahe, dass nur eine einzige Form zu jedem Zeitpunkt dominieren sollte.

Ausserdem demonstrieren wir die Relevanz der Akkretion, die von dem Gravitationspotential des Filamentes verursacht wird. Die Akkretion ist in der Lage durchgehend turbulente Bewegungen in Filamenten anzutreiben und dies in einem Ausmass, das mit Beobachtungen übereinstimmt. Ohne einem Treiber der Turbulenz würde diese auf kurzen Zeitskalen dissipieren. Unsere Ergebnisse zeigen, dass die Dissipation der Turbulenz in Filamenten mit seiner radialen Entwicklung zusammenhängt. Wir analysieren die Eigenschaften der erzeugten Turbulenz und untersuchen ihre Bedeutung für das hydrostatische Gleichgewicht. Obwohl die Turbulenz sich auf die radiale Entwicklung des Filamentes auswirkt, erhöht es nicht seine Stabilität, wie so häufig angenommen.

Kleinskalige Filamentsimulationen sind wichtig für die Beurteilung der Auswirkungen einzelner physikalischer Prozesse. Diese Arbeit befasst sich mit einigen entscheidenden Bestandteilen der Kernbildung. Es bleiben jedoch viele unerforschte Voraussetzungen, z.B. die kombinierte Wirkung von Magnetfeldern und Turbulenz oder der gravitative Kollaps entlang der Hauptachse des Filamentes, die von zukünftige Studien ergründet werden müssen.

Summary

Interstellar filaments are a crucial step in the star formation process. In the last few years, observations have proven decades' worth of analytic and numerical studies which have shown that molecular clouds in the interstellar medium are highly filamentary and that these filaments host low mass star formation. However, there are still many unresolved questions with regard to the physical conditions inside filaments and the mechanism involved in how exactly the gas fragments into individual cores.

The thesis at hand contributes to the understanding of core formation. Many physical processes influence and shape the creation of the birth-sites of future stars. In a series of studies we explore models of idealised filaments under different conditions by means of numerical simulations using the adaptive mesh refinement code RAMSES.

We apply the theoretical model of pure gravitational fragmentation to observational data of the L1517 region in Taurus where a consistent velocity structure was measured. Not only are we able to reproduce the observed density and line-of-sight velocity to a reasonable degree, but we can furthermore show that the method of matching observables allows us to determine the inclinations of filaments and the ambient pressure in the surrounding medium.

In addition, we use the model of gravitational fragmentation to predict the observed morphology of the density structure of cores. The measured form of a core is directly dependent on the line-mass of the filament and can be used by observers to distinguish low line-mass from high line-mass filaments. The timescales involved in the growth of cores also suggest that only one single morphology should be dominant at any given time.

Furthermore, we demonstrate the importance of accretion triggered by the gravitational potential of a filament itself. Accretion is able to continuously drive turbulent motions in filaments at a level which is in agreement with observations. Without a driving mechanism, turbulence would dissipate on short timescales. Our results show that the dissipation of turbulence in filaments is connected to its radial evolution. We analyse the properties of the turbulence created and evaluate its importance for the hydrostatic equilibrium. While turbulence does have an effect on the radial evolution of the filament, it does not increase its stability as is often assumed.

Small scale filament simulations are important for the evaluation of the impact of individual physical processes. This thesis addresses some crucial elements of core formation. However, many unexplored factors remain such as the combined effect of magnetic fields and turbulence or the gravitational collapse along the major axis, and future studies will need to address these.

Contents

1 Preface

When the Jesuit mathematician and astronomer Johann Baptist Cysat used a refracting telescope in 1618 and spotted the nebulous gas distribution in the constellation of Orion the Hunter, he first compared it to a comet (Lynn, 1887):

> "one sees how in like manner some stars are compressed into a very narrow space and how round about and between the stars a white light like that of a white cloud is poured out"

He probably was not the first to spot the gaseous nebula - its discovery is usually credited to the astronomer Nicolas-Claude Fabri de Peiresc in 1610 - but little did he know that he had observed a stellar nursery. The idea that stars are not fixed in the night sky but undergo a complex life cycle was revolutionary and did not come to fruition until much later in history, but the stars inside that stellar nursery had formed relatively recently, a process that must have taken place innumerable times since the Big Bang, which did not create the Universe already full of stars, but only filled with gas.

Historically, one can argue that the most important astronomical objects are stars. The first astronomical bodies to be observed by eye were indeed stellar objects, ranging from our own star, the sun, to the plethora of different stellar constellations in the night sky. While in the beginning a mythological meaning was attributed to them, the field of astronomy was driven by the desire to understand the fundamental processes governing stellar objects. The physics of the life and death of stars has been explored thoroughly and has been very successful in explaining observations. However, there is still no comprehensive theory of how stars form out of a reservoir of gas.

In general, star formation theory can be separated into two broad classes. On large scales, the goal is to understand the formation of stellar systems, from clusters up to individual galaxies. It ranges from the mass distribution of newly formed stars, the initial mass function, through the formation of giant molecular clouds and their properties to the overall galactic distribution of star-forming gas. Tied to the latter are the questions of why star formation only occurs in a fraction of the gas and what determines the overall rate of star formation on a galactic scale.

On small scales, star formation theory tries to explain the formation of individual stellar objects. This involves the gravitational collapse of dense cores and the loss of angular momentum, the influence of the interstellar medium on stellar properties, the formation of massive stars in the presence of their enormous radiation pressure and the properties of protostellar disks, jets and outflows.

While the formation mechanism of massive stars is still relatively unknown, the formation of low mass stars is well-supported by observations since the discovery of T Tauri stars (Joy, 1945) in the 1940s and their recognition as a class of object which condense out of the gas of a dark cloud in which they currently still reside. Their discovery led to the development of stellar pre-main-sequence models, and the advent of infrared astronomy in the 1970s allowed observers to lift the veil of obscuring

dust revealing even younger objects. A relatively modern development is the discovery of extra-solar planets which form out of proto-planetary discs around young stars. In the last few decades, this scientific advance has been aided by numerical simulations which allow us to develop and test theories under controlled physical conditions. While admittedly we are far from a comprehensive theory of star formation, the thesis at hand is an example of how we can learn more about our Universe utilising the power of simulations.

2 The interstellar medium

In our galaxy, the *Milky Way*, the space between stars is not empty. On the contrary, it is filled with gas, dust and energetic particles which collectively are called the interstellar medium (ISM). The ISM is essential for the galactic matter cycle as it constitutes the repository out of which stars are born and into which they deposit their energy, momentum and material over their lifetime and after their death. Where and how stars are formed is determined by dynamic processes in the ISM. However, these processes are also interconnected over many scales. The dynamics of the large scale set the local properties of small scale clouds but are also connected via various feedback processes. Therefore, the formation of stars in the ISM is truly a multi-scale problem.

2.1 Composition

2.1.1 Gas

The gaseous phase of the ISM consists of a mixture of different elements dominated by around 70% hydrogen, a smaller amount of 28% helium and traces of about 2% of heavier elements such as carbon, nitrogen and oxygen. The total amount of gas in the Milky Way cannot by easily determined, but it is estimated to be close to $10^{10}\,M_\odot$, about 1% of the Milky Way's total mass (Kalberla and Kerp, 2009). Hydrogen in the ISM exists in different chemical forms, either molecular, atomic or ionised. Most of the volume of the ISM is made up of ionised gas. However, ionised gas also has the lowest mass fraction due to its low densities. In contrast, the larger fraction of the mass in the ISM is contained in the cold neutral and molecular phases which are concentrated in dense clouds that have a volume filling factor of only a few percent.

Star formation predominantly correlates with the presence of molecular gas which is mostly contained in discrete, non-spherical and clumpy molecular clouds with densities greater than $100\,cm^{-3}$, temperatures of around 10 K and individual masses of 10^4-$10^6\,M_\odot$. The total distribution of molecular clouds has a total mass of about $2 \cdot 10^9\,M_\odot$ and closely follows the spiral structure. Its surface density peaks in the central 500 pc which is known as the Central Molecular Zone, has a dip between 0.5 and 3 kpc Galactocentric radius, possibly as a consequence of the Milky Way's central stellar bar (Morris and Serabyn, 1996), and peaks again at around $4-6$ kpc in a structure which is known as the Molecular Ring, outside of which it declines exponentially (Heyer et al., 1998).

Molecular clouds are embedded in a cold atomic envelope: the *cold neutral medium* (CNM), a component which can also be found in discrete clumps known as HI clouds with densities of 10-$100\,cm^{-3}$ and temperatures of around 50-100 K. However, atomic hydrogen is also observed at much larger temperatures as the *warm neutral medium* (WNM) which is distributed throughout the disk following the spiral arms and having a filamentary morphology in inter-arm regions. It has a density

of about $0.5\,\mathrm{cm}^{-3}$ and a temperature of around 8000 K. Both components are assumed to be in rough pressure equilibrium due to the thermal instability (Field, 1965). As the equilibrium temperature drops drastically between their respective densities, there exists an unstable region between both phases where the gas either expands and heats up or is compressed and cools down in order to adjust to the outside pressure. Both phases then represent local stable points for the same equilibrium pressure.

This model of a two phase ISM has been extended to include a third component in pressure equilibrium produced by supernovae and OB associations which fill the intercloud regions with large ionised bubbles of low density gas of about $10^{-3}\,\mathrm{cm}^{-3}$ and temperatures of around 10^6 K (McKee and Ostriker, 1977). Supernova remnants stir the ISM, drive turbulence in molecular clouds and also extend far above the disk. This so-called *hot ionised medium* (HIM) has by far the highest volume filling factor in the Galaxy of at least 50% but also the lowest mass fraction. It is responsible for the observed soft X-ray radiation and explains the emission of highly ionised species of oxygen such as OVI and OVII.

There are also observational indications for an additional ionised phase, the *warm ionised medium*, which is evident from lower ionised species such as OII and NII (Mierkiewicz et al., 2006), and the widespread diffuse emission of Hα (Reynolds et al., 1973). It has approximately the same temperature and density as the WNM but, by contrast, is highly ionised. Thus, it is assumed to be located in the coronal gas at the outer surface of neutral clouds which is ionised by stellar radiation. Furthermore, ionised hydrogen also exists around massive stars as HII regions where the central star provides the ionizing radiation. HII regions have similar densities and temperatures compared to the WIM, but in general it is not included as part of the WIM.

No observational technique can give a complete, comprehensive picture of the ISM and it has not yet been resolved if the ISM shows a distinct division as predicted by the three phase model. Indeed there have been indications that the CNM and WNM are not as clearly separated and that a significant fraction of the gas cannot be assigned to one phase or the other in a straightforward manner (Heiles and Troland, 2003; Roy et al., 2013). This is possibly due to the fact that the ISM is highly turbulent which tends to mix the distinct phases together.

2.1.2 Dust

There is evidence for an additional component in the ISM which causes a diminution and reddening of background light sources such as stars. The amount of reddening correlates closely with the hydrogen column density and not with distance. Moreover, one can observe a widespread continuum emission with a spectrum similar to a black body in the mid- and far-infrared and whose intensity also correlates with hydrogen column density. Furthermore, when measuring the elemental abundance in the solar neighborhood, one can detect a depletion of a number of elements, such as silicon and iron, compared to the solar gas metallicity. This leads to the conclusion that there are solid grains mixed in with the gas which are generally called dust.

The reason for a reddening of background light is that dust scatters and absorbs photons with wavelengths smaller than its physical grain size. This effect is quantified in an extinction curve which shows that the extinction increases for shorter wavelengths implying a power-law distribution of -3.5 in dust grain sizes between $0.003 - 1.0\,\mu\mathrm{m}$ where small grain sizes dominate by number (Mathis et al., 1977; Draine and Lee, 1984). The amount of extinction depends on the environment and the exact distribution of grain sizes, but modeling both allows the determination of the dust opacity κ which is shown in Figure 2.1. The steepness of the curve is parameterised by the value of the total-to-

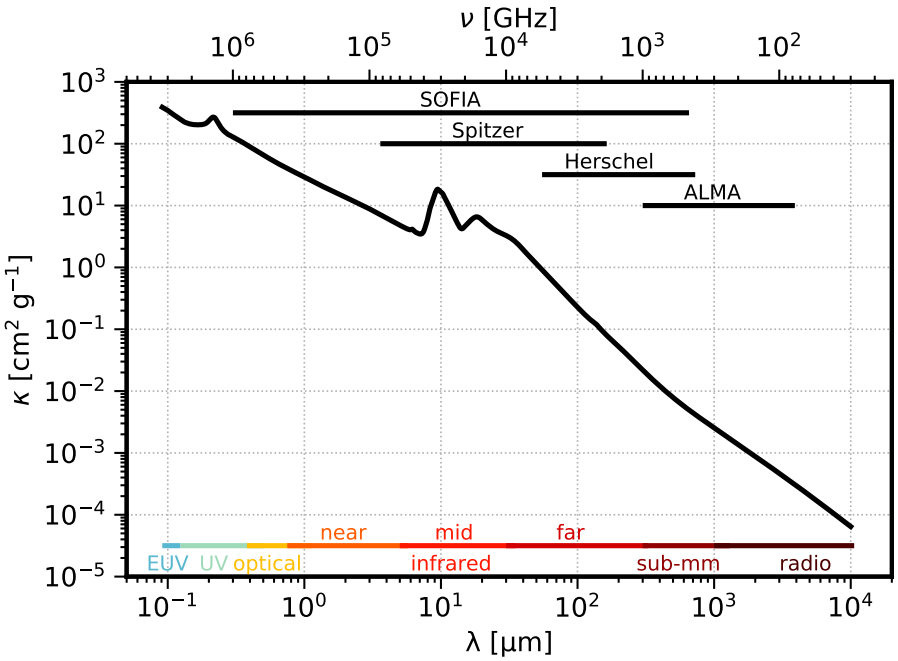

Figure 2.1: Milky Way dust opacity per unit gas mass above the Lyman-break as a function of wavelength λ and frequency ν for a value of the total-to-selective extinction of R_V=5.5. Also shown are selected wavelength coverages of different infrared and sub-millimeter telescopes. Opacity values are taken from Weingartner and Draine (2001) and Draine (2003).

selective extinction $R_V = A_V/E_{(B-V)}$, which depends on the dust environment along the line-of-sight. The total mass of dust is much harder to determine, but the extinction together with metal depletion measurements give an average value for the Milky Way of the order of 1% and has been shown to be close to constant independent of density (Bohlin et al., 1978; Predehl and Schmitt, 1995). Distinct broad spectral features in the extinction curve allow the identification of a particular type of dust grain, e.g. graphite in the case of the 217.5 nm peak (Mathis et al., 1977) or amorphous silicates in the case of the 9.7 μm and the 18 μm bump (Draine and Lee, 1984). The absorbed radiation results in an increased temperature of the dust which then in turn leads to emission of thermal radiation in the infrared.

Another important effect of dust is that it is able to polarise light. This is not only the result of scattering but in the presence of a magnetic field, the non-spherical, elongated dust grains align their long axis perpendicular to the magnetic field lines. As absorption and emission of radiation is most effective parallel to the long axis of the grains, this leads to a linear polarisation which, compared to the magnetic field lines, is parallel in the case of absorption of background radiation and perpendicular in the case of emission (Hall, 1949; Hiltner, 1949; Davis and Greenstein, 1951). This makes it possible to map the magnetic field structure of the Galaxy and even star-forming regions.

Furthermore, dust acts as a catalyst for many chemical reactions which happen on the grain surface. An example is the formation of H_2 whose formation in the gas phase is much less efficient than on grain surfaces (Gould and Salpeter, 1963; Hollenbach and Salpeter, 1971).

2.1.3 Cosmic Rays

Cosmic Rays are highly energetic, relativistic particles mainly accelerated in magnetised shock waves of supernova explosions. They are made up of approximately 1% electrons and 99% nuclei, of which most are protons, some are alpha particles and a few are metal nuclei. Their energies lie in the range of 10 MeV to more than 100 TeV and follow a broken power-law distribution. As they are bound by the galactic magnetic field, they scatter repeatedly within the disk and as a result have a high degree of isotropy and a nearly uniform energy density of the same order as the thermal and magnetic energy density of the ISM (Amenomori et al., 2006). The main effect of cosmic rays on the ISM is the ionisation of molecular hydrogen which couples the gas to the internal magnetic field and provides a source of heat even in the dense interiors of molecular clouds.

2.2 Observing the cold ISM

In atomic form, hydrogen has a hyperfine transition at 21 cm due to a flip of the electron spin from parallel to anti-parallel in respect to the spin of the proton. This makes atomic hydrogen easily observable even at temperatures much colder than that of typical star-forming regions of $10 - 100$ K. However, the main constituent of star-forming regions is molecular hydrogen. In contrast to its atomic form, molecular hydrogen has no permanent dipole moment as it is a homonuclear molecule. The lowest allowed excited state is a rotational transition at 510 K above the ground state. Thus, at low temperatures essentially no H_2 molecules are in an excited state capable of emitting. Therefore, cold, dense gas is usually observed using other tracers.

2.2.1 Dust emission

One possibility to observe cold material is to use the dust which traces dense gas and emits thermal radiation in the infrared. In contrast, the gaseous component will only show line emission and never thermal radiation as its densities are not large enough to be in equilibrium with the radiation field. In order to calculate the column density one needs to know the dust temperature and the dust opacity, which itself is independent of temperature. The dust opacity is shown in Figure 2.1 and has typical values of around $\kappa_\nu \sim 0.01$ cm^2 g^{-1} in the far infrared. Generally, surface densities of molecular clouds lie around $\Sigma \sim 0.1$ g cm^{-2} and no molecular cloud has larger values than 100 g cm^{-2}. Thus, the optical depth in the infrared $\tau_\nu = \Sigma\kappa_\nu$ is far below one and absorption of radiation from dust grains from the back of the cloud does not play a role, which simplifies the calculation of the emitted intensity. In thermal equilibrium, Kirchhoff's law of thermal radiation states that the emissivity is given by

$$j_\nu = \kappa_\nu \rho B_\nu(T) \tag{2.1}$$

where ρ is the density and $B_\nu(T)$ is the Planck function of temperature T:

$$B_\nu(T) = \frac{2h\nu^3}{c^2} \frac{1}{e^{h\nu/k_B T} - 1} \tag{2.2}$$

with h being Planck constant, c the speed of light and k_B the Boltzmann constant. As almost none of the radiation is absorbed, the total intensity is then simply the integrated emission throughout the cloud along the line-of-sight:

$$I_\nu = \int j_\nu ds = \Sigma\kappa_\nu B_\nu(T) = \tau_\nu B_\nu(T). \tag{2.3}$$

Figure 2.2: Three colour composite image of the Orion Nebula taken by the PACS and SPIRE instruments of Herschel. Blue is PACS 100 µm data, green is PACS 160 µm data and red is SPIRE 250 µm data. Credit: ESA/Herschel/PACS/SPIRE

Thus, if one knows the temperature and the properties of the dust grains, one can determine the column density in each telescope beam from the measured intensity. The uncertainties of this method lie in the dust opacity and the temperature, which both are known to around a factor of a few. The margin of error can be substantially reduced by using multi-wavelength observations, as then the column density, temperature and opacity can be fit simultaneously. An example of this technique is shown in Figure 2.2 which was taken by the *Herschel* satellite which specifically targeted multiple infrared wavelengths inaccessible from the ground.

2.2.2 Dust extinction

In addition to emitting infrared radiation, dust also absorbs and scatters background starlight, which makes it possible to measure the column density of molecular clouds by dust extinction as there exists a direct correlation between the extinction A_λ and the optical depth

$$A_\lambda = 2.5(\log e)\tau_\lambda = 1.086\,\Sigma\kappa_\lambda, \tag{2.4}$$

from which the column density can be determined if the opacity is known. There are two basic approaches to measuring the amount of extinction.

One way is the classical star count method (e.g. Wolf (1923); Bok (1956)) where the number of stars in rectilinear subregions of the image is determined and compared to the number of stars in unobscured regions. The extinction is then given by

$$A_\lambda = \log(N_{\rm off}/N_{\rm on})/b_\lambda \tag{2.5}$$

where N is the number density of stars on and off the cloud and b the slope of the logarithmic cumulative luminosity function of the stars in the control field. The major shortcoming of this method is that it suffers from uncertainties due to Poisson statistics especially at wavelengths with large extinction.

The other approach is to measure the amount of reddening of background stars which is usually done in the near infrared and therefore called the Near-Infrared Color Excess (e.g. Lada et al. (1994)). In order to determine the colour index, the H (1.65 μm) and K (2.2 μm) bands are used as they can be observed from the ground. In principle one could also measure the change in brightness of stellar light but the relative intrinsic variation of stellar colour is much smaller than that in brightness if not affected by extincting. The colour excess is given by the difference of measured colour index compared to the intrinsic value of main sequence stars:

$$E(\mathrm{H}-\mathrm{K}) = (\mathrm{H}-\mathrm{K})_{\rm observed} - (\mathrm{H}-\mathrm{K})_{\rm intrinsic}. \tag{2.6}$$

This can be converted into an extinction value by using the constant of proportionality R_λ given by the adopted extinction law:

$$A_\lambda = \mathrm{R}_\lambda E(\mathrm{H}-\mathrm{K}). \tag{2.7}$$

This method can also be generalised for more than two bands as shown in Lombardi and Alves (2001) which further enhances its accuracy. An example of this technique is shown in Figure 2.3 which depicts the Pipe nebula in dust extinction.

Compared to dust emission observations, there are several advantages to this technique: lower wavelength observations in the near- compared to the far-infrared can be carried out from the ground and are able to achieve a higher resolution due to a smaller Rayleigh criterion, dust extinction does

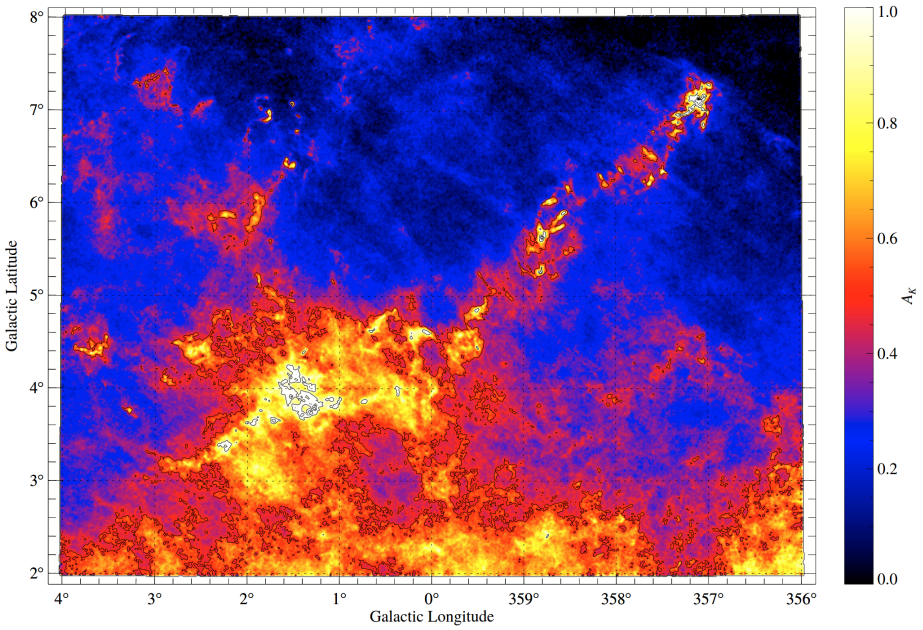

Figure 2.3: Dust extinction map of the Pipe nebula (Lombardi et al., 2006).

not depend on the dust temperature and the opacity in the near-infrared is better known compared to longer wavelengths. But there are also disadvantages: as the opacity is higher in the near-infrared this method can only be used for relatively diffuse regions where the background stars are not completely extincted. Furthermore, in order to obtain a complete map, one needs a clean field of background stars which is often not the case.

2.2.3 Molecular lines

The most revealing observations, but also the most complicated to interpret, are molecular line observations. The transitions of lowest energy and therefore the easiest to excite are rotational transitions where only a change in angular momentum quantum number of $J \pm 1$ is allowed for dipole radiation with J=1-0 being the lowest and therefore most prominent transition. In homonuclear molecules such as H_2, this transition is forbidden and it can only decay via the J=2-0 quadrupol with a greatly reduced probability. The most abundant molecule after molecular hydrogen is carbon monoxide (CO) which is excited at temperatures of around 5.5 K. It comes in several different isotopes of which $^{12}C^{16}O$ is the most abundant and emits at 2.6 mm, followed by $^{13}C^{16}O$ and $^{12}C^{18}O$ which are used as optically thin tracers for higher density gas. Popular tracers of higher density regions are NH_3, HCN, HCO^+ and N_2H^+.

In order to calculate the energy emission rate of a line, one needs to know the level populations of the respective line transition. As a simple example, we consider a system with two bound states given by the upper and lower level u and l with respective statistical weights g_u and g_l. They are separated by the energy ΔE and the number densities of molecules in the respective state are given by n_u and n_l. The species has a number density $n = n_l + n_u$ in a gas of total number density $n_{\rm tot}$ and temperature T. We ignore chemical reactions and only consider the optically thin regime. The number density of

molecules in the upper level changes as individual molecules transition from the lower to the upper state via collisional excitation and absorption and from the upper to the lower state via spontaneous emission, stimulated emission and collisional de-excitation. The collisional rates of excitation and de-excitation are given by $k_{lu}\, n_{\rm tot} n_u$ and $k_{ul}\, n_{\rm tot} n_l$ and the rate of spontaneous and stimulated emission as well as absorption are given by the respective Einstein coefficients $A_{ul} n_u$, $B_{ul} I_\nu n_u$ and $B_{lu} I_\nu n_l$, where I_ν is the specific intensity of the local radiation field at the frequency of the transition. As radiative and collisional transitions occur on a much shorter timescale than any timescale of interest in the ISM, we assume that the level populations have reached an equilibrium. Thus the rates equalise to:

$$k_{lu}\, n_{\rm tot} n_u + B_{lu} I_\nu n_l = k_{ul}\, n_{\rm tot} n_u + B_{ul} I_\nu n_u + A_{ul} n_u. \tag{2.8}$$

For a high total density $n_{\rm tot}$, radiative transition rates are negligible compared to collisional ones and the system reaches local thermodynamic equilibrium where the levels are populated according to a Boltzmann distribution. Thus, we can determine a general relation between the collisional rates:

$$\frac{k_{lu}}{k_{ul}} = \frac{n_u}{n_l} = \frac{g_u}{g_l} e^{-\Delta E / k_B T}. \tag{2.9}$$

Furthermore, we assume that the gas is optically thin which allows us to neglect the ambient radiation field. Therefore, the rates of stimulated emission and absorption are small in comparison, the radiation is dominated by spontaneous emission and we can simplify Equation 2.8 to

$$\frac{n_u}{n_l} = \frac{(g_u/g_l) e^{-\Delta E/k_B T}}{1 + A_{ul}/(k_{ul}\, n_{\rm tot})} = \frac{(g_u/g_l) e^{-\Delta E/k_B T}}{1 + n_{\rm crit}/\, n_{\rm tot}} \tag{2.10}$$

where $n_{\rm crit} = A_{ul}/k_{ul}$ is the critical density. For densities much higher than $n_{\rm crit}$, the level population is close to the thermal equilibrium and for densities much lower than $n_{\rm crit}$, the upper state is underpopulated compared to the thermal equilibrium. The fraction of molecules which populate the upper level is given by

$$\frac{n_u}{n} = \frac{g_u e^{-\Delta E/k_B T}}{1 + e^{-\Delta E/k_B T} + n_{\rm crit}/n_{\rm tot}}. \tag{2.11}$$

For densities much lower than $n_{\rm crit}$, most molecules have time to emit a photon. The second term in the denominator dominates and the fraction simplifies to

$$\frac{n_u}{n} \approx g_u e^{-\Delta E/k_B T} \frac{n_{\rm tot}}{n_{\rm crit}}, \tag{2.12}$$

which means that the fraction of molecules in the upper state increases with density. However, for densities larger than $n_{\rm crit}$, the system reaches local thermodynamic equilibrium with a fixed level distribution given by Equation 2.9 as almost all molecules are de-excited by collisions. The second term in the denominator goes to zero and the fraction of molecules in the upper state reaches the constant value

$$\frac{n_u}{n} \approx \frac{g_u e^{-\Delta E/k_B T}}{1 + e^{-\Delta E/k_B T}} = const \tag{2.13}$$

The consequence of the latter is that the emitted flux per molecule reaches a maximum when the total density reaches the critical density. Thus, assuming that there is a constant fraction of the molecule throughout the cloud, the total emitted flux becomes proportional to the total column density. For total densities below the critical density, the emitted flux is negligible and as different isotopes and different

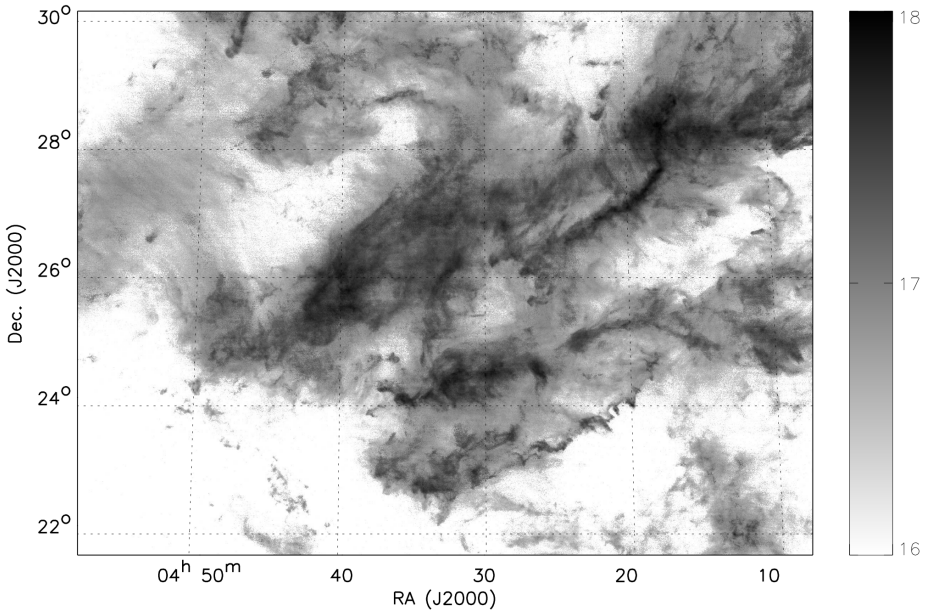

Figure 2.4: Logarithmic $^{12}C^{16}O$ column density map of the Taurus molecular cloud form Goldsmith et al. (2008).

molecules have their own distinct critical density. Thus, in the case that one can observe certain molecules transition already reveals information about the volume density of the gas and allows the determination of the density structure of the cloud. For instance, the $^{12}C^{16}O$(J=1-0) transition is a low density tracer with a critical density of around $10^3\,\mathrm{cm}^{-3}$ and the HCN(J=1-0) transition a high density tracer with a critical density of around $10^5\,\mathrm{cm}^{-3}$. An example of an observation of the Taurus molecular cloud in $^{12}C^{16}O$ is shown in Figure 2.4.

Note that this derivation is only valid for optically thin tracers. Many of the strongest lines are optically thick and one only can observe the surface of the cloud. Another effect of optically thick gas is that one can no longer ignore stimulated emission and absorption which reduces the effective critical density. Furthermore, there are also chemical changes which depend on density such as the freeze-out of molecules onto dust grains at high densities which leads to a depletion of the species. This means that chemical abundances and excitation conditions can vary drastically throughout a cloud of gas compared to a relatively constant dust-to-gas ratio.

Another important piece of information one can derive from molecular line observations is the velocity dispersion of the gas, as there is a one-to-one mapping of the line-of-sight velocity and frequency due to Doppler shifting. For optically thin gas, where other broadening processes do not play a role, one can determine the range of turbulent motions since they typically produce a Gaussian distribution around the mean bulk flow. In order to measure the amount of non-thermal motion, one has to subtract the thermal broadening from the line profile. The thermal broadening is produced by the Maxwellian velocity distribution of the gas at temperature T which gives an additional width of $\sqrt{k_B T/m}$ where m is the molecular mass. Therefore, it is essential to measure the temperature of the gas independently which is possible by observing multiple lines of the same species.

2.3 Temperature of the cold ISM

Molecular line observations show that the cold ISM has extremely low temperatures of around 10 K. There are several heating and cooling processes active in the ISM. The sum of the rates of the different processes give the equilibrium temperature. This section gives a short overview of the most dominant processes in the dense ISM.

2.3.1 Heating processes

There are assumed to be two important heating processes, the grain photoelectric effect in the atomic phase and cosmic ray heating in the molecular phase. In the atomic phase in the outer layers of a molecular cloud, photons in the far ultraviolet (FUV) with energies of about $8 - 13.6\,\mathrm{eV}$ eject fast electrons from dust grains via the photoelectric effect. These in turn thermalise and heat the surrounding gas. The heating rate per hydrogen nucleus is given by (Bakes and Tielens, 1994)

$$\Gamma_{\mathrm{PE}} \sim 4.0 \cdot 10^{-26} \chi_{\mathrm{FUV}} \mathrm{Z}_d e^{-\tau_d}\ \mathrm{erg\ s^{-1}} \tag{2.14}$$

where χ_{FUV} is the intensity of the FUV radiation field scaled to its value in the Solar neighborhood, Z_d is the dust abundance scaled to its value in the Solar neighborhood and τ_{FUV} is the dust optical depth of FUV photons. The optical depth of FUV photons increases rapidly in the interiors of molecular clouds, strongly suppressing photoelectric heating to values of about $10^{-29}\,\mathrm{erg\ s^{-1}}$ per hydrogen nucleus. Therefore, there is a more important heating process in the centre of clouds. As cosmic rays are relativistic particles they are able to penetrate far into the cloud interiors. They interact with the molecular gas by ionizing molecular hydrogen and releasing electrons with typical energies of about 30 eV. These then distribute their energy by secondary ionisation, dissociation and excitation of hydrogen molecules. Additionally, there is also chemical heating caused by reactions of the ionised hydrogen molecules (see e.g. Glassgold et al. (2012) for a full discussion). In total, the energy released per cosmic ray ionisation is approximately $\Delta E \sim 13\,\mathrm{eV}$ and together with an observational cosmic ray ionisation rate derived from the abundance of $\mathrm{H_3^+}$ of about $\zeta_{\mathrm{H}} \sim 10^{-16}$ per hydrogen nucleus (Indriolo and McCall, 2012) gives the total heating rate per hydrogen nucleus by cosmic ray ionisation as

$$\Gamma_{\mathrm{CR}} = \zeta_{\mathrm{H}} \Delta E \sim 2.0 \cdot 10^{-27}\,\mathrm{erg\ s^{-1}}. \tag{2.15}$$

2.3.2 Cooling processes

The two main cooling processes in molecular clouds are dust cooling and cooling by molecular line emission. Dust grains cool by emitting thermal radiation but can only cool the gas if the densities are high ($10^4 - 10^5\,\mathrm{cm^{-3}}$) and the dust couples thermally to the gas via collisions. At lower densities, the main cooling process is molecular line emission and the most important molecule contributing to the cooling is CO due to its abundance. As stated earlier, at low temperatures the only transitions that are important are between the rotational levels. Since photons need to leave the molecular cloud in order to cool the material, line cooling is strongly suppressed for low level transitions as the low rotational levels of CO are the most highly populated and therefore have the largest optical depths. As the optical depth depends on the column density of the path of the photon and a large velocity dispersion can shift the emission due to the Doppler effect and thus reduce the probability of reabsorption, the cooling rate is a complicated function of position within the cloud and is generally largest at the edge within one optical depth. Consequently, the cooling rate depends on the cloud geometry and has to be modeled

numerically. However a good estimate can be given by considering the cooling rate of the transition which is marginally optically thin as it is still close to a thermal equilibrium but its photons can escape the cloud. The cooling rate of CO decreases with lower temperature and reaches a value of around $\Lambda_{\mathrm{CO}} \sim 10^{-27}\,\mathrm{erg\,s^{-1}}$ at about 10 K where it equalises the heating rate by cosmic rays (Goldsmith and Langer, 1978). As both photoelectric and cosmic ray heating are approximately independent of the temperature and the cooling rate changes with T to a power of $p \sim 2-3$, a change in the heating rate of a factor of a will only change the equilibrium temperature by a factor of $a^{1/p}$. Therefore, we assume the cold ISM to be close to isothermal at a temperature of 10 K. Furthermore, we can calculate the time it takes to reach this temperature after being pushed out of equilibrium for instance by contraction. The characteristic cooling time is

$$t_c = \frac{e_{\mathrm{th}}}{\Lambda_{\mathrm{CO}}} \approx \frac{1}{2}\left(\frac{3}{2}kT\right)/\Lambda_{\mathrm{CO}} \approx 3.2\left(\frac{T}{10\,\mathrm{K}}\right)\,\mathrm{kyr} \tag{2.16}$$

where e_{th} is the thermal energy per hydrogen nucleus and T is the temperature of the state out of equilibrium. Comparing this value to a mechanical time scale for example the sound crossing time in a filament $t_{\mathrm{cr}} = 0.2\,\mathrm{pc}/c_s = 0.5\,\mathrm{Myr}$, it becomes clear that heating caused by compressions such as shocks cannot push the gas significantly out of equilibrium.

3 Observing filamentary structure

The importance of filaments, i.e. elongated overdensities usually with an aspect ratio greater than 5-10, in the ISM and their possible connection to prestellar core formation has already been recognised for more than thirty years. Initial dust extinction observations of interstellar filaments, such as those by Schneider and Elmegreen (1979), already showed regular condensation patterns of globules. Since then, filaments have also been detected in diffuse as well as dense gas not only in actively star forming molecular clouds, for instance Taurus (Abergel et al., 1994; Mizuno et al., 1995; Falgarone et al., 2001; Hartmann, 2002; Nutter et al., 2008; Goldsmith et al., 2008) and Orion A (Bally et al., 1987; Chini et al., 1997; Johnstone and Bally, 1999), but also in quiescent regions such as the Polaris flare (Hily-Blant and Falgarone, 2007). On larger scales and further distances, filamentary structure has also been observed in dark clouds (Perault et al., 1996; Alves et al., 1998; Egan et al., 1998; Hennebelle et al., 2001; Peretto and Fuller, 2009; Miettinen and Harju, 2010), some of which are considered to host cluster and massive star formation. Moreover, on a higher hierarchical level, there are filaments which form "hubs", locations of star forming overdensities where filaments converge and overlap (Myers, 2009).

Recent years have shown a renaissance in the field of filamentary structure led by the observations of the *Herschel* Space Observatory (Pilbratt et al., 2010). These were a major improvement on previous dust emission observations due to its simultaneous access to far infrared and submillimeter wavelengths ($55 - 672\,\mu$m) and its superior spacial resolution as a result of its larger diameter compared to the former infrared satellite missions such as *Spitzer*. One goal of its mission was to map the structure of molecular clouds ($\geq 10\,$pc) down to the scale of individual cores and protostars ($\leq 0.1\,$pc) as done in the *Gould Belt* study. It revealed a web-like filamentary structure which is omnipresent in every molecular cloud independent of star-forming activity or mass (André et al., 2010; Arzoumanian et al., 2013; André et al., 2014), for example in Figure 3.1 which shows Aquila together with prestellar objects. The filaments detected by *Herschel* all seem to share common properties. It is remarkable that the prestellar cores predominantly align with the densest filaments, where estimates of the line-mass exceed the maximum possible value of hydrostatic equilibrium (see Chapter 4). This shows that filaments and cores are two interconnected key steps in the star formation process. While the structure in low-mass star-forming regions appears in general to be well ordered with filaments being quasi linear and co-aligned with their parent clouds, the situation is not as clear in high-mass clouds. Here, filaments seem to form more disorganised networks while being more linear in high column density regions, as observed in Vela C (Hill et al., 2011) and the Rosette cluster (Schneider et al., 2012), where the latter shows star formation predominantly occurring in filament junctions. Furthermore, filaments appear to share the same characteristic central width of 0.1 pc Arzoumanian et al. (2011), which is presently an ongoing controversial topic which is discussed in Section 3.3).

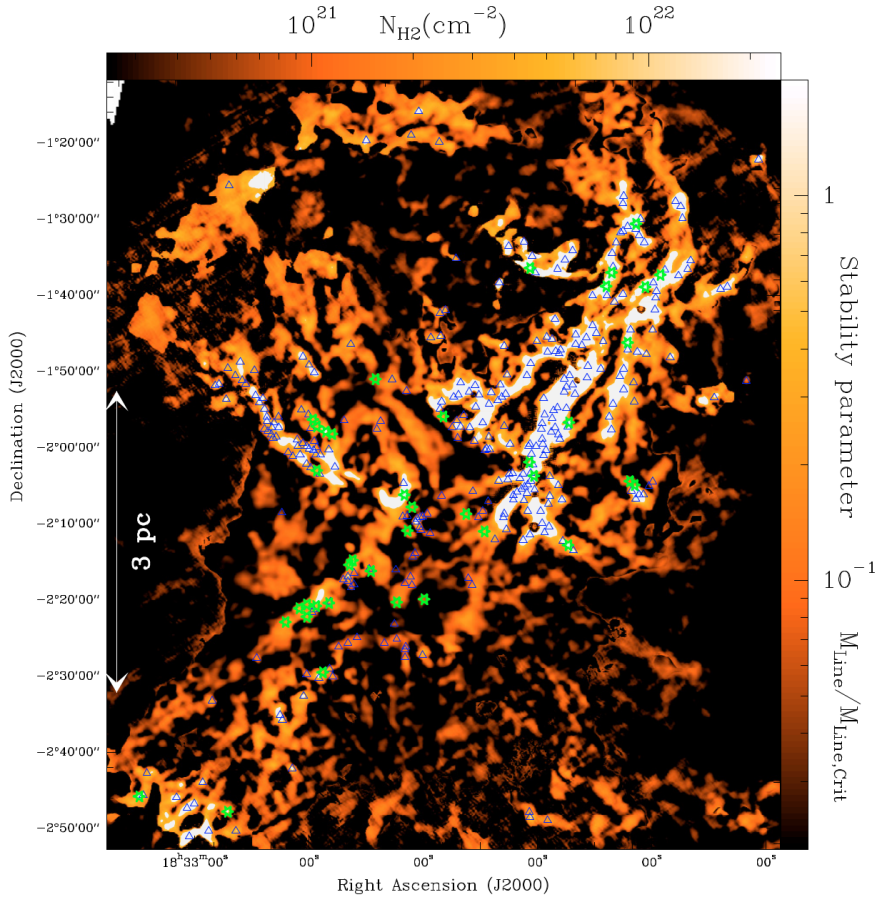

Figure 3.1: Column density map of Aquila (André et al., 2010) where the contrast has been enhanced by using a curvelet transform (Starck et al., 2003). The colour scale is in approximate units of the critical line-mass (see Chapter 4). The green stars and blue triangles give the positions of Class 0 and prestellar cores identified by Bontemps et al. (2010) and Könyves et al. (2010), respectively.

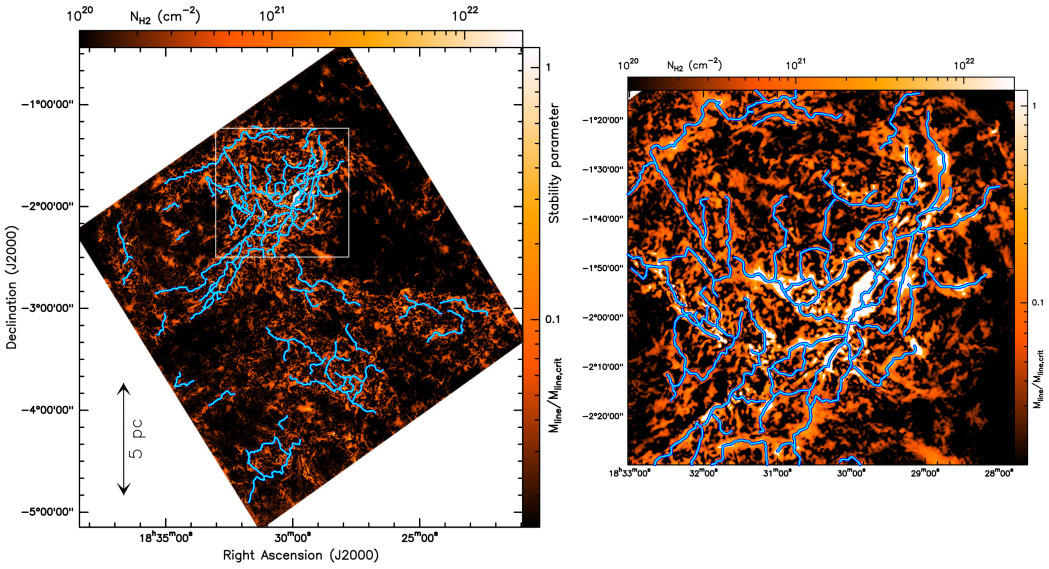

Figure 3.2: Network of filaments in the Aquila cloud complex as detected by the DISPERSE algorithm (Könyves et al., 2015). The colour scale is the same as in Figure 3.1.

3.1 Ways to detect filamentary structures

In order to analyse filamentary structure further, e.g. by means of a simple task such as creating an average density profile perpendicular to its axis, one has to identify the ridge and extent of the filament independent of its scale, which is not easy in itself given observational data which suffers from background noise. Although some authors identify filaments by eye and approximate them by straight lines which often works well enough, considerable effort has been made in identifying filamentary structure automatically. To this end a filament detection algorithm is typically used. In principle, these techniques can not only be applied to observational but also simulated data in two and three dimensions.

One popular example is the DISPERSE algorithm (Sousbie, 2011) which applies discrete Morse theory. The method uses gradients of the discrete density field obtained using the Delaunay tessellation field estimator (Schaap and van de Weygaert, 2000) to identify critical points (maxima, minima and saddle points in 2D) defining critical surfaces and volumes in 2D and 3D density fields whose interfaces determine the filamentary structures. Poisson noise in the data can be handled by setting a persistence level which smoothes the topology by excluding critical points. A typical result of the algorithm is shown in Figure 3.2.

Other methods make use of the local Hessian matrix in order to identify filamentary structure (Schisano et al., 2014) as applied by the *Hi-GAL* survey team (Molinari et al., 2010). At the ridge of filamentary structures the eigenvalues of the Hessian matrix are both negative, with the eigenvector of the smaller and larger curvature giving the direction along and perpendicular to the filament axis, respectively. The noise of the observation is handled by applying a Gaussian smoothing kernel to the image.

A different approach is chosen by the GETFILAMENTS algorithm Men'shchikov (2013) which distinguishes filaments by decomposing the original image on different spacial scales. The signal is

continuously smoothed by an increasing Gaussian kernel and subtracted from the image. Filaments are then identified as structures which do not significantly increase in length but have widths equal to the smoothing beam over several spatial scales.

Finally, the FILFINDER algorithm (Koch and Rosolowsky, 2015) detects filaments by using adaptive thresholding on flattened and smoothed data which discards pixels which are not a local maximum in intensity. This creates a mask of filamentary structure and background noise where the latter is removed by a globally thresholded mask. The filamentary structures are then broken down to their skeletal form by using a Medial Axis Transform. This method allows even very faint structures to be detected.

In general, all methods do give results which agree well with each other. All algorithms reliably identify the most prominent filaments present in an image. However, there are some differences when it comes to the sensitivity of detection, for instance in the FILFINDER algorithm, and it is important to define what physical entities one is interested in.

3.2 Observed density profiles - flatter than expected

The theoretical prediction of the hydrostatic profile of a cylinder of gas is given by a Plummer-like density profile (Plummer, 1911) with a central region $R_{\rm flat}$ of an approximately flat density $\rho_{\rm flat}$ which drops as a power-law with index $\eta = 4$ in the envelope (Equation 4.16):

$$\rho(r) = \rho_{\rm flat}\left[\frac{R_{\rm flat}}{\left(R_{\rm flat}^2 + r^2\right)^{\frac{1}{2}}}\right]^{\eta} = \frac{\rho_{\rm flat}}{\left(1 + r^2/R_{\rm flat}^2\right)^{\frac{\eta}{2}}} \tag{3.1}$$

which transforms to a column density profile (Arzoumanian et al., 2011) of

$$\Sigma(r) = A_{\rm p}\frac{\rho_{\rm flat}R_{\rm flat}}{\left(1 + r^2/R_{\rm flat}^2\right)^{\frac{\eta-1}{2}}} \tag{3.2}$$

where $A_{\rm p}$ is a finite constant factor which depends on the inclination of the filament on the plane of the sky. In contrast to the theoretical prediction, fits to the global average density profile of most dust observations detected a power-low index of $\eta \approx 1.5 - 2.5$ (Alves et al., 1998; Lada et al., 1999; Arzoumanian et al., 2011; Contreras et al., 2013; Palmeirim et al., 2013). An example from Arzoumanian et al. (2011) is given in Figure 3.3, which shows the column density profile of a high line-mass filament in IC 5146. Density profiles determined by radiative transfer modeling have found larger best-fit values (Nutter et al., 2008). The same is true for molecular line observations (Hacar and Tafalla, 2011; Pineda et al., 2011; Bourke et al., 2012; Tafalla and Hacar, 2015), even for identical filaments measured by dust emission. However, they often cannot distinguish different indices as they do not trace the filament signal out far enough (Panopoulou et al., 2014; Henshaw et al., 2017). However, in high-mass star forming regions such as Orion, the signal is better matched by a Gaussian profile (Hacar et al., 2018). There are several possible explanations for the discrepancy between theory and observation.

One potential reason is that dense filaments are not exactly isothermal but have a polytropic exponent γ close to unity and are undergoing gravitational collapse. Models of collapsing filaments predict a density scaling $\rho \propto r^{-\frac{2}{2-\gamma}}$ for large radii (Kawachi and Hanawa, 1998; Nakamura and Umemura,

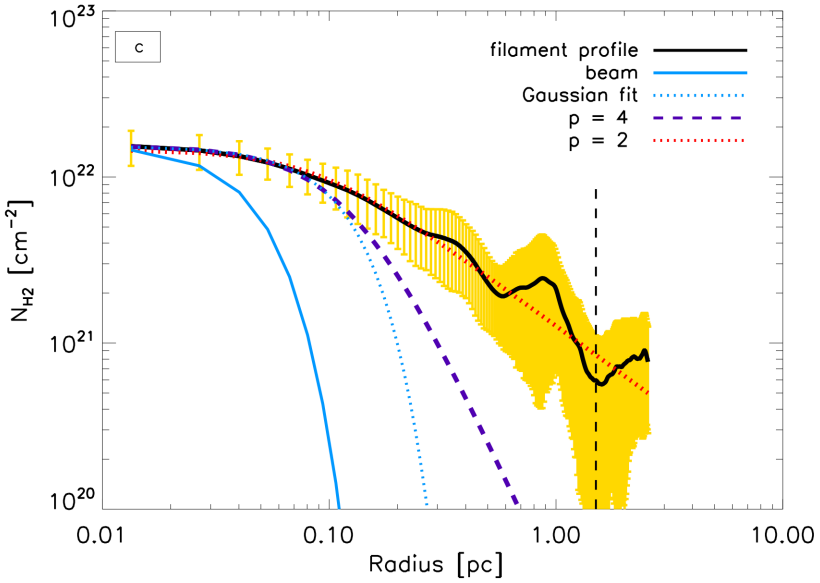

Figure 3.3: Average column density profile of a filament in IC 5146 (Arzoumanian et al., 2011) given by the black solid line. The yellow error bars show the dispersion of the profile along the filament. The best-fit Plummer-like profiles are plotted by the dotted red line for an index of $\eta = 2$ and by the dashed purple line for an index of $\eta = 4$.

1999) and observations of dust temperature profiles indeed show a good agreement with polytropic indices marginally lower than unity (Arzoumanian et al., 2011; Palmeirim et al., 2013). Along similar lines, it has been shown that the observed density profile can be well reproduced by hydrostatic models with a negative index polytrope with $1/3 \lesssim \gamma \lesssim 2/3$ (Toci and Galli, 2015a), which indicates either an increasing temperature profile for large radii or a dominant non-thermal contribution to the pressure such as magnetohydrodynamic turbulence. Moreover, theoretical models which include a toroidal magnetic field with a constant mass to flux ratio predict a flatter density profile of $\eta \approx 1.8 - 2.0$ (Fiege and Pudritz, 2000a). The toroidal magnetic field wraps around the filament and helps to confine the gas. However, the magnetic field structure inside filaments is unknown and very hard to observe directly. Another straightforward reason is given by the fact that the density profile of pressure bound filaments is truncated at the boundary radius. As the theoretical profile varies smoothly from the flat inner region to a steep $\eta = 4$ power-law at large radii, the locally measured density profile at the cut-off radius is indistinguishable from a profile with a flatter index, in particular for filaments at low line-masses where the inner region is larger (Fischera and Martin, 2012). However, most observations show a profile which is wide enough to distinguish both cases. An alternative explanation comes from simulations of filaments forming in a turbulent medium as they also often exhibit a density drop-off with indices around 2 (Gómez and Vázquez-Semadeni, 2014; Kirk et al., 2015; Smith et al., 2014). Here, filaments form as a result of two planar shocks either from turbulent initial condition or by continuous driving of the material. In contrast, if there are no turbulent motions present in the simulation, filaments formed by gravitational collapse do not show the observed density scaling (Federrath, 2016).

Nevertheless, re-analysis of the Herschel data revealed that the observed index of the filament profile depends strongly on the position of measurement along the filament, with sections indeed

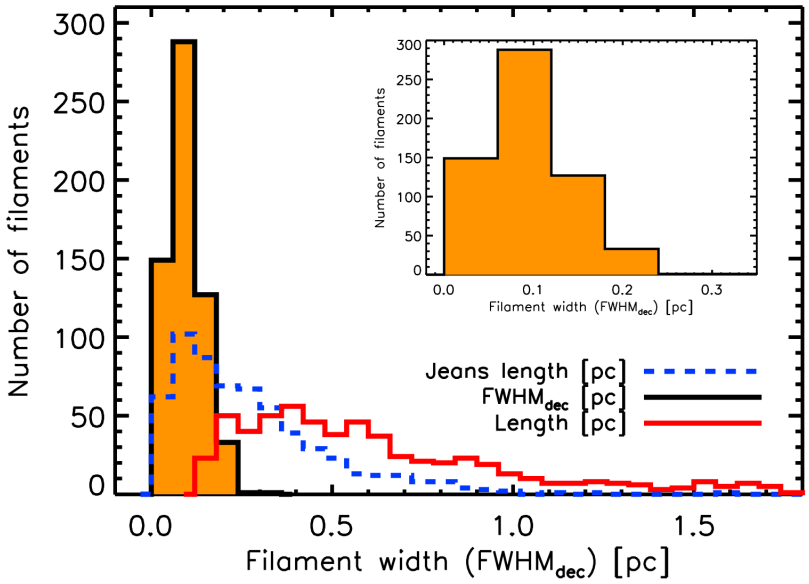

Figure 3.4: Histogram of measured FWHM of Gaussian fits to averaged filament profiles observed by *Herschel* (Arzoumanian et al., 2019). The distribution has a sharp peak at 0.10 pc with a standard deviation of 0.05 pc, which is a much narrower variation than other filament parameters exhibit.

showing an isothermal profile (Howard et al., 2019). Thus, it cannot be excluded that the isothermal model is not applicable at least for hydrostatic sections of the filament.

3.3 Is there a universal inner width of filaments?

The existence of a characteristic width, a constant extent of the inner filament region, has been a very controversial topic as there is no straightforward theoretical basis to support it. *Herschel* results have shown evidence that Gaussian fits to the inner profile of observed filaments in dust emission have a very narrowly peaked distribution of full widths at half maximum (FWHM) with a mean of 0.1 pc and a very small standard deviation of 0.05 pc over a wide range of column densities (Arzoumanian et al., 2011, 2019). This is not only true for low column density, low mass regions independent of their star formation activity as seen in the different clouds of Chamaeleon (Alves de Oliveira et al., 2014), in quiescent regions such as the Polaris flare (Men'shchikov et al., 2010; Miville-Deschênes et al., 2010; Ward-Thompson et al., 2010) or in actively star forming regions such as IC 5146 (Arzoumanian et al., 2011), Musca (Cox et al., 2016), the Pipe nebula (Peretto et al., 2012) and Taurus (Kirk et al., 2013; Palmeirim et al., 2013; Marsh et al., 2014, 2016), but also for high column density, actively cluster forming, intermediate and high mass regions such as the Aquila rift (Bontemps et al., 2010; Könyves et al., 2010; Men'shchikov et al., 2010; Könyves et al., 2015) and Orion B (Schneider et al., 2013).

Below a maximum value based on the ambient pressure, theoretical predictions allow a wide range of values of the scale height for a varying local line-mass. However, there is a valid reason for assuming the existence of a characteristic scale. The observed characteristic scale is roughly in agreement with the scale where the Larson's linewidth-size relation (Larson, 1981) breaks down and there is a transition from supersonic to subsonic motions (Vázquez-Semadeni et al., 2003). Below this sonic

scale, supersonic turbulence of compressible gas consisting of an ensemble of shocks as described by Burgers (1948), is incapable of producing overdensities and a "transition to coherence" is observed (Goodman et al., 1998; Pineda et al., 2010).

Nevertheless, several observations in various environments did not obtain the same characteristic width as the *Herschel* measurements, with high density tracers showing thinner widths (Pineda et al., 2011; Fernández-López et al., 2014; Lee et al., 2014; Dhabal et al., 2018; Hacar et al., 2018; Suri et al., 2019) and low density tracers showing broader widths (Panopoulou et al., 2014) of the inner region. Moreover, dust observations of massive filaments (Henshaw et al., 2017) also obtained differing values, even for measurements taken by the *Herschel* satellite (Hennemann et al., 2012; Schisano et al., 2014). The existence of a characteristic filament width has been questioned by the studies of Smith et al. (2014) and Panopoulou et al. (2017) which both note that the obtained FWHM depends on the applied fitting range of the Gaussian to the observed Plummer-like column density profile. However, the study by Arzoumanian et al. (2019) shows that the distribution of inner widths remains the same if measured by fitting Plummer-like profiles directly. Another important point of criticism is the lack of a characteristic scale in the power spectrum of the Polaris region (Miville-Deschênes et al., 2010) in which a characteristic width should leave its imprint. This issue has been addressed in the study of Roy et al. (2019) which shows that as long as the total imprint of a characteristic length scale is not strong enough, which is indeed the case for the *Herschel* observations, its signal in the power spectrum can be hidden below the global imprint of the image. Finally, the study of Panopoulou et al. (2017) re-analysed the filament widths in the Polaris, Aquila and IC 5146 maps and conclude that they actually measure a wide distribution of filament widths along a single filament and only obtain a sharp peak when plotting the distribution of average filament widths. They argue that this is due to the central limit theorem and that the sharp peak only represents the mean of filament widths with a large spread even within a single filament.

Taking everything into account, theory still has to explain why the mean of the distribution is around 0.1 pc independent of region. If it is not the end of the turbulent cascade, an alternative straightforward answer would be that the background pressure in all clouds observed by *Herschel* is comparable. A similar mean FWHM is then a consequence of its weak dependence on variations of the background pressure (Fischera and Martin, 2012). However, the background pressure is likely influenced by several different mechanisms such as accretion and magnetic fields. Therefore, a characteristic width, even if it only represents a mean filament width, still remains an unsolved mystery.

3.4 Fibres and striations - substructure of filaments

Parallel to the novel *Herschel* observations, there was another discovery which revolutionised our view of star-forming filaments - the existence of substructure in filaments (Hacar et al., 2013), also known as "fibres". Rather than being single monolithic entities, some filaments show multiple velocity coherent components in the line-of-sight velocity (Hacar and Tafalla, 2011; Fernández-López et al., 2014; Lee et al., 2014; Panopoulou et al., 2014; Hacar et al., 2017, 2018). Velocity coherence means that the velocity structure of the fibre gas does not show the characteristics of a turbulent velocity field, such as following the linewidth-size relation (Larson, 1981), and can be correlated over large scales. An example is given in Figure 3.5 which shows line-of-sight measurements in position-position-velocity (PPV) space, where two axes represent the positions in the sky with the third axis showing the line-of-sight velocity. As one can see, the data points form connected systems in velocity. This means that the gas has decoupled from the supersonic turbulent cloud regime and formed inherently sub- and

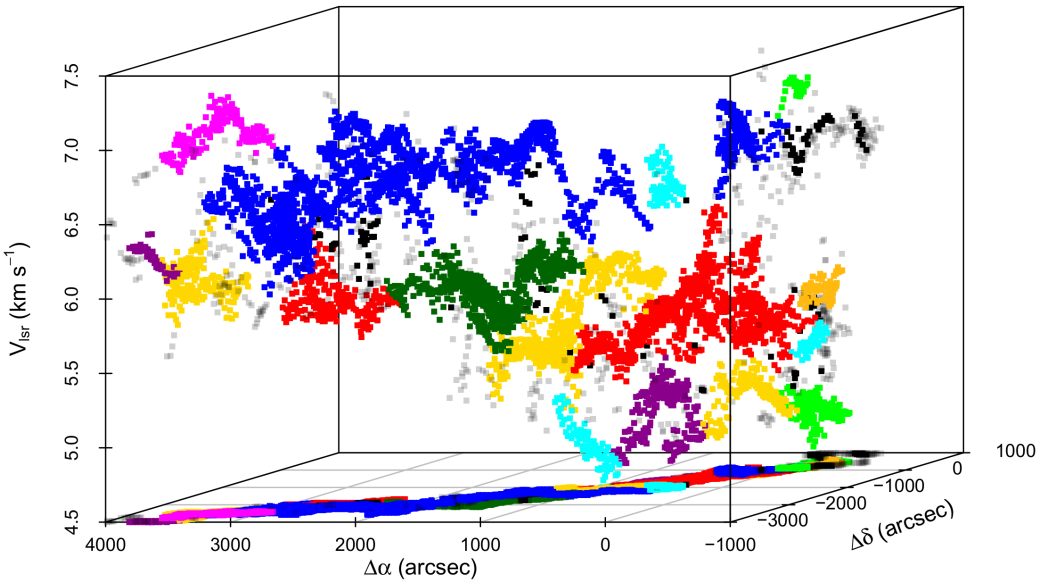

Figure 3.5: Line-of-sight velocities of the Taurus B211-B213 region in position-position-velocity space (Hacar et al., 2013). The data points are assigned to individual fibres using a friends-of-friends algorithm and coloured accordingly.

transonic structures matching the picture of the end of the turbulent cascade. However, in contrast to forming single filaments, fibres often occur in bundles, appearing as a single supersonic entity in the line-of-sight velocity of lower density tracers due to line blending (Hacar et al., 2016a). How they form tangled bundles is still unclear but there are several models which describe their formation. One the one hand, in the "fray and fragment" scenario (Tafalla and Hacar, 2015) the filament first forms as a result of colliding flows as seen in simulations (Vazquez-Semadeni, 1994; Padoan et al., 2001; Hennebelle, 2013; Federrath, 2016) and consequently splits into parallel fibres by the sweep up of residual turbulent motions while being concentrated by gravitational forces, a process which also has been observed in numerical simulations (Kirk et al., 2015; Moeckel and Burkert, 2015; Clarke et al., 2017). On the other hand, other numerical studies have found fibres that form independently and are collected in extended filamentary structures (Smith et al., 2014, 2016; Zamora-Avilés et al., 2017). Independent of the formation mechanism, an important question is whether every velocity coherent structure found in PPV space has a physical counterpart. Simulations show that this condition only applies for the densest structures and that there is a substantial contamination of the projection of distinct physical structures in the line-of-sight (Zamora-Avilés et al., 2017; Clarke et al., 2018).

Another fundamental discovery is that of low-density parallel filamentary structures in the diffuse parts of molecular clouds called striations which are mostly arranged perpendicular to high density filaments (Goldsmith et al., 2008; Narayanan et al., 2008; Palmeirim et al., 2013) as shown in Figure 3.6. The most popular explanation is that they are formed by accretion flows along magnetic field lines, the path of least resistance (Miville-Deschênes et al., 2010; Palmeirim et al., 2013; Alves de Oliveira et al., 2014; Cox et al., 2016; Shimajiri et al., 2019). Observations of dust polarisation have shown that filaments often appear either parallel or perpendicular to the magnetic field (Li et al., 2014) with low-density striations mainly oriented parallel and higher density star-forming filaments roughly

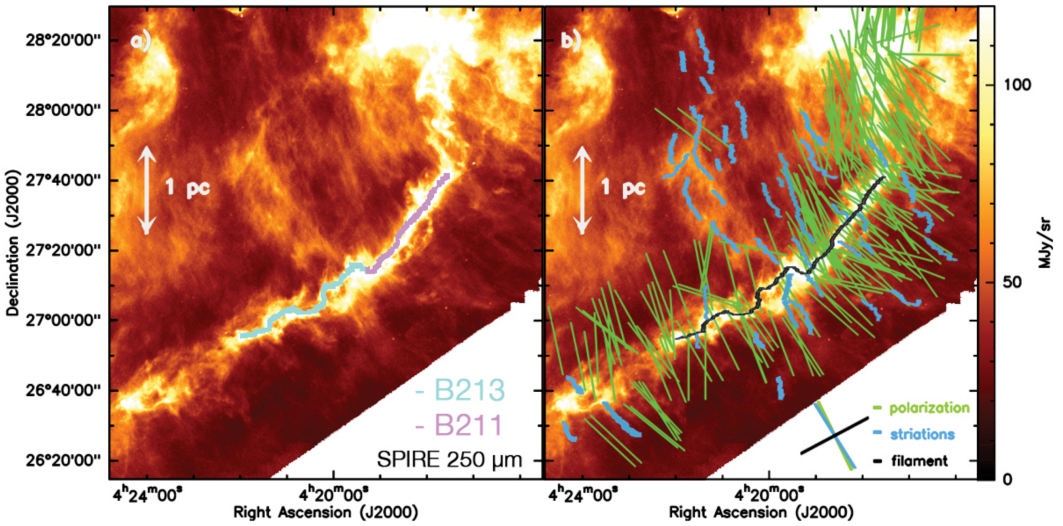

Figure 3.6: *Herschel* map of the Taurus B211/B213/L1495 region (Palmeirim et al., 2013) together with optical and infrared polarisation vectors given by the green lines (Heyer et al., 2008; Chapman et al., 2011). The projected magnetic field lines are approximately oriented perpendicular to the dense filament, similar to the low-density striations in blue.

oriented perpendicular to the field lines (Chapman et al., 2011; Planck Collaboration et al., 2016), a pattern which is well reproduced in simulations (Hennebelle, 2013; Soler et al., 2013; Chen and Ostriker, 2014; Inutsuka et al., 2015; Zamora-Avilés et al., 2017; Gómez et al., 2018). An alternative model by Tritsis and Tassis (2016) explains the formation of striations as modes of fast magnetosonic waves. They further analyse the power-spectrum of these low-density perturbations which allows them to draw conclusions on the geometry of larger structures such as Musca (Tritsis and Tassis, 2018) and which acts as an independent measurement of the magnetic field strength (Tritsis et al., 2018) where other methods usually suffer from instrumental effects (see Crutcher (2012) for a review).

3.5 Cores and the fragmentation of filaments

Observations have shown that cores, gravitationally bound, local overdensities, form preferentially along the spine of filaments. Their density usually follows a Bonnor-Ebert-like (Ebert, 1955; Bonnor, 1956) density profile of an isothermal sphere (Johnstone et al., 2000; Alves et al., 2001; Tafalla et al., 2004; Roy et al., 2014) which does not necessarily imply that they are in hydrostatic equilibrium (Ballesteros-Paredes et al., 2003). Cores are either prestellar or protostellar depending on whether a protostar has formed or not. As they are dense compact objects, they can usually be identified by spherical objects of higher column densities, a relation also generally witnessed in simulations (Gong and Ostriker, 2011). Molecular line observations however suffer from the effects of freeze-out (Kuiper et al., 1996; Caselli et al., 1999), a depletion of the species due to freezing onto the surface of dust grains, and self-absorption in optically thick gas. Therefore, it is imperative to use low optical depth tracers which are resistant to freeze-out up to much higher densities, such as NH_3 or N_2H^+.

Dust continuum observations of low-mass filaments in nearby clouds have shown that cores preferentially form in the densest filaments above an extinction threshold of around $A_V \sim 8$ (André et al.,

2010) or a column density of $7 \cdot 10^{21}$ cm^2 which can be translated approximately to the critical line-mass for a temperature of 10 K, above which a filament is unstable. This suggests that core formation is tied to the radial collapse of filaments which would result in cores of similar masses and may be a good explanation for a mean stellar mass as a "base" of the initial mass function (IMF), the distribution of the number of stars formed with a particular stellar mass (Bastian et al., 2010). Indeed, there seems to be a close similarity between the prestellar core mass function (CMF) and the IMF (Motte et al., 1998; Johnstone et al., 2000; Stanke et al., 2006; Alves et al., 2007; Enoch et al., 2008; Könyves et al., 2010, 2015), where cores lose $\sim$ 30% of their mass in the protostellar phase, possibly due to outflows (Matzner and McKee, 2000). There even seems to be a similarity to a filament mass function and a filament line-mass function which shows the same Salpeter power-law of -1.5 (Salpeter, 1955) in the supercritical regime (André et al., 2019). However, the situation is more complicated. One the one hand, there are examples of filaments with ongoing core formation which lie below the critical threshold (Hacar and Tafalla, 2011; Hacar et al., 2013, 2017). On the other hand, in order to determine the core mass, one has to distinguish the core material from that of the ambient filament, a task which introduces large errors in the CMF (Pagani et al., 2015; Steinacker et al., 2016). Moreover, there are also many cases of massive filaments which greatly exceed the critical line-mass by factors of $\sim$ 100 and are therefore likely not in equilibrium or supported only by thermal pressure (Beuther et al., 2015; Contreras et al., 2016) and are forming massive stars and stellar clusters.

An interesting theoretical prediction is that of a regular fragmentation pattern which can be seen in the core distances. As discussed in the next chapter, linear perturbation theory shows that, depending on the line-mass, there is a fixed separation of a few times the scale height where overdensities grow fastest, also known as the fastest growing mode (Nagasawa, 1987). If the line-mass along a filament is uniformly distributed, this prediction leads to the expectation of regularly spaced cores along the filament axis. However, the observational evidence has been inconclusive. While the *Herschel* observations did not reveal a periodic core distance, other measurements not only found evenly spaced cores but even oscillations in the velocity structure which indicate accretion onto the cores, as shown in Figure 3.7 (Hacar and Tafalla, 2011). Although some studies report a mismatch between the theoretical expectation and observations where fragments are seen too close together to be explained by a simple thermal model (André et al., 2010) or are better fitted by a Jeans length spacing, especially for high line-mass filaments (Kainulainen et al., 2013; Takahashi et al., 2013; Lu et al., 2014; Wang et al., 2014; Henshaw et al., 2016; Teixeira et al., 2016; Kainulainen et al., 2017; Lu et al., 2018; Palau et al., 2018; Williams et al., 2018; Zhou et al., 2019), other filaments match remarkably well (Jackson et al., 2010; Miettinen, 2012; Busquet et al., 2013; Beuther et al., 2015; Contreras et al., 2016; Kainulainen et al., 2016). There are obvious effects which can impact the expected core distance and have to be taken into account, for instance the inclination of the filament in the plane of the sky and processes which stabilise the filament and alter its radial extent such as turbulence or magnetic fields. Moreover, filaments are susceptible to gravitational collapse along their axis (Pon et al., 2012; Clarke and Whitworth, 2015) which could not only reduce the distances between cores, but also can lead to clumps forming at the ends of the filament due to gravitational focussing, an effect known as "edge effect" (Bastien, 1983; Burkert and Hartmann, 2004; Pon et al., 2012).

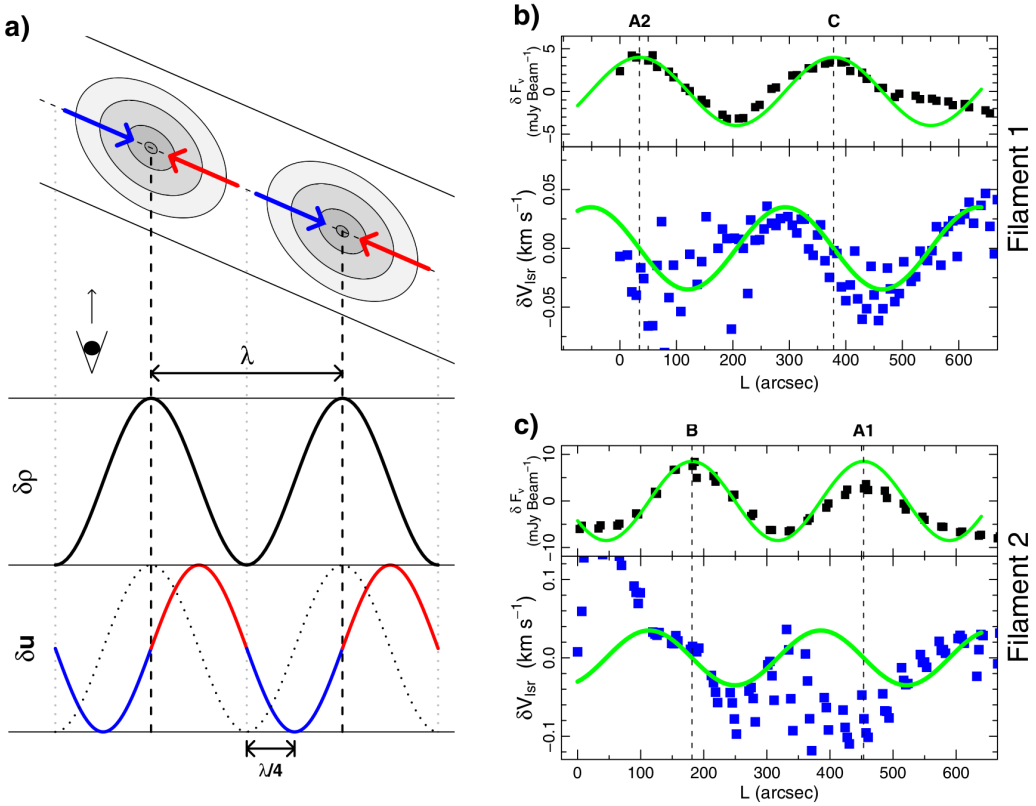

Figure 3.7: Density and velocity perturbations in two filaments of the L1517 region in Taurus (Hacar and Tafalla, 2011). In b) and c) respectively, the upper panel shows the mm continuum flux compared to its mean in black as a proxy for the density perturbation and the lower panel the variation in the line-of-sight velocity centroid compared to its mean. The phases of both perturbations are shifted by quarter of a wavelength which is expected for a flow of material onto the cores as demonstrated by the model in a).

4 Theoretical filament models

Filaments are mainly thought of as cylindrical configurations of self-gravitating gas. Theoretical models of filaments have been explored for nearly seven decades, initially due to their relevance for spiral arms in galaxies (Chandrasekhar and Fermi, 1953). Not only have solutions been found for their hydrostatic equilibrium, but also for their fragmentation behaviour under linear perturbations, both of which will be discussed here.

However, before going into the details of filament fragmentation, we briefly review the theoretical mechanisms of how filaments are assembled in the ISM themselves. For about thirty years, continuously driven turbulent box simulations have consistently shown that filamentary and sheet-like structure develops naturally due to the compression of the gas in the crossing of two planar shocks, even in the absence of gravity (Porter et al., 1994; Vazquez-Semadeni, 1994; Padoan et al., 2001). Gravity then acts on the denser structures which in turn leads to gravitational collapse and star formation (Ballesteros-Paredes et al., 1999; Klessen and Burkert, 2000; Tilley and Pudritz, 2004; Federrath, 2013, 2016). An example is given in Figure 4.1 which shows that turbulent motions can even create filaments with visible fibre-like substructure. The turbulent motions are driven by continuously inserting kinetic energy artificially on the largest scales in order to build up and maintain a turbulent spectrum (see Section 5.2). Observations of molecular clouds show highly supersonic line profiles and without driving mechanism, supersonic turbulent motions usually decay within a cloud crossing time (Mac Low et al., 1998; Stone et al., 1998; Ostriker et al., 1999; Padoan and Nordlund, 1999; Mac Low and Klessen, 2004; Kitsionas et al., 2009). However, there are many natural sources that drive turbulence in the ISM via different instabilities, for instance Kelvin-Helmholtz and Rayleigh-Taylor instabilities or the non-linear thin shell instability. Examples of turbulent drivers include rotational shear, supernovae, gravitational collapse, stellar winds, cosmic rays and HII regions (Elmegreen and Scalo, 2004). Many of these processes drive converging flows (Ntormousi et al., 2011; Dobbs et al., 2012) which trigger the thermal instability (Field, 1965) in the compressed post-shock regions of the warm atomic medium, rapidly cooling down the gas which leads to the formation of molecular clouds (Hennebelle and Pérault, 1999, 2000; Vázquez-Semadeni et al., 2000; Koyama and Inutsuka, 2002; Heitsch et al., 2006; Vázquez-Semadeni et al., 2006; Clark et al., 2012). Not only is the thermal instability able to drive turbulence in molecular clouds (Kritsuk and Norman, 2002), but together with gravity it also determines the internal structure (Heitsch et al., 2008; Ballesteros-Paredes et al., 2011; Seifried et al., 2017; Körtgen et al., 2019) where the smallest unstable scale of the thermal instability is limited by thermal conduction (Burkert and Lin, 2000; Koyama and Inutsuka, 2004).

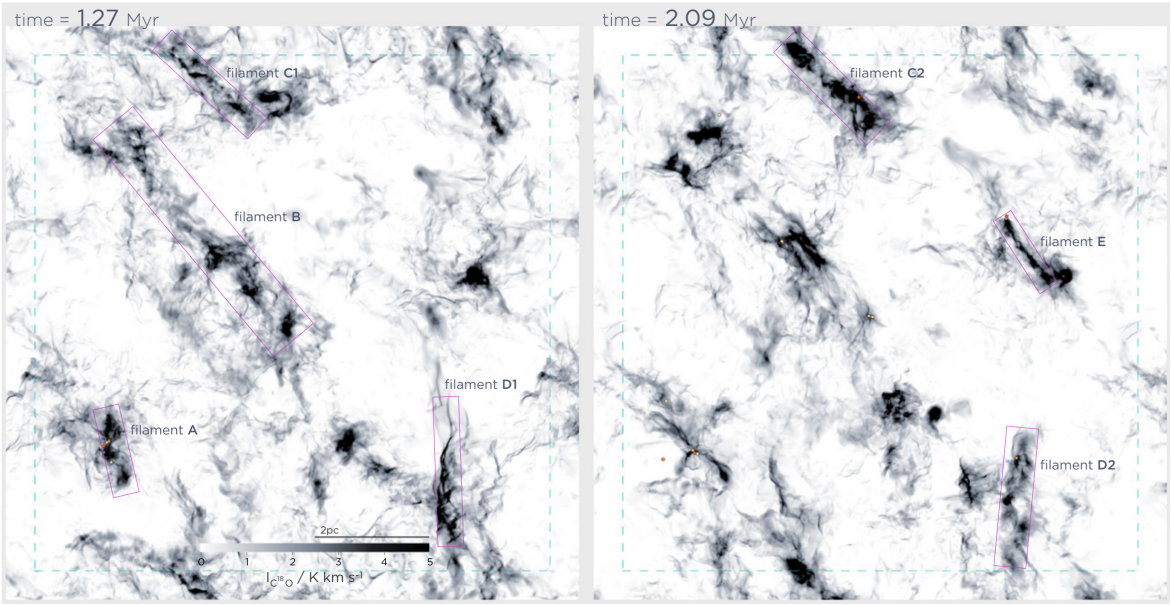

Figure 4.1: Example of a decaying turbulent box simulation from Moeckel and Burkert (2015). Shown are filaments visible in the projected surface density which is converted to an optically thin $^{12}C^{18}O$ observation. The dashed lines show the periodic boundaries of the domain and the orange dots show the positions of sink particles.

4.1 The appropriate equation of state

The radial density, temperature and pressure profile and, moreover, the fragmentation scale depend on the equation of state. A more general form is given by the parameterisation of a polytropic equation of state:

$$P = K\rho^{\gamma_p} \tag{4.1}$$

with $\gamma_p = 1+1/n$ being the polytropic exponent and n the polytropic index with $\gamma_p = 1$ or equivalently $n = \pm\infty$ being isothermal and $\gamma_p = 0$ or equivalently $n = -1$ being logatropic.

Historically, logatropic models have been used to explain observation of the line-width size relation of molecular clouds (Larson, 1981) and as a proxy for turbulent motions (Lizano and Shu, 1989; Gehman et al., 1996a,b; McLaughlin and Pudritz, 1997; Fiege and Pudritz, 2000a). However, dust temperature measurements imply an exponent marginally below one (Palmeirim et al., 2013), as is consistent with the observed radial profiles of a power law of -2 (Kawachi and Hanawa, 1998; Nakamura and Umemura, 1999) and even flatter observed profiles entail an exponent of $1/3 \leq \gamma_p \leq 2/3$ (Toci and Galli, 2015a). Values below one, or equivalently negative indices, imply that the gas temperature increases with lower densities which is consistent with clouds being heated by external radiation (Viala and Horedt, 1974). While low exponents require an unrealistic large temperature at large filament radii (Recchi et al., 2013), this issue can be resolved by assuming that the stabilising source is non-thermal in nature as it is in the case of hydromagnetic turbulence (Fatuzzo and Adams, 1993; McKee and Holliman, 1999). However, 'softer' equations of state with lower polytropic indices can only support a lower density contrast or less and less mass per unit length which is inconsistent with already observed line-masses exceeding even the maximum isothermal prediction. A solution to this

issue could be presented by non-isentropic models, where the adiabatic exponent γ is not equal to the polytropic exponent γ_p (Toci and Galli, 2015a) and which can support much larger masses.

Regarding fragmentation scales, Gehman et al. (1996b) and Hosseinirad et al. (2018) showed that lower exponents usually show larger fragmentation scales. However, observed core separations are already preferentially even shorter than the predictions of the isothermal model. In absence of a decisive argument as to which equation of state is applicable, the isothermal model still remains the one studied in the greatest detail and the most applied one. Therefore it is the one discussed here.

4.2 The isothermal profile

The analytical profile for the isothermal infinite cylindrical configuration of self-gravitating gas was first determined by Stodólkiewicz (1963) and almost simultaneously by Ostriker (1964). Because of its importance for filamentary structure, we demonstrate how to solve the cylindrical Lane-Emden Equation by reproducing the calculation of Ostriker (1964). Starting from hydrostatic equilibrium (Equation 5.17):

$$\frac{1}{\rho}\nabla_r P = -\nabla_r \Phi \tag{4.2}$$

and using the coordinate transform of

$$\rho = \rho_c e^{-\psi}, \qquad r = \left(\frac{c_s^2}{4\pi G \rho_c}\right)^{1/2} \xi \tag{4.3}$$

one can derive the isothermal Lane-Emden Equation

$$\Delta_\xi \psi = e^{-\psi}. \tag{4.4}$$

Using the radial Laplace operator in cylindrical coordinates we can rewrite the equation as

$$\frac{d^2\psi}{d\xi^2} + \frac{1}{\xi}\frac{d\psi}{d\xi} = e^{-\psi}. \tag{4.5}$$

The boundary conditions translate to

$$\rho(r = 0) = \rho_c \rightarrow \psi(\xi = 0) = 0 \tag{4.6}$$

$$\frac{d\rho}{dr}(r = 0) = 0 \rightarrow \frac{d\psi}{dr}(r = 0) = 0 \rightarrow \frac{d\psi}{d\xi}(\xi = 0) = 0 \tag{4.7}$$

With the coordinate transform

$$y = -\psi + 2\ln\xi = \ln(\xi^2 e^{-\psi}), \qquad t = \ln\xi \tag{4.8}$$

we can rewrite equation Equation 4.5 as

$$\frac{d^2 y}{dt^2} = -\xi^2 e^{y - 2\ln\xi} = -\xi^2 e^y e^{\ln\xi^{-2}} = -e^y. \tag{4.9}$$

Multiplying both sides with dy/dt and integrating gives

$$\frac{1}{2}\left(\frac{dy}{dt}\right)^2 = -e^y + C. \tag{4.10}$$

Using the boundary conditions, we obtain $C = 2$. With the additional coordinate transform

$$u = e^y = \xi^2 e^{-\psi} = \xi^2 \rho \rho_c^{-1} \tag{4.11}$$

we rewrite the equation as

$$\sqrt{2}dt = \frac{du}{u(2-u)^{1/2}}. \tag{4.12}$$

We integrate both sides and choose the integration constant as $\ln D$:

$$\sqrt{2}t + \sqrt{2}\ln D = -\sqrt{2}\tanh^{-1}\left(\sqrt{1-u/2}\right) = \frac{1}{\sqrt{2}}\ln\frac{\sqrt{2}-\sqrt{2-u}}{\sqrt{2}+\sqrt{2-u}}. \tag{4.13}$$

This expression transforms to

$$\xi^2 D^2 = \frac{\sqrt{2}-\sqrt{2-\xi^2\rho\rho_c^{-1}}}{\sqrt{2}+\sqrt{2-\xi^2\rho\rho_c^{-1}}}, \tag{4.14}$$

which can be rewritten as

$$\rho(\xi) = \frac{8D^2\rho_c}{\left(1+D^2\xi^2\right)^2}. \tag{4.15}$$

As $\rho = \rho_c$ for $\xi = 0$, it follows that $D^2 = 1/8$ and thus we arrive at the *Ostriker profile*

$$\rho(r) = \frac{\rho_c}{\left(1+(r/H)^2\right)^2} \tag{4.16}$$

with the scale height

$$H^2 = \frac{2c_s}{\pi G \rho_c}. \tag{4.17}$$

This profile is illustrated in Figure 4.2 and in principle extends to infinity but has a maximal mass per length it can support in hydrostatic equilibrium. It is calculated by integrating the profile outward

$$\frac{M}{L} = \int_0^R 2\pi\rho(r)rdr = \frac{2c_s^2}{G\left(1+(H/R)^2\right)} \tag{4.18}$$

and thus for $R \to \infty$ the maximum line mass is given by

$$\left(\frac{M}{L}\right)_{\rm crit} = \frac{2c_s^2}{G} \approx 1.06\cdot 10^{16}\left(\frac{T}{10\,\mathrm{K}}\right)\mathrm{g\,cm^{-1}} \approx 16.4\left(\frac{T}{10\,\mathrm{K}}\right)\mathrm{M_\odot\,pc^{-1}} \tag{4.19}$$

for a typical molecular weight in the ISM of $\mu = 2.36$. Exceeding this line mass inevitably leads to the collapse of the filament.

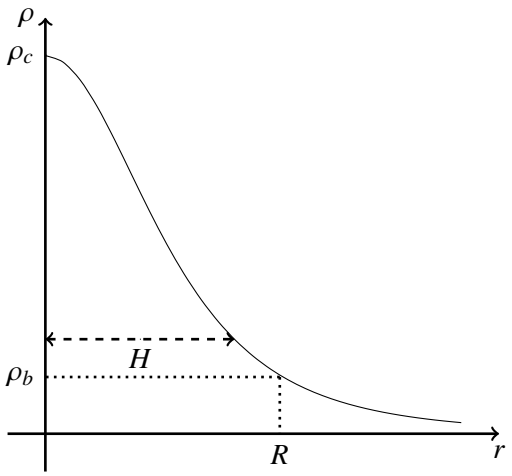

Figure 4.2: Schematic view of the solution to the isothermal filament profile together with the scale height H. In principle, the profile extends to infinity but can be limited by an ambient pressure. The corresponding radius and boundary density are then given by the dotted values.

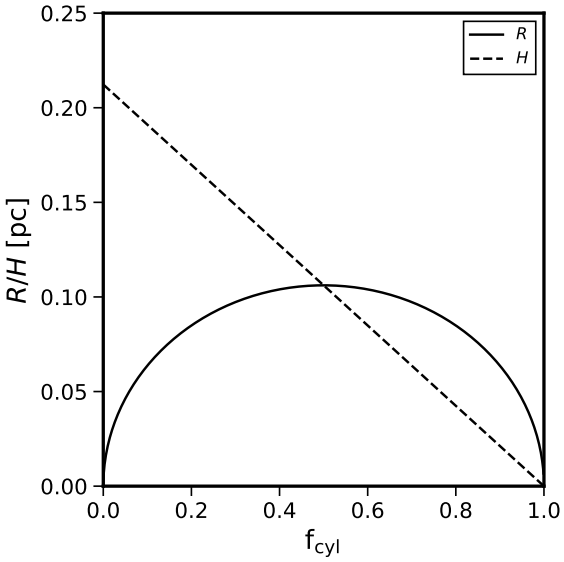

Figure 4.3: Dependence of the radius R (solid line) and the scale height H (dashed line) on the line-mass of a filament for a given ambient pressure of $2 \cdot 10^4$ K cm^{-3}.

4.3 Pressure truncation

In reality, filaments do not extend indefinitely but blend into the background radiation for large radii. Therefore, Nagasawa (1987) considered the case of an external pressurised medium which truncates the radial profile at the radius R where the filament pressure equals the ambient pressure. A pressure-bound filament is in a stable configuration for all line-masses below the critical threshold as its expansion is compensated by the ambient pressure. In this case, the amount of mass contained in the filament is measured by the parameter

$$f_{\rm cyl} = \left(\frac{M}{L}\right) \Big/ \left(\frac{M}{L}\right)_{\rm crit} = \left(1 + (H/R)^2\right)^{-1} \tag{4.20}$$

which is the ratio of the actual line-mass to the maximum line-mass (Fischera and Martin, 2012). The ratio of the central and boundary filament density is then equal to

$$\rho_c/\rho_b = \left(1 - f_{\rm cyl}\right)^{-2} \tag{4.21}$$

and the boundary radius is given by

$$R = H\left(\frac{f_{\rm cyl}}{1 - f_{\rm cyl}}\right)^{1/2}. \tag{4.22}$$

In Figure 4.2 this situation is depicted by the dotted lines which show the position at which the filament connects to the ambient pressure. As shown in Figure 4.3, for a given ambient pressure, the radius has a maximum at $f_{\rm cyl} = 0.5$, where it is equal to the scale height H. In the limiting cases of $f_{\rm cyl} \to 0$ and $f_{\rm cyl} \to 1$ the radius decreases to zero. In contrast to a pressure bound isothermal sphere which collapses for a large enough ambient pressure (Ebert, 1955; Bonnor, 1956), a filament never loses pressure support by compression (McCrea, 1957) and always finds a stable configuration. Moreover, magnetic fields also play a vital role in the value of the maximum line-mass. In general, the magnetic field of a filament consists of a poloidal component parallel to the filament spine and a toroidal component where the field lines wrap around the filament axis. By means of a virial analysis, Fiege and Pudritz (2000a) showed that poloidal fields support a filament against radial contraction, thus enhancing the maximum line mass, but toroidal fields assist gravity by squeezing down onto the surface of the filament and hence reducing the maximum line mass. This compression effect of toroidal fields has also been found for increasingly softer equations of state in scale-free models (Toci and Galli, 2015b).

4.4 Linear perturbation analysis

Pioneering work on the stability of infinite cylindrical configurations of gas was done by Chandrasekhar and Fermi (Chandrasekhar and Fermi, 1953), but only for the case of incompressible gas in which case the filament profile is flat. In order to understand on which length scales filaments fragment, one has to introduce a deviation to the unperturbed hydrostatic quantities q_0 along the axis of the filament, similar to the derivation of the Jeans length:

$$q_0(r, z, t) = q_0(r) + q_1(r, z, t) = q_0(r) + \epsilon q_0(r) \exp(ikz - i\omega t) \tag{4.23}$$

where $q_1(r, z, t)$ is the first order perturbation, ϵ is the perturbation strength, z is the parameter along the filament axis, $k = 2\pi/\lambda$ is the perturbation wave vector and ω is the perturbation growth rate.

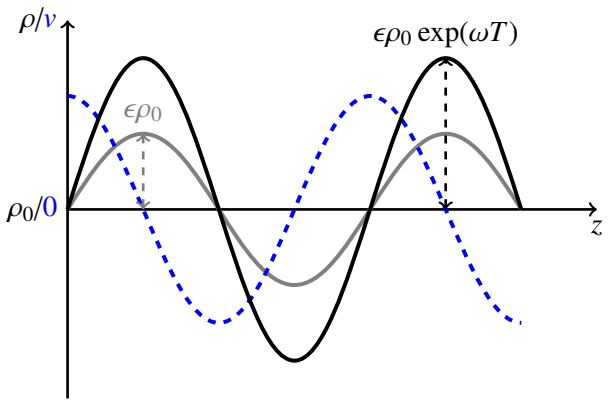

Figure 4.4: Schematic view of the growth of linear perturbations for large enough perturbation scales. At time $t = 0$ the density along the filament spine is given by the gray line. At time $t = T$ the density is given by the black line. As one can see, the perturbation effectively leads to a redistribution of mass inside the filament with a corresponding velocity structure from the density minimum to the maximum given in blue.

Perturbations grow for values of k, where the solution to the dispersion relation $\omega^2(k)$ is smaller than zero. This means that the perturbation wavelength λ must be large enough to encompass enough mass in order to trigger run-away growth. For smaller wavelengths, perturbations will not grow but will form a density wave propagating back and forth. A schematic view of the growth of perturbations is shown in Figure 4.4, where the initial density perturbation is given by the gray line. After some time T and for large enough perturbation scales, the density maxima and minima have grown and decreased respectively to arrive at the black status. As mass is transported from the minima to the maxima, a corresponding velocity structure emerges, given by the blue dashed line which has the same sinusoidal form as the density perturbation but is shifted by a value of $\pi/4$.

In order to calculate the dispersion relation, one inserts the perturbed state of Equation 4.23 into the mass and momentum equations of the Euler equations (Equation 5.26) and neglects second order terms:

$$\begin{aligned} -i\omega\rho_1 + \nabla(\rho_0\mathbf{u}_1) &= 0 \\ -i\omega\rho_0\mathbf{u}_1 &= -\rho_0\nabla\Phi_1 - \rho_1\nabla\Phi_0 - \nabla P_1 \end{aligned} \tag{4.24}$$

which can be summarised into a single equation

$$\omega^2\rho_0\mathbf{u}_1 = -i\omega\rho_0\nabla\Phi_1 - \nabla(\rho_0\mathbf{u}_1)\nabla\Phi_0 - c_s^2\Delta(\rho_0\mathbf{u}_1) \tag{4.25}$$

Together with the perturbed Poission's equation

$$i\omega\Delta\Phi_1 = 4\pi G\nabla(\rho_0\mathbf{u}_1) \tag{4.26}$$

these two equations form an eigensystem in terms of the perturbed momentum density $\rho_0\mathbf{u}_1$ and the perturbed gravitational potential Φ_1, which can only be solved numerically. The solution to this system gives two important perturbation scales. As stated before, there is the minimum scale above which perturbations grow. This is also called the critical scale and was determined to be $\lambda_{\rm crit} = 3.96H$ for the isothermal case (Stodólkiewicz, 1963). In addition, there is the scale of the fastest growing mode $\lambda_{\rm dom} = 7.82H$ with a growth rate of $|\omega_{dom}| = 0.339(4\pi G\rho_c)^{1/2}$ (Nagasawa, 1987) which, for a

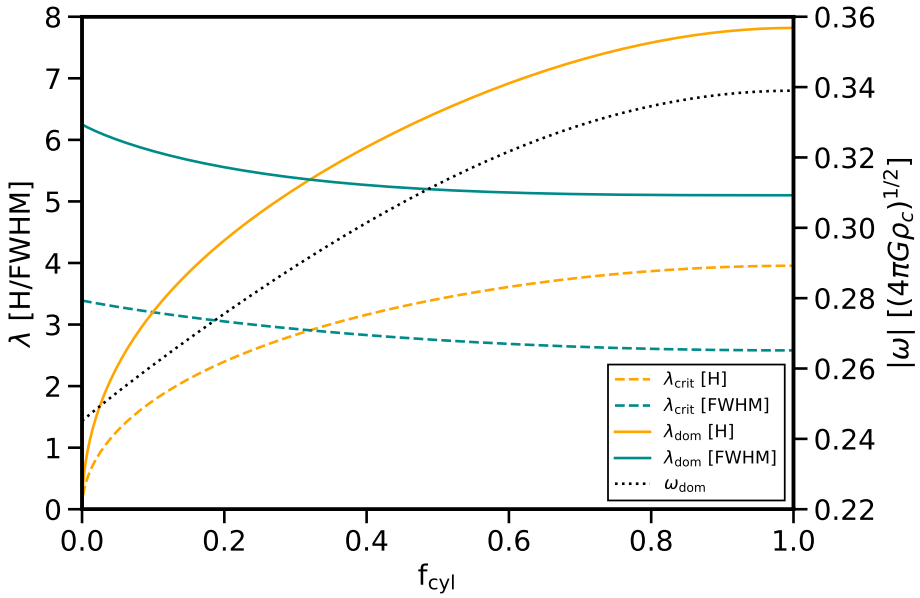

Figure 4.5: Dependence of the critical and dominant fragmentation scales (left axis) and the dominant growth rate (right axis) on the line mass of the filament. Data is taken from Nagasawa (1987) and interpolated by Fischera and Martin (2012). The orange lines represent the fragmentation scales in units of the scale height and the cyan lines represent the same in the units of the FWHM.

random distribution of initial modes, should dominate at later times and is expected to be the scale on which cores are distributed along the filament. Both length scales were reproduced by other studies (Larson, 1985; Inutsuka and Miyama, 1992; Gehman et al., 1996a; Hosseinirad et al., 2017) and the dependence of the fastest growing mode on the scale height is usually simplified by expecting cores to be separated by four times the filament diameter. This statement, however, depends on the definition of the filament diameter. As can be seen from Equation 4.22, the scale height is not a good estimate of the filament radius. Moreover, observations often define the filament diameter as the FWHM which is not necessarily equal to two times the scale height.

Furthermore, Nagasawa (1987) showed that the perturbation length- and growth timescale both depend on $f_{\rm cyl}$. One can distinguish two different types of collapse depending on line-mass. For $f_{\rm cyl} \rightarrow 1$ the dispersion relation converges to the radially infinite case. The radius is larger than the scale height and the ambient medium is negligible due to the already high density contrast in the filament. This leads to the "compressible instability" where self-gravity drives the compression of the filament. In contrast, for $f_{\rm cyl} \rightarrow 0$ the dispersion relation is similar to the case of the incompressible cylinder as there is only a low density contrast in the filament. The radius is much smaller than the scale hight and the Jeans-like instability leads to a deformation of the filament resembling a string of sausage and therefore is called "sausage instability". The dependence of the fragmentation length- and timescale on $f_{\rm cyl}$ for intermediate values which was interpolated by Fischera and Martin (2012) is given in Table 6.1 and visualised in Figure 4.5. Fischera and Martin (2012) also estimated the observable FWHM of filaments depending on their line-mass. The dependence of the fragmentation scales is therefore given in two different units, in multiples of the scale height in orange and in multiples of the FWHM in cyan. Consequently, one would expect the fragments to be separated by a factor of about

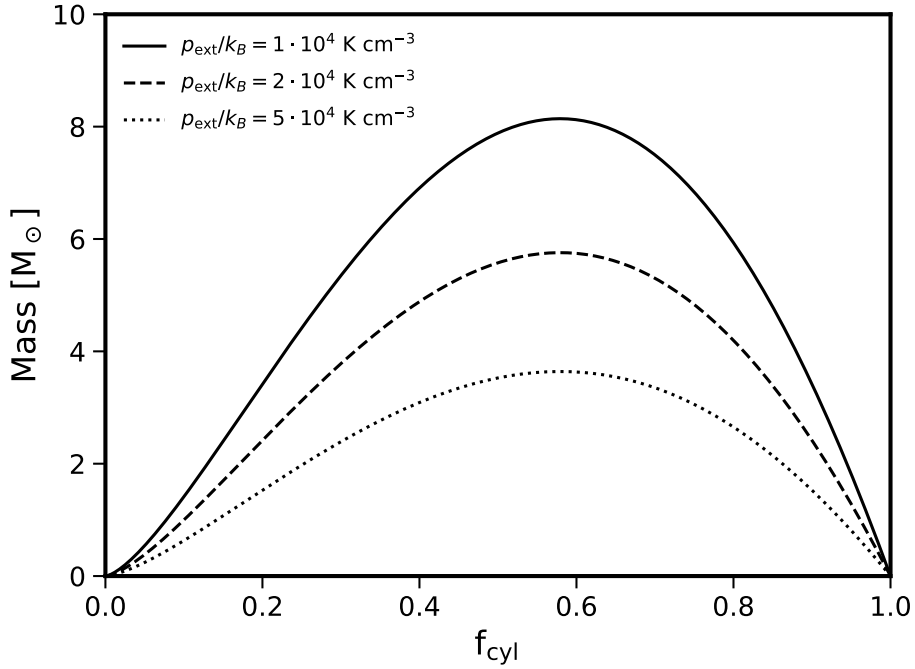

Figure 4.6: Expected core mass in dependence of the line-mass for varying external pressures under the assumption that the cores evolve on the dominant fragmentation length.

five times the FWHM for high line-mass filaments.

An interesting aspect of the core formation process is the mass a fragment can potentially accrete by linear perturbations. A simple estimate is given by the line-mass times the dominant fragmentation length:

$$M_{\mathrm{core}} = f_{\mathrm{cyl}} \cdot \frac{2c_s^2}{G} \cdot \lambda_{\mathrm{dom}}. \tag{4.27}$$

The core mass is shown in Figure 4.6 in dependence of f_{cyl} for various external pressures around an assumed typical ISM pressure of $p_{\mathrm{ext}}/k_B = 2 \cdot 10^4\,\mathrm{K\,cm^{-3}}$. Note that this represents an upper limit of the core mass, as high line-mass cores collapse radially before they can accrete all of the material in the filament and feedback effects can halt accretion. Interestingly, a larger background pressure or conversely a thinner filament only produces less massive cores. In dense, highly pressurised regions this mode of star formation, while still possibly important for the formation of low mass stars, cannot apply to massive stars which typically form in hubs where several filaments combine. Fischera and Martin (2012) also showed that, compared to the Bonnor-Ebert mass, only intermediate line-mass cores are able to collapse from ambient overpressure alone and form prestellar objects. This, however, does not apply to the high line-mass end, as here collapse is driven by the radial instability as soon as the local line-mass reaches supercritical values.

4.5 Additional influences

The picture of linear fragmentation growth is further complicated by the effects of magnetic fields. For $f_{\rm cyl} \rightarrow 1$, a uniform poloidal magnetic field reduces the growth rate while the fastest growing mode stays relatively constant. This effect saturates when the magnetic pressure is of the order of the thermal pressure or equivalently when the Alvén speed $v_a = B/\sqrt{4\pi\rho}$ is comparable to the sound speed (Nagasawa, 1987; Gehman et al., 1996b; Hosseinirad et al., 2017). Conversely, when $f_{\rm cyl} \rightarrow 0$, stronger uniform poloidal magnetic fields not only strongly suppress the growth but also increase the perturbation length (Chandrasekhar and Fermi, 1953; Nagasawa, 1987). This stabilizing effect of magnetic fields can, however, be suppressed if ambipolar diffusion is significant (Hosseinirad et al., 2018). Moreover, the effect of magnetic fields on the fragmentation depends on the field configuration. For instance, if the field is not uniform but drops off as $B \sim \rho^{-1/2}$, a stronger magnetic field reduces the stability of the filament, shortening fragmentation lengths and increasing growth rates (Stodólkiewicz, 1963; Nakamura et al., 1993). There can be even more complicated magnetic field configurations, as in the case of the field lines being perpendicular to the filament axis (Hanawa et al., 2017). Here, a stronger magnetic field again suppresses the growth of perturbations.

Another important issue is the longitudinal collapse of filaments (Pon et al., 2012; Toalá et al., 2012) which leads to an end-dominated mode where two prominent cores form at both ends of the filament due to gravitational focusing (Bastien, 1983; Burkert and Hartmann, 2004; Clarke and Whitworth, 2015). Pon et al. (2011) predicted that the local collapse timescales are shorter than the overall global collapse and Bastien et al. (1991) found fragmentation in simulations of finite filaments with the result that the fragments typically lie closer together than the predicted value for infinite filaments with a separation of about four times less.

Finally, core growth is also influenced by the filament geometry, where the gravitational straightening of bends can lead to cores on the scale of the displacement (Gritschneder et al., 2017). It is also unclear how turbulence and the asymmetric displacement of material with different initial perturbation strengths can influence core growth as non-linear effects can become important (Inutsuka and Miyama, 1997; Seifried and Walch, 2015). A more general approach was taken by Inutsuka (2001) who applied a well known cosmological method, the so-called Press-Schechter formalism (Press and Schechter, 1974), which predicts the mass function of cores from the initial power spectrum of density perturbations. They find that observed power spectra with indices of -1.5 (Roy et al., 2015), close to the Kolmogorov scaling (see Section 5.2), reproduce the observed mass function of cores with a power of -2.5.

In summary, it is not easy to determine the length scale filaments should fragment on or if there even is a dominant wavelength. While individual filaments can be fitted well by theoretical models (Heigl et al., 2016), giving insight into which physical processes are important for core formation, idealised conditions are not likely to apply often and a statistical approach needs to be found to obtain a general picture of the star formation process.

5 Principles of hydrodynamics and numerical implementation

This chapter discusses the physical foundations as well as the numerical implementation of the equations that govern the dynamic behavior of fluids, namely hydrodynamics. To this end, it loosely follows the book "The physics of astrophysics volume II - gas dynamics" by Frank Shu (Shu, 1992).

First and foremost, we want to treat the gas as a continuum with a velocity and not calculate the path of individual gas atoms and molecules. In order to do so, the condition is that the mean free path of the particles is much smaller than the scale of the system we are interested in. This means that for particles moving with velocities

$$\mathbf{v} = \mathbf{u} + \mathbf{w}, \tag{5.1}$$

the displacements due to scattering with random motions $\mathbf{w}$ are unimportant and the particles tend to move around a mean bulk motion $\mathbf{u}$. The mean free path l is given by

$$l = (n\sigma)^{-1} \tag{5.2}$$

where n is the mean number density of the particles and σ is the average cross section. For proton-proton collisions the cross section is typically of the order of the size of a proton, e.g. $\sigma \sim 10^{-15}\,\mathrm{cm}^2$. For a molecular cloud with a density of $n = 100\,\mathrm{cm}^{-3}$ the mean free path is $l = 10^{13}\,\mathrm{cm}$ which is several magnitudes smaller than the typical size of a molecular cloud of $10 - 100\,\mathrm{pc}$. In the centre of cores, densities can rise up to $n = 10^6\,\mathrm{cm}^{-3}$ and thus the mean free path is $l = 10^9\,\mathrm{cm}$ which is also much smaller than the typical core size of 0.1 pc. Thus, we can treat the gas as a continuum at all times.

5.1 Euler equations

In order to connect the continuum treatment to the microscopic collection of particles, we define a distribution function $f(\mathbf{x}, \mathbf{p}, \mathrm{t})$ where the number of identical particles inside a phase space element is given by

$$\mathrm{N} = \int f(\mathbf{x}, \mathbf{p}, \mathrm{t}) \mathrm{d}\mathbf{x}\mathrm{d}\mathbf{p}. \tag{5.3}$$

In the absence of collisions, every particle at time t at the position $\mathbf{x}$ and with the momentum $\mathbf{p}$ experiencing an external force $\mathbf{f}$ will be at the position $\mathbf{x} + (\mathbf{p}/m)\mathrm{dt}$ with a momentum $\mathbf{p} + \mathbf{f}\mathrm{dt}$ at the time $\mathrm{t} + \mathrm{dt}$ and the particle number will be conserved. Taking collisions into account, the change in particle

number is then equal to the number of particles scattering into and out of the phase space element under consideration:

$$\mathrm{dN_{coll}} = \left(\frac{\partial f}{\partial \mathrm{t}}\right)_{\mathrm{coll}} \mathrm{d}\mathbf{x}\mathrm{d}\mathbf{p}\mathrm{dt} = f(\mathbf{x} + \frac{\mathbf{p}}{m}\mathrm{dt}, \mathbf{p} + \mathbf{f}\mathrm{dt}, \mathrm{t} + \mathrm{dt})\mathrm{d}\mathbf{x}\mathrm{d}\mathbf{p} - f(\mathbf{x}, \mathbf{p}, \mathrm{t})\mathrm{d}\mathbf{x}\mathrm{d}\mathbf{p}. \tag{5.4}$$

Dividing by d**x**d**p**dt and taking the limits, we obtain the Boltzmann Equation

$$\frac{\partial f}{\partial \mathrm{t}} + \frac{\partial f}{\partial \mathbf{x}}\frac{\mathbf{p}}{m} - m\frac{\partial f}{\partial \mathbf{p}}\frac{\partial \Phi}{\partial \mathbf{x}} = \left(\frac{\partial f}{\partial \mathrm{t}}\right)_{\mathrm{coll}} \tag{5.5}$$

where we rewrite the force as the gradient of a scalar potential Φ. As we want to derive the equations for the evolution of a fluid in relation to space and time, we multiply Equation 5.5 by a function χ which takes the form of the first few velocity moments, e.g. mass, momentum and kinetic energy, and integrate over the velocity space to obtain the mass density, the momentum density and the energy density:

$$\begin{pmatrix} \rho \\ \rho\mathbf{u} \\ \rho e_{\mathrm{tot}} \end{pmatrix} = \int \begin{pmatrix} m \\ m\mathbf{v} \\ m|\mathbf{v}|^2/2 \end{pmatrix} f(\mathbf{x}, \mathbf{p}, \mathrm{t})\mathrm{d}\mathbf{v} \tag{5.6}$$

where e_{tot} is the specific total energy, e.g. the total energy per unit mass, and **u** is the average velocity of **v**. Thus, we arrive at the equation:

$$\int \left(\chi\frac{\partial f}{\partial \mathrm{t}} + \chi \mathrm{v}_k \frac{\partial f}{\partial \mathrm{x}_k} - \chi\frac{\partial \Phi}{\partial \mathrm{x}_k}\frac{\partial f}{\partial \mathrm{v}_k}\right)\mathrm{d}^3\mathrm{v} = \int \chi\left(\frac{\partial f}{\partial \mathrm{t}}\right)_{\mathrm{coll}} \mathrm{d}^3\mathrm{v} \tag{5.7}$$

We assume that the particle collisions are elastic. This means that mass, momentum and energy are conserved and that collisions only change the velocity and not the positions of the particles. As we integrate over the velocity space the changes in velocity do not contribute to the change of $f(\mathbf{x}, t)$ in time and therefore it must be zero:

$$\int \chi\left(\frac{\partial f}{\partial \mathrm{t}}\right)_{\mathrm{coll}} \mathrm{d}^3\mathrm{v} = 0. \tag{5.8}$$

Defining the average value of a quantity as

$$\langle Q \rangle = n^{-1} \int Q f(\mathbf{x}, \mathbf{v}, t)\mathrm{d}\mathbf{v} \tag{5.9}$$

where $n = \int f d\mathbf{v}$ is the particle volume density, we can rewrite the Boltzmann equation as

$$\frac{\partial}{\partial \mathrm{t}}\left(n\langle\chi\rangle\right) + \frac{\partial}{\partial \mathrm{x}_k}\left(n\langle \mathrm{v}_k\chi\rangle\right) + n\frac{\partial \Phi}{\partial \mathrm{x}_k}\left\langle\frac{\partial \chi}{\partial \mathrm{v}_k}\right\rangle = 0 \tag{5.10}$$

where we apply the divergence theorem to the last term and use the fact that every distribution function goes faster to zero than any power of **v** as $\mathbf{v} \to \infty$.

$$\int_V \chi\frac{\partial f}{\partial \mathrm{v}_k}\mathrm{d}^3\mathrm{v} = \int_V \left[\frac{\partial(\chi f)}{\partial \mathrm{v}_k} - f\frac{\partial \chi}{\partial \mathrm{v}_k}\right]\mathrm{d}^3\mathrm{v} = \underbrace{\int_S \chi f \mathrm{d}^2\mathrm{v}}_{=0} - n\left\langle\frac{\partial \chi}{\partial \mathrm{v}_k}\right\rangle \tag{5.11}$$

5.1.1 Mass conservation

Substituting $\chi = m$ in Equation 5.10 and applying that the mean of the velocity v_k is u_k, we obtain the continuum equation:

$$\frac{\partial \rho}{\partial \mathrm{t}} + \frac{\partial}{\partial \mathrm{x}_k}(\rho \mathrm{u}_k) = 0 \tag{5.12}$$

5.1.2 Momentum conservation

Using $\chi = m v_i$ in equation Equation 5.10, we arrive at the equation of momentum conservation:

$$\frac{\partial}{\partial \mathrm{t}}(\rho \mathrm{u}_i) + \frac{\partial}{\partial \mathrm{x}_k}\left(\rho \langle \mathrm{v}_i \mathrm{v}_k \rangle\right) + \rho \frac{\partial \Phi}{\partial \mathrm{x}_k}\delta_{ik} = 0 \tag{5.13}$$

We can rewrite the particle velocity v_i as the sum of the bulk velocity u_i and the random motion w_i and as the mean of the random motion is zero, terms with only one order in w disappear:

$$\langle \mathrm{v}_i \mathrm{v}_k \rangle = \mathrm{u}_i \mathrm{u}_k + \langle \mathrm{w}_i \mathrm{w}_k \rangle \tag{5.14}$$

Now we can separate out the trace of the symmetric dyadic $\mathrm{w}_i \mathrm{w}_k$:

$$\rho \langle \mathrm{w}_i \mathrm{w}_k \rangle = P \delta_{ik} - \pi_{ik} \tag{5.15}$$

where P is the gas pressure and π_{ik} is the viscous stress tensor. The former is connected to the density ρ and the specific internal energy $e_{\mathrm{in}} = 1/2 \langle |\mathbf{w}|^2 \rangle$ via the equation of state (EOS), which for an ideal gas takes the form:

$$P = \rho e_{\mathrm{in}} (\gamma - 1), \tag{5.16}$$

where γ is the adiabatic index of the gas. Therefore we can rewrite the momentum equation as

$$\frac{\partial}{\partial \mathrm{t}}(\rho \mathrm{u}_i) + \frac{\partial}{\partial \mathrm{x}_k}(\rho \mathrm{u}_i \mathrm{u}_k) + \frac{\partial P}{\partial \mathrm{x}_i} - \frac{\partial \pi_{ik}}{\partial \mathrm{x}_k} + \rho \frac{\partial \Phi}{\partial \mathrm{x}_i} = 0 \tag{5.17}$$

5.1.3 Energy conservation

Inserting $\chi = m|\mathbf{v}|^2/2$ in equation Equation 5.10, we obtain the equation of energy conservation:

$$\frac{\partial}{\partial \mathrm{t}}\left[\frac{\rho}{2}\left(|\mathbf{u}|^2 + \langle |\mathbf{w}|^2 \rangle\right)\right] + \frac{\partial}{\partial \mathrm{x}_k}\left[\frac{\rho}{2}\langle (\mathrm{u}_k + \mathrm{w}_k)(\mathrm{u}_i + \mathrm{w}_i)^2 \rangle\right] + \rho \mathrm{u}_k \frac{\partial \Phi}{\partial \mathrm{x}_k} = 0 \tag{5.18}$$

Again, as the mean of terms containing only one order of the random motion is zero we can simplify the equation using:

$$\langle (\mathrm{u}_k + \mathrm{w}_k)(\mathrm{u}_i + \mathrm{w}_i)^2 \rangle = |\mathbf{u}|^2 \mathrm{u}_k + 2\mathrm{u}_i \langle \mathrm{w}_i \mathrm{w}_k \rangle + \mathrm{u}_k \langle |\mathbf{w}|^2 \rangle + \langle \mathrm{w}_k |\mathbf{w}|^2 \rangle \tag{5.19}$$

By applying Equation 5.15 and the definition of the specific kinetic energy given by

$$e_{\mathrm{kin}} = \frac{1}{2}|\mathbf{u}|^2; \; e_{\mathrm{tot}} = e_{\mathrm{in}} + e_{\mathrm{kin}} \tag{5.20}$$

and defining the conduction heat flux by

$$\mathrm{F}_k \equiv \rho \langle \mathrm{w}_k \frac{1}{2} |\mathbf{w}|^2 \rangle \tag{5.21}$$

we can rewrite the equation of energy conservation as

$$\frac{\partial}{\partial \mathrm{t}}(\rho e_{\mathrm{tot}}) + \frac{\partial}{\partial \mathrm{x}_k}(\rho e_{\mathrm{tot}} \mathrm{u}_k + \mathrm{u}_k P + \mathrm{F}_k - \mathrm{u}_i \pi_{ik}) + \rho \mathrm{u}_k \frac{\partial \Phi}{\partial \mathrm{x}_k} = 0 \tag{5.22}$$

5.1.4 Closure conditions

The moment equations are a system of five linearly independent equations, but they contain thirteen variables: the density ρ, the three velocity components of $\mathbf{u}$, the pressure P, five due to the viscous stress tensor π_{ik} and three for the conduction heat flux $\mathbf{F}$. In order to obtain a closed set of equations we need to introduce closure conditions which is achieved by a Chapman-Enskog procedure in the limit $l \ll L$. We expand the distribution function in orders of $\delta = l/L$:

$$f = f_0 + \delta f_1 + \delta^2 f_2 \ldots \tag{5.23}$$

To zeroth order, f is given by the local Maxwellian:

$$f_0 = n(m/2\pi kT)^{3/2} \exp(-m|\mathbf{w}|^2/2kT) \tag{5.24}$$

Using this distribution, it is possible to show that the non-ideal terms, the viscous stress tensor and the conduction heat flux, are both zero:

$$\pi_{ik} = 0 \quad F_k = 0 \tag{5.25}$$

This leaves us with the remaining equations, also known as the Euler equations, which in our example includes an external force on the right hand side:

$$\begin{aligned} \frac{\partial}{\partial \mathrm{t}}\rho + \nabla(\rho \mathbf{u}) &= 0 \\ \frac{\partial}{\partial \mathrm{t}}(\rho \mathbf{u}) + \nabla \cdot (\rho \mathbf{u} \otimes \mathbf{u} + P\mathbb{I}) &= -\rho \nabla \Phi \\ \frac{\partial}{\partial \mathrm{t}}(\rho e_{\mathrm{tot}}) + \nabla \cdot [\mathbf{u}(\rho e_{\mathrm{tot}} + P)] &= -\rho \mathbf{u} \nabla \Phi \end{aligned} \tag{5.26}$$

Neglecting the external force, these equations form a system of hyperbolic conservation laws of the form

$$\frac{\partial}{\partial \mathrm{t}}\mathbf{U} + \nabla \cdot \mathbf{F}(\mathbf{U}) = 0. \tag{5.27}$$

Hyperbolic means that as long as the initial and boundary conditions are known, we can determine the state of the system at any later time. For a higher-order distribution function, we would obtain the Navier-Stokes equations, which do contain the extra viscous and heat conduction terms. However, under normal conditions inside molecular clouds the dynamic viscosity and the thermal conductivity are close to zero and both effects can be neglected.

5.2 Fully developed turbulence

As mentioned above, the dynamic viscosity in the ISM is close to zero. However, this depends on the scale under consideration. A way to quantify the importance of viscosity is the dimensionless Reynolds number

$$\mathrm{Re} = \frac{VL}{\nu}, \tag{5.28}$$

where the dynamic viscosity μ is rewritten as the diffusion-like term of the kinetic viscosity, $\nu = \mu/\rho$. V and L are typical velocities and length scales of the system, where the velocity is given by the order of random fluctuations. For Reynolds numbers above $\sim 10^3$ viscous effects can be ignored and the flow is highly turbulent. On molecular cloud scales the Reynolds number reaches typical values of $\sim 10^9$. However, one can define the Reynolds number for any given scale as

$$\mathrm{Re}_\lambda = \frac{V_\lambda \lambda}{\nu}. \tag{5.29}$$

When λ becomes similar to the mean free path, the Reynolds number reaches a value of order one and viscous effects dominate. This is called the dissipation scale λ_0 where kinetic energy is converted into heat. The closest model for a theory of turbulence was developed by Kolmogorov (1941) and is only truly valid for subsonic incompressible gas. It describes turbulence as a locally homogeneous and isotropic series of eddies where energy is cascaded from the largest scale, where turbulent motions are generated, down to the dissipation scale. This cascade is called the inertial regime and here turbulent energy is neither produced nor lost. The constant rate at which energy is transferred to smaller scales is given by

$$\epsilon = \frac{E}{t} \propto \frac{v^2}{t} = \frac{V_\lambda^3}{\lambda}. \tag{5.30}$$

Solving this equation for the velocity gives the relation

$$V_\lambda \propto \epsilon^{1/3} \lambda^{1/3}, \tag{5.31}$$

which directly corresponds to the Larson linewidth-size relation (Larson, 1981). Furthermore, one can derive the energy power-law scaling in k-space with $k \propto 1/\lambda$ known as Kolmogorov-scaling:

$$E(k)dk \propto V_\lambda^2 \rightarrow E(k) \propto V_\lambda^2 k^{-1} \propto \epsilon^{2/3} k^{-5/3}. \tag{5.32}$$

Assuming isotropy, one can transform the one-dimensional $-5/3$ scaling to higher dimensions by reducing the exponent by one for each dimension. Thus, three-dimensional turbulence has a scaling of $-11/3$.

In contrast to subsonic turbulence, the energy in supersonic turbulence decays via the formation of shocks. Due to shock formation, the velocity field is dominated by a series of step functions. This leads to a power-law scaling of -2 in one dimension as shown by Burgers (1948). This is due to the fact that the power spectrum of a step function is proportional to k^{-2} as the Fourier transformation is only non-zero where the signal changes with an amplitude proportional to the length of the change. An isotropic system of overlapping shocks, therefore, should follow a corresponding power-law scaling.

5.3 Magnetohydrodynamics (MHD)

Zeeman measurements in molecular clouds have shown that magnetic fields are an important component of the energy density budget of the ISM (Crutcher, 2012). Thus, we cannot neglect the effects of electromagnetic forces and have to expand the fluid equations. In electrodynamics, the Maxwell equations describe the evolution of the electric **E** field and magnetic **B** field:

$$\begin{aligned} \nabla \times \mathbf{E} &= -\frac{1}{c}\frac{\partial \mathbf{B}}{\partial \mathrm{t}}, \\ \nabla \times \mathbf{B} &= \frac{4\pi}{c}\mathbf{j} + \frac{1}{c}\frac{\partial \mathbf{E}}{\partial \mathrm{t}}, \\ \nabla \cdot \mathbf{E} &= 4\pi\rho_e, \\ \nabla \cdot \mathbf{B} &= 0, \end{aligned} \tag{5.33}$$

where c is the speed of light, ρ_e is the electric charge density and $\mathbf{j}$ is the electric current. As electric fields cancel out almost instantaneously in a plasma, the electric field is weak compared to the magnetic field and thus we can neglect the electric displacement current and derive the induction equation

$$\frac{\partial \mathbf{B}}{\partial \mathrm{t}} = \nabla \times (\mathbf{u} \times \mathbf{B}) \tag{5.34}$$

As the ionisation fraction in molecular clouds is relatively low, the gas does not behave as a good plasma. The magnetic field only exerts forces on the ions and electrons. The neutral particles, however, can drift freely across field lines and couple only through collisions with ions, diffusing magnetic energy into heat. For low ionisation fractions this coupling is imperfect and thus we have to include non-ideal diffusive terms in the induction equation

$$\frac{\partial \mathbf{B}}{\partial \mathrm{t}} = \nabla \times (\mathbf{u} \times \mathbf{B}) - \nabla \times \left[\eta_\Omega(\nabla \times \mathbf{B}) + \eta_\mathrm{H}\{(\nabla \times \mathbf{B}) \times \mathbf{B}\} + \eta_\mathrm{AD}\mathbf{B} \times \{(\nabla \times \mathbf{B}) \times \mathbf{B}\}\right]. \tag{5.35}$$

The first non-ideal term is the Ohmic dissipation, which is caused by the drift between electrons and ions/neutrals. It dominates at very high densities and weak magnetic fields when both, electrons and ions, are not coupled dynamically to the magnetic field. The second non-ideal term is the Hall effect, which is important at intermediate densities when only the electrons couple dynamically to the magnetic field and which is caused by the drift between electrons and ions. Finally, the third non-ideal term describes the effect of ambipolar diffusion, the drag due to collisions between the neutrals and ions. It dominates at low densities and high magnetic field strengths for lightly ionised gas, conditions usually found in star-forming regions, where both electrons and ions couple to the magnetic field. The respective resistivities η are functions of the respective microscopic collision frequencies (see e.g. Wardle (2007) for a full discussion). Non-ideal terms are likely to have an influence on the system where magnetic fields are dynamically important. A crude estimate of the dynamical importance of non-ideal effects is given by the magnetic Reynolds number

$$\mathrm{Re}_m = \frac{VL}{\eta}. \tag{5.36}$$

On cloud scale, a typical value for the magnetic Reynolds number is $100 - 1000$ and thus magnetic dissipation does not play a major role. However, on small scales the dissipation scale of the magnetic

field is similar to the size of prestellar cores. The relative importance of the respective diffusion processes is given by the magnetic Prandtl number as the ratio of the viscous to magnetic diffusion:

$$P_m = \frac{\nu}{\eta} \tag{5.37}$$

which is usually smaller than one on prestellar core scales. This means that the magnetic field dissipates on a larger scale and the velocity dispersion on scales below the magnetic dissipation scale is dominated by thermal motions.

For the ideal MHD equations it is assumed that all dissipation terms are zero and the magnetic field is perfectly frozen into the plasma. This means we can also neglect non-ideal heating terms in the energy equation. Thus, together with the induction equation, the zero divergence of the magnetic field and including the Lorentz force, the Euler equations are extended to the ideal MHD equations as

$$\begin{aligned} \frac{\partial}{\partial \mathrm{t}}\rho + \nabla(\rho\mathbf{u}) &= 0 \\ \frac{\partial}{\partial \mathrm{t}}(\rho\mathbf{u}) + \nabla\cdot(\rho\mathbf{u}\otimes\mathbf{u} - \frac{1}{4\pi}\mathbf{B}\otimes\mathbf{B} + P_{\mathrm{tot}}\mathbb{I}) &= -\rho\nabla\Phi \\ \frac{\partial}{\partial \mathrm{t}}(\rho e_{\mathrm{tot}}) + \nabla\cdot\left[\mathbf{u}(\rho e_{\mathrm{tot}} + P_{\mathrm{tot}}) - \frac{1}{4\pi}\mathbf{B}(\mathbf{B}\cdot\mathbf{u})\right] &= -\rho\mathbf{u}\nabla\Phi \end{aligned} \tag{5.38}$$

where P_{tot} now also includes the magnetic pressure

$$P_{\mathrm{tot}} = P + \frac{1}{8\pi}\mathrm{B}^2 \tag{5.39}$$

and the total specific energy now includes the magnetic energy

$$e_{\mathrm{tot}} = e_{\mathrm{in}} + e_{\mathrm{kin}} + \frac{1}{8\pi}\mathrm{B}^2 \tag{5.40}$$

5.4 Numerical implementation

There are two well-established concepts for solving gas dynamics in numerical simulations. On the one hand, there is the smooth-particle hydrodynamics (SPH) approach which represents the fluid by moving integration points. Note that these so-called particles are not a real physical representation of matter but only have fluid variables in a weighted spacial distribution associated with them and purely serve as integration positions. On the other hand, there are grid codes which have fixed integration positions and represent the fluid variables as contained inside a fixed cell volume. Both methods have advantages and disadvantages, which largely depend on which processes are simulated. As the integration points move with the flow of the fluid in the SPH method, the resolution is automatically increased in regions where matter converges and where a higher resolution is desired while decreasing the resolution in empty regions. However, grid codes are numerically less diffusive and naturally capture discontinuities and shocks in the fluid flow, a property SPH methods only achieve by using artificial viscosity. Here, we discuss the numerical implementation of solving the fluid dynamics in grid codes. Notable examples of grid codes are the ZEUS code (Stone and Norman, 1992) and its successor ATHENA (Stone et al., 2008), the PLUTO code (Mignone et al., 2007), FLASH (Fryxell et al., 2000) and RAMSES (Teyssier, 2002), of which the last was used in this work. Recent developments

have seen the implementation of hybrid schemes: the so-called moving mesh codes, for example AREPO (Springel, 2010), and meshless schemes. The idea behind these hybrid approaches is that in a similar manner to traditional grid codes, the domain is partitioned into separate regions and a Riemann solver is applied at the boundaries to solve the equation of hydrodynamics, whereby the cell defining positions are no longer fixed but move with the flow of the gas which reduces numerical diffusion.

5.4.1 The Godunov Method

As the Euler equations are conservation laws, we can discretise the computational volume in fixed volume elements of any form and size. The flow of conserved quantities is then determined by a summation of the net fluxes over the volume boundaries which allows the conserved quantities to be discontinuous. The most popular numerical technique for doing so is the Godunov method (Godunov, 1959). In contrast to the Finite Difference approach, which defines values at single points in order to calculate the flux between cells, this Finite Volume method uses cell-averaged quantities:

$$\mathbf{U}_i^n = \frac{1}{V_i} \int \mathbf{U}(\mathbf{x}, t^n) \mathrm{d}V \tag{5.41}$$

where the index i is the ordering of the cells and the index n is the ordering in time. By using the time averaged flux function

$$\bar{\mathbf{F}} = \frac{1}{\Delta t} \int_{t^n}^{t^{n+1}} \mathbf{F}(\mathbf{x}, t) \mathrm{d}t \tag{5.42}$$

and the divergence theorem, the exact solution of the conservation laws in integral form is

$$\mathbf{U}_i^{n+1} = \mathbf{U}_i^n + \frac{\Delta t}{V_i} \int_{S_i} \bar{\mathbf{F}} \cdot \mathbf{n} \mathrm{d}S. \tag{5.43}$$

This method can in principle be used for any kind of grid geometry (Harten et al., 1983). However, the advantage of using a regularly spaced grid is that it allows the construction of numerical schemes of higher order than for irregular meshes due to the exact cancellation of terms in the Taylor expansion. As the flux is orthogonal to the faces of each cell in the case of a cartesian mesh geometry, the above equation simplifies to the sum of the in- and outgoing fluxes over all faces of each cell, for example in one spatial dimension:

$$\begin{aligned} \mathbf{U}_i^{n+1} &= \mathbf{U}_i^n + \frac{\Delta t}{\Delta x} \left[\frac{1}{\Delta t} \int_{t^n}^{t^{n+1}} \mathbf{F}\left(\mathbf{U}(x_{i-1/2}, t)\right) \mathrm{d}t - \frac{1}{\Delta t} \int_{t^n}^{t^{n+1}} \mathbf{F}\left(\mathbf{U}(x_{i+1/2}, t)\right) \mathrm{d}t \right] = \\ &= \mathbf{U}_i^n + \frac{\Delta t}{\Delta x} \left[\bar{\mathbf{F}}_{i-1/2} - \bar{\mathbf{F}}_{i+1/2} \right]. \end{aligned} \tag{5.44}$$

5.4.2 Riemann problem

The first-order Godunov scheme assumes that the fluid variables are piecewise constant in each cell as shown in Figure 5.1. This means at each cell interface, we have a discontinuity and in order to calculate the flux function we can define a so-called Riemann problem of which we can determine the exact solution. As the Euler equations are a set of nonlinear differential equations, the exact solution involves non-linear features such as shock and rarefaction waves. The solution is self-similar in the

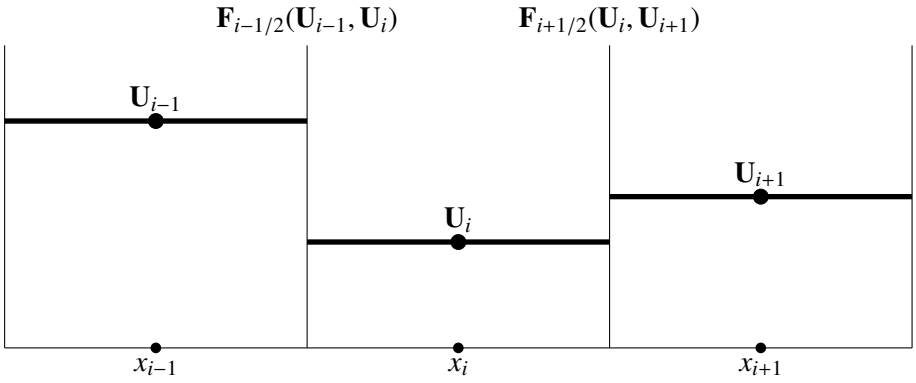

Figure 5.1: Schematic view of the first order Godunov method. The fluid variables are represented by piecewise constant cell-averaged quantities which are used to determine the fluxes between the cells.

variable x/t and thus the time average is equal to its value at $x/t = 0$. This simplifies the calculation as the flux function is then simply determined by the adjacent states at $x/t = 0$:

$$\bar{\mathbf{F}}_{i+1/2} = \mathbf{F}_{i+1/2}(\mathbf{U}_i, \mathbf{U}_{i+1}). \tag{5.45}$$

As the exact solution involves an iterative scheme and therefore is too computationally expensive, an approximate Riemann solver is used in practice. The book by Toro (1999) gives an overview of the various implementations of different approximate Riemann solvers. Many Riemann solvers approximate the solution by finding a linearisation to the Euler equations and representing the non-linear features such as the shock and rarefaction waves by jumps. A popular example is the Roe solver (Roe, 1981) where the wave propagation speeds are determined from the eigenvectors and eigenvalues of the linearisation. Here we discuss the example of the HLLC Riemann Solver (Toro et al., 1994) which is a modification of the HLL Riemann solver developed by Harten, Lax and van Leer (Harten et al., 1983). In contrast to the Roe solver, the family of HLL solvers represent the solution by two waves whose propagation speed is estimated using physical arguments. The waves split the solution into different regions: a left and right unaffected region $\mathbf{U}_L$ and $\mathbf{U}_R$ to either side of the boundary and a central region $\mathbf{U}^*$. The HLLC solver restores the contact discontinuity in the central region and thus splits the solution into four regions

$$\mathbf{U}_{HLLC} = \begin{cases} \mathbf{U}_L & \text{if } x/t \leq S_L \\ \mathbf{U}_L^* & \text{if } S_L \leq x/t \leq S^* \\ \mathbf{U}_R^* & \text{if } S^* \leq x/t \leq S_R \\ \mathbf{U}_R & \text{if } x/t \geq S_R \end{cases} \tag{5.46}$$

with the left, right and central wave speeds S_L, S_R and S^* as represented in Figure 5.2. The respective fluxes are calculated by applying the Rankine-Hugoniot jump conditions across each wave

$$\begin{aligned} \mathbf{F}_L^* &= \mathbf{F}_L + S_L(\mathbf{U}_L^* - \mathbf{U}_L) \\ \mathbf{F}_R^* &= \mathbf{F}_L^* + S^*(\mathbf{U}_R^* - \mathbf{U}_L^*) \\ \mathbf{F}_R^* &= \mathbf{F}_R + S_R(\mathbf{U}_R^* - \mathbf{U}_R) \end{aligned} \tag{5.47}$$

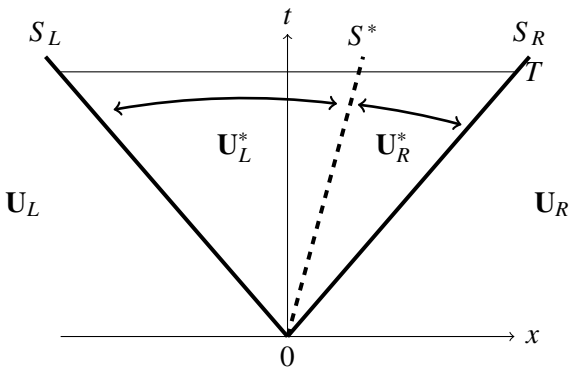

Figure 5.2: Structure of the approximate solution of the HLLC Riemann solver. The vertical axis shows the advancement in time. The thick lines represent the outer waves, the dashed line the contact discontinuity.

where the middle states are determined by using the fact that the velocity in the propagation direction u_x^* and pressure P^* in the central region are constant:

$$\mathbf{U}_K^* = \rho_K \left(\frac{S_K - u_{x,K}}{S_K - S^*} \right) \begin{pmatrix} 1 \\ S^* \\ u_{y,K} \\ u_{z,K} \\ e_{\mathrm{tot},K} + (S^* - u_{x,K}) \left[S^* + \frac{P_K}{\rho_K (S_K - u_{x,K})} \right] \end{pmatrix} \tag{5.48}$$

where K represents either the left or right middle region. Thus, the HLLC flux used in the Godunov scheme is

$$\mathbf{F}_{HLLC}(\mathbf{U}_L, \mathbf{U}_R) = \begin{cases} \mathbf{F}_L & \text{if } 0 \le S_L \\ \mathbf{F}_L^* = \mathbf{F}_L + S_L(\mathbf{U}_L^* - \mathbf{U}_L) & \text{if } S_L \le 0 \le S^* \\ \mathbf{F}_R^* = \mathbf{F}_R + S_R(\mathbf{U}_R^* - \mathbf{U}_R) & \text{if } S^* \le 0 \le S_R \\ \mathbf{F}_R & \text{if } 0 \ge S_R \end{cases} \tag{5.49}$$

where the flux function is determined in this case along the x-axis by

$$\mathbf{F}_x(\mathbf{U}) = \begin{pmatrix} \rho u_x \\ \rho u_x^2 + P \\ \rho u_x u_y \\ \rho u_x u_z \\ \rho E u_x + P u_x \end{pmatrix} \tag{5.50}$$

The real difference between various implementations is given by different physically motivated expressions for the wave speeds. In RAMSES this is done by using the velocities of the fastest moving signal:

$$\begin{aligned} S_L &= \min\{u_{x,L}, u_{x,R}\} - \max\{c_{s,L}, c_{s,R}\} \\ S_R &= \max\{u_{x,L}, u_{x,R}\} + \max\{c_{s,L}, c_{s,R}\} \end{aligned} \tag{5.51}$$

where $c_{s,K}$ is the respective sound speed. The central wave speed is then determined by the implementation by Batten et al. (1997):

$$S^* = \frac{P_R - P_L + \rho_L u_{x,L}(S_L - u_{x,L}) - \rho_R u_{x,R}(S_R - u_{x,R})}{\rho_L(S_L - u_{x,L}) - \rho_R(S_R - u_{x,R})}. \tag{5.52}$$

The maximum wave speed is also a limiting factor in evolving individual time steps. As the waves are not allowed to travel further than one grid cell in order to ensure a stable algorithm, the maximum integration time step is limited by

$$\Delta t \leq \frac{\Delta x}{S_{\max}}, \tag{5.53}$$

where S_{max} is the maximum wave speed in any spatial dimension. This condition can be rewritten to

$$\Delta t = \frac{C_{cfl}\Delta x}{S_{\max}}, \tag{5.54}$$

where C_{clf} is the Courant-Friedrichs-Lewy (CFL) condition (Courant et al., 1928) with

$$0 < C_{cfl} < 1 \tag{5.55}$$

in order to ensure a stable code. Typically there are further time step constraints in codes when gravitational collapse or cosmological evolution is involved. The maximum time step is then set by the most limiting factor.

The diffence between the various approximate Riemann solvers lies in the amount of numerical diffusion they create. The evolution of quantities along a grid inevitably leads to numerical diffusion as the content of cells is not transported uniformily but the flux between two cells leads to an interpolation of the states after the time Δt. Indeed, some level of numerical diffusion is necessary in order to stabilise the numerical integration and methods which are overly suppressive can create spurious features. For first-order schemes numerical diffusion is proportional to the cell size, but can be significantly reduced with higher-order schemes. In the limit of zero cell size the numerical diffusion also reduces to zero which is why numercal methods do not solve the ideal Euler equations but are referred to as the weak solution of the non-ideal Euler equations where the viscous terms tend to zero. Numerical diffusion also has implications for the dissipation of energy in simulations. As the mean free path of individual particles is not resolved, energy is dissipated numerically at the resolution limit.

5.4.3 Higher-order extensions

The numerical diffusion of the first-order Godunov scheme is usually too large in practice and any features are quickly smoothed out. The leading error terms are proportional to the grid spacing and thus only converge slowly for a higher resolution. Therefore, higher-order schemes were developed such as the first second-order algorithm: the MUSCL-Hancock scheme ("Monotonic Upwind-centred Scheme for Conservation Laws" (van Leer, 1976, 1984)). Here, the cell-averaged quantities are no longer piecewise constant but are represented by piecewise linear functions which conserve the integral average of the cell as illustrated by Figure 5.3. The local reconstruction of the quantities is then given by

$$\mathbf{U}_i(x) = \mathbf{U}_i + \frac{(x - x_i)}{\Delta x}\Delta_i, \;\; x \in [0, \Delta x] \tag{5.56}$$

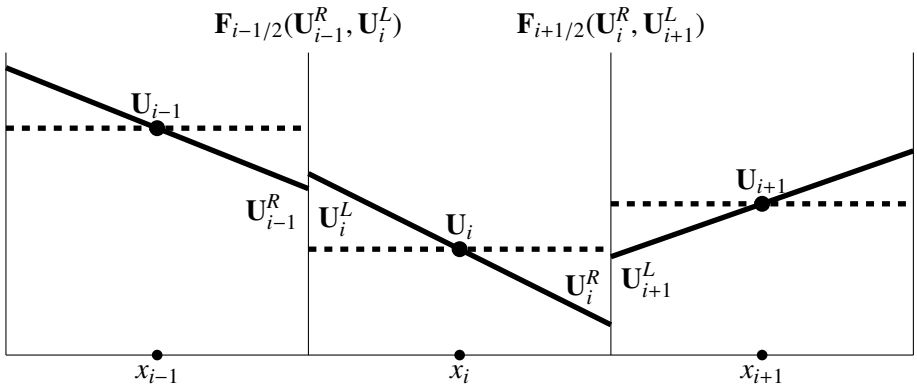

Figure 5.3: Illustration of the MUSCL-Hancock method. The piecewise constant data states are replaced with piecewise linear functions.

with the slope Δ_i defined as

$$\Delta_i = \frac{1}{2}(1+\omega)(\mathbf{U}_i - \mathbf{U}_{i-1}) + \frac{1}{2}(1-\omega)(\mathbf{U}_{i+1} - \mathbf{U}_i),\ \omega \in [-1, 1]. \tag{5.57}$$

For $\omega = 0$, Δ_i is a central finite difference approximation of the slope. The boundary extrapolated values are then given by

$$\begin{aligned} \mathbf{U}^L_i &= \mathbf{U}_i - \frac{1}{2}\Delta_i \\ \mathbf{U}^R_i &= \mathbf{U}_i + \frac{1}{2}\Delta_i. \end{aligned} \tag{5.58}$$

Note that here left and right does not represent the left and right state of the boundary as in the Riemann solver but the left and right extrapolated value inside a single cell as shown in Figure 5.3. As now the flux function is not self-similar anymore and in order to stabilise the scheme, these values are evolved for half a time-step similar to a predictor-corrector scheme:

$$\begin{aligned} \bar{\mathbf{U}}^L_i &= \mathbf{U}^L_i + \frac{1}{2}\frac{\Delta t}{\Delta x}[\mathbf{F}(\mathbf{U}^L_i) - \mathbf{F}(\mathbf{U}^R_i)] \\ \bar{\mathbf{U}}^R_i &= \mathbf{U}^R_i + \frac{1}{2}\frac{\Delta t}{\Delta x}[\mathbf{F}(\mathbf{U}^L_i) - \mathbf{F}(\mathbf{U}^R_i)] \end{aligned} \tag{5.59}$$

This evolution step is entirely carried out in a single cell and the evolved values are then used in the Riemann problem at the cell boundaries:

$$\mathbf{F}_{i+1/2} = \mathbf{F}_{i+1/2}(\bar{\mathbf{U}}^R_i, \bar{\mathbf{U}}^L_{i+1}). \tag{5.60}$$

The MUSCL-Hancock scheme is second-order in time and space but Godunov's theorem states that any scheme higher than first-order will produce oscillations at large gradients (Godunov, 1959). This is due to the fact that the linear reconstruction can introduce maxima in the gradient over several cells as is the case on the left boundary in Figure 5.3. In order to reduce the occurrence of maxima, the slopes are limited to a maximum incline by a slope limiter. The maximum value is set locally for every cell and in order to have a total variance diminishing scheme (Harten, 1983) the condition is that the

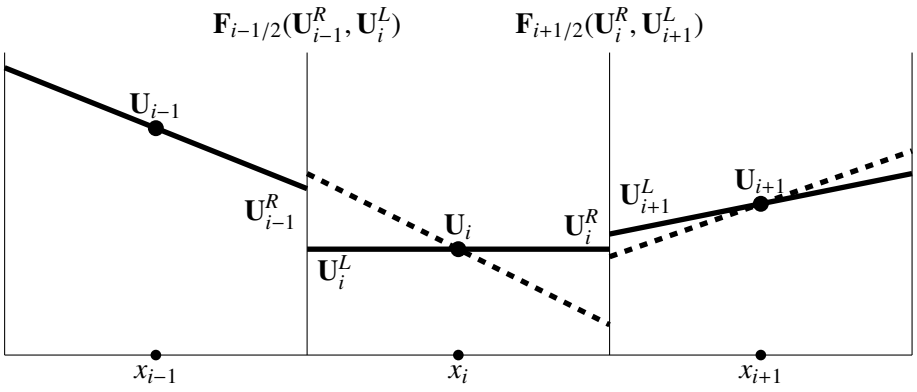

Figure 5.4: Illustration of the MUSCL-Hancock method after applying a slope limiter. The slope limiter decreases the incline of the slopes in order to reduce the occurrence of maxima.

updated state in the cell is bounded by the initial adjacent average states. This is ensured by various different slope limiters, less rigorously for instance by the minmod slope limiter where the boundary extrapolated values must be monotonous:

$$\Delta_i = \text{minmod}(\mathbf{U}_i - \mathbf{U}_{i-1}, \mathbf{U}_{i+1} - \mathbf{U}_i) \tag{5.61}$$

with

$$\text{minmod}(a, b) = \begin{cases} 0 & \text{if } ab \leq 0 \\ a & \text{if } |a| < |b| \text{ and } ab > 0 \\ b & \text{if } |b| < |a| \text{ and } ab > 0 \end{cases} \tag{5.62}$$

This method sets the slope to the lower value of the differences to the neighboring cells or to zero if the differences have different signs as illustrated in Figure 5.4. A slope limiter effectively reduces the order of the scheme locally where large gradients are present. In order to reduce numerical diffusion, it is more effective to use even higher-order schemes (ENO, WENO or discontinuous Garlekin methods) for smooth regions, while discontinuities are better treated by a local increase in resolution which is achieved for instance by adaptive mesh refinement (AMR) (Berger and Oliger, 1984; Berger and Colella, 1989).

AMR works by splitting existing cells usually by a factor of two (or eight in three dimensions) which leads to a finer resolution. In principle there are three different approaches to refining cells. The block-based method refines large regions of the code as soon as one cell of the region has reached the refinement criteria which results in a simple data structure but also in a larger amount of refined cells than necessary, which increases computational time and storage. The cell-based approach refines individual cells on a cell-by-cell basis, leading to a minimal refinement which can reduce the computational cost dramatically but also necessitates a complex data structure to store the cells. A compromise between the two methods is the patch-based method where rectangular refined regions are adapted to the geometry of the cells needing refinement, leading to a lower number of refined cells than the block-based method while still having a relatively easy data structure. Special care has to be taken when defining the refinement criteria in order to actually improve the solution. Typical criteria are the cell density or the density gradient. The flux at the boundary of the coarse cell is replaced by

the sum of the fluxes on the fine level and the boundary values have to be interpolated down to the refined cells. As the CFL condition depends on the spatial resolution, highly refined cells can dictate the time advancement of the whole simulation. In order to reduce the impact of highly refined cells, subcycling is employed where the code is advanced separately on each refinement level according to the respective timestep size.

5.4.4 Gravity source terms

Source terms refer to all terms which are added to the right-hand side of the Euler equations as done for a generic external force in Equation 5.26. The general equation including a source term $\mathbf{S}(\mathbf{U})$ has the form

$$\frac{\partial \mathbf{U}}{\partial \mathrm{t}} + \nabla \cdot \mathbf{F}(\mathbf{U}) = \mathbf{S}(\mathbf{U}). \tag{5.63}$$

While various physical processes exist which are included via source terms, e.g. radiation, with their respective numerical techniques, for astrophysical applications the most important source term is the force of gravity which is given by the gradient of the gravitational potential which is calculated by solving the Poisson equation:

$$\mathbf{F}_{\mathrm{grav}} = -\rho \nabla \Phi \quad \text{with} \quad \Delta \Phi = 4\pi G \rho. \tag{5.64}$$

There are various numerical methods for solving the Poisson equation, ranging from Particle-In-Cell methods over Fast Fourier solvers to relaxation methods or some combination thereof which we will not discuss in detail. If the characteristic timescale to reach an equilibrium state with the source terms is much larger than the typical timescale associated with the hydrodynamic evolution

$$t_{\mathrm{HD}} = \frac{\Delta x}{S_{\max}}, \tag{5.65}$$

as is usually the case with gravity, the source terms are called non-stiff and can be implemented by using the so-called operator split approach where the overall equation is split into two successive separate steps. First the hyperbolic equation is solved without the source term as done by the Godunov scheme in order to obtain the temporary state $\overline{\mathbf{U}}^{n+1}$. Thereafter, in a second step, the evolved temporary solution is updated by either a first-order scheme:

$$\frac{\mathbf{U}^{n+1} - \overline{\mathbf{U}}^{n+1}}{\Delta t} = \mathbf{S}(\mathbf{U}^n) \tag{5.66}$$

or a second-order scheme:

$$\frac{\mathbf{U}^{n+1} - \overline{\mathbf{U}}^{n+1}}{\Delta t} = \frac{\mathbf{S}(\mathbf{U}^n) + \mathbf{S}(\mathbf{U}^{n+1})}{2} \tag{5.67}$$

where, in the case of gravity, the final update is performed after solving the Poisson equation for the evolved temporary state:

$$\frac{(\rho \mathbf{u})^{n+1} - \overline{(\rho \mathbf{u})}^{n+1}}{\Delta t} = -\frac{(\rho \nabla \Phi)^n + (\rho \nabla \Phi)^{n+1}}{2} \tag{5.68}$$

$$\frac{(\rho e_{\mathrm{tot}})^{n+1} - \overline{(\rho e_{\mathrm{tot}})}^{n+1}}{\Delta t} = -\frac{(\rho \mathbf{u} \nabla \Phi)^n + (\rho \mathbf{u} \nabla \Phi)^{n+1}}{2} \tag{5.69}$$

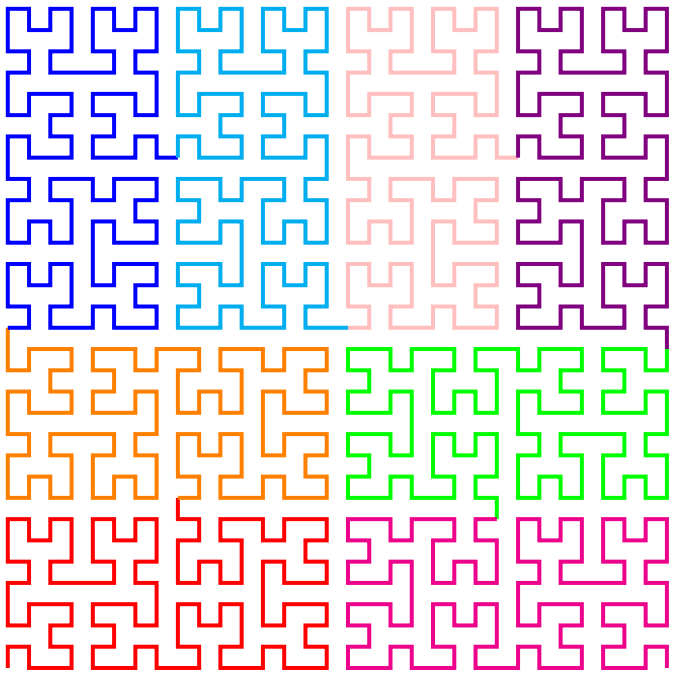

Figure 5.5: Example of the domain decomposition using a Peano-Hilbert curve. The two-dimensional domain of a 32 x 32 grid is filled by a one-dimensional line. The colour coding shows the ideal partitioning of the domain on eight processors.

$$\Delta\Phi^{n+1} = 4\pi G\bar{\rho}^{n+1} \tag{5.70}$$

When self-gravity is involved, it is important to be aware of the effects of numerical fragmentation which can lead to the artificial formation of dense gas clumps. This issue was explored in a study by Truelove et al. (1997) who noted that the Jeans length of the gas must be resolved locally at least by four cells at all times in order to prevent artificial fragmentation.

5.4.5 Parallelisation

Executing serial, computationally demanding simulations on a single processor is not very efficient and is not a viable option in many situations. The computation can be significantly accelerated by spreading the workload over several processors using MPI (Message Passing Interface). The three-dimensional domain is split into sections which are each computed by a separate processor respectively. The sectioning is done by using the one-dimensional Peano-Hilbert space-filling curve. This guarantees well-balanced processes as the curve optimises the geometry of the sub-domains by creating continuous sections of cells. Each individual sub-domain has its own boundary conditions given by copies of the adjacent cells of neighboring sections, so-called ghost cells, which have to be exchanged after every time-step. Therefore, the Peano-Hilbert curve reduces the amount of communication necessary between the processors. An example in two-dimensions is given in Figure 5.5 which shows the partitioning of sections onto separate processors as given by the different colours.

6 Paper I: Non-linear dense core formation in the dark cloud L1517

S. Heigl, A. Burkert, A. Hacar, 2016, *Monthly Notices of the Royal Astronomical Society*, 463, 4301-4310

We present a solution for the observed core fragmentation of filaments in the Taurus L1517 dark cloud which previously could not be explained (Hacar and Tafalla, 2011). Core fragmentation is a vital step for the formation of stars. Observations suggest a connection to the filamentary structure of the cloud gas, but it remains unclear which process is responsible. We show that the gravitational instability process of an infinite, isothermal cylinder can account for the exhibited fragmentation under the assumption that the perturbation grows on the dominant wavelength. We use numerical simulations with the code RAMSES, estimate observed column densities and line-of-sight velocities, and compare them to the observations. A critical factor for the observed fragmentation is that cores grow by redistributing mass within the filament and thus the density between the cores decreases over the fragmentation process. This often leads to wrong dominant wavelength estimates, as it is strongly dependent on the initial central density. We argue that non-linear effects also play an important role on the evolution of the fragmentation. Once the density perturbation grows above the critical line-mass, non-linearity leads to an enhancement of the central core density in comparison to the analytical prediction. Choosing the correct initial conditions with perturbation strengths of around 20%, leads to inclination corrected line-of-sight velocities and central core densities within the observational measurement error in a realistic evolution time.

Key words: stars:formation – ISM:kinematics and dynamics – ISM:structure

6.1 Introduction

Individual or binary stars are formed in dense cores (Benson and Myers, 1989; di Francesco et al., 2007) which are condensations within larger molecular cloud complexes. The critical process of how a tens of parsec sized cloud fragments into a few 0.1 pc sized cores nevertheless remains an unresolved challenge for star formation. Especially, as core formation appears to be tied to the low efficiency of the star-formation process (Evans et al., 2009).

The recent large-scale cloud images taken by the *Herschel* Space Observatory show that molecular clouds exhibit a ubiquity of complex filamentary structures, forming a network over several size scales (André et al., 2010; Molinari et al., 2010; Arzoumanian et al., 2011; Schneider et al., 2012) and dense cores being aligned with large-scale filaments like pearls in a string. This is a strong indication that core formation is tied to some kind of filament fragmentation process, a connection which has long been proposed (Schneider and Elmegreen, 1979; Larson, 1985).

Recent observations however have shown that filamentary clouds with trans-sonic internal motions are not one single entity, but consist of fibers: velocity-coherent structures of subsonic gas (Hacar et al., 2013; Arzoumanian et al., 2013; Tanaka et al., 2013; Tafalla and Hacar, 2015). The existence of filamentary substructure has also been found recently in numerical simulations (Moeckel and Burkert, 2015; Smith et al., 2016). Dense cores are embedded within these fibers and often show similar kinematic properties with a smooth transition from fiber to core gas. This suggests that turbulence does not dissipate at the scale of dense cores, but at the typical scale of the velocity-coherent fibers of about 0.5 pc. Tafalla and Hacar (2015) propose a model they call "*fray and fragment*": At first, the filament forms through a colliding flow. Over time, residual turbulent motions together with gravity form velocity-coherent fibers. Finally, some of the fibers form dense cores through gravitational instability. The model suggests that cores form by subsonic motions and gives rise to the question of the exact mechanism that leads to core formation in fibres and filaments. The key to understanding the core fragmentation process and to distinguish between different models, such as a pure gravitational fragmentation, dissipation of turbulence due to supersonic shocks (Padoan et al., 2001; Klessen et al., 2005; Vázquez-Semadeni et al., 2005) or the loss of magnetic support due to ambipolar diffusion (Shu et al., 1987), is the internal velocity structure of the filaments, as well as their kinematic properties.

A detailed study of the L1517 dark cloud in Taurus and its core population was presented by Hacar and Tafalla (2011). They observed the cloud in four different molecular transitions, ranging from $N_2H^+(J = 1-0)$ and $SO(J_N = 3_2-2_1)$ to $C^{18}O(J = 1-0)$ and $C^{17}O(J = 1-0)$ as well as in dust continuum emission. This allows them to study different density regimes, from the less dense filament gas to the very dense core interior, in great detail. In addition they show that the cores are in different evolutionary states, with more evolved cores having increasing N_2H^+ abundance and anti-correlated, depleted SO emission (Tafalla et al., 2006). The region is made up of four velocity coherent filaments consisting predominantly of subsonic gas. In two of the filaments, two cores are forming separately and the interior motion of the filaments show a smooth transition to the core gas kinematics. The line-of sight velocity centroid shows an oscillatory motion with a periodicity that matches the periodicity of the cores and is clearly associated with the core positions. This oscillatory motion is expected from the gravitational

instability model and suggests that the cores form by gravitational contraction of the filament gas. Nevertheless, the authors claim that the fragmentation distance is not consistent with the model of pure gravitational fragmentation, a claim we want to test using numerical methods as the model is strongly dependent on its initial condition and the inclination of the filament.

In the following sections, we recapitulate the filament and core population of L1517 (Section 6.2) and the characteristic properties our models have to replicate. We also summarise the theory of the fragmentation of pressure-bound isothermal filaments (Subsection 6.3.1), the basis of our models and how we use it in our simulations (Subsection 6.3.2). Next, we discuss the simulation set-up (Section 6.4) and present our numerical results (Section 6.5). We start by comparing our data to the observations (Subsection 6.5.1), then we discuss the evolution of the core growth in the linear and non-linear regime (Subsection 6.5.2). Finally, we finish with an analysis of the external pressure in the dark cloud (Subsection 6.5.3) which is a crucial part of the model of a pressure-bound isothermal filament.

6.2 Filaments and cores in L1517

The L1517 dark cloud has several properties in favour of an idealised analysis. The cloud is relatively isolated, only to be disturbed by the near PMS stars AB Aurigae and SU Aurigae, which are physically associated with L1517 and are heating the near-by gas (Nachman, 1979; Duvert et al., 1986; Heyer et al., 1987), although no influence on the dense gas can be seen. Furthermore, the filament gas is predominantly subsonic. Thus, turbulence only plays a minor role in the dynamics of the gas.

The density profiles of three of the four filaments can be reproduced by an isothermal cylinder in pressure equilibrium with its self-gravity. This profile was first described by Stodólkiewicz (1963) and Ostriker (1964), and is given by the analytic form

$$\rho(r) = \frac{\rho_c}{\left(1 + (r/H)^2\right)^2} \tag{6.1}$$

where r is the cylindrical radius, ρ_0 is the central density. The radial scale height H is given by

$$H^2 = \frac{2c_s^2}{\pi G \rho_c} \tag{6.2}$$

where c_s is the isothermal sound speed and G the gravitational constant. The gas is assumed to have a temperature of approximately 10 K (Tafalla et al., 2004) and assuming a molecular weight of $\mu = 2.36$ gives the isothermal sound speed of $c_s \approx 0.2\,\mathrm{km\,s^{-1}}$. Integrating the profile to $r \to \infty$ gives a line mass of

$$\left(\frac{M}{L}\right)_{\mathrm{crit}} = \frac{2c_s^2}{G} \approx 16.4\,\mathrm{M_\odot\ pc^{-1}} \tag{6.3}$$

This is called the critical line-mass, as it determines the threshold above which a filament will collapse under its self-gravity.

It is important to note that the observations do not extend out far enough in radius to distinguish between different outer density profiles. The filaments could also be reproduced by

a shallower softened power law and it is practically impossible to say if they are in pressure equilibrium. Although, the fact that they form well-separated cores (Inutsuka and Miyama, 1997) and do not show supersonic motions (Burkert and Hartmann, 2004) are good indicators that they indeed are in pressure equilibrium. Only one of the filaments can be better reproduced by using a softened power law and does not follow the isothermal profile. We will concentrate on filaments 1 and 2, following the nomenclature of Hacar and Tafalla (2011), both of which show an agreement with a profile in pressure equilibrium. They exhibit a prominent core fragmentation for which detailed measurements of densities and line-of-sight velocities along the filament are available.

Filament 1 has a total mass of $M_{\rm fil} = 8.0\,{\rm M}_\odot$ and an observed projected length $L_{\rm obs} = 0.52\,{\rm pc}$. It contains the cores A2 and C with central number densities of $6.0 \cdot 10^4\,{\rm cm}^{-3}$ and $4.7{\cdot}10^4\,{\rm cm}^{-3}$ which, assuming a molecular weight of $\mu = 2.36$, correspond to $2.4{\cdot}10^{-19}\,{\rm g\,cm}^{-3}$ and $1.8 \cdot 10^{-19}\,{\rm g\,cm}^{-3}$, respectively. The filament profile fit provides a central number density between the cores of about $10^4\,{\rm cm}^{-3}$ or $3.9 \cdot 10^{-20}\,{\rm g\,cm}^{-3}$. The observed projected core distance is about 340 arcsec or 0.23 pc, assuming a distance of 144 pc to AB Aur (van den Ancker et al., 1998). The line-of-sight velocity centroid variation along the filament shows a core forming motion following a sinusoidal pattern with an amplitude of $0.04\,{\rm km\,s}^{-1}$ after subtracting a smooth linear gradient of $1.0\,{\rm km\,s}^{-1}\,{\rm pc}^{-1}$.

Filament 2 is measured to have a total mass of $M_{\rm fil} = 7.2\,{\rm M}_\odot$ and an observed projected length $L_{\rm obs} = 0.42\,{\rm pc}$. It contains the cores A1 and B, which have a central density of $7.0 \cdot 10^4\,{\rm cm}^{-3}$ and $2.2 \cdot 10^5\,{\rm cm}^{-3}$, which corresponds to $2.7 \cdot 10^{-19}\,{\rm g\,cm}^{-3}$ and $8.6 \cdot 10^{-19}\,{\rm g\,cm}^{-3}$ respectively. The central density between the cores is determined to be $7.0 \cdot 10^3\,{\rm cm}^{-3}$ which is equivalent to $2.7 \cdot 10^{-20}\,{\rm g\,cm}^{-3}$. The observed core distance is about 270 arcsec or 0.19 pc. In contrast to filament 1, the line-of-sight velocity centroid variation does not follow a well defined pattern as filament 1. Nevertheless, Hacar and Tafalla (2011) fit a linear gradient of $1.4\,{\rm km\,s}^{-1}\,{\rm pc}^{-1}$ and a sinusoidal pattern with an amplitude of $0.04\,{\rm km\,s}^{-1}$ to the data. While it does match the observed velocity pattern in certain regions, it fails to explain the overall form.

6.3 Filament fragmentation

6.3.1 Theory of filament fragmentation

There has been extensive theoretical work on the fragmentation of infinite, isothermal filaments over the last fifty years. In reality, filaments are neither infinite nor isothermal. The approximation of isothermality is probably a valid approach in the case of L1517 as the density profiles match the isothermal profile. Also the typical dust temperature gradients in filaments are smaller than a few Kelvin (Arzoumanian et al., 2011; Palmeirim et al., 2013). The bigger caveat is that filaments have a finite length. It has already been shown that filaments collapse globally via the end-dominated mode where clumps form at both ends of the filament due to gravitational focusing (Bastien, 1983; Burkert and Hartmann, 2004; Pon et al., 2012). But it still remains unclear how equilibrium filaments fragment exactly under global collapse. While solutions have been found for a radial equilibrium of non-isothermal filaments (Recchi et al., 2013), they only apply to infinite filaments. This is also true for the

above mentioned radial solution found by Stodólkiewicz (1963). There is still a lack of detailed theoretical studies on the structure and fragmentation of finite filaments. Bastien et al. (1991) looked at the fragmentation of finite cylinders with a uniform density profile. They discover a similar behaviour as for the pressure truncated infinite equilibrium case presented below and also find a critical wavelength beneath which density perturbations will not grow. It differs by a factor of four from the infinite filament case predicting more fragments in finite filaments. They also find that in most cases it is possible to form growing fragments along the cylinder before a complete collapse and that the dominance of the end fragments decreases for a higher mass of the clouds. But the study still misses a detailed numerical prediction of dominant fragmentation scales and its dependence on the line-mass. We therefore stress the fact that due to a lack of a better theory we use the approximation of an infinite, isothermal filament which we present here.

We introduce a small density perturbation in the linear regime along the filament axis of the form:

$$\rho(r,z,t) = \rho_0(r) + \rho_1(r,z,t) = \rho_0(r) + \epsilon\rho_0(r)\exp(ikz - i\omega t) \tag{6.4}$$

In this case, z is the filament axis, ω is the growth rate, $k = 2\pi/\lambda$ the wave vector and ϵ the perturbation strength. Neglecting second order terms, perturbations will grow for values of k where the solution of the dispersion relation $\omega^2(k)$ is smaller than zero. This will also lead to a perturbation in velocity, pressure and potential of the form:

$$q_1(r,z,t) \propto \exp(ikz - i\omega t) \tag{6.5}$$

It was shown that there are two important parameters for the fragmentation of an infinite, isothermal filament: the critical and the dominant wavelength. On the one hand, the critical wavelength determines the separation above which a small perturbation will grow. It was first determined by Stodólkiewicz (1963) to be $\lambda_{\rm crit} = 3.94H$ for a filament extending to infinite radius. The dominant wavelength, on the other hand, gives the separation of the perturbation which will grow the fastest. It is therefore the most likely perturbation length a filament will show after letting random perturbations grow. It was first determined by Larson (1985) to be about twice the critical wavelength: $\lambda_{\rm dom} = 7.82H$ with a growth rate of $|\omega_{\rm dom}| = 0.339\,(4\pi G\rho_c)^{1/2}$ (Nagasawa, 1987; Inutsuka and Miyama, 1992; Nakamura et al., 1993; Gehman et al., 1996a).

Nagasawa (1987) was the first to also consider the more realistic situation of a pressure truncated filament. In this case the filament follows the pressure equilibrium profile until it extends to the radius where the internal pressure matches the external pressure. The external pressure stabilises the filament against expansion and filaments below the critical line-mass do not extend to infinity and are stable. The factor of line-mass to critical line-mass is given by

$$f_{\rm cyl} = \left(\frac{M}{L}\right) \Big/ \left(\frac{M}{L}\right)_{\rm crit} \tag{6.6}$$

This leads to the boundary radius of

$$R = H\left(\frac{f_{\rm cyl}}{1 - f_{\rm cyl}}\right)^{1/2} \tag{6.7}$$

Table 6.1: Constants of polynomial approximations by Fischera and Martin (2012). FWHM is the approximated full width half maximum of the filament. $\tau_{\rm dom} = 1/\omega_{\rm dom}$ is the growth timescale of the dominant mode given in units of $\sqrt{4\pi G\rho_c}$.

	a_0	a_1	a_2	a_3	a_4	a_5
$\tau_{\rm dom}\sqrt{4\pi G\rho_c}$	4.08	0.00	-2.99	1.46	0.40	0.00
$\lambda_{\rm crit}$/FWHM	3.39	0.00	-2.414	1.588	0.016	0.00
$\lambda_{\rm dom}$/FWHM	6.25	0.00	-6.89	9.18	-3.44	0.00
FWHM/H	0.00	1.732	0.00	-0.041	0.818	-0.976

and the boundary density of

$$\rho_b = \rho_0 \left(1 - f_{\rm cyl}\right)^2 \tag{6.8}$$

For $f_{\rm cyl} \rightarrow 1$ the dispersion relation tends to the same dispersion relation as for the non-truncated filament. In the case that the filament exceeds the critical line-mass ($f_{\rm cyl} > 1$), Inutsuka and Miyama (1992) demonstrated that the filament collapses faster to the axis than perturbations can grow.

Nagasawa (1987) chose an external density of zero for the computation of dominant length- and timescales, corresponding to an infinite temperature. But even for a non-infinite external temperature of ten times greater than the filament temperature, Fiege and Pudritz (2000b) found no difference to the case of an infinite external temperature. In the isothermal case this is equal to setting the external density to a value of ten times less than the boundary density. We also follow this approach and set the external density even lower in order to reduce the effect of accretion onto the filament. A more realistic approach would consider that observations show a smooth transition of filaments into the surrounding medium (Arzoumanian et al., 2011; Palmeirim et al., 2013).

The findings on dominant fragmentation lengthscales and growth timescales for pressure truncated filaments by Nagasawa (1987) were summarised and interpolated by Fischera and Martin (2012) using a fifth-order polynomial function with vanishing derivatives at the extremes:

$$y(x) = \sum_{i=0}^{5} a_i f_{\rm cyl}^{i/2} \tag{6.9}$$

They find the interpolation values given in Table 6.1. As one can see the dominant timescale $\tau_{\rm dom}$, the critical wavelength $\lambda_{\rm crit}$ and the dominant wavelength $\lambda_{\rm dom}$ are all polynominals of different power of f_{cyl}. FWHM is the approximated full width half maximum of the filament. Table 6.1 makes it possible to express the dominant timescale and the dominant wavelength as a factor of the scale height H. We also use this interpolation for our simulations to define our initial density perturbation length and to find the expected growth timescale of the dominant mode.

6.3.2 Analytical prediction for L1517

The linear model relies on an exponential growth of a sinusoidal density and velocity perturbation as seen from Equation 6.4. This implies that the perturbation is symmetrical in

the sense that as the density enhancement grows, the density minimum depletes on the same timescale. Thus, as soon as the peak density reaches twice the initial density, the gas between the cores should be completely accreted and the model has to break down. Therefore, it is not clear how long a sinusoidal redistribution of mass is maintained.

For a first test, we adopt an initial central density that is the simple average between the filament and maximum core density, where we take the average of both cores respectively as density maximum. This leads to the values of about $1.2 \cdot 10^{-19}$ g cm^{-3} for filament 1 and about $2.9 \cdot 10^{-19}$ g cm^{-3} for filament 2, corresponding to the number densities of $3.1 \cdot 10^4$ cm^{-3} and $7.4 \cdot 10^4$ cm^{-3} respectively. In the case we do not achieve a minimum density as low as the observed minimum density when running the fragmentation simulation, we use the mean of our guess value and the observed minimum central density to calculate a new initial central density and iterate until a good agreement with the observation is found.

We expect the cores to grow on the dominant wavelength and thus the observed core separation is the dominant wavelength affected by inclination. We use the inclination angle ϕ where the projected dominant wavelength $\lambda_{\mathrm{dom}} \cdot \cos(\phi)$ corresponds to the observed fragmentation length. The value of λ_{dom} is computed using Table 6.1, where H is calculated according to Equation 6.2 and the line-mass fraction f_{cyl} is determined by using the filament mass $\mathrm{M_{fil}}$ and the observed filament length L_{obs}, which is corrected for inclination:

$$f_{\mathrm{cyl}} = \frac{M_{\mathrm{fil}} \cdot \cos(\phi)}{L_{\mathrm{obs}}} \Big/ \left(16.4\ \mathrm{M_\odot\ pc^{-1}}\right) \tag{6.10}$$

With the central density and f_{cyl} determined, we have everything we need to set-up a filament in pressure equilibrium.

6.4 Simulation set-up

The numerical simulations were executed with the RAMSES code (Teyssier, 2002). The code is capable of solving the discretised Euler equations in their conservative form on an Cartesian grid in 1D, 2D and 3D with a second-order Godunov scheme. For our simulation we used the MUSCL scheme (Monotonic Upstream-Centred Scheme for Conservation Laws, van Leer (1976)) in combination with the HLLC-Solver (Toro et al., 1994) and the multidimensional MC slope limiter (van Leer, 1979) was applied in order to achieve a total variation diminishing scheme. The gravity is solved using the built-in multigrid solver.

We place the filament axis in the x-direction of a 3D box and use periodic boundary conditions in this dimension in order to simulate an infinite filament. We set the boxsize to twice the dominant perturbation length in order to resolve it correctly and to stay close to the observations. The boundaries in perpendicular directions of the filament are set as outflow condition. The potential of the ghost cells has to be set to zero in order to not introduce a gravitational focus to the box centre due to the mixed boundary conditions.

The filament gas is set to be isothermal with a temperature of 10 K and a molecular weight of $\mu = 2.36$. The external gas surrounding the filament is fixed to be isobaric at all times and in pressure equilibrium with the boundary pressure of the filament:

$$P_b = \rho_b c_s^2 \tag{6.11}$$

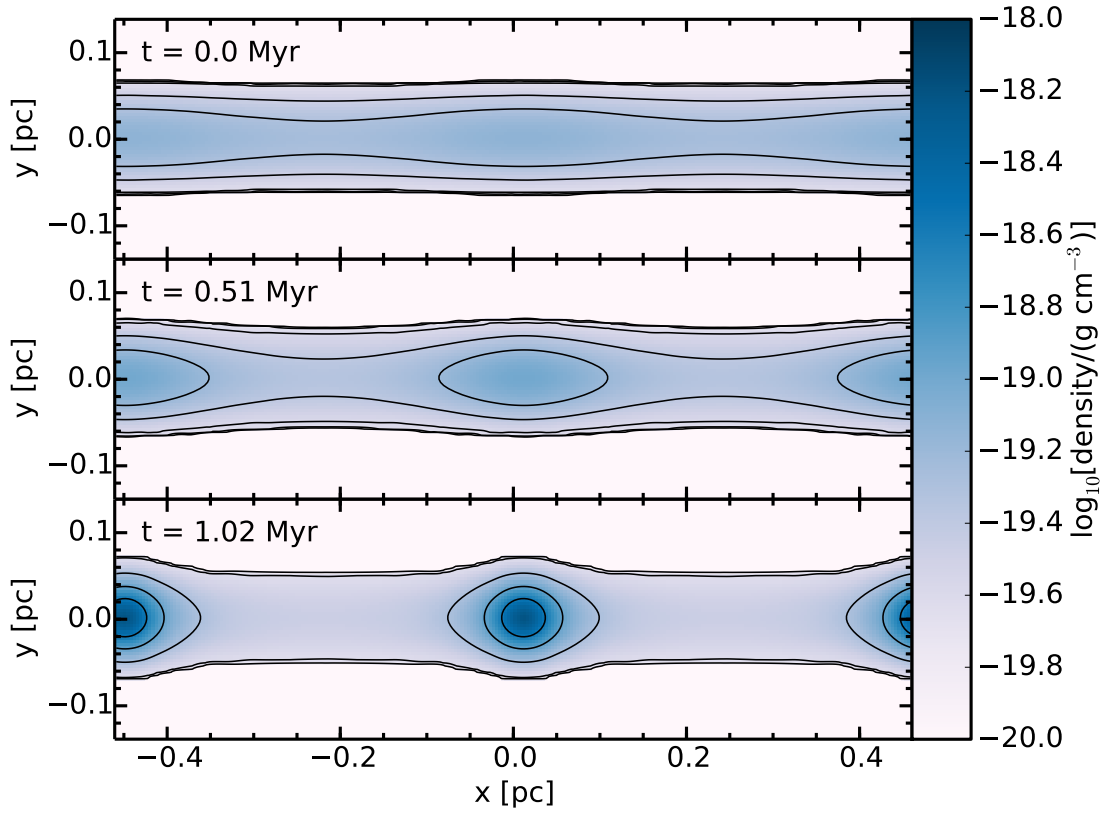

Figure 6.1: Density slice in the x-y plane through the centre of the simulation of filament 2 in log-space. Only the filament gas is plotted ($\rho > 10^{-20}\,\mathrm{g\,cm^{-3}}$). The upper panel shows the filament at the beginning which we define to be 1 Myr before the final state. The lower panel shows the final state that is compared with the observations. The timestep of the middle panel is exactly in between the two. The contours show equi-density levels normalised on the maximum density of the respective timestep and increase linearly in log-space to always show five contours. As one can see, the form of the emerging density clump changes from prolate in the linear evolution phase to becoming more and more roundish in the non-linear phase, a behavior which was also seen in SPH-simulations executed by Inutsuka and Miyama (1992).

In order to minimise the effect of accretion we set the external density to a very low value of 10^{-4} times the filament boundary density. Real physical accretion would affect the growth of perturbations, but to quantify this is above the scope of this paper.

As the boxsize is larger than the filament diameter, we employ adaptive mesh refinement (AMR), which allows us to keep the resolution low in the low-density external gas. We enforce a refinement of the central region to give us an effective resolution of 256^3 for the dense filament gas, which is enough to fulfill the Truelove criterion for the maximum occurring density within a factor of 16 at all times (Truelove et al., 1997) aside from the late core collapse in filament 2 where we still fulfill the Truelove criterion within a factor of 8. In order to check for consistency and rule out a limitation by resolution we also repeat the simulations with half the resolution and look for mayor differences between the results.

The density perturbation is set according to Equation 6.4 with a very small amplitude of 1% of the initial density, as the velocity has to adjust to the perturbed state. The phase of the density perturbation is set at random, but as the box is periodic in the direction of the filament axis, it has no influence on the solution.

6.5 Simulations

6.5.1 Comparison with the observation

We let the simulations run until the maximum density matches the observed central core density. An example of a simulation can be seen in Figure 6.1 where we plot a density slice through the centre of the filament with overlaying density contours. The timescale is restricted by the lifetime of a molecular cloud, which is estimated to be of the order of a few Myr, especially for Taurus (Palla and Stahler, 2000; Hartmann, 2001; White and Ghez, 2001). It is therefore reasonable to assume 1 Myr as typical timescale for filament fragmentation. This timescale also coincides with the average lifetime of a core with typical densities of 10^4 cm^{-3} (Lee and Myers, 1999; Jessop and Ward-Thompson, 2000; Nakamura and Li, 2005), which serves as a good approximation for the total starless core phase. In our case, as the evolution should be effectively self-similar in the linear phase, the evolution timescale is then a function of the initial amplitude of the perturbation. Starting with a very small initial perturbation and running the simulation until the observed state is reached, allows us to actually determine the most likely initial amplitude as the perturbations strength reached one Myr before the finale state.

In order to compare our simulation result with the observations, we assume an inclination as described in Subsection 6.3.2. We then use this inclination to determine the line-of-sight velocity distribution for each spatial pixel. In order to get the centroid velocity, we treat every volume element of the computational grid as an emitter of a discrete line-of-sight velocity value. These are converted to Gaussian line profiles with a dispersion of $\sigma = 0.0526$ km s^{-1}, corresponding to the thermal linewidth of $C^{18}O$, and are weighted with the respective density. The line profiles are binned into histograms with a bin width of 0.05 km s^{-1} in order to get a complete line emission for each observed spatial pixel and we measure the velocity centroid by fitting a Gaussian to the line, as an observer would do.

The result for our converged models is shown in Figure 6.2 for filament 1 and Figure 6.3

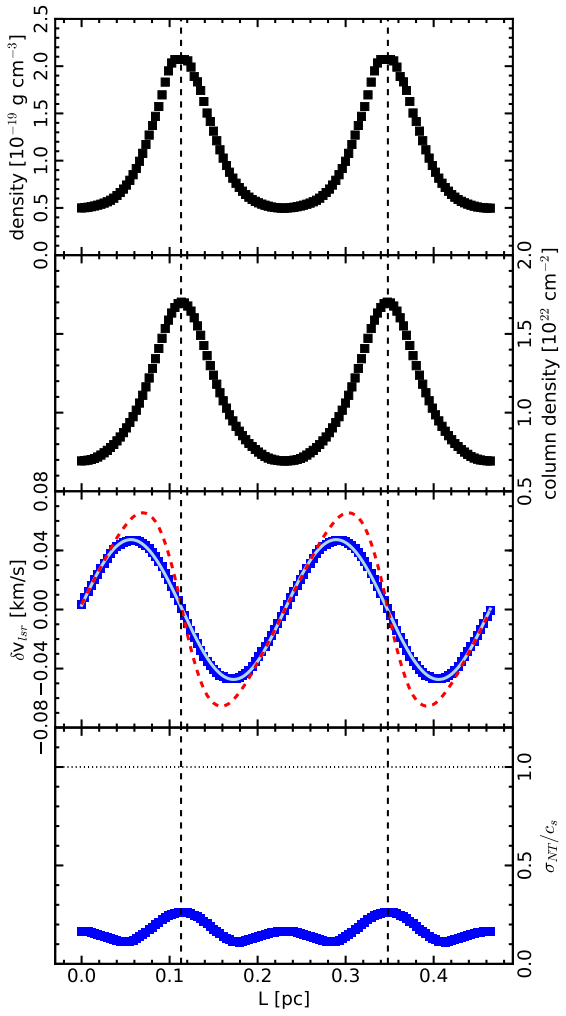

Figure 6.2: Results of the simulation for filament 1 in a line-of-sight projection of 57°along the axis of the filament. The upper panel shows the central volume density along the filament with two distinct cores also marked by the dashed, vertical lines. The density maximum and minimum matches the observation within a factor of two. The second panel shows the surface density summed up along the line-of-sight for a gas with a molecular weight of $\mu = 2.36$. The third panel shows the velocity centroid variation as blue squares. Our fit to the data is given by the light blue line and the true projected central axis velocity is shown by the dashed, red line. As one can see, the true central velocity pattern is hidden with the maxima being damped by the velocity structure inside the filament. The velocity centroid pattern shows nearly the same amplitude of 0.05 km s^{-1} compared to the observed amplitude of 0.04 km s^{-1}. The lower panel shows the non-thermal velocity dispersion in units of the sound speed. The dispersion is subsonic throughout with a mean value of $\langle \sigma_{\rm nt} \rangle / c_s \approx 0.17$ which is about a third of what is observed in filament 1 ($\langle \sigma_{\rm nt} \rangle / c_s = 0.57 \pm 0.15$ (Hacar and Tafalla, 2011)).

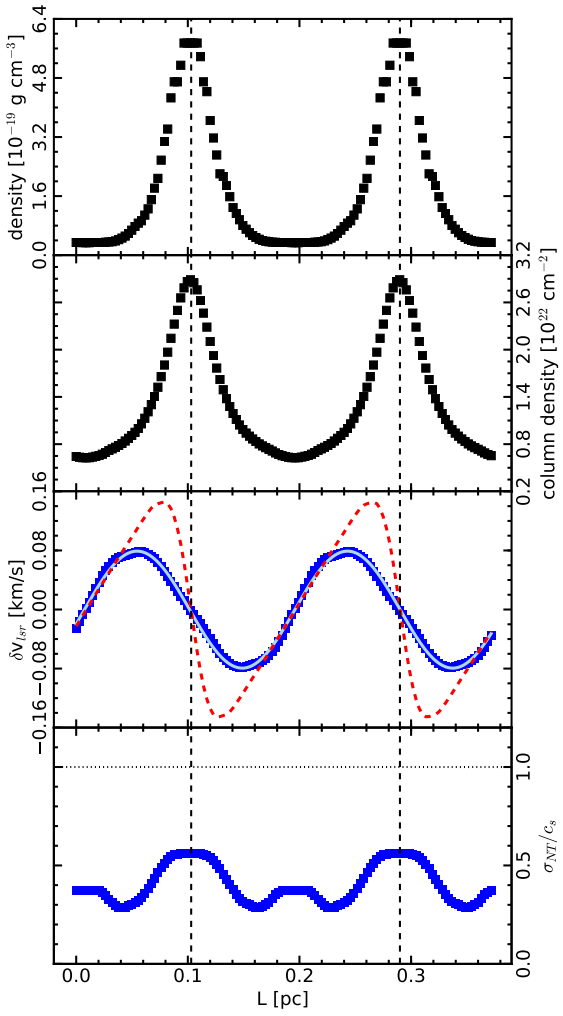

Figure 6.3: As in Figure 6.2 but for filament 2 in a line-of-sight projection of 66°. Again, the upper panel shows that the volume density matches the observation within a factor of two. The cores are more pronounced than for filament 1 and the volume density does not follow a sinusoidal pattern along the filament but shows a flat decreased density between the cores. This feature is harder to see in the surface density in the second panel. The amplitude of the velocity centroid variation is somewhat higher than the fit of the observations, 0.08 km s^{-1} compared to 0.04 km s^{-1}, but the original observed velocity data of filament 2 does not follow a well defined sinusoidal curve (Hacar and Tafalla, 2011). The true central velocity structure is even more damped than in filament 1. It shows more pronounced slopes which indicates that matter from a broader region is pulled onto the density maxima. The non-thermal velocity dispersion in the lower panel is about twice that of the simulation of filament 1 with a mean value of $\langle\sigma_{\rm nt}\rangle/c_s \approx 0.40$ which is around a factor of 1.5 lower compared to the observed value of $\langle\sigma_{\rm nt}\rangle/c_s = 0.63 \pm 0.16$.

for filament 2 together with the central volume density, the column density in the line-of-sight and the non-thermal velocity dispersion of the Gaussian fit. Filament 1 has an unprojected wavelength of 0.43 pc, an inclination angle of 57°and an initial line-mass of $f_{\rm cyl} = 0.51$. Filament 2 has an unprojected wavelength of 0.46 pc, an inclination angle of 66°and an initial line-mass of $f_{\rm cyl} = 0.43$. The projected core distances of 0.23 pc and 0.19 pc respectively match the observed spacing and the maximum central volume densities of $2.07 \cdot 10^{-19}$ g cm^{-3} and $5.74 \cdot 10^{-19}$ g cm^{-3} also agree with the observations. The minimum central volume densities of $4.98 \cdot 10^{-20}$ g cm^{-3} and $3.37 \cdot 10^{-20}$ g cm^{-3} match the observed densities between the cores within a factor of two, which is the estimated error of measurement of Hacar and Tafalla (2011).

The spacial distribution of the line-of-sight centroid velocities is in good agreement with the observations. Especially filament 1 where the observed velocity data shows a sinusoidal curve with an amplitude of 0.04 km s^{-1} is well matched. Our fit, given by the solid light blue line, has an amplitude of 0.05 km s^{-1} but this is still within the measurement error of 0.01 km s^{-1}. Hacar and Tafalla (2011) also fitted an amplitude of 0.04 km s^{-1} to the line-of-sight centroid velocity distribution of filament 2 but the observed velocity structure is ambiguous. The observed centroid velocity of filament 2 varies up to a value of 0.1 km s^{-1} and does not follow a sinusoidal pattern very well. Contrarily to the observation, we see a sinusoidal pattern in the centroid velocity variation. We find an amplitude about twice as large as the observed fit, namely 0.08 km s^{-1}. Why the observed centroid velocity does not follow a clear pattern is not clear and could be due to more complex motions inside the filament. The velocity patterns of both filaments show a clear $\lambda/4$ shift in phase compared to the density perturbation, as they do in the observations, which is an indicator of the core-forming motions (Gehman et al., 1996a).

The dashed, red lines in Figure 6.2 and Figure 6.3 show the true, inclination corrected, central axis velocity in longitude direction of the filament. Due to the central axis being the densest component, we would have expected that this velocity agrees with the projected line-of-sight velocity pattern as we only see weak radial infall motions in the majority of the filament. However, contrarily to our expectation, the true motion differs significantly from the line-of-sight velocity structure. Its maxima are large with a difference that is almost a factor of 2 in filament 2. In addition, the location of the maxima is shifted towards the clumps. In the strong non-linear case of filament 2 the true velocity pattern cannot be modeled well by a sinusoidal pattern. Interestingly, however, the projected velocity structure still resembles a sinusoidal pattern well.

The lowest panel shows the non-thermal velocity dispersion in the line of sight through the centre of the filament. It is calculated by measuring the FWHM, here denoted by Δv, of the Gaussian fit to the line-of-sight velocity data and by using the fact that the contribution of the thermal and non-thermal gas motions to the linewidth add in quadrature (e.g. Myers, 1983):

$$\sigma_{\rm nt} = \sqrt{\frac{\Delta v^2}{8 \ln 2} - \frac{k_B T}{m}} \tag{6.12}$$

where m is the mass of the observed molecule, in this case $C^{18}O$. We find that the gas is very subsonic throughout the filaments, with variations due to higher velocity dispersions inside

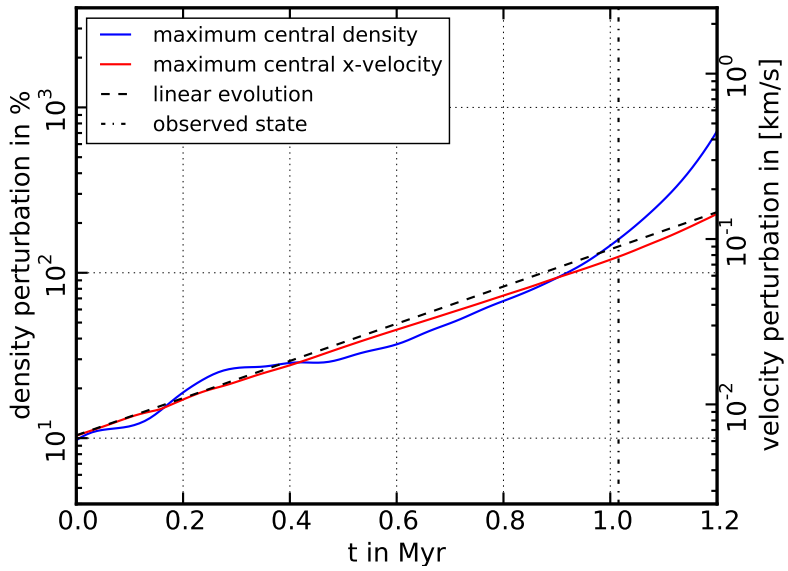

Figure 6.4: Evolution of the maximum central density (blue, left axis) and x-velocity (red, right axis) of filament 1. Both follow the analytic prediction until the density reaches a perturbation strength of about 100% where a non-linear evolution in density sets in. The dashed-dotted vertical line gives the point in time of the observation.

and between the cores. We find that the higher velocity dispersion inside the cores is not only due to the radial collapse of the filament but is dominated by the infall of gas coming from the bulk of the filament. It is interesting to note that, although we do not model subsonic turbulence, the ordered motions inside the filament already lead to a considerable amount of non-thermal velocity dispersion. The mean of the dispersion in units of the sound speed is about $\langle\sigma_{\rm nt}\rangle/c_s \approx 0.17$ for filament 1 and $\langle\sigma_{\rm nt}\rangle/c_s \approx 0.40$ for filament 2. Comparing the modeled velocity dispersion to the observed values of $\langle\sigma_{\rm nt}\rangle/c_s = 0.57 \pm 0.15$ and $\langle\sigma_{\rm nt}\rangle/c_s = 0.63 \pm 0.16$ respecitvely and taking into account that velocity dispersions add in quadrature it becomes clear that in the case of the observations subsonic turbulence still dominates the non-thermal component of the velocity dispersion even with strong underlying ordered motion.

In the end, we find that the initial, unperturbed central density of the filaments was $8.2 \cdot 10^{-20}$ g cm^{-3} for filament 1 and $6.1 \cdot 10^{-20}$ g cm^{-3} for filament 2. Both lie considerably below the mean value of the maximum and minimum observed density of about $1.2 \cdot 10^{-19}$ g cm^{-3} for filament 1 and $2.9 \cdot 10^{-19}$ g cm^{-3} for filament 2. This signifies that there is a considerable amount of asymmetrical evolution where more mass is transferred to the density maxima than is taken from the density minima. This leads to an enhancement of the maximum density while leading to a slower density decrease between the cores. This effect is stronger in filament 2 than in filament 1 as can be seen from the bigger discrepancy of the initial central density and the observed density mean.

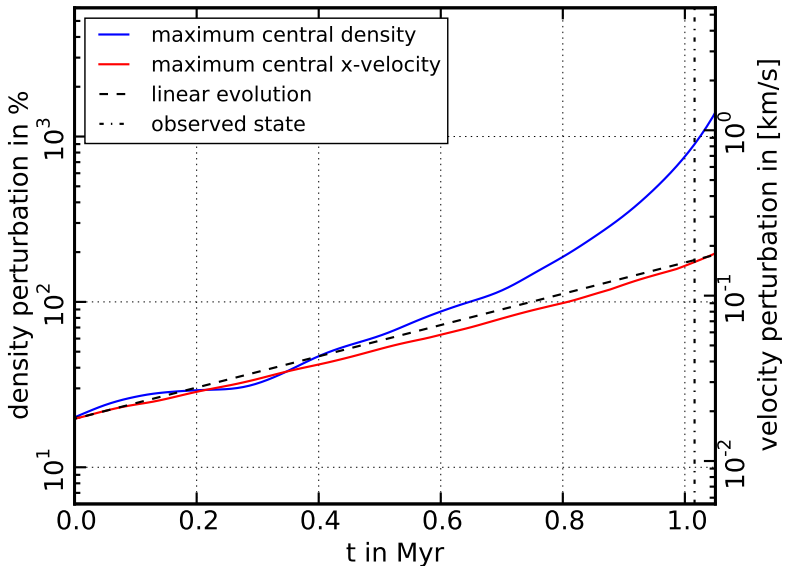

Figure 6.5: As in Figure 6.4, but for filament 2. Filament 2 shows the same evolutionary characteristics as filament 1, but in order to fulfill the time constraint of about 1 Myr, we need an initial density perturbation of around 20%. One can see that the observed state lies far deeper in the non-linear regime than for filament 1.

6.5.2 Dynamical evolution

In order to understand the asymmetrical evolution of the maximum and minimum density, we take a closer look at the time evolution of the perturbed quantities. Each perturbation of every variable should follow Equation 6.5. Thus, they should follow a linear evolution in log-space. This is shown for the central maximum density and central maximum velocity in the filament axis in Figure 6.4 for filament 1 and in Figure 6.5 for filament 2. In order to stay close to a reasonable limit of 1 Myr (see previous subsection), we start the evolution of filament 1 at about 10% perturbation strength and of filament 2 at about 20%. Both the maximum density and maximum velocity follow the linear prediction for the majority of the evolution with the density showing some oscillation around the linear prediction. In the late phase of the evolution, both filaments show a clear non-linear growth of the maximum density. It is worth noting that this non-linear phase is not short in the sense that all the mass of the filament collapses into a core in a fast period of time, but it is a smooth process, which can easily take up to 0.4 Myr or nearly half of the whole formation time of a core and still leaves diffuse gas to make up the filament. Also note that the velocity does not follow the same non-linear evolution initially. Only when we let the simulations run further, we see that the velocity follows with a delay of about 0.3 Myr. At that point in time, the cores are in a much more developed state and the simulations brake down due to resolution issues.

In order to have a deeper look into the non-linear phase we look at the line-mass in the

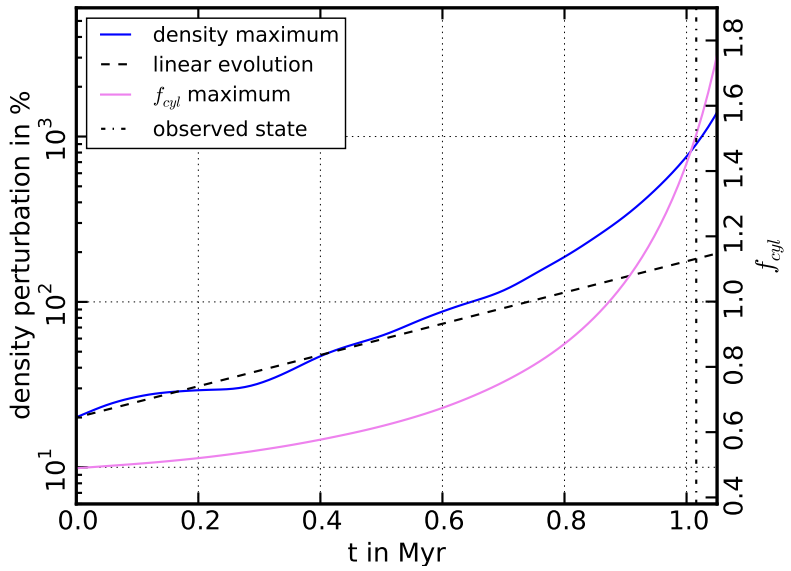

Figure 6.6: Evolution of the maximum density perturbation in log-space (blue, left axis, logarithmic scale) of filament 2 together with the evolution of f_{cyl} (violet, right axis, linear scale) in the maximum density filament slice. One can see that the non-linear evolution of the maximum density is tied to the fact that the line-mass enters the critical regime ($f_{\text{cyl}} > 1$). This means the maximum density evolution is driven primarily by the radial collapse of the filament in this section.

slice of the maximum density. The line-mass of a pressure-bound filament is given by:

$$\frac{M}{L} = \int_0^R 2\pi r \rho(r) dr \tag{6.13}$$

Inserting Equation 6.4, one can show, as the perturbation is independent of radius and the integration just gives the initial line-mass, that the time evolution is given by:

$$\left(\frac{M}{L}\right)(t) = \left(\frac{M}{L}\right)_0 [1 + \epsilon \exp(ikz - i\omega t)] \tag{6.14}$$

This indicates that, not only is there a redistribution of mass inside the filament, but that the line-mass also follows exactly the same evolution as the density.

We plot the time evolution of the maximum density together with its respective line-mass ratio f_{cyl} of filament 2 in Figure 6.6. The scale of f_{cyl} is linear in order to see when the line-mass becomes supercritical. One can clearly see that f_{cyl} exceeds 1.0 after about 0.85 Myr. This coincides more or less with the maximum central density entering the non-linear part of its evolution and dominates the late evolution. This indicates that the reason for the non-linear evolution of the maximum central density is that the region containing the cores are supercritical in the line-mass. This leads to a radial collapse of the filament at the position of the core as it cannot sustain hydrodynamical equilibrium which in turn enhances the central density.

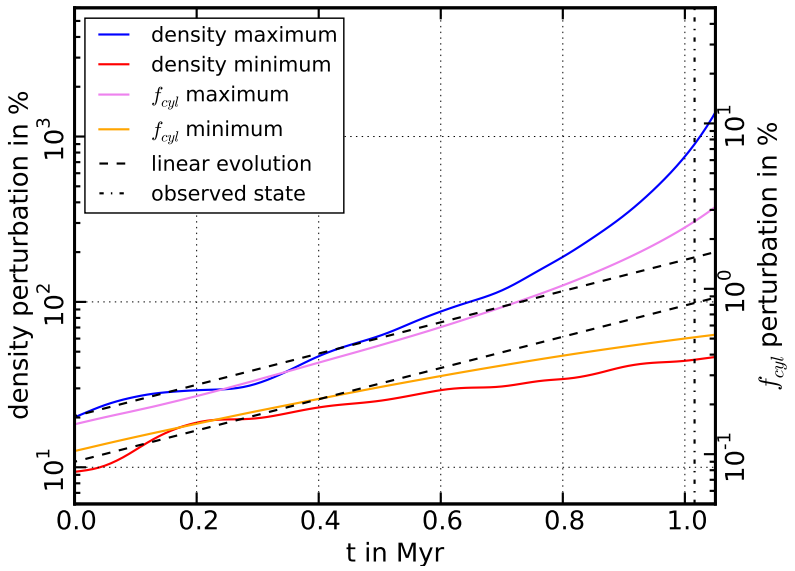

Figure 6.7: Evolution of the maximum and absolute minimum value of the density perturbation (left axis) of filament 2 together with the evolution of the absolute value of the perturbation in f_{cyl} (right axis) in the respective filament slice. The minimum density perturbation evolves slower as predicted, growing even slower as time progresses. This means that the cores are not feeded symmetrically by the density minima, but accrete mass from over the whole filament.

This effect can account for the majority of the asymmetry but we also observe a reduced growth of the perturbation of the density minimum. In Figure 6.7 we plot the evolution of the maximum and the minimum density as well as the evolution of the maximum and minimum line-mass, both on a logarithmic scale to show the linear evolution. Note that, not only does the density follow the linear prediction but also the line-mass as predicted by Equation 6.14. One can also see the non-linear evolution of the maximum density in the line-mass maximum but it does not grow as fast as the density. As radial collapse of the filament would not lead to a difference in line-mass, this indicates that the density growth is not fed by radial collapse alone.

An interesting effect is that the evolution of the minimum density, as well as the minimum line-mass, flattens as the perturbation of the maximum becomes non-linear. This implies that the mass is not redistributed from the minimum to the maximum anymore but that the cores accrete mass from all over the bulk of the filament, which can be seen in the central volume density of filament 2 in Figure 6.3. The area between the cores shows a flat decreased density, with the cores being very pronounced and peaked, indicating that the cores also pull in mass from the filament axis. This means that as we approach the supercritical state of the cores, the accretion changes from a simple linear enhancement and reduction of the maximum and minimum respectively to a radial, spherical symmetric accretion onto the cores. This effect has also been shown and studied by Inutsuka and Miyama (1992) in SPH-simulations where they see the same behavior in the non-linear phase.

The change from linear to non-linear evolution also leads to a difference in core morphol-

ogy and has an important implication for observed cores. This change can be seen in Figure 6.1 where the density contours show the cores initially forming to have a prolate shape, as matter is only transferred from the minimum to the maximum density. This changes drastically in the non-linear phase at the end of the simulation where the dense cores clearly show a generally round form in the density distribution. This was also seen in the simulations of Inutsuka and Miyama (1992) where the cores approached a near spherical form for late times in the non-linear phase. If one were to observe a dense core that displays an elongated, prolate form, it could be a strong hint that it is situated in the linear evolutionary phase. Indeed, observed cores typically show an elongated form (Benson and Myers, 1989) which is consistent with the fact that cores spend the bigger part of their lifetime in the linear evolutionary phase. However, it is obvious that there is an observational bias to detect dense cores which are likely to be in the non-linear phase already as they would not easily stand out of the filament gas otherwise. For instance, at the beginning of the non-linear phase of the simulation of filament 2 the cores only have an over-density of a factor of about two with respect to the filament gas.

The factor of two difference in the initial perturbation of the density maximum and the density minimum in Figure 6.7 stems from the fact that we start the simulation at an even earlier time with a very small perturbation strength in order to let the filament adjust to the perturbation. Although it is a relatively small difference, it highlights the fact that the density minimum already evolved slower than the density maximum. Starting with different values for the initial perturbation strength shows that the factor of two is robust and seems to be hard to avoid. Nevertheless, it is of relatively minor impact, since a factor two is also the inherent error in the observation and would not lead to an offset of the mean density as initial condition.

6.5.3 External pressure

From Equation 6.8, it is possible to determine the boundary density of the filaments. This value can then be used in Equation 6.11 to get an estimate of the pressure of the surrounding material. Using our derived values of $\rho_0 = 8.18 \cdot 10^{-20}\,\mathrm{g\,cm^{-3}}$ and $f_{\mathrm{cyl}} = 0.51$ for filament 1 and $\rho_0 = 6.12 \cdot 10^{-20}\,\mathrm{g\,cm^{-3}}$ and $f_{\mathrm{cyl}} = 0.43$ for filament 2, both filaments give nearly the exact same value for the external pressure of $P_{\mathrm{ext}}/k_B = 5.01 \cdot 10^4\,\mathrm{K\,cm^{-3}}$ and $P_{\mathrm{ext}}/k_B = 5.08 \cdot 10^4\,\mathrm{K\,cm^{-3}}$ where k_B is the Boltzmann constant. The consistency of both values could be a coincidence, but is reassuring and shows the power of the pressure truncated filament method to predict the environmental pressure.

However, the source of the external pressure is not clear and is open to debate. It is larger than the usually assumed total (thermal + turbulent) gas pressure of the interstellar medium, which is estimated to be of the order of $P_{\mathrm{ISM}}/k_B \approx 10^3 - 10^4\,\mathrm{K\,cm^{-3}}$, e.g. by Bertoldi and McKee (1992), although they also estimate the gravitational pressure of the weight of the overlying material of different molecular clouds on cores and get values in a range of $P_G/k_B \approx 10^4 - 10^5\,\mathrm{K\,cm^{-3}}$. While this pressure is more important in quiescent clouds and not necessarily as high for turbulent clouds, gravitational pressure can add to the overall external pressure.

In addition, warm ionised gas can also lead to a supportive pressure, as has been shown

for the Pipe Nebula (Gritschneder and Lin, 2012). They also determine pressure values in the range of $P_{\rm ion}/k_B \approx 10^4 - 10^5$ K cm^{-3}. A possible source for ionizing radiation is AB Aurigae, which has been shown to heat the diffuse gas component while having nearly no influence on the dense gas (Duvert et al., 1986; Ladd and Myers, 1991). However, for the estimated environmental densities of order $5 \cdot 10^2$ cm^{-3} we would require a temperature of around 100 K which is not observed in the external medium.

Another source of external pressure is turbulent ram pressure $P_{\rm ram} = \rho\sigma^2_{\rm turb}$ where $\sigma_{\rm turb}$ is calculated according to Equation 6.12. The relevant velocity dispersion $\sigma_{\rm turb}$ for an external ram pressure is not the intrinsic velocity dispersion of the filaments but that of the whole region. The observations of Hacar and Tafalla (2011) show that the $C^{18}O$ gas is measured over the range of $\Delta v = 1.2$ km s^{-1}. Assuming an external density of $\rho_b \sim 5 \cdot 10^2$ cm^{-3} leads to an external pressure of about $P_{\rm ram}/k_B \approx 4 \cdot 10^4$ K cm^{-3} which is in excellent agreement with our external pressure estimate.

Although the source of the external pressure still remains unclear, a good candidate is therefore turbulent ram pressure. The theoretical model does not allow for a big leeway in the external pressure estimate and further observations are required to confirm this conjecture and determine the origin of the external pressure.

6.6 Discussion and conclusions

Even though we can reproduce the observational data well, some caveats remain. First and foremost, we simulate an infinite filament by using periodic boundary conditions. This is not a perfect representation of reality and our choice of boundary prevents the global collapse and edge-effects expected in finite filaments. A future study must include effects of a non-periodic boundary. It was shown by Clarke and Whitworth (2015) using semi-analytical methods and simulations that the global timescale for collapse of filaments with greater aspect ratios than $A > 2$ is:

$$t_{\rm col} = \frac{0.49 + 0.25A}{\sqrt{G\frac{(M/L)}{\pi R^2}}} \tag{6.15}$$

Using this formula, we find that the timescales for global collapse of our filaments are around 1.5 Myr. Thus, although fragmentation is physically possible, the filament will also change its form on a Myr scale. This will definitely influence fragmentation length- and timescales and if it is not possible to find other stabilizing processes, e.g. rotation or magnetic fields, this effect has to be taken into account.

Furthermore, although we can explain the observed densities, some differences to the observations remain. Most notably, the cores in Figure 6.2 and Figure 6.3 are more peaked than the observed cores. Also the observed filaments have a diameter of about 0.2 pc in contrast to our simulations where the filaments have a diameter of about 0.14 pc. The reason for this could be that we do not include the intrinsic turbulence. Hacar and Tafalla (2011) do find that a considerable amount of sub-sonic turbulence of about 0.5 times the sound speed dominates the filaments. This will naturally lead to puffed-up cores and a wider filament itself. Turbulence could indeed also change the form of the filament and fragmentation length- and timescales and is a factor to take into account but as it does not change the line-mass

that regulates the fragmentation the impact should be relatively small. Still, a detailed study on the effect of turbulence would be interesting in order to understand better whether the fragmentation presented here is still possible.

Additionally, the observed cores are not symmetrical. For an idealised analysis we treat them as symmetric with a central density corresponding to their mean, but in reality their central density differs up to a factor of about three for filament 2. This could be either an effect of a clumpy or uneven initial mass distribution or of an asymmetrical evolution out of an evenly mass-distributed idealised filament. In an extended study, it should be possible to break their symmetrical evolution by introducing a power spectrum on the initial perturbation instead of only using the dominant wavelength.

Nevertheless, we have shown that the fragmentation length scale can indeed be explained by subsonic gravitational fragmentation of the filament, assuming an idealised model. Together with a constraint on the inclination we can estimate line-of-sight centroid velocity variations and compare them to the observations. Our models give the most likely properties to be:

Filament 1

- an unprojected length of 0.95 pc
- an inclination of 57°
- a line-mass of $f_{\mathrm{cyl}} = 0.51$
- an initial central density of $\rho_0 = 8.18 \cdot 10^{-20}\,\mathrm{g\,cm^{-3}}$
- an external pressure of $P_{\mathrm{ext}}/k_B = 5.01 \cdot 10^4\,\mathrm{K\,cm^{-3}}$

Filament 2

- an unprojected length of 1.03 pc
- an inclination of 66°
- a line-mass of $f_{\mathrm{cyl}} = 0.43$
- an initial central density of $\rho_0 = 6.12 \cdot 10^{-20}\,\mathrm{g\,cm^{-3}}$
- an external pressure of $P_{\mathrm{ext}}/k_B = 5.08 \cdot 10^4\,\mathrm{K\,cm^{-3}}$

Moreover, we demonstrated that cores can spend a considerable amount of their lifetime in a non-linear phase where their central density grows faster than a simple symmetrical mass transfer from the density minimum to the core. This is due to the fact that the densest regions of a filament exceed the line-mass where a radial hydrodynamic equilibrium is possible. This does not lead to an instant radial collapse, but the cores accrete matter radially, as well as from the whole filament. This makes them live long enough to be observed in the non-linear phase.

Most importantly, the change from linear to non-linear evolution is indicated in a change of core morphology. While a symmetrical redistribution of material from the minimum to maximum density leads to a prolate form, the radial collapse in all directions of the cores in the non-linear phase makes the core roundish in appearance. The high density contrasts from core to filament gas which are only achieved in the non-linear evolution makes cores more likely to be observed in the non-linear phase.

6.7 Acknowledgements

We thank Matthias Gritschneder and the whole CAST group for helpful comments and discussions. We also thank the anonymous referee for improving the structure of the paper. SH wants to thank Alexander Beck for useful comments that clarified the presentation of the paper. AB and SH are supported by the priority programme 1573 "Physics of the Interstellar Medium" of the German Science Foundation and the Cluster of Excellence "Origin and Structure of the Universe"

7 Paper II: Accretion-driven turbulence in filaments - I. Non-gravitational accretion

S. Heigl, A. Burkert, M. Gritschneder, 2018, *Monthly Notices of the Royal Astronomical Society*, 474, 4881-4893

We study accretion driven turbulence for different inflow velocities in star forming filaments using the code RAMSES. Filaments are rarely isolated objects and their gravitational potential will lead to radially dominated accretion. In the non-gravitational case, accretion by itself can already provoke non-isotropic, radially dominated turbulent motions responsible for the complex structure and non-thermal line widths observed in filaments. We find that there is a direct linear relation between the absolute value of the total density weighted velocity dispersion and the infall velocity. The turbulent velocity dispersion in the filaments is independent of sound speed or any net flow along the filament. We show that the density weighted velocity dispersion acts as an additional pressure term supporting the filament in hydrostatic equilibrium. Comparing to observations, we find that the projected non-thermal line width variation is generally subsonic independent of inflow velocity.

Key words: stars:formation – ISM:kinematics and dynamics – ISM:structure

7.1 Introduction

Turbulent motions are ubiquitous on all astrophysical scales. There is evidence for highly complex non-thermal motion from the intergalactic medium to the interstellar medium (ISM) and individual molecular clouds down to even the smallest scales of protostellar discs. Likewise, as part of the ISM, star forming filaments are no exception to this observational fact. In contrast to its importance the origin of turbulence is still not fully understood and there are numerous potential sources for turbulent motions in the ISM (Mac Low and Klessen, 2004; Elmegreen and Scalo, 2004; Elmegreen and Burkert, 2010; Klessen and Glover, 2016). On cloud scale, molecular line observations are dominated by supersonic motions and show a direct correlation between size and line width (Larson, 1981). This is usually interpreted as the direct result of a turbulent cascade from the scale of a tens of parsec sized molecular cloud down to the scale of parsec sized filaments (Kritsuk et al., 2013; Federrath, 2016; Padoan et al., 2016). Filaments then inherit their internal velocity dispersion from the motions on larger scales. This model is also favoured by *Herschel* observations which show that filamentary structures are ubiquitous in molecular clouds (André et al., 2010; Arzoumanian et al., 2011, 2013; André et al., 2014). This picture has recently been challenged by the discovery that more massive filaments are actually complex bundles of fibers whose line-of-sight superposition create the observed supersonic linewidths (Hacar et al., 2013) and which were also found to form in numerical simulations (Smith et al., 2014; Moeckel and Burkert, 2015). Independent of the formation process, we argue that accretion driven by the gravitational potential of the filaments alone can be enough to stimulate turbulent motions that are in agreement with the observations (see also Ibáñez-Mejía et al., 2016).

Recent images of the high column density gas, traced by the usually optically thin $C^{18}O$ line of nearby filaments have shown that the non-thermal linewidth is predominantly sub- and transsonic along filaments. This is true for L1517 in Taurus (Hacar and Tafalla, 2011), where the mean is about half the sound speed, as well as for the fibre-like substructure of the L1495/B213 region in Taurus (Hacar et al., 2013), where the mean is about the sound speed. Moreover, even in the Musca filament, a 6 pc long structure, subsonic non-thermal linewidths dominate along the filament (Hacar et al., 2016b). Larson was the first to connect the velocity dispersion to the size of molecular clouds (Larson, 1981). While not strictly valid for filamentary structures, it predicts a factor of about three times higher velocity dispersion corresponding to the supersonic regime for a filament like Musca with a width of 0.14 pc (Cox et al., 2016). Although still within the spread of the overall relation, Musca is definitely an outlier in terms of its length and it is unclear which process leads to a structure of that size and that low velocity dispersion. In this paper we explore a possible origin of turbulence in filaments.

In the following sections, we introduce the basic concepts we use to constrain our model (Section 7.2). We then discuss the code and the numerical set-up (Section 7.3). Thereafter, we present our results of the simulations and discuss them in detail (Section 7.4). Additionally, we show that turbulence plays a role in creating a hydrostatic equilibrium (Section 7.5). Finally, we compare our data to the observations (Section 7.6) and investigate the dependence on filament inclination.

7.2 Basic concepts

In order to sustain turbulence inside a filament there has to be an external driving mechanism. Otherwise, turbulent motions decay on the timescale of a crossing time (Mac Low et al., 1998; Stone et al., 1998; Padoan and Nordlund, 1999; Mac Low, 1999; Mac Low and Klessen, 2004). Here, we discuss a possible source of the external driving and the theoretical prediction.

7.2.1 Gravitational accretion onto a filament

Although there are different ways to accrete mass onto a filament, e.g. a converging flow, these processes are typically limited in time. A counterexample for a radial converging flow which is stable over longer timescales is the gravitational attraction of the filament itself. If we assume that the filament is isothermal and in hydrostatic equilibrium, then it has a density profile first described by Stodólkiewicz (1963) and Ostriker (1964):

$$\rho(r) = \frac{\rho_c}{\left(1 + (r/H)^2\right)^2} \tag{7.1}$$

where r is the cylindrical radius and ρ_c is its central density. The radial scale height H is given by

$$H^2 = \frac{2c_s^2}{\pi G \rho_c} \tag{7.2}$$

where c_s is the isothermal sound speed and G the gravitational constant. We assume that the gas has an isothermal temperature of 10 K. Using a molecular weight of $\mu = 2.36$ gives the isothermal sound speed of $c_s = 0.19\,\mathrm{km\ s^{-1}}$. One can integrate the profile to $r \to \infty$ to get the critical line mass of

$$\left(\frac{M}{L}\right)_{\mathrm{crit}} = \frac{2c_s^2}{G} \approx 1.06 \cdot 10^{16}\,\mathrm{g\ cm^{-1}} \approx 16.4\,\mathrm{M_\odot\ pc^{-1}} \tag{7.3}$$

above which a filament will collapse under its self-gravity. Following Heitsch et al. (2009), for a given line mass M/L the gravitational acceleration of the filament is:

$$a = -\frac{2GM/L}{r} \tag{7.4}$$

One can calculate the potential energy which a gas parcel of mass m loses in free-fall starting with zero velocity at a distance R_0 to the filament radius R by integrating over r:

$$E_{\mathrm{pot}} = 2G(M/L)m \ln\left(\frac{R_0}{R}\right) \tag{7.5}$$

Therefore, the inflow velocity at the point of accretion R is:

$$v_r = 2\sqrt{G(M/L)\ln\left(\frac{R_0}{R}\right)} \tag{7.6}$$

Note that similar to the free fall velocity, the value does not depend on the mass of the gas parcel. It is also not sensitive to neither the starting position nor the line mass while depending stronger on the latter. As the filament accretes mass and increases in line-mass, the inflow velocity grows. However, as we want to analyse accretion driven turbulence in an equilibrium state we keep the inflow velocity constant. Therefore we choose to neglect the effects of gravity and use an artificial but constant mass inflow where we set the inflow velocity also to a constant value. The effects of gravity will be discussed in a subsequent paper. Assuming the extreme case of a filament with a gravitational influence of a hundred times the filament radius, which for a typical radius of 0.05 pc (Arzoumanian et al., 2011) is the size of a typical molecular cloud, we still need a line mass which is several times higher than the critical line-mass to achieve an inflow velocity of even Mach 10.0. Thus, we limit our maximum inflow velocity to Mach 10.0.

A consequence of a constant inflow velocity is a constant mass accretion rate. The absolute value is set by the radius of the inflow region R_0 and the density at that radius ρ_0:

$$\dot{M} = \rho_0 v_r 2\pi R_0 L \tag{7.7}$$

This should stay constant for every radial shell and thus leads to the following density profile outside of the filament:

$$\rho(r) = \rho_0 \frac{R_0}{r} \tag{7.8}$$

As there is an isothermal accretion shock formed at the filament boundary, pressure equilibrium requires that the mean density inside the filament is the outside density times a factor of the Mach number $\mathcal{M}$ squared. This leads to the following filament mass-radius relation:

$$M(R) = \rho_0 \mathcal{M}^2 \pi R R_0 L \tag{7.9}$$

This has to be the same as the accreted mass given by the mass accretion rate given by Equation 7.7 times the time t. Therefore the radius of the filament evolves as:

$$R(t) = \frac{2c_s^2 t}{v_r} \tag{7.10}$$

7.2.2 Turbulence driven by accretion

Following Klessen and Hennebelle (2010), Heitsch (2013) derived an analytical expression for the velocity dispersion depending on the inflow velocity. We expect turbulence to decay on the timescale of a crossing time:

$$\tau_d \approx \frac{L_d}{\sigma} \tag{7.11}$$

where σ is the velocity dispersion in three dimensions and L_d is the driving scale of the system. Klessen and Hennebelle (2010) use the approach that the change in turbulent kinetic energy is given by the balance of the accretion of kinetic energy and the dissipation of turbulent energy:

$$\dot{E}_t = \dot{E}_a - \dot{E}_d = (1 - \epsilon)\dot{E}_a \tag{7.12}$$

with the energy accretion rate

$$\dot{E}_a = \frac{1}{2}\dot{M}v_r^2 \tag{7.13}$$

and the loss by dissipation as

$$\dot{E}_d \approx \frac{E_t}{\tau_d} = \frac{1}{2}\frac{M\sigma^3}{L_d}. \tag{7.14}$$

They also introduce an efficiency factor ϵ as fraction of accreted energy which can sustain the turbulent motions:

$$\epsilon = \left|\frac{\dot{E}_d}{\dot{E}_a}\right| \tag{7.15}$$

Thus, if the driving scale is the filament diameter $L_d = 2R$, Heitsch (2013) predicted a turbulent velocity dispersion of

$$\sigma = \left(2\epsilon R(t)v_r^2\frac{\dot{M}}{M(t)}\right)^{1/3} \tag{7.16}$$

This assumes that ϵ is independent of the inflow velocity. In our simple case the radius depends on the constant inflow velocity as $1/v_r$ and the radial accretion leads to a radius and mass growing linear in time. Therefore, we expect a constant level of velocity dispersion which should behave as

$$\sigma \sim v_r^{1/3}. \tag{7.17}$$

This is the relationship we want to confirm or disprove using numerical methods.

7.3 Numerical set-up

We executed the numerical simulations with the code RAMSES (Teyssier, 2002). The code uses a second-order Godunov scheme to solve the conservative form of the discretised Euler equations on a cartesian grid. For the simulations we applied the MUSCL scheme (Monotonic Upstream-Centred Scheme for Conservation Laws, van Leer (1977)) together with the HLLC-Solver (Toro et al., 1994) and the multidimensional MC slope limiter (van Leer, 1979).

We simulate a converging radial flow onto a non-gravitating filament in order to study the generated turbulence. We use a 3D box with periodic boundary conditions in the x-direction and outflow boundaries in the other directions. The periodic boundary prohibits the loss of turbulent motions in x-direction. As RAMSES cannot use a radial inflow boundary we define a cylindrical inflow zone which lies at the edges of the box and has a thickness of two cells from where material flows onto the central x-axis of the box. The initial gas density inside of the box is set to a mean of $3.92 \cdot 10^{-21}$ g cm^{-3}, corresponding to about 10^2 particles per cubic centimeters for a molecular weight of $\mu = 2.36$. Additionally, a random perturbation is added inside of the inflow zone at the beginning of the simulation. This is illustrated in Figure 7.1 where we show a density slice through the y-z plane. The inflow has a constant density of $3.92 \cdot 10^{-21}$ g cm^{-3} and a constant velocity. Thus, it leads to a build-up of material in form of a filament with a radius that grows over time as it is not restricted by gravity. Consequently, one has to ensure a big enough box that an equilibrium can be established. The surrounding

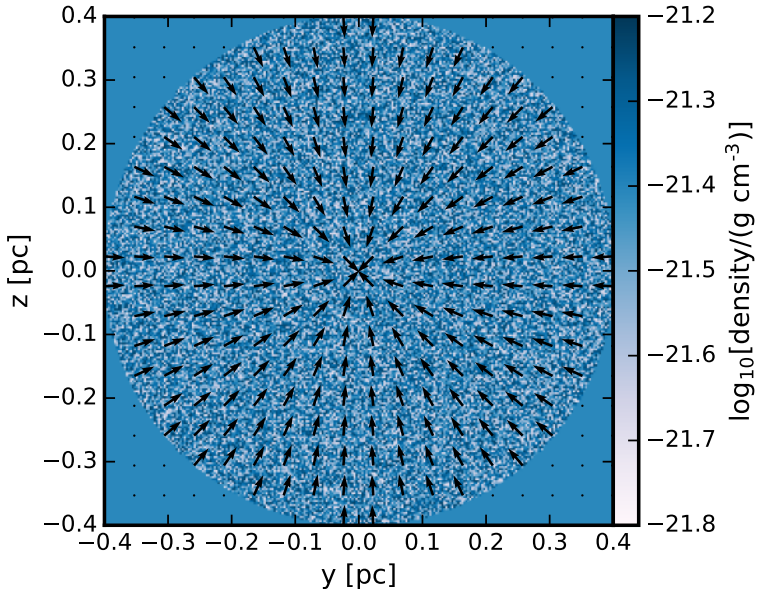

Figure 7.1: Density cut through the y-z plane of the initial conditions for all simulations. The material inside the inflow zone is perturbed with a random perturbation and has a constant velocity directed to the central line of the box as shown by the black arrows.

cells around the inflow zone are given a constant density with the same value as the inflow zone and pressure and do not affect the simulation.

The complete box is set to be isothermal with a temperature of 10 K and a molecular weight of $\mu = 2.36$. In general, the boxsize is 0.8 pc. For the control runs with a higher temperature the boxsize is doubled to ensure enough space to reach a velocity dispersion equilibrium.

As the inflow initially leads to a thin, compressed central filament with a high density, we employ adaptive mesh refinement (AMR) to resolve high density regions while keeping the resolution low in the remainder of the box. We test different refinement strategies by varying the maximum resolution to fulfill the Truelove criterion for the maximum occurring density (Truelove et al., 1997) while keeping the minimum resolution constant at 256^3 cells. Our initial approach is to resolve the Jeans length by 16 cells. We also test a more conservative criterion suggested by Federrath et al. (2011) using 32 cells to resolve the Jeans length in order to sufficiently resolve the turbulent cascade. However, we cannot detect a quantitative difference in the velocity dispersion to the previous case with lower maximum resolution. Furthermore, even a lower maximum resolution of 8 cells per Jeans length does not show any difference in the value of the velocity dispersion. Despite there being no change in behavior for the maximum resolved density, we see a difference for a varying minimum resolution. We present the details and a resolution study in the next section.

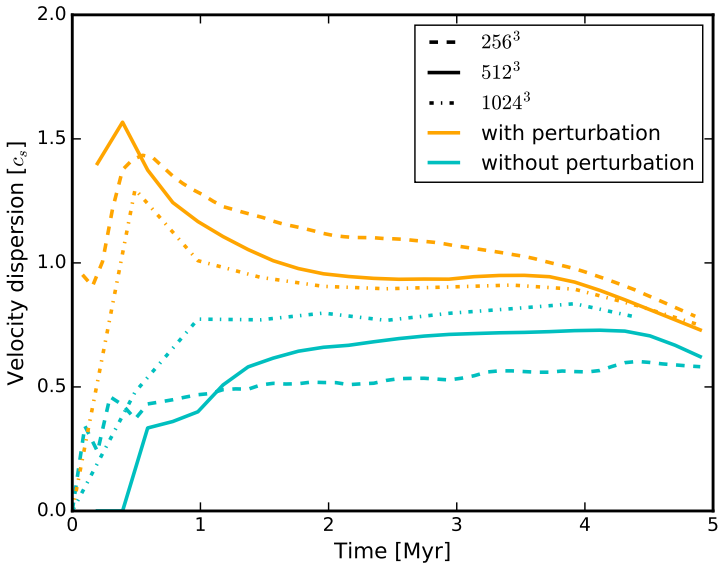

Figure 7.2: Evolution of the density weighted total velocity dispersion for the reference case with and without an initial density perturbation and for varying minimum resolution. After a short settling phase an equilibrium is established where the value of the velocity dispersion is constant. The simulations which do not include an initial density perturbation converge to the same equilibrium level as the ones including an initial density perturbation. Our later analysis is based on the case represented by the solid lines.

7.4 Simulations

In this section we present the outcome of our simulations. In order to measure the velocity dispersion and the mass of the filament one has to distinguish between filament material and ambient medium. As the inflowing material is shocked at the filament surface there is a clear increase in density and a clear drop in radial velocity. As the internal density of the filament decreases over time due to Equation 7.9, we use the radial velocity to distinguish inflowing material from filament material instead of a density threshold. To measure the filament radius we use the mean position of the highest density gradient which traces the general shock position.

7.4.1 Initial perturbation

As a reference test case we set up a converging flow with a velocity of Mach 5.0 with and without a perturbation of the initial density field. As material streams in, it is compressed on the central axis of the box. In order to avoid unphysical densities in the initial phase of the case without initial perturbation we add an already existing filament to the initial conditions with a radius of 0.05 times the boxlength and with a constant density of ten times the ambient density corresponding to a total mass of $0.23\,\mathrm{M}_\odot$. Note that we do not need to include an initial filament for the simulations including an initial perturbation, as the generated turbulence prevents the density from reaching values which cannot be resolved. For a low

resolution there is a stark contrast in the structure between both cases. An initial perturbation leads to a considerable amount of substructure which resembles observed filaments. The case lacking an initial perturbation does not obviously exhibit signs of turbulence being present. The motions are purely angular and radial and the little substructure which is generated is obscured due to the projection. However, as the inflow is perfectly symmetrical, only radial motions should exist. In order to understand this effect we vary the minimum resolution of the simulation and calculate the velocity dispersion over time. The volume weighted velocity dispersion is defined as the standard deviation of the spatial velocity distribution. We calculate the total velocity dispersion by taking the square root of the sum of the variances of the spatial components. For the density weighted velocity dispersion we normalise the velocities with the density of its respective cell divided by the average density before calculating the variance. Note that we use the central axis of the box to define the centre of the filament. As we use a cartesian grid code this can lead to a wrong split-up in the cylindrical components if the filament axis lies not exactly in the centre of the box. We analysed the error in the total velocity dispersion using a cartesian and a cylindrical calculation and the difference is at most one per cent and therefore negligible. We show the evolution of the density weighted velocity dispersion in Figure 7.2. One can see that an equilibrium is established after about two Myr where the velocity dispersion becomes almost constant. We observe this behavior in all our simulations, with and without initial perturbation, and it is also found in turbulent smooth-particle-hydrodynamical simulations of filaments forming in a turbulent medium (Clarke et al., 2017). Varying the minimum resolution, one can see that the equilibrium level of the simulations including a perturbation decreases for higher resolution showing no more substantial change going from 512^3 to 1024^3 in minimal resolution. In contrast, the simulations without an initial perturbation develop higher and higher values of turbulence the better the resolution and begin to converge to a similar value as the cases with an initial perturbation. Moreover, even the visual impression of the turbulent structure for the cases with and without initial perturbations becomes increasingly similar with higher resolution. This is shown in Figure 7.3 where we compare the cases of highest minimal resolution. We interpret this in such a way that there is an inherent physical level of generated turbulence from accretion. As long as there is a source of perturbation the growth in turbulence will tend to this value. In the case of a smooth initial inflow the perturbation is given by numerical noise which is smeared out for lower minimal resolutions due to numerical viscosity. For higher resolution, numerical viscosity is low enough that the numerical noise can grow to the same level of turbulence as in the case containing an added perturbation. The interstellar medium is not completely smooth and will always contain density fluctuations. In order to validate if the generated velocity dispersion depends on the initial density perturbation we vary the initial density perturbation in strength and form for a constant minimum resolution. Using a flat, "white noise" perturbation on the one hand and a Gaussian perturbation on the other shows no quantitative difference in magnitude of the intrinsic filament velocity dispersion. Varying the perturbation strength also shows no dependence on the initial perturbation. In Figure 7.4 we show that even changing the perturbation amplitude over five orders of magnitude, the resulting value of velocity dispersion varies only minimally. As there is no more significant change for a minimum resolution of 1024^3 all following analysis is carried out for a minimum resolution of 512^3.

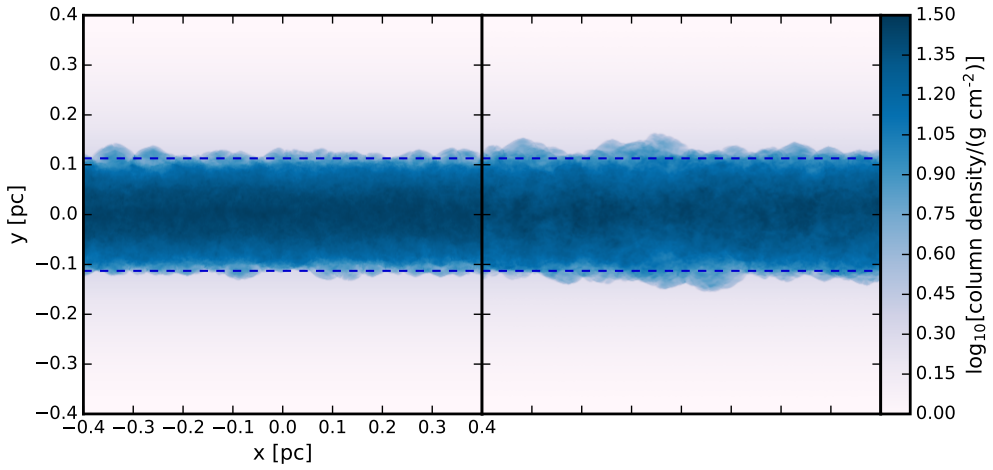

Figure 7.3: Projection of the highest minimum resolution test cases of a filament without initial perturbation on the left compared to one including an initial perturbation on the right after 1.5 Myr. Both cases have an inflow of Mach 5.0. The horizontal dashed lines indicate the analytical prediction for the radius.

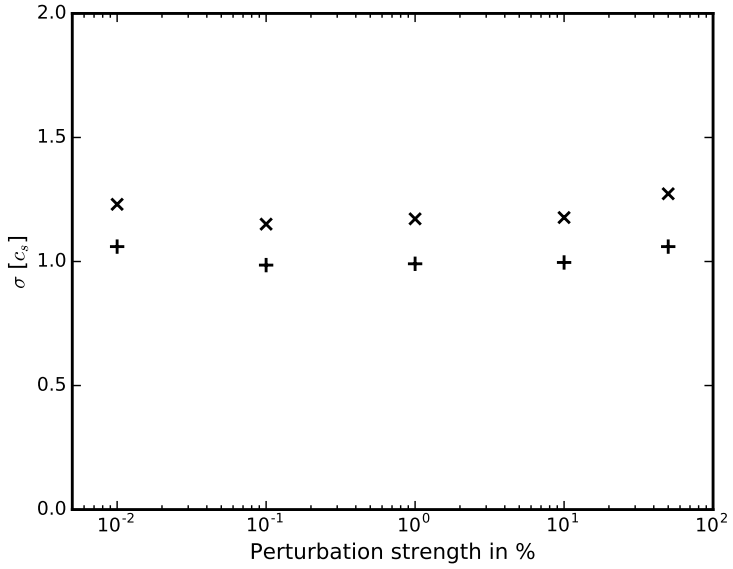

Figure 7.4: Value of the generated velocity dispersion with varying perturbation strength for the same resolution. The points show simulations including an initial density perturbation. The crosses give the volume weighted and the pluses the density weighted velocity dispersion.

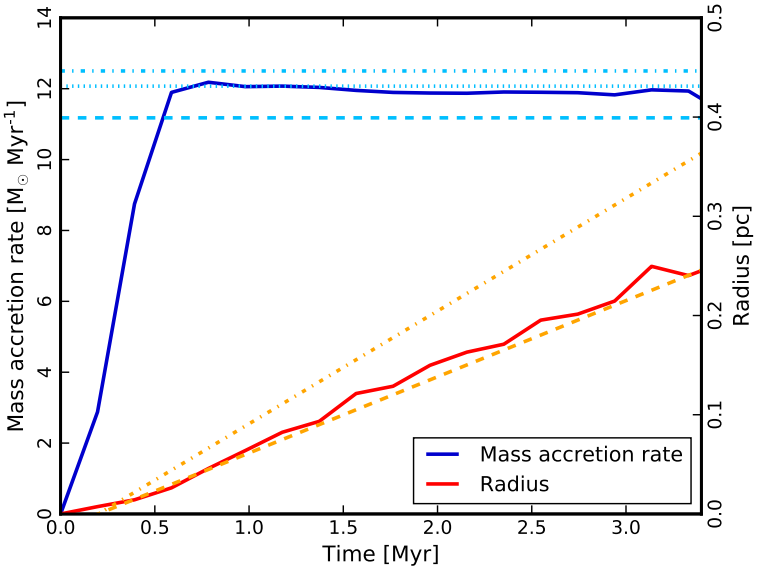

Figure 7.5: Evolution of the mass accretion rate (blue) and the filament radius (red) for the reference case with an initial density perturbation. The analytical predictions are given by the light blue and orange dashed lines respectively. The mass accretion rate is higher than the prediction but matches it if we take the radial expansion of the filament into account, as shown by the dotted line. Correcting both terms with a radial turbulent pressure overpredicts the measured evolution as can be seen by the dashed-dotted lines.

We also evaluate the radial evolution and mass accretion rate of the filament including an initial perturbation in order to verify if Equation 7.7 and Equation 7.10 hold. In Figure 7.5 we show both of them together with the analytical expectations. As our analytical prediction, the measured mass accretion rate is constant. Despite being close to the predicted value given by the blue dashed line, it has a small but measurable constant offset. This effect can be explained if we add the increase in mass accretion given by the expansion of the filament. Adding the radial growth velocity to Equation 7.7 gives the blue dotted line. This effect itself also should lead to a faster radial growth but the effect is minimal as we cannot see a significant offset of the analytical expectation for filament radius $R(t)$. We also consider that radial turbulent motions could increase the radial growth. Correcting the velocity for the radial expansion given by Equation 7.10 as $2c_s^2/v_r$ by including the contribution of the density weighted radial turbulence as $2(c_s^2 + \sigma_r^2)/v_r$ and adding this term to the inflow velocity in the mass accretion rate Equation 7.7, gives an overestimation for the radial growth and a mass accretion rate (dashed-dotted lines in Figure 7.5). At about 3.5 Myr the filament reaches the limits of the box and its maximum numerically resolved extent. This means that mass cannot be effectively accreted and the mass accretion rate goes to zero which leads to a decay in velocity dispersion seen in later evolution plots.

We show a detailed analysis in the next subsections where we present the cases of an inflow velocity generating a super- and subsonic internal velocity dispersion. This leads to the following conclusion: As long as one includes a symmetry breaking perturbation, either numerical or artificial the amount of generated turbulence is robust as long as the minimal

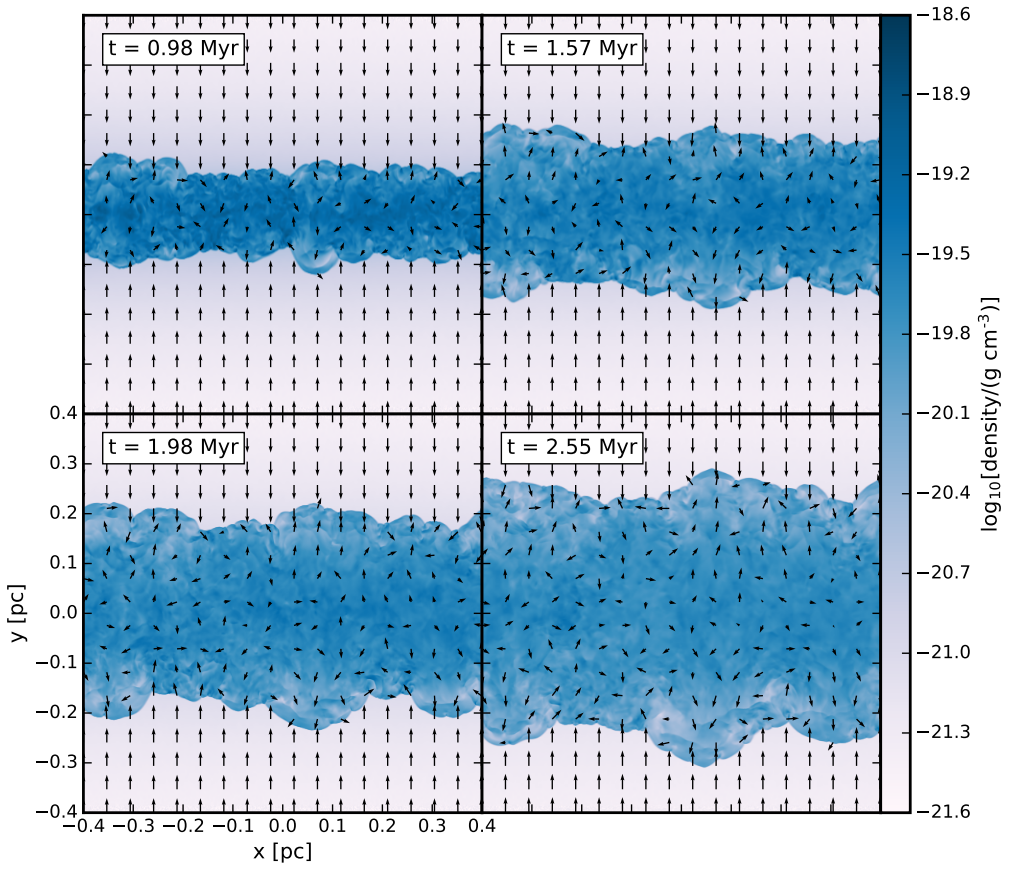

Figure 7.6: Density cut through the centre of the filament with a Mach 5.0 inflow. The arrows show the log-scaled velocities in the plane. In the inflow region their length corresponds to Mach 5.0 and they are normalised to zero at Mach 0.01. The filament shows clear signs of ongoing turbulent motions.

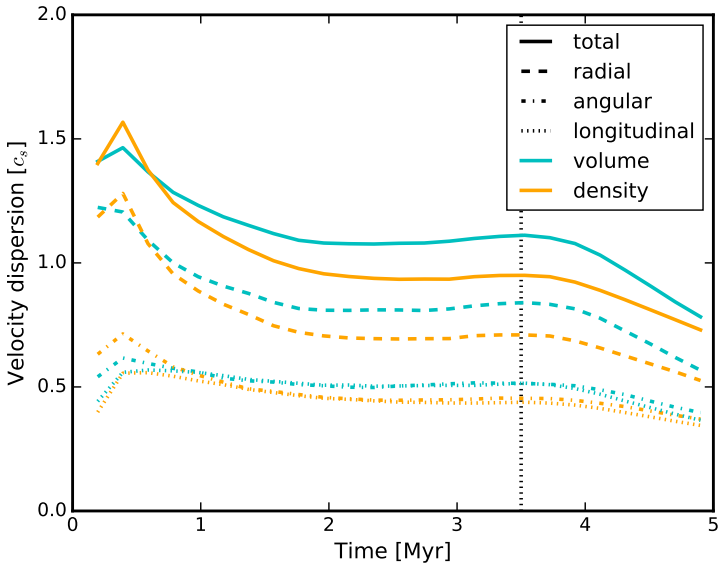

Figure 7.7: Evolution of the velocity dispersion of a Mach 5.0 inflow with an initial density perturbation. The volume weighted values are given by the cyan lines, the density weighted values by the orange lines. As in the reference case, an equilibrium is established after two Myr. The dotted vertical line shows the timestep when the filament radius reaches the domain boundary.

resolution is high enough.

7.4.2 Trans- and supersonic turbulence

In Figure 7.6 we plot the evolution of a Mach 5.0 inflow with an initial density perturbation. The filament shows every indication of turbulent motions rearranging material constantly. The bubbling and sloshing in the filament forms temporary ridges and overdensities, the most prominent on the central line at the beginning of the simulation. Over time the central overdensity weakens as the lack of gravity allows the material to spread freely. Nevertheless, the visual impression is that of an observable filament albeit the filament broadens to an unrealistic width. The velocity dispersion settles to an equilibrium as shown in Figure 7.7. The volume weighted velocity dispersion is in the supersonic regime and dominated by the radial velocity dispersion. Interestingly, the longitudinal and angular velocity dispersions, both volume and density weighted, settle to the same level of about half the sound speed. Furthermore, their values are at about 2/3 of the radial and about half the total velocity dispersion. This relation between the radial velocity dispersion and the other components remains robust and true for all cases of generated velocity dispersion, not only in the supersonic case. As the filament reaches the boundary of the box earlier than the reference case, the velocity dispersion decays after 3.5 Myr. Additionally, we show the build-up of the kinetic energy power spectrum of the filament in Figure 7.8. As the filament grows, the maximum of the distribution shifts to bigger scales. It always follows closely the filament radius, given by the dashed vertical lines. Thus, the radius is the scale for the driving mechanism. Included in

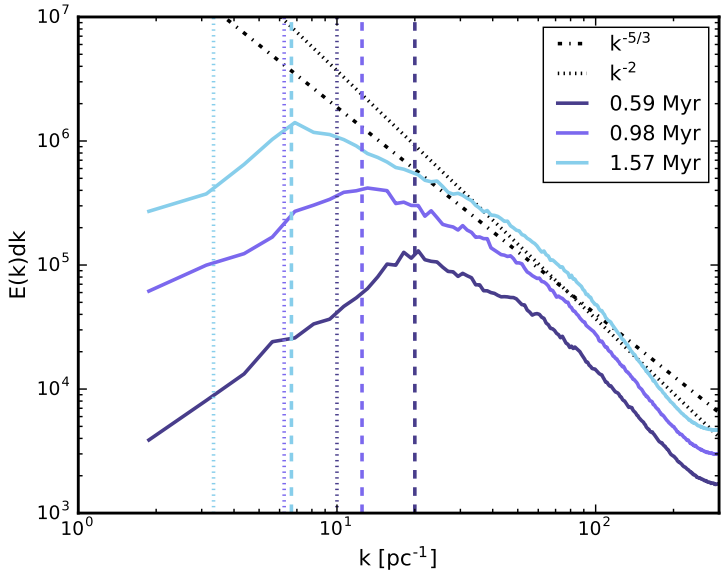

Figure 7.8: The kinetic energy power spectrum of the filament with Mach 5.0 inflow at different times. The black dashed-dotted line shows the expectation from Kolmogorov's theory and the black dotted line the expectation of Burgers turbulence. The vertical dashed lines show the respective filament radius and the vertical dotted lines the filament diameter.

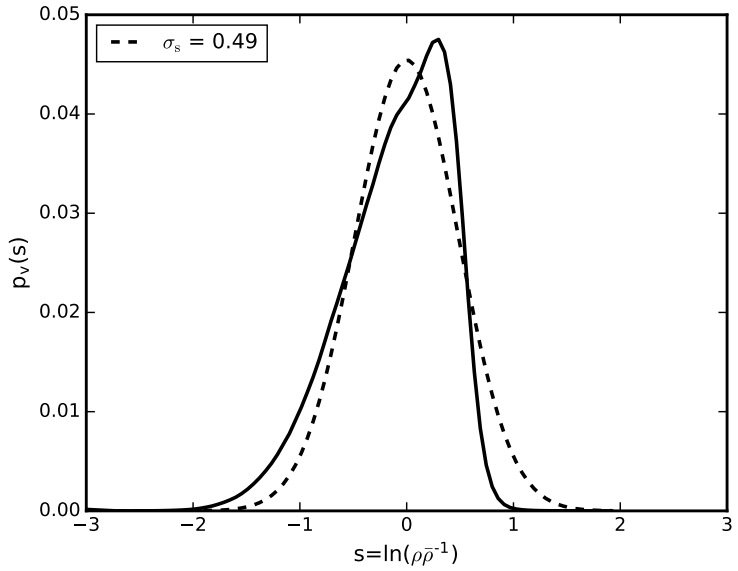

Figure 7.9: Volume weighted PDF of the logarithmic density $s = \ln(\rho\bar{\rho}^{-1})$. The density follows largely a log-normal distribution. The Gaussian fit leads to a standard deviation of 0.56.

the plot are the predicted scaling relations for the power spectrum. In the supersonic regime, numerical studies (Kritsuk et al., 2007; Federrath et al., 2010; Federrath, 2013) have shown that a pure velocity power spectrum should follow Burgers turbulence (Burgers, 1948) with a scaling of -2. In the subsonic regime, Kolmogorov's theory of incompressible turbulence (Kolmogorov, 1941) predicts a decay to smaller scales with a power law of $-5/3$. As one can see, the geometrical form of the filament limits the power on large scales. Nevertheless, the power spectrum follows the expectation quite well on intermediate scales. However, it is impossible to distinguish between supersonic and Kolmogorov decay as both of them lie too close together. In Figure 7.9 we show the volume weighted probability density function (PDF). As expected for fully developed, supersonic turbulence it follows a log-normal distribution (Vazquez-Semadeni, 1994; Padoan et al., 1997; Passot and Vázquez-Semadeni, 1998). The width of the distribution is correlated to the Mach number as

$$\sigma_s^2 = \ln\left(1 + b^2\mathcal{M}^2\right). \tag{7.18}$$

The parameter b depends on the ratio of solenoidal to compressional driving of the turbulent motions, varying smoothly from $b = 1/3$ for purely solenoidal to $b = 1$ for purely compressive driving with a value of $b \approx 0.4$ for a natural mix of modes $F_{\rm comp}/(F_{\rm sol} + F_{\rm comp}) = 1/3$ (Federrath et al., 2008, 2010). All of our simulations with supersonic turbulence show about the same value of $b \approx 0.55$ but there is also some variation over time.

7.4.3 Subsonic turbulence

In contrast to the turbulent motions of the Mach 5.0 inflow, a slower inflow velocity is only capable of generating subsonic turbulent motions despite itself being supersonic. In Figure 7.10 we show the visual impression of a Mach 3.0 inflow. It is not strong enough to generate substructure inside the filament. Only the surface is mildly perturbed. The lack of internal motions can also be seen in the velocity dispersion evolution in Figure 7.11. At all times it is below the sonic line. Nevertheless, it again reaches an equilibrium after about 2.0 Myr which decays after reaching the size of the box at about 3.4 Myr. We also show the kinetic energy power spectrum for the subsonic turbulent case in Figure 7.12. The power spectrum shows a similar behavior to the supersonic case and again the maximum of the cascade, the indicator of the driving scale, corresponds to the filament radius. As in the supersonic case, it is not easy to distinguish between a Kolmogorov and an k^{-2} cascade but at later times the power law seems more similar to the former one which is to be expected for subsonic turbulence. In contrast to the supersonic case, we see a strong lack of compressional modes in the split-up of the power spectrum. This is also confirmed by Equation 7.18 where we get a value of $b = 1/3$.

7.4.4 Dependence on inflow velocity

The crucial question of accretion driven turbulence is how much internal velocity dispersion in a filament is generated in dependence of the inflow velocity. Therefore, we repeat the simulation for inflow velocities of Mach number 1.5, 2.0, 2.5, 3.0, 3.5, 4.0, 5.0, 6.0, 7.5 and 10.0 for a minimum resolution of 512^3. We show the resulting values of the velocity

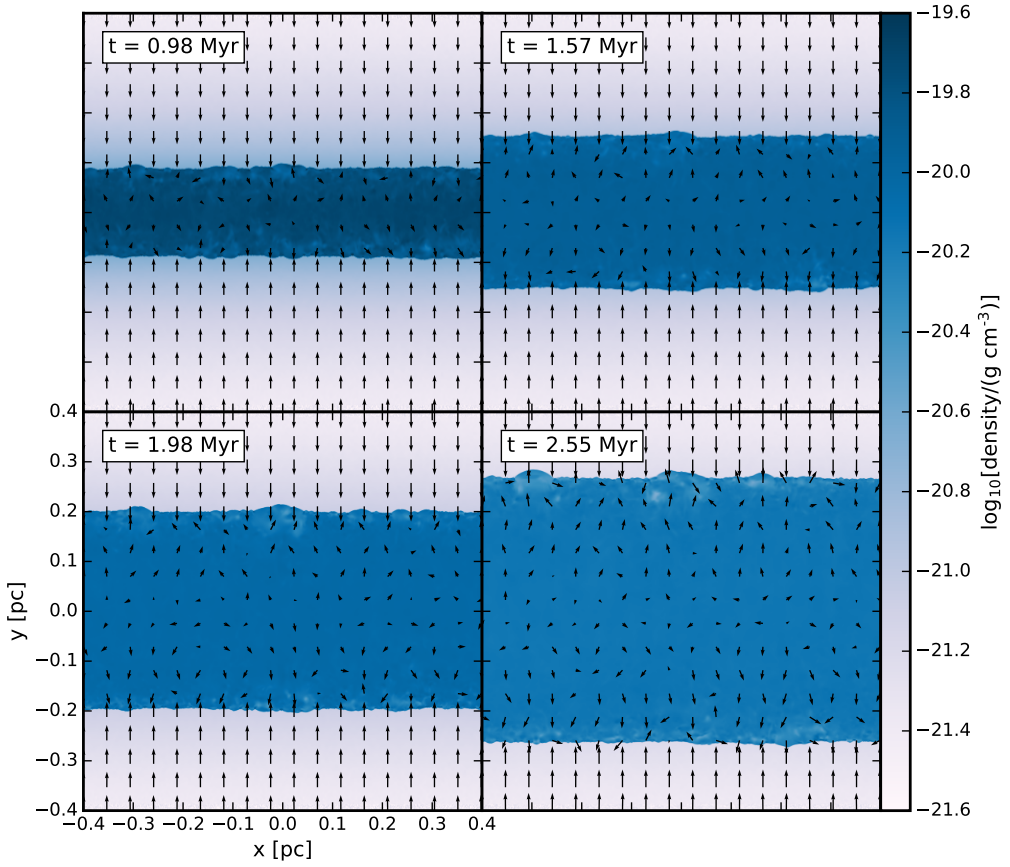

Figure 7.10: Density cut through the centre of the filament with a Mach 3.0 inflow. The velocities are again given by log-scaled arrows. Only the surface of the filament is mildly perturbed.

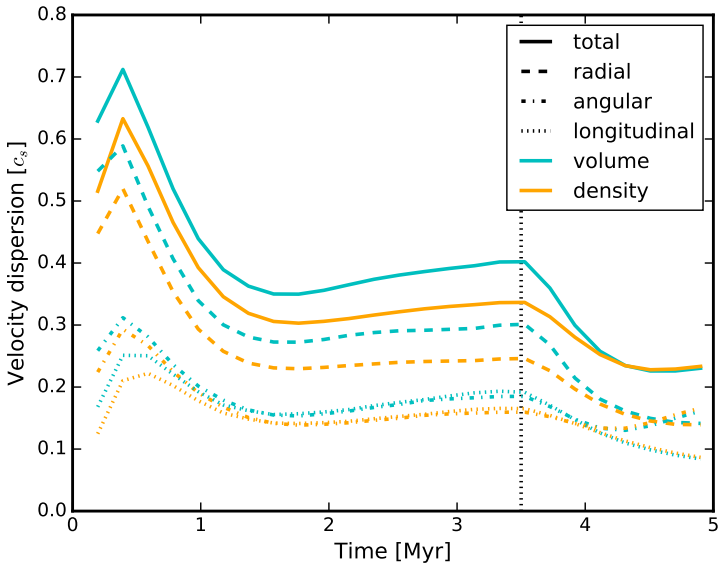

Figure 7.11: Evolution of the velocity dispersion of a Mach 3.0 inflow. As in the case of a Mach 5.0 inflow an equilibrium is established where the velocity dispersion is quasi constant albeit there is a slight increase over time. After the filament reaches the domain boundary (dotted vertical line) the velocity dispersion decays.

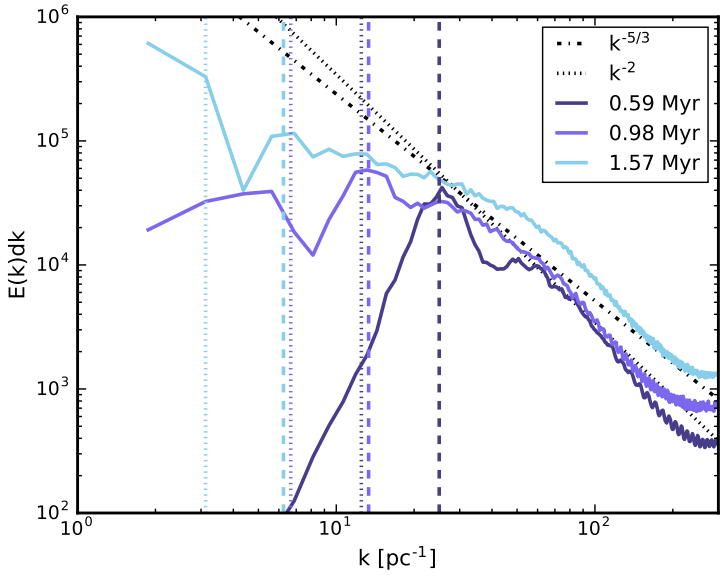

Figure 7.12: The kinetic energy power spectrum of a filament with Mach 3.0 inflow at different times. Similar to the Mach 5.0 case there is a maximum at the radial scale length. For late stages, modes along the filament contribute significantly to the power spectrum.

dispersion in Figure 7.13 where we plot them against their inflow velocity. The errorbars are given by the inherent variance of the velocity dispersion for different initial seeds of the perturbation spectrum and is about five per cent of the measured turbulence. In Figure 7.14 we also show the dependence of the Mach number squared on the inflow Mach number squared as this is the measure of the turbulent and inflowing energy. Both the accreted kinetic energy and the turbulent energy depend on the total accreted mass of the filament. Nevertheless, one does not have to account for mass as all the accreted material also has to be set into turbulent motions and thus the mass term cancels from both energy terms. This is illustrated later in Equation 7.24. In both figures we show the volume weighted velocity dispersion on the left hand side and the density weighted velocity dispersion on the right hand side. One can see that the measurement method has a major impact on the results. First, we look at the volume weighted velocity dispersion in Figure 7.13. We observe three distinct regimes: A high inflow velocity (light blue) leads to supersonic turbulence, an intermediate inflow velocity (medium blue) generates subsonic turbulence and a low inflow velocity (dark blue) results in nearly no turbulence. All of these regimes can be well fitted by linear relationships which do not necessarily go through the zero point. The fitting parameters are always given in the legend. Striking is the break at the sonic line (dashed horizontal line) going from the intermediate subsonic regime to the high velocity supersonic regime. This break does not appear in the density weighted velocity dispersion on the right hand side of Figure 7.13. Now the high and medium inflow velocity values follow one and the same relation. Thus, we now can fit the data by one single linear relationship that connects both regimes and that is shown by the dashed orange line with the parameters:

$$\sigma = 0.30 v_r - 0.60 c_s. \tag{7.19}$$

The fact that we can fit a single line from the high supersonic end down to low subsonic turbulent velocities shows that there is no difference in the physics at work in both regimes. The break in the volume weighted relation also occurs for the squared volume weighted velocity in Figure 7.14. Although the slope stays roughly the same there is a gap between the supersonic and the subsonic regime. Contrarily, the density weighted velocity dispersion squared shows a smooth transition from nearly no turbulence to a constant slope. The density weighted velocity dispersion is also a measurement of the kinetic energy in the turbulence of the filament, a fact that we have confirmed by calculating the kinetic energy. The break in the volume weighted velocity dispersion results from the fact that the nature of the velocity and density distribution changes from the subsonic to the supersonic regime. Supersonic turbulence is shock dominated and due to compression most of the kinetic energy is in high densities. The information about the high densities is lost if one only measures the volume weighted velocity dispersion.

In the right panel of Figure 7.14 we also overplot Equation 7.19. Despite being a linear correlation between velocity dispersion and infall speed it fits the numerical results remarkably well and deviates only slightly for very low Mach numbers. We also attempt to fit a parabola to all of the density weighted data but are not able to get a good match. Therefore, we conclude that the linear relation of Equation 7.19 provides the best analytical description of the underlying physics. While the data points could also be fitted reasonable well with an

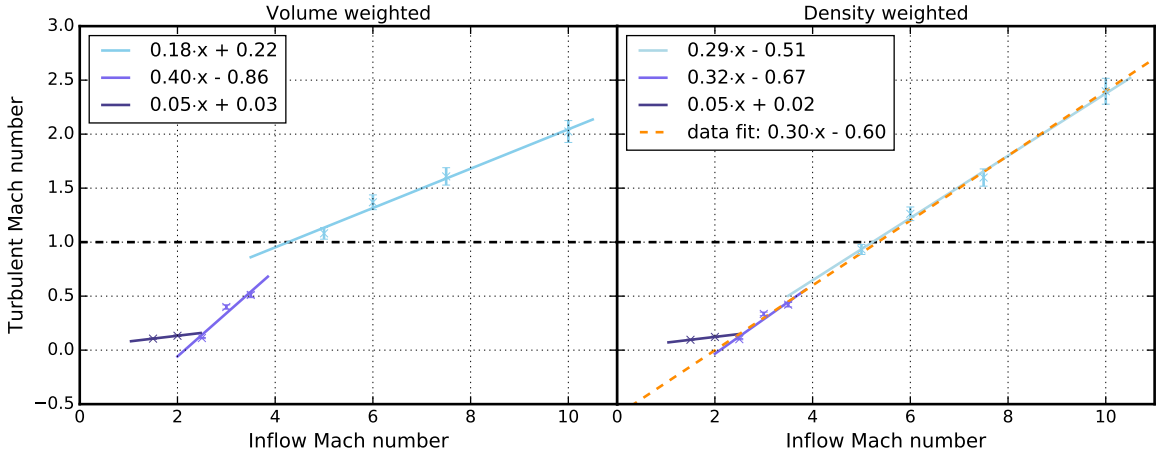

Figure 7.13: The level of driven velocity dispersion as a function of inflow velocity. The volume weighted velocity dispersion is shown on the left and the density weighted velocity dispersion on the right. The parameters of the fitted lines are given in the legend. The errorbars illustrate the inherent variance in the velocity dispersion in different simulations of about five per cent. The dashed orange line is fitted over all light and intermediate blue values.

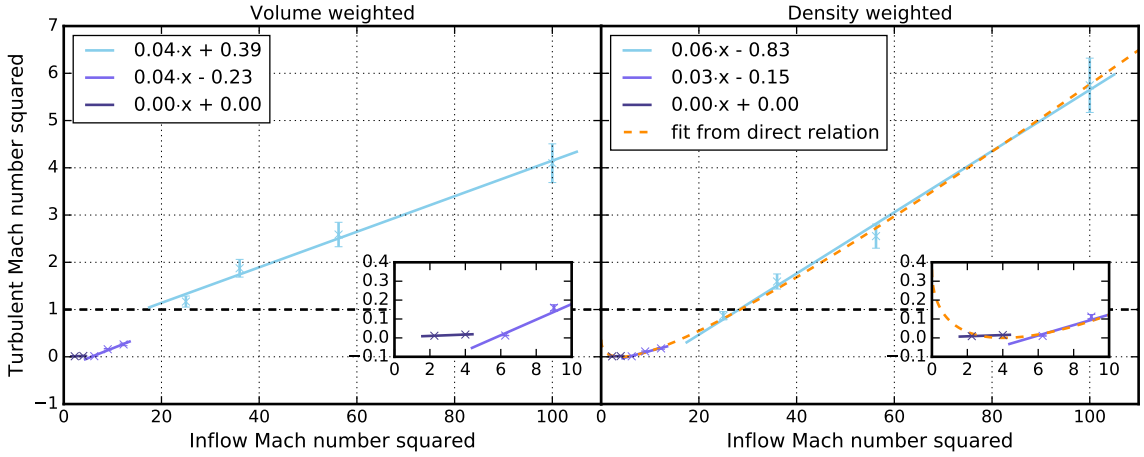

Figure 7.14: The level of driven turbulent Mach number squared as a function of inflow Mach number squared. To calculate the energies one has to multiply both terms by half the mass accretion rate. It is a constant factor and thus the plot shows also the relation between the respective kinetic energies. The volume and density weighted velocity dispersion is shown on the left and right respectively. The dashed orange line is the fitted relation from Figure 7.13.

offset power law of 1/3rd, they do not follow the simple prediction of Heitsch (2013), given by Equation 7.16. We discuss the implication of this in Section 7.7.

We repeat a subset of the simulations for a higher temperature of 40 and 100 K and get similar results, all lying on the analytical relation given by Equation 7.19. Thus our results are independent of the temperature. We also repeat a subset of the simulations with an additional longitudinal velocity component in the inflow. The result in velocity dispersion is unchanged and the only difference is that the whole filament now begins to move in x-direction with constant velocity.

7.5 Pressure equilibrium

In order to see the impact of turbulence on the pressure we analyse its components as function of radius and time. In Figure 7.15 we show the different contributions to the pressure calculated in radial bins for the Mach 5.0 case with an initial density perturbation. We calculate the velocity dispersion, the average density and average thermal pressure in each slice along the filament and in radial bins which are chosen to be four cells wide. We use these values to calculate the respective pressure terms and take the mean along the filament in order to determine an average value for the whole filament. There is an overlap region where filament gas and environment gas mix due to the filament not being completely straight and round. Therefore, we only use the filament gas to calculate the pressure components in the overlap region. We determine the turbulent pressure component with the density weighted velocity dispersion. Thus, the turbulent pressure is given by

$$P_{\mathrm{turb}} = \langle \rho \rangle \, \sigma^2, \tag{7.20}$$

where the braket notation represents the expectation value. The average ram pressure is calculated by the average density and radial velocity as:

$$P_{\mathrm{ram}} = \langle \rho \rangle \, \langle v_r \rangle^2 \tag{7.21}$$

One can see in Figure 7.15 that outside of the filament the turbulent pressure (dashed-dotted line) is zero and the thermal pressure (dashed line) is negligible. As material streams towards the filament the ram-pressure (dotted line) increases as the density increases. When the accretion flow reaches the filament the ram-pressure breaks down and some of the energy is converted into turbulent motions giving rise to a turbulent pressure component. In the overlap region of filament and environment gas we see both a contribution of turbulent pressure and ram pressure due to our split-up of components. As one can see the average pressure inside the filament given by the average thermal pressure together with the average turbulent pressure (solid line) has nearly the same value as the average ram pressure. The filament is compressed and restrained by the accretion flow. Before the filament has settled there is quite an overpressure in the centre of the filament. As the filament grows outward, it adjusts to the outside ram-pressure and a constant pressure inside the filament is established. Note that there is a gradient in the pressure components inside the filament where the thermal pressure decreases and the turbulent pressure increases towards the edge of the filament. Most of the turbulent motions are created at the boundary and propagate inwards. This also explains why

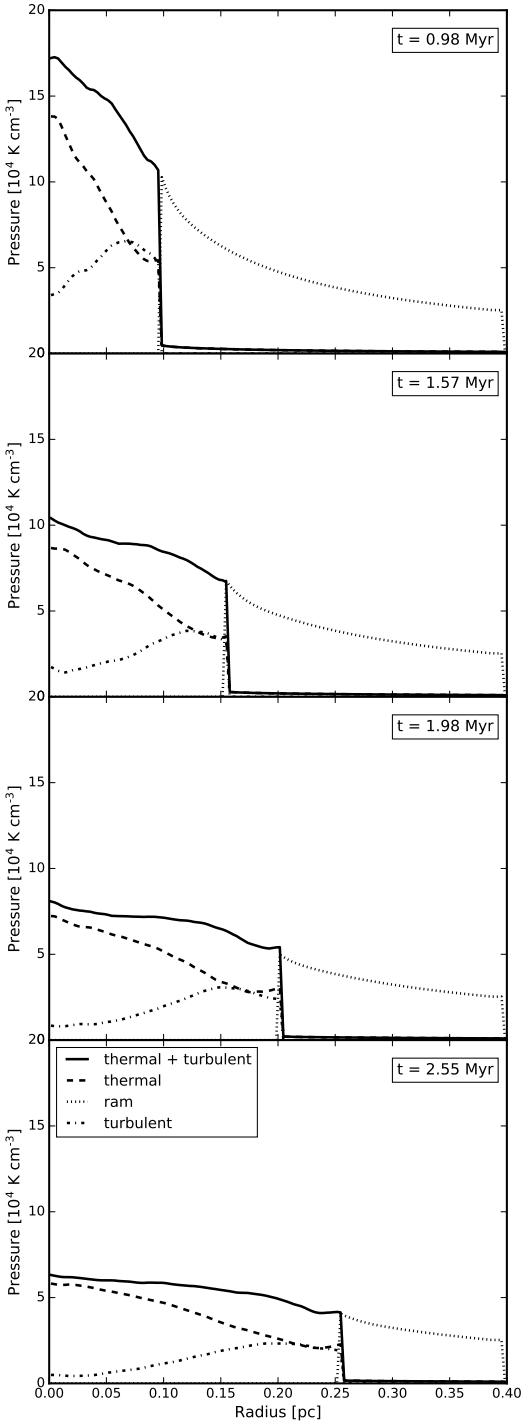

Figure 7.15: Radial pressure profile of the Mach 5.0 case with an initial density perturbation for different times. Inside the filament a pressure equilibrium is established through the combination of thermal and turbulent pressure.

there is no turbulent component supporting the filament radially as the turbulence acts in a localized region.

7.6 Observable velocity dispersion

In order to compare our simulations to observations we derive the line-of-sight velocity by sending a ray through the computational domain. We vary the inclination of the filament and treat every crossed volume element with its respective density as a discrete emitter of a line-of-sight velocity value. These are converted to density weighted Gaussian line profiles with a dispersion width corresponding to the thermal linewidth of $C^{18}O$ at 10 K with a given value of $\sigma = 0.0526\,\mathrm{km\,s^{-1}}$. We bin the resulting line profiles into histograms with a bin width of $0.05\,\mathrm{km\,s^{-1}}$ to get a complete line emission for each observed spatial pixel. We then measure the velocity centroids and the linewidths as an observer would do by fitting Gaussians to the line. As several line profiles show multiple components in velocity space, we fit multiple Gaussians to a single line. In contrast, fitting only one Gaussian to a line overestimates the velocity dispersion as multiple components are grouped together to form one broad line. To prevent false detections we discard peaks which are smaller than a quarter of the maximum line profile and closer together than 1.5 times their respective width. To obtain the non-thermal velocity dispersion we have to subtract the contribution of the thermal gas motions of the full width half maximum (FWHM) of the line as e.g. Myers (1983):

$$\sigma_{\mathrm{NT}} = \sqrt{\frac{\mathrm{FWHM}^2}{8\ln 2} - \frac{k_B T}{m}} \tag{7.22}$$

We show the non-thermal linewidth along a filament through its centre for the case of turbulence forming due to inflows of Mach 3.0, 5.0 and 10.0 in Figure 7.16, Figure 7.17 and Figure 7.18, all of which include an initial perturbation. At a first glance it is important to note the striking similarity to real observations (Hacar and Tafalla, 2011; Hacar et al., 2013; Tafalla and Hacar, 2015; Hacar et al., 2016b). As in the actual measurements we see an inherent spatial variation due to the non-homogeneous nature of the turbulence. The variation is also not stationary but changes with time, mimicking the sloshing motions of the total filament. However, the mean of the data distribution stays relatively stable, only varying by about 10%. Comparing the mean to the analytical value of the velocity dispersion it becomes clear that an observer cannot see the full picture of the internal motions of the filament. The observer will preferentially see the density weighted radial velocity dispersion (dashed line) as filaments are more likely to be detected for small inclinations. Thus, the line-of-sight is parallel to the radial motions. While the subsonic case shows mean values which lie below any velocity dispersion typically observed, it is also the only one where the mean of the observed distribution lies above the expected value of the radial velocity dispersion. Going to higher inflow speeds, the mean of the observed distribution generally lies below the expected value. The situation becomes even worse for cases of high turbulence as shown in Figure 7.18 where the discrepancy can be even as large as a factor of two. Moreover, the discrepancy between the observed mean and the total velocity dispersion is even larger. Despite having a supersonic total density weighted velocity dispersion, most of the data points of the Mach

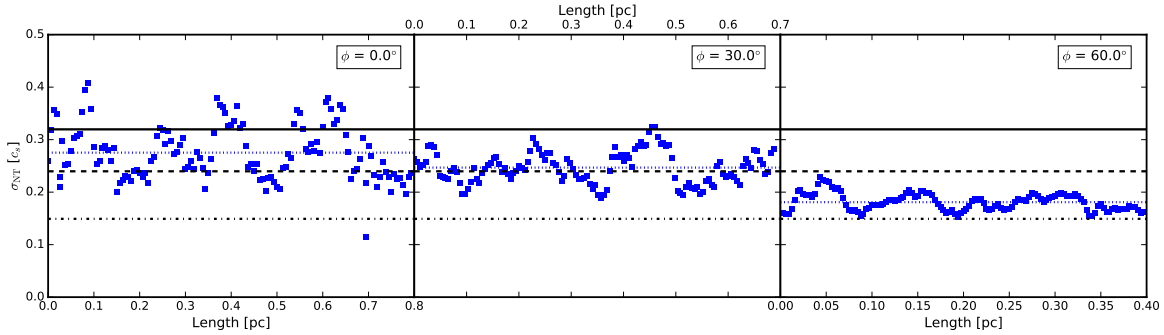

Figure 7.16: The measured non-thermal linewidth along the central axis of the filament for the case with a Mach 3.0 inflow for different inclinations. Data points are given by the blue squares and their mean by the blue dotted line. The solid, dashed and dashed-dotted black lines show the total, the radial and the longitudinal density weighted velocity dispersion respectively.

10 inflow show a subsonic or at best a transsonic non-thermal line width. This means that the interpretation of the inherent motions in an observed filament can be severely flawed. A filament dominated by supersonic motions will be classified as only having subsonic motions. With the addition of gravity the problem will become even worse as there is an internal density gradient enhancing the signal of the central region. This leads to an overall thinner line as the outer region, which contains a high radial velocity component, is neglected and thus the measured line width becomes even smaller. There is not even a constant correction factor as for example assumed for isotropic turbulence of $\sqrt{3}$. The measured mean is relatively constant for different inclinations, going from zero to sixty degrees, but if one does not split the individual components in the line its broadness is overestimated the more the filament is seen from the side. The larger the inclination, the more is the filament dominated by longitudinal motions which give only one thin component. Therefore, the observable mean decreases and finally approaches the longitudinal velocity dispersion. This can be seen to some degree in the subsonic case. If one fits one component to the line-of-sight this effect is stronger and can also be observed in the cases of higher inflow velocity. It is even possible for the mean to be below the longitudinal velocity dispersion as a single line-of-sight does not contain the complete information on the total line-of-sight velocity dispersion of the whole filament. Striking is also the fact that the variance of the distribution decreases for a higher inclination. This behavior could potentially be used to determine the inclination of a filament. We will study the effect of the inclination angle on the measurements of the turbulent velocity and its variance in a subsequent paper.

7.7 Discussion and conclusions

We have presented a numerical study on accretion driven turbulence in filaments. The focus of this paper was to analyse the dependence of the velocity dispersion on the inflow velocity. We deliberately neglected the effects of gravity in order to have a constant inflow velocity and to be able to follow the driving of turbulence long enough without the radial collapse of the filament or its condensation into collapsing clumps. The formation of turbulent filament,

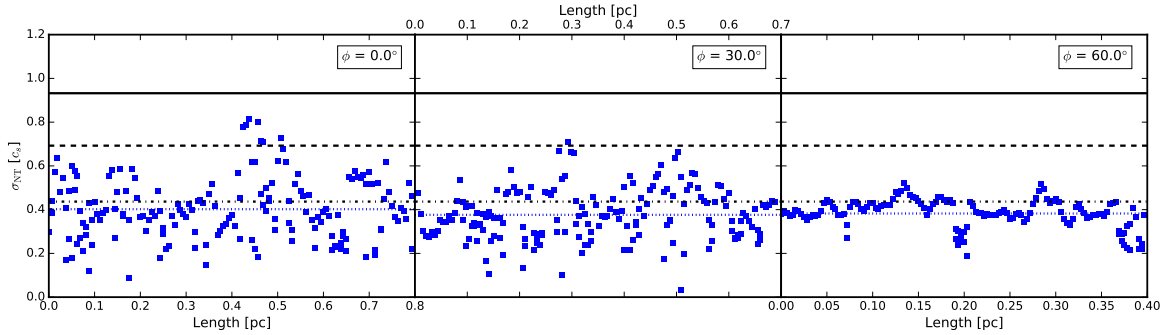

Figure 7.17: The same as in Figure 7.16 but for an inflow of Mach 5.0.

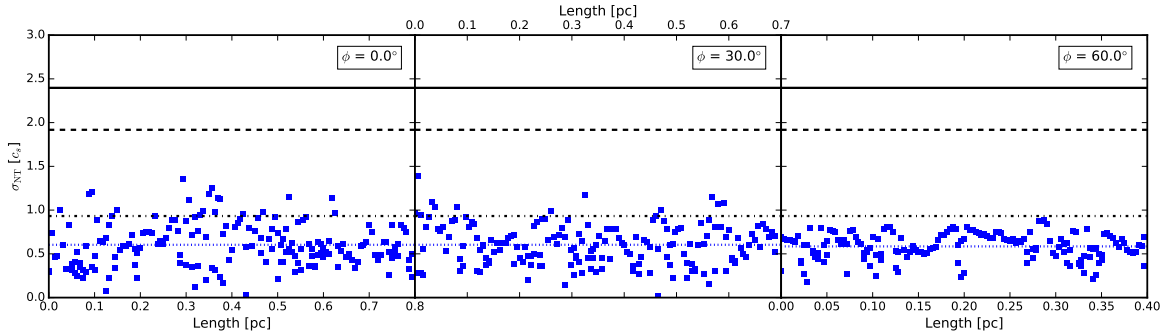

Figure 7.18: The same as in Figure 7.16 but for an inflow of Mach 10.0.

including self-gravity will be discussed in a subsequent paper. We find that there is a linear dependency of the density weighted velocity dispersion on the inflow velocity. Below Mach 2.0 the relationship flattens as shown in the right panels of Figure 7.13 and Figure 7.14. Why there is a break in the relation is not completely clear. One possibility is that the low inflow velocity region is an artifact of numerical noise. In this case it must be dominated by perturbations on small scales. Therefore, we smooth our data to remove the small scale signal and recalculate the velocity dispersion. The result shows that the velocity dispersion is unchanged. Therefore, the measured velocity dispersion is in the large scale structure. Even for a high degree of smoothing the velocity dispersion remains the same. Thus, there must be a physical reason for the break in the slope. An explanation could be that filaments have a bottom level of minimal velocity dispersion comparable to a basic eigenmode which is exited by the constant inflow. In the subsonic regime sound waves are supposed to be very inefficient in dissipating energy and indeed if one sets up a filament with a random velocity perturbation there is a level of velocity dispersion below which the kinetic energy does not decay. Its dependence on form and density of the filament is out of the scope of this paper and will be discussed elsewhere.

We now want to focus on the form of the linear fit. As shown in Figure 7.13 we measure a linear relationship of

$$\sigma = 0.30 v_r - 0.60 c_s \tag{7.23}$$

It is possible to show that this is equivalent to an energy balance. In order to get a kinetic

energy we take the square of the equation and multiply it with half of the mass accretion rate which gives

$$\frac{1}{2}\dot{M}\sigma^2 = 0.09 \cdot \frac{1}{2}\dot{M}v_r^2 - 0.18\dot{M}c_s v_r + 0.18\dot{M}c_s^2 \tag{7.24}$$

with the restriction that

$$v_r \geq 2.0c_s. \tag{7.25}$$

For a constant velocity dispersion the term on the left hand side is the change in turbulent energy and the first term on the right hand side the rate of accreted kinetic energy. To show the meaning of the remaining terms we use the equation of change in turbulent energy given by

$$\dot{E}_t = \alpha\dot{E}_a - \dot{E}_d \tag{7.26}$$

where $\dot{E}_t$ is the change in turbulent energy, $\dot{E}_a$ is the kinetic energy accretion rate and $\dot{E}_d$ is the energy dissipation rate. In the case of a constant velocity dispersion, the change in turbulent energy is due to the change in total mass of the filament. The same is true for a constant accretion velocity where the change in total accreted kinetic energy is due to the change in the total accreted mass. We also consider that energy is lost in the isothermal accretion shock and is radiated away. As the fraction of the lost energy should be roughly constant per time we introduce a constant efficiency α which has a value between zero and one. Comparing Equation 7.26 to Equation 7.24 we determine the efficiency to be:

$$\alpha = 0.09. \tag{7.27}$$

This means that the energy lost to dissipation is given by the remaining terms

$$\dot{E}_d = 0.18\dot{M}c_s v_r - 0.18\dot{M}c_s^2 = 0.18\dot{M}\left(c_s v_r - c_s^2\right) \tag{7.28}$$

A possible explanation for both terms is the assumption that turbulence is mainly dissipated in an inner region of the filament where radial waves travelling inwards interact. We assume that this region is proportional to the total radius of the filament:

$$R_i = bR(t) = b\frac{2c_s^2 t}{v_r} \tag{7.29}$$

The proportionality b has to be constant for a single run but can vary with accretion velocity. The mass contained in the inner region is then the density given by the shock times the volume:

$$M_i = \rho(R)\pi R_i^2 L = \rho_0 \mathcal{M}^2 R_0 \pi b^2 RL = b^2 M(R) \tag{7.30}$$

This means that the mass contained in a region proportional to the radius is also proportional to the total mass. Thus, if we use the definition of the energy dissipation rate given by Equation 7.14, assume that the scale relevant for the crossing time is the radius of the inner region and assume that the speed for the crossing time is the sound speed we get:

$$\dot{E}_d = \frac{1}{2}\frac{M_i c_s^3}{R_i} = \frac{b}{4}\frac{Mc_s^3 v_r}{c_s^2 t} = \frac{b}{4}\dot{M}c_s v_r \tag{7.31}$$

As the inner region should be larger for greater inflow Mach number $\mathcal{M}$ we assume that:

$$b = a\,(1 - 1/\mathcal{M}) \tag{7.32}$$

where a is a constant. Thus the energy decays as:

$$\dot{E}_d = \frac{a}{4}\,(1 - c_s/v_r)\,\dot{M} c_s v_r = \frac{a}{4}\dot{M}(c_s v_r - c_s^2) \tag{7.33}$$

If we compare our result to Equation 7.28 we find this fits both terms with $a = 0.72$.

Our results can be summarized as follows:

1. The accretion of material leads to non-isotropic, sub- and supersonic turbulence depending on the energy accretion rate as long as the symmetry is broken. The efficiency of transferred energy is independent of the accretion rate and equal to 9%.
2. The amount of turbulence generated is independent of the perturbation strength of the initial density field and independent of an additional velocity component parallel to the filament.
3. The turbulence reaches an equilibrium level which scales linearly with the accretion rate.
4. The filament radius grows linearly with time and is the driving scale of the turbulence.
5. The density weighted velocity dispersion contributes to the pressure equilibrium inside the filament.
6. In most situations, an observer cannot measure the true velocity dispersion and will even misinterpret the level of turbulence to be subsonic while the intrinsic velocity dispersion could still be supersonic.

7.8 Acknowledgements

We thank the whole CAST group for helpful comments and discussions. AB, MG and SH are supported by the priority programme 1573 "Physics of the Interstellar Medium" of the German Science Foundation and the Cluster of Excellence "Origin and Structure of the Universe". The simulations were run using resources of the Leibniz Rechenzentrum (LRZ, Munich; linux cluster CoolMUC2). We would also like to thank the referee whose input lead to an improvement of the results of the paper.

8 Paper III: Morphology of prestellar cores in pressure-confined filaments

S. Heigl, M. Gritschneder, A. Burkert, 2018, *Monthly Notices of the Royal Astronomical Society*, 481, L1-L5

Observations of prestellar cores in star-forming filaments show two distinct morphologies. While molecular line measurements often show broad cores, submillimeter continuum observations predominantly display pinched cores compared to the bulk of the filament gas. In order to explain how different morphologies arise, we use the gravitational instability model where prestellar cores form by growing density perturbations. The radial extent at each position is set by the local line-mass. We show that the ratio of core radius to filament radius is determined by the initial line-mass of the filament. Additionally, the core morphology is independent of perturbation length scale and inclination, which makes it an ideal diagnostic for observations. Filaments with a line-mass of less than half its critical value should form broad cores, whereas filaments with more than half its critical line-mass value should form pinched cores. For filaments embedded in a constant background pressure, the dominant perturbation growth times significantly differ for low and high line-mass filaments. Therefore, we predict that only one population of cores is present if all filaments within a region begin with similar initial perturbations.

Key words: stars:formation - ISM:kinematics and dynamics - ISM:structure

8.1 Introduction

It has long been proposed that core formation in filaments is tied to some kind of fragmentation process (Schneider and Elmegreen, 1979; Larson, 1985). This connection has only been reinforced by observations of the *Herschel* Space Observatory (André et al., 2010; Könyves et al., 2010; Men'shchikov et al., 2010; Ward-Thompson et al., 2010; Arzoumanian et al., 2011, 2013; Kirk et al., 2013; André et al., 2014), which show that dense cores are contained in an ubiquitous filamentary structure in molecular clouds. As cores are the birth-site of stars (Benson and Myers, 1989; Klessen et al., 1998; McKee and Ostriker, 2007), it is essential to understand the process of core formation in order to develop a coherent model for stellar formation. Different models of core formation have been proposed, e.g. by the dissipation of turbulence (Padoan et al., 2001; Klessen et al., 2005) or by collapse of density enhancements due to intersecting filaments, so called "hubs" (Myers, 2009). The complexity of core formation has increased with the observations of fibres (Hacar et al., 2013; Tafalla and Hacar, 2015), trans- and subsonic velocity coherent substructures in filaments, again opening the possibility that cores form by subsonic motions due to gravitational instabilities, potentially modified by magnetic fields either hindering core formation due to magnetic pressure (Nagasawa, 1987; Gehman et al., 1996b; Fiege and Pudritz, 2000b) or facilitating core formation in a magnetically stabilized filament by ambipolar diffusion (Shu et al., 1987; Hosseinirad et al., 2017).

A possible indicator to validate this model is the comparison of observed cores with the analytical predictions of overdensities forming by gravitational instabilities. High dynamic range observations in the submillimeter continuum, for instance in the Taurus region, show very thin cores compared to the filament radius (Marsh et al., 2014). Contrarily, molecular line observations, which often only trace the dense gas, have mainly revealed cores which are broader than the filament (Hacar and Tafalla, 2011; Hacar et al., 2013; Tafalla and Hacar, 2015). Thus, the interpretation of core radius is complex and core morphology obviously depends on the tracer of observation.

Numerical predictions by Nagasawa (1987) showed that there are two regimes of the perturbation. One for low line-mass filaments, called deformation instability or "sausage" instability, where the forming cores bulge out and one for high line-mass, named compressional instability, where cores form by compression and thus pinch in. Both morphologies exist in simulations throughout the literature (Gehman et al., 1996a,b; Inutsuka and Miyama, 1997; Fiege and Pudritz, 2000b). However, in order to determine the morphology of cores it is important to not only predict the radius evolution of the core itself, but also the radius evolution of the material making up the rest of the filament. For a growing perturbation, both evolve simultaneously. We expand on the picture by Nagasawa (1987) and show an analytical prediction for the evolution of the radius ratio.

8.2 Basic concepts

In order to be able to calculate the radial extent of a filament, it is necessary to define the underlying density structure. The basic hydrostatic, isothermal model predicts a profile which drops off as r^{-4} (Stodólkiewicz, 1963; Ostriker, 1964). Observationally, filaments often show

a shallower power law exponent of -1.6 to -2.5 at large radii (Arzoumanian et al., 2011; Palmeirim et al., 2013). Several processes can explain this difference: truncation of the filament radius in pressure equilibrium (Fischera and Martin, 2012), magnetic fields (Fiege and Pudritz, 2000b), the equation of state (Gehman et al., 1996a; Toci and Galli, 2015a) or filaments formed by shock interaction (Federrath, 2016). As the physical reason for the observed profile and how it would impact the radial stability is still unclear, we use the basic isothermal model. In this case the density goes as:

$$\rho(r) = \rho_c \left(1 + (r/H)^2\right)^{-2} \tag{8.1}$$

where r is the cylindrical radius and ρ_c is its central density. It has the radial scale height H given by

$$H^2 = \frac{2c_s^2}{\pi G \rho_c} \tag{8.2}$$

where c_s is the isothermal sound speed and G is the gravitational constant. Integrating the density profile to $r \to \infty$, one can calculate the critical line-mass, e.g. the line-mass at which a filament is marginally stable, of

$$\left(\frac{M}{L}\right)_{\rm crit} = \frac{2c_s^2}{G}. \tag{8.3}$$

If the line-mass of a filament is above this value, there is no hydrostatic solution and the filament will collapse to a spindle. If the line-mass is below this value the filament will expand freely unless it is bound by an additional outside pressure (Nagasawa, 1987). In this case, the filament follows the hydrostatic equilibrium profile until it extends to the radius where the internal pressure matches the external pressure. Following Fischera and Martin (2012), the integral of the density profile then is given by

$$\frac{M}{L} = \int_0^R 2\pi r \rho(r) dr = \left(\frac{M}{L}\right)_{\rm crit} \left(1 + (H/R)^2\right)^{-1} \tag{8.4}$$

and the factor of line-mass to critical line-mass becomes

$$f_{\rm cyl} = \left(\frac{M}{L}\right) \Big/ \left(\frac{M}{L}\right)_{\rm crit} = \left(1 + (H/R)^2\right)^{-1}. \tag{8.5}$$

This allows us to derive the filament radius as

$$R = H \left(\frac{f_{\rm cyl}}{1 - f_{\rm cyl}}\right)^{1/2}. \tag{8.6}$$

For a fixed external pressure the scale height is not set by the central density but by the ambient pressure via the boundary density $\rho_b = p_{\rm ext}/c_s^2$. It is related to the central density by

$$\rho_b = \rho_c \left(1 - f_{\rm cyl}\right)^2 \tag{8.7}$$

and therefore the scale height adjusts as

$$H^2 = \frac{2c_s^2}{\pi G \rho_b} \left(1 - f_{\rm cyl}\right)^2 = \frac{2c_s^4}{\pi G p_{\rm ext}} \left(1 - f_{\rm cyl}\right)^2. \tag{8.8}$$

Subsequently, the radius has a maximum at $f_{\rm cyl} = 0.5$ and declines to zero as $f_{\rm cyl}$ approaches 0 or 1.
Linear perturbation analysis introduces a perturbation along the filament axis of the form

$$\rho(r, z, t) = \rho_0(r) + \rho_1(r, z, t) = \rho_0(r) + \epsilon\rho_0(r) \exp(ikz - i\omega t) \tag{8.9}$$

where z is the filament axis, $\omega = 2\pi/\tau$ is the perturbation growth rate with τ being the perturbation growth time, $k = 2\pi/\lambda$ is the wave vector with λ being the perturbation length scale and ϵ is the perturbation strength. This also leads to a perturbation in velocity, pressure and potential of the form:

$$q_1(r, z, t) \propto \exp(ikz - i\omega t). \tag{8.10}$$

Solving the mass and momentum conservation as well as Laplace's equation for the gravitational potential while second order terms are ignored, perturbations grow for values of k where the solution of the resulting dispersion relation $\omega^2(k)$ is smaller than zero. As the perturbation term of Equation 8.9 does not depend on radius, one can insert it into the definition of the line-mass Equation 8.4 and easily show that the line-mass

$$f_{\rm cyl}(z, t) = f_0 \left(1 + \epsilon \exp\left(ikz - i\omega t\right)\right) \tag{8.11}$$

evolves analogous to the density with f_0 being the initial line-mass. Therefore, the filament radius now depends on the local line-mass at the position z.

8.3 Core morphology

While Nagasawa (1987) already pointed out the two different core formation regimes, it is important to look at the dynamical evolution of both core and filament radius. As the radius has its maximum at half the critical line-mass, it can both grow or shrink for an increase or decrease in the local line-mass, depending on the initial line-mass. In low line-mass filaments, where the mean line-mass is below half the critical value, the growing core will first increase in radius. But as soon as its local line-mass exceeds a value of $f_{\rm cyl} = 0.5$, the radius will decrease again. At the same time, in absence of accretion the core is fed by filament gas, thus reducing the line-mass and the radius of the rest of the filament. Contrarily, in a filament with initially high line-mass, where the mean line-mass is above half the critical value, the radius of the core decreases as it grows. As mass is accreted from the rest of the filament, the overall filament radius will at first increase but then also decrease as soon as the local line-mass is below a value of $f_{\rm cyl} = 0.5$.

In order to determine the core morphology, one has to compare the radius $R_{\rm max}$ of the slice with the maximum line-mass to the radius $R_{\rm min}$ of the slice with the minimum line-mass. In a perturbed filament both evolve simultaneously and determine how a core appears visually. If $R_{\rm max} > R_{\rm min}$ then the core will bulge out and will be broader than the rest of the filament gas. If $R_{\rm max} < R_{\rm min}$ the core will be narrower than the filament gas and will pinch in. The radii are given by the respective scale height and line-mass as shown in Equation 8.6. The ratio of the

two is given by

$$R_{\max}/R_{\min} = \frac{H_{\max}\left(f_{\max}/(1-f_{\max})\right)^{1/2}}{H_{\min}\left(f_{\min}/(1-f_{\min})\right)^{1/2}} = \\ = \left(\frac{f_{\max}(1-f_{\max})}{f_{\min}(1-f_{\min})}\right)^{1/2} \tag{8.12}$$

with

$$f_{\max} = f_0(1+\epsilon\exp(\omega t)) = f_0 c_+ \tag{8.13}$$

and

$$f_{\min} = f_0(1-\epsilon\exp(\omega t)) = f_0 c_-. \tag{8.14}$$

Note that $c_- = 2 - c_+$. This means that

$$R_{\max}/R_{\min} = \left(\frac{c_+ - f_0 c_+^2}{c_- - f_0 c_-^2}\right)^{1/2}. \tag{8.15}$$

Setting this equation equal to 1, one can calculate the line-mass where cores stay exactly as broad as the filament to be half the critical line-mass. For smaller line-masses the ratio between the radii will at all times be larger than one and vice versa. This means that for a filament which has a line-mass of less than half the critical value, the decrease in radius of the core when it reaches a local line-mass greater than half the critical value will always be slower than the overall decrease of radius due to the loss of mass in the rest of the filament. Therefore, the core will bulge out at all times. The inverse is true for filaments with a line-mass above half the critical line-mass, where the core will always pinch in. This fact is illustrated in the top panel of Figure 8.1 where we show the evolution of the ratio between core to filament radius over time for a fixed initial central density of 10^4 cm^{-3} and an initial perturbation strength of 1%. As the central density and the external pressure are not independent of each other, a constant central density with a varying initial line-mass means that we vary the external pressure from $p_{\rm ext}/k_B \sim 10^5$ K cm^{-3} for low line-masses to $p_{\rm ext}/k_B \sim 10^3$ K cm^{-3} for high line-masses. The perturbation growth times are taken from Fischera and Martin (2012) where we assume the perturbation grows on the dominant wavelength. For the same initial density the growth time only depends weakly on the line-mass. Thus at the same point in time they have evolved by approximately the same factor. Note that although the radius in general does depend on the initial central density the ratio does not.

Interestingly, for filaments below half the critical line-mass the radius ratio does not depend much on the line-mass itself at a specific point in its evolution. As long as the cores have grown by about the same amount we do not expect a significant difference in core to filament radius. As $f_{\min}$ goes to zero as soon as the core has accreted nearly all material, the radius ratio diverges to infinity. Note that Fischera and Martin (2012) predicted that cores could form an unstable Bonnor-Ebert sphere (Ebert, 1955; Bonnor, 1956) depending on the perturbation length. We do not include this effect in our analytical model but note that it can lead to the collapse of an initially broad core and therefore also could lead to a pinched, albeit protostellar core.

The evolution of cores is significantly different for filaments with a line-mass above half the critical value. They tend to evolve much faster than their counterparts in low line-mass

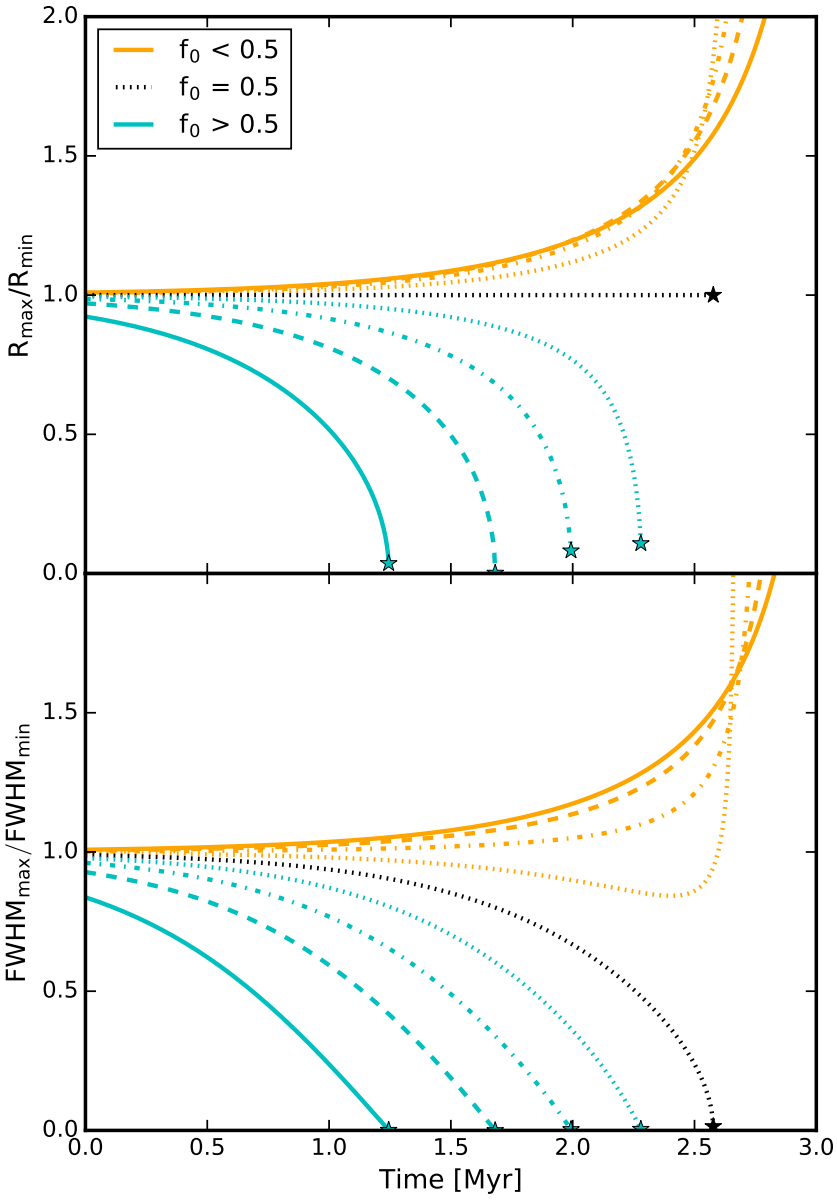

Figure 8.1: The top figure shows the analytical prediction of the ratio between the core radius (at the maximum central density) and filament radius (at the minimum central density) for a constant initial central density of $\rho_0 = 10^4\,\mathrm{cm}^{-3}$, starting with a perturbation of 1%. The bottom figure shows the same for the FWHM. From top to bottom the curves show different values of the line-mass in values of f_0, starting at 0.1 (solid orange) and incrementally increased by 0.1. The stars symbolize the time when the line-mass locally becomes supercritical and the core collapses. Note that the radius ratio of cores in low line-mass filaments diverges to infinity as all the gas of the filament is accreted.

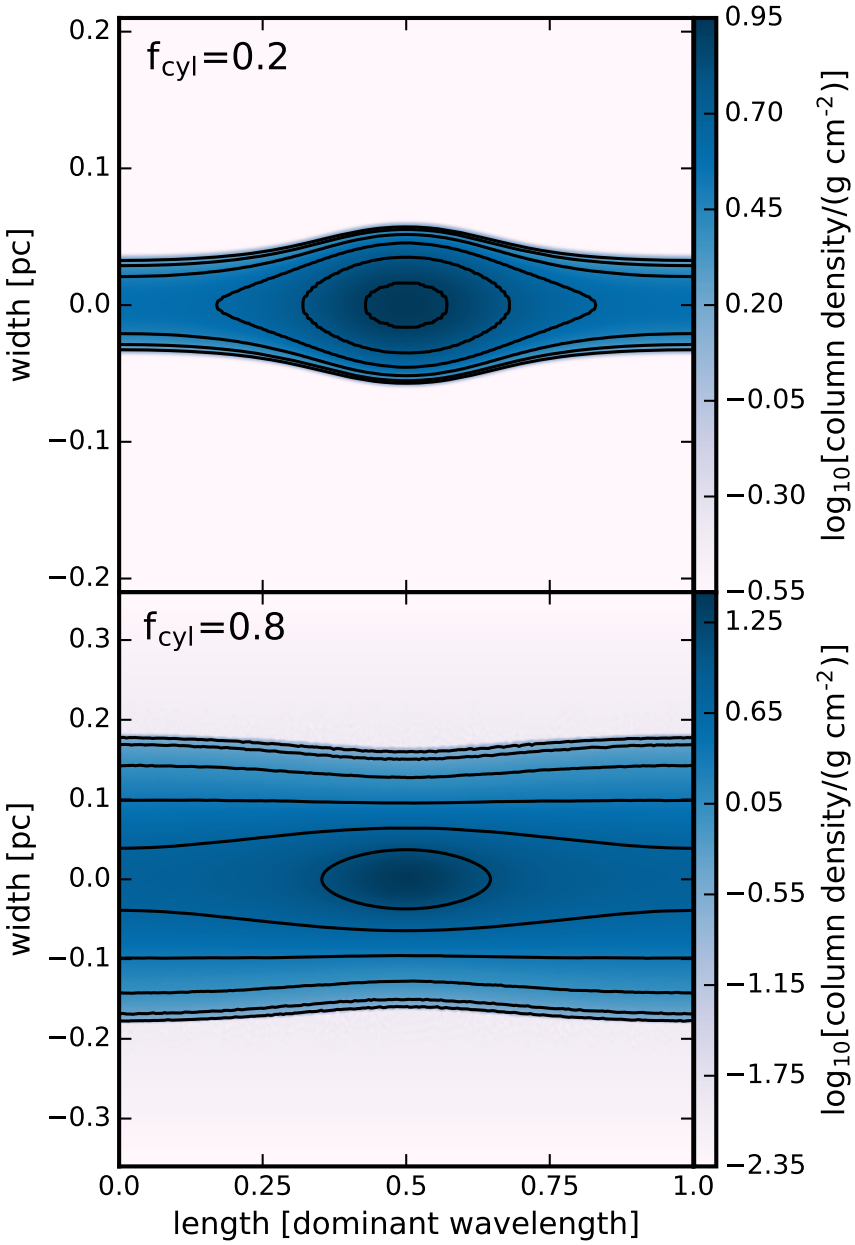

Figure 8.2: Column density plots of simulated cores forming in filaments with different line-masses. A low line-mass filament forms a broad core while a core forming in a high line-mass filament causes the radius to pinch.

filaments. As soon as they come close to the limit of hydrostatic equilibrium, their radius collapses away quite rapidly. This restricts their lifetime and the chance to actually observe pinched cores.

Additionally, we test our predictions by simulating the evolution of cores which start with a one per cent perturbation in filaments with a central density of $10^4\,\mathrm{cm}^{-3}$ and a line-mass of $f_{\mathrm{cyl}} = 0.2$ and 0.8 in order to show the qualitative difference in morphology. We use the grid code RAMSES (Teyssier, 2002) to set up boxes with the size of the respective dominant perturbation length with periodic boundary condition in the filament axis and open boundaries perpendicular to the filament. In order to test our prediction independent of accretion onto the filaments, they are embedded in a low-density warm medium in pressure equilibrium. The simulation set-up is similar to that of Heigl et al. (2016). Both results of the simulations are shown in projection in Figure 8.2 at the same time, shortly before the high line-mass filament collapses. The difference in morphology is clearly visible. The core in the low line-mass filament is broader then the filament, whereas the core in the high line-mass filament causes the radius to decrease. We only see a divergence of the Ostriker profile at late times, where both cores profiles become softer and closer to the radial dependence of an isothermal sphere.

Therefore, our analysis provides observers with a useful tool to determine the line-mass a filament, independent of inclination and perturbation scale, by identifying the cores. If a core bulges out of the filament, the mean line-mass is below 0.5. If a core pinches inwards, the mean line-mass is above 0.5. A caveat of this method is the way the radius is determined in the observations. The filament width is often determined by measuring the full-width at half maximum (FWHM) of the radial profile. If the filament follows an Ostriker profile, the FWHM is not a perfect tracer of the radius and a correction term has to be taken into consideration. This correction was derived in Fischera and Martin (2012) and changes the analytical prediction of the radius ratio as shown in the bottom of Figure 8.1. In general, using the FWHM will underestimate the core radius and therefore introduces a bias to lower radius ratios. This effect does not change the predicted curves significantly except for cores forming in filaments with $f_{\mathrm{cyl}} = 0.5$, which would be observed as a pinched core.

We assume that filaments in the same region of a molecular cloud are embedded in a constant background pressure. In this case, filaments with different line-masses will vary substantially in central density and therefore also in the perturbation growth time as it goes as $\tau_{\mathrm{dom}} \sim 1/\sqrt{\rho_c}$. This fact is illustrated in Figure 8.3 where we show the same evolution of the core to filament radius ratio as in Figure 8.1 under the assumption that the cores grow on the dominant timescale now for a constant external pressure of $p_{\mathrm{ext}}/k_B = 10^5\,\mathrm{K\,cm}^{-3}$. Consequently the central density varies from $\rho_c \sim 10^4\,\mathrm{cm}^{-3}$ for low line-masses to $\rho_c \sim 10^6\,\mathrm{cm}^{-3}$ for high line-masses. There is an interesting dichotomy visible in the state of evolution of the cores. High line-mass filaments forming pinched cores evolve much faster than low line-mass filaments which form broad cores. This implies that, as long as there is not much spread in initial perturbation strength in filaments, a region will most likely only contain one population of cores. Either there are mainly pinched cores and broad cores will not have had enough time to grow or there are mainly broad cores and their high line-mass counterparts have already collapsed away and formed stars. Varying the value of the external pressure only shifts the evolutionary tracks in Figure 8.3 (higher external pressure imply larger central densities and thus faster growth times) and does not change the general behavior.

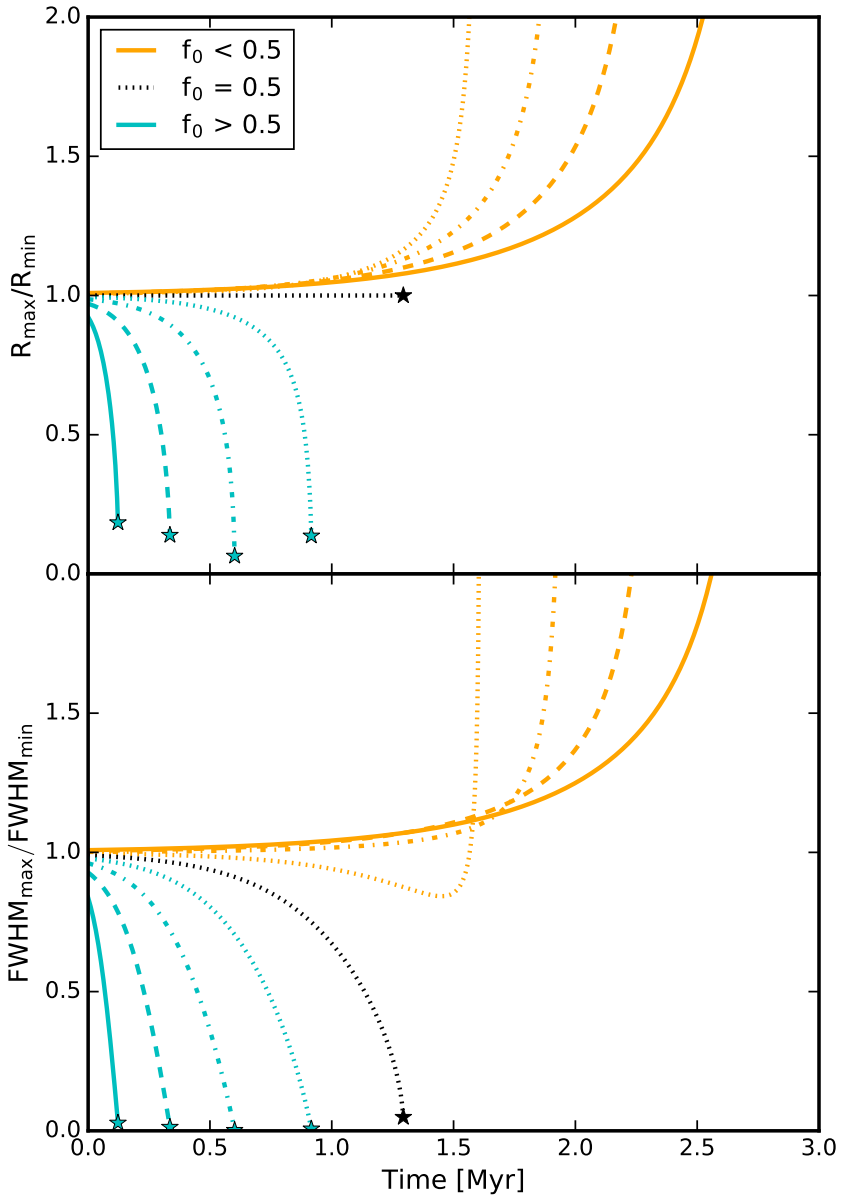

Figure 8.3: The same as in Figure 8.1 but now for a constant external pressure of $p_{\rm ext}/k_B = 10^5$ K cm^{-3}. For varying central densities there is a broad spread in perturbation growth time. The line properties are the same as in Figure 8.1. Starting at $f_0 = 0.1$ for the curve with the longest perturbation growth time (solid orange), f_0 increases incrementally by 0.1 going to faster perturbation growth times.

8.4 Discussion and conclusions

The gravitational instability model has several shortcomings. The main assumption is that filaments are very idealized cylindrical entities where the mean initial line-mass does not vary much along its length. Moreover, the filament profile requires a certain timescale to adjust to density changes. If the local line-mass varies faster than the radius can adjust, a broad core could be embedded in a filament with a line-mass larger than half the critical value. There are two processes which can lead to a major change in local line-mass on a short timescale. On the one hand, mass accretion increases the overall line-mass. Observed rates are estimated to be on the order of $10 - 100\,M_\odot\,pc^{-1}\,Myr^{-1}$ (Palmeirim et al., 2013). On the other hand, a filament will longitudinally contract due to self-gravity. In addition, the rapid formation of two cores at the ends of the filament seems to be a typical outcome of the edge-effect (Burkert and Hartmann, 2004).

A different equation of state or additional physical contribute to the radial stability and can change the morphology of cores. Observed radial density profiles are better matched by polytropic indices lower than one (Toci and Galli, 2015a). As long as there is a maximum radius in dependence of the line-mass we still expect a dichotomy in morphology but with the division not necessarily at half the critical line-mass.

Observationally, it is important to not only include the dense gas in order to reliably measure both filament and core radius. As the density of the outer filament gas is lower than the core gas, the filament radius has to be determined with a tracer of low gas density. If only the dense gas is observed, e.g. N_2H^+, even cores which are nominally pinched can appear broader than the dense gas in the rest of in filament.

Moreover, projection effects can reduce the length of a filament and thus increase the apparent line-mass by a substantial factor. This effect is limited by the fact that higher inclined filaments will not resemble a filamentary structure.

Additionally, more cores are observed which are thinner than the average widths of star-forming filaments (Palmeirim et al., 2013; Marsh et al., 2014; Roy et al., 2014), indicating that most filaments have high line-masses. Nevertheless, higher number statics on the local ratio of core-to-filament radius are desirable in order to estimate line-masses.
All in all, our model allows for the following predictions:

- The morphology of cores embedded in filaments is set by the initial line-mass. Filaments with an initial line-mass below half the critical value will develop broad cores. Filaments with an initial line-mass above half the critical value will develop pinched cores.

- For filaments which are embedded in the same constant background pressure, the perturbation growth times for low and high line-masses are drastically different. If all filaments start with similar perturbation strengths we expect only one population of cores to be present, only pinched cores at early times and broad cores at late times.

- Using the FWHM to determine the radius underestimates the extent of high density regions of the filament and thus underestimates the ratio of core to filament radius.

- The phase where the radius of pinched cores is significantly different from the overall filament radius is very short and indicates an imminent collapse due to loss of hydrostatic equilibrium.

8.5 Acknowledgements

We thank the anonymous referee for the valuable input that greatly increased the quality of the paper. AB, MG and SH are supported by the priority programme 1573 "Physics of the Interstellar Medium" of the German Science Foundation and the Cluster of Excellence "Origin and Structure of the Universe". The simulations were run using resources of the Leibniz Rechenzentrum (LRZ, Munich; linux cluster CoolMUC2).

9 Paper IV: Accretion-driven turbulence in filaments - II. Effects of self-gravity

S. Heigl, A. Burkert, M. Gritschneder, 2019, submitted to *Monthly Notices of the Royal Astronomical Society*

We extend our previous work on simulations with the code RAMSES on accretion driven turbulence by including self-gravity and study the effects of core formation and collapse. We show that radial accretion onto filaments drives turbulent motions which are not isotropic but radially dominated. Low accretion rate filaments decay to an equilibrium velocity dispersion which does not differ from their non-gravitational counterparts. Filaments with high mass accretion rates, despite roughly showing the same amount of driven turbulence, continually dissipate their velocity dispersion until the onset of core formation. This difference is connected to the evolution of the radius as it determines the dissipation rate. In the non-gravitational case filament growth is not limited and its radius grows linearly with time. In contrast, there is a maximum extent in the self-gravitational case resulting in an increased dissipation rate. Furthermore, accretion driven turbulence shows a radial profile which is anti-correlated with density. This leads to a constant turbulent pressure throughout the filament. As the additional turbulent pressure does not have a radial gradient it does not contribute to the stability of filaments and does not increase the critical line-mass. However, this radial turbulence does affect the radius of a filament, adding to the extent and setting its maximum value. Moreover, the radius evolution also affects the growth timescale of cores which compared to the timescale of collapse of an accreting filament limits core formation to high line-masses.

Key words: stars:formation – ISM:kinematics and dynamics – ISM:structure

9.1 Introduction

Turbulent motions are a key feature in the highly complex dynamics of the interstellar medium (ISM) as demonstrated by the famous "Larson's Laws" (Larson, 1981). Line observations of molecular clouds show a direct correlation between size and molecular linewidth which is usually interpreted as a consequence of a Kolmogorov-like turbulent cascade from supersonic motions on the scale of a tens of parsec sized molecular cloud down to the sonic point on the scale of parsec sized filaments (Kolmogorov, 1941; Kritsuk et al., 2013; Federrath, 2016; Padoan et al., 2016). As density structures are formed by the collision of supersonic flows in the turbulent cascade, the transition from supersonic to subsonic motions is essential for setting the scale at which turbulence stops to dominate and the first subsonic density structures form.

Dust observations show that filamentary structure is ubiquitous on parsec sized scales in star-forming as well as quiescent molecular clouds and directly associated with core formation for supercritical line-masses (André et al., 2010; Arzoumanian et al., 2011; André et al., 2014). The fact that these supercritical filaments show an increasing supersonic internal velocity dispersion for larger line-masses, has been interpreted as a consequence of their gravitational collapse (Arzoumanian et al., 2013). However, molecular line observations have shown that some filaments are actually made up of bundles of velocity coherent subcomponents in the line-of-sight velocity called fibres (Hacar et al., 2013, 2018) which also form in numerical simulations (Smith et al., 2014; Moeckel and Burkert, 2015; Clarke et al., 2017). While these subcomponents show trans- or subsonic linewidths, here relative motions create supersonic linewidths in spectrally low resolved superposition. Moreover, filaments which do not show any substructure are observed to be inherently subsonic (Hacar and Tafalla, 2011; Hacar et al., 2016b). This motivated the "fray and fragment" scenario (Tafalla and Hacar, 2015) where the formation of fibres is explained by the sweep-up of residual motions in a filament. Together with gravity, these motions concentrate material into subsonic velocity coherent entities in which core fragmentation takes place.

However, in the absence of a driving source, turbulent motions decay on the timescale of a crossing time (Mac Low et al., 1998; Stone et al., 1998; Padoan and Nordlund, 1999; Mac Low, 1999; Mac Low and Klessen, 2004). This timescale can be very short for filaments if one assumes the driving scale is given by the filament diameter. In a first study (Heigl et al. (2018a), hereafter called paper I), we used an external accretion flow motivated by the filaments self-gravity to provide a driving source of turbulence. While we explored the effects of accretion driven turbulence on non self-gravitating filaments, we now take self-gravity and core formation into account. Observationally, accreting material is expected to flow along striations, weak filamentary density enhancements perpendicular to the filaments and aligned with the magnetic field, and have accretion rates of the order of 10-100 $M_\odot$ pc^{-1} Myr^{-1} (Palmeirim et al., 2013; Cox et al., 2016). Independent of their formation process, we show that as long as a filament is embedded in surrounding material, self-gravity leads to a continuous inflow onto the filament which causes the creation of turbulent motions.

In the following sections, we first introduce the basic concepts that we apply to our model (Section 9.2). Thereafter, we discuss the numerical set-up of our simulations (Section 9.3). Then we present our findings (Section 9.4) and discuss the implications for core formation

(Section 9.5). Finally, we summarize our findings (Section 9.6).

9.2 Basic concepts

This section presents the fundamental principles which we use to derive our models. We discuss the theoretical hydrostatic profile of filaments and how filaments behave in an ambient medium. Then we derive expected accretion rates onto filaments motivated by their self-gravity and how the accretion affects their radii. Finally, we present a simple model of how accreted kinetic energy is transformed into turbulent velocities and how they are able to add pressure support.

9.2.1 Hydrostatic equilibrium

We use the isothermal and hydrostatic equilibrium model of a filament with a density profile described by Stodólkiewicz (1963) and Ostriker (1964):

$$\rho(r) = \frac{\rho_c}{\left(1 + (r/H)^2\right)^2} \tag{9.1}$$

where r is the cylindrical radius and ρ_c is its central density. The radial scale height H is given by the term:

$$H^2 = \frac{2c_s^2}{\pi G \rho_c} \tag{9.2}$$

where c_s is the isothermal sound speed and G the gravitational constant. For our simulations we assume that the isothermal gas has a temperature of 10 K. With a molecular weight of $\mu = 2.36$ the isothermal sound speed is $c_s = 0.19\,\mathrm{km\ s^{-1}}$. The critical line mass above which a filament will collapse under its self-gravity is calculated by integrating the profile to $r \to \infty$:

$$\left(\frac{M}{L}\right)_{\mathrm{crit}} = \frac{2c_s^2}{G} \approx 1.06 \cdot 10^{16}\,\mathrm{g\ cm^{-1}} \approx 16.4\,\mathrm{M_\odot\ pc^{-1}}. \tag{9.3}$$

Filaments with less line-mass than the critical value expand as long as there is no outside pressure. If one now assumes the filament is embedded in an ambient medium with a source of external pressure p_{ext}, the filament radius and line-mass are limited and one can introduce the parameter f_{cyl} which is a measure of how close to the critical value the filament is:

$$f_{\mathrm{cyl}} = \left(\frac{M}{L}\right) / \left(\frac{M}{L}\right)_{\mathrm{crit}}. \tag{9.4}$$

It varies from 0 for a non-existing filament to 1, where a filament has exactly its critical line-mass. The radius R of the filament is then given by (Fischera and Martin, 2012):

$$R = H \left(\frac{f_{\mathrm{cyl}}}{1 - f_{\mathrm{cyl}}}\right)^{1/2}. \tag{9.5}$$

Together with the relation between the central density ρ_c and the density on the boundary of the filament,

$$\rho_c = \frac{\rho(R)}{(1 - f_{\rm cyl})^2}, \tag{9.6}$$

one can write the radius as function of the boundary density:

$$R = \left(\frac{2c_s^2}{\pi G \rho(R)} \left(f_{\rm cyl}(1 - f_{\rm cyl}) \right) \right)^{1/2}. \tag{9.7}$$

For a given boundary density, the radius has a maximum at $f_{\rm cyl} = 0.5$ with a symmetric drop-off to zero at $f_{\rm cyl} = 0.0$ and $f_{\rm cyl} = 1.0$. The boundary density $\rho(R)$ depends on the outside pressure and thus on the mechanism responsible for the pressure. One possible source of pressure is the thermal pressure of the surrounding medium itself. If the density on the outside of the surface is given by $\rho_{\rm ext}$ and the medium can be assumed to be isothermal with sound speed c_s, the pressure acting onto the surface is:

$$p_{\rm ext} = \rho_{\rm ext} c_s^2. \tag{9.8}$$

If both, the filament and the surrounding gas, have the same temperature then the boundary density $\rho(R)$ and the density of the surrounding gas are the same. Different temperatures however, lead to a jump in density in order to establish hydrostatic equilibrium.

9.2.2 Filament accretion

Another possible source of outside pressure is accretion of material onto the filament. We are particularly interested in accretion by the gravitational potential of the filament itself. The gravitational acceleration of a cylindrical distribution of mass with a given line-mass M/L is (Heitsch et al., 2009):

$$a = -\frac{2GM/L}{r}. \tag{9.9}$$

The potential energy that a gas parcel with mass m loses in free-fall when starting with zero velocity at a distance R_0 and accreting to the filament radius R is given by integrating the acceleration over r:

$$E_{\rm pot} = 2Gm(M/L) \ln\left(\frac{R_0}{R}\right) \tag{9.10}$$

This leads to the accretion velocity v_a at the surface R in the case of cylindrical free-fall:

$$\begin{aligned} v_a &= 2\sqrt{G(M/L)\ln\left(\frac{R_0}{R}\right)} \\ &= 1.1 \text{ km s}^{-1} \left(\frac{M/L}{16.4 \text{ M}_\odot \text{ pc}^{-1}} \right)^{1/2} \left(\frac{\ln(R_0/R)}{\ln(100)} \right)^{1/2}. \end{aligned} \tag{9.11}$$

Assuming a reasonable filament with a radius of order 0.1 pc and a large region of gravitational influence on the scale of a molecular cloud (a factor of a hundred times its own radius) allows us to estimate an upper limit on the accretion velocity. A filament at 10 K needs

a line mass several times larger than the critical line-mass to achieve an inflow velocity of even Mach 10.0. In our simulations, we set the inflow velocity to a fixed value at the inflow boundary. As the simulated domain is relatively small compared to the filament itself and the filament is not massive enough to accelerate accreting gas over the time it takes to reach the filament, we can assume a constant accretion rate set by the radius of the inflow region R_0 and the density at that radius ρ_0:

$$\frac{\dot{M}}{L} = 2\pi\rho_0 R_0 v_a. \tag{9.12}$$

This leads to a time-independent density profile outside of the filament,

$$\rho(r) = \rho_0 \frac{R_0}{r} \tag{9.13}$$

with the outside density at the filament radius R being

$$\rho_{\rm ext} = \rho_0 \frac{R_0}{R}. \tag{9.14}$$

If the inflow onto the filament is fast enough, ram pressure will dominate over the isothermal boundary pressure. Comparing to Equation 9.8, this is the case if the inflow velocity is greater than the isothermal sound-speed. The total external pressure is then given by

$$p_{\rm ext} = \rho_{\rm ext}\left(c_s^2 + v_a^2\right) = \frac{\rho_0 R_0 c_s^2\left(1 + \mathcal{M}_a^2\right)}{R}. \tag{9.15}$$

where $\mathcal{M}_a$ is the Mach number of the accretion flow. The external pressure is balanced by the internal pressure of the filament at the position of the boundary. If there are turbulent motions inside the filament, the internal pressure is not only given by the isothermal part but also has an additional turbulent contribution. The pressure equilibrium can then be written as:

$$\rho(R) c_s^2\left(1 + \mathcal{M}_t^2\right) = \frac{\rho_0 R_0 c_s^2\left(1 + \mathcal{M}_a^2\right)}{R}, \tag{9.16}$$

where $\mathcal{M}_t$ is the Mach number of the turbulent motions within the filament at the boundary. Solving for the boundary density and inserting the result into Equation 9.7 gives the radius of a filament with an additional accretion pressure and internal turbulent motions as:

$$R = \frac{2c_s^2\left(1 + \mathcal{M}_t^2\right)}{\pi\rho_0 R_0 G\left(1 + \mathcal{M}_a^2\right)}\left(f_{\rm cyl}(1 - f_{\rm cyl})\right). \tag{9.17}$$

Although the radius evolution has now lost its dependence on the square root, the general shape of the curve remains unchanged. There still is a maximum at $f_{\rm cyl} = 0.5$ which only differs in its maximum value. Note that for $G \to 0$, Equation 9.17 transforms to the non-gravitational counterpart of Equation 9.39.

9.2.3 Accretion driven turbulence

The analytical prediction of accretion driven turbulence is based on the energy budget of accreted kinetic energy being converted to turbulent energy and its subsequent dissipation. Following Elmegreen and Burkert (2010) and Klessen and Hennebelle (2010), the change in turbulent energy $\dot{E}_t$ is given by the energy accretion rate $\dot{E}_a$ and the energy dissipation $\dot{E}_d$:

$$\dot{E}_t = \dot{E}_a - \dot{E}_d = (1 - \epsilon)\dot{E}_a. \tag{9.18}$$

The energy accretion rate is given by the accreted kinetic energy

$$\dot{E}_a = \frac{1}{2}\dot{M}v_a^2 \tag{9.19}$$

and the energy loss through dissipation by

$$\dot{E}_d \approx \frac{E_t}{\tau_d} = \frac{1}{2}\frac{M\sigma^3}{L_d}, \tag{9.20}$$

where the turbulent energy is expected to decay on the timescale of a crossing time:

$$\tau_d \approx \frac{L_d}{\sigma}. \tag{9.21}$$

Elmegreen and Burkert (2010) also introduce the efficiency factor ϵ as fraction of accreted energy used to sustain the turbulent motions:

$$\epsilon = \left|\frac{\dot{E}_d}{\dot{E}_a}\right|. \tag{9.22}$$

Heitsch (2013) used this approach together with a driving scale of the filament diameter $L_d = 2R$ to calculate the velocity dispersion in dependence of inflow velocity:

$$\sigma = \left(2\epsilon R(t) v_a^2 \frac{\dot{M}}{M(t)}\right)^{1/3}. \tag{9.23}$$

For a linear evolution in time of the radius and mass, this relation predicts a constant level of velocity dispersion which is determined by the inflow velocity. While our simulations do find an equilibrium in velocity dispersion, we cannot match the scaling of the prediction. In contrast, our simulations show a linear relation of the density weighted velocity dispersion and inflow velocity as shown in paper I. Note that any model for the scaling of velocity dispersion and inflow velocity or even an equilibrium is directly tied to the evolution of the radius. This is due to the fact that the energy dissipation rate depends on the crossing time. Rewriting the energy dissipation rate as

$$\dot{E}_d = \frac{1}{2}\frac{M\sigma^3}{L_d} = \frac{1}{2}\frac{\dot{M}\sigma^3 t}{2R(t)}, \tag{9.24}$$

all terms in Equation 9.18 depend on the mass accretion rate and can be simplified to

$$\sigma^2 = \alpha v_a^2 - \frac{\sigma^3 t}{2R(t)}. \tag{9.25}$$

Here we introduce the factor α to account for energy losses in the isothermal oblique accretion shocks at the surface of the filament where the turbulent motions are created. In order to reach an equilibrium velocity dispersion, all terms must be independent of time. This is only the case under two conditions. Either the radius grows linear in time as then the dissipation rate is constant or the radius evolves superlinear in time for which the last term vanishes at large timescales. This explains why we have an equilibrium in the non self-gravitational case as we find a linear time evolution of the radius. We revisit the equilibrium level and give an explanation for the scaling in the appendix. In the case including self-gravity discussed in this paper, the radius evolves as a complicated function of time (Equation 9.7) and core formation could impact the velocity dispersion substantially.

9.2.4 Effect of turbulence on radial stability

An important question that we want to answer is if turbulence can increase the stability of filaments. Previous studies modeled the effects of turbulence on the equation of state either by logatropic models based on the scaling relations of molecular clouds (Larson, 1981) where $p_{\rm turb} \sim \ln \rho$ (Lizano and Shu, 1989; Gehman et al., 1996a,b; McLaughlin and Pudritz, 1997; Fiege and Pudritz, 2000a), or negative index polytropes, where the polytropic exponent is between zero and one, as is the case for Alfénic turbulence (Maloney, 1988; Fatuzzo and Adams, 1993; McKee and Zweibel, 1995). One could also assume that isotropic turbulence behaves as an additional component to the thermal pressure and add it to the scale height:

$$H^2 = \frac{2c_s^2\left(1 + \mathcal{M}_t^2\right)}{\pi G \rho_c}. \tag{9.26}$$

Integrating over the filament profile as done for Equation 9.3, leads to an adjustment of the critical line-mass:

$$\left(\frac{M}{L}\right)_{\rm crit} = \frac{2c_s^2\left(1 + \mathcal{M}_t^2\right)}{G}. \tag{9.27}$$

Thus, turbulence would be able to increase the maximum line-mass a filament could sustain. Note that this adjustment does not affect the formula for the radius in Equation 9.17 as the additional turbulent term not only enters directly over the scale height, but also over $f_{\rm cyl}$ and thus cancels out. However, an increased maximum line-mass would lead to an offset to the point of the maximum radial extent from the value 0.5 if plotted against the unadjusted maximum thermal line-mass. In addition, an increased stability would lead to a delayed collapse of cores in a filament as long as they do not dissipate their turbulence on a much faster timescale. Therefore, we will also directly test the impact of turbulence by investigating the radial evolution and core collapse in filaments.

9.3 Numerical set-up

All our simulations were executed with the code RAMSES (Teyssier, 2002) which uses a second-order Godunov scheme to solve the conservative form of the discretised Euler equations on an Cartesian grid. For our runs we applied the MUSCL scheme (Monotonic Upstream-Centred Scheme for Conservation Laws, van Leer (1977)) together with the HLLC-Solver (Harten-Lax-van Leer-Contact (Toro et al., 1994)) and the multidimensional MC slope limiter (monotonized central-difference (van Leer, 1979)).

Our simulations cannot resolve the evolution of the molecular cloud and the detailed velocity dispersion inside the filament at the same time. Therefore we focus on a preset converging radial flow onto a self-gravitating, isothermal filament in the centre of the box. We use a 3D box with a periodic boundary condition in the x-direction and outflow boundaries in the other two directions. As RAMSES has no radial boundary we define a cylindrical inflow zone with a radius of the boxsize and a thickness of two cells from which we drive a radial inflow onto the central x-axis of the box. The inflow zone has a fixed density and inflow velocity which is continuously renewed every timestep. The inflow leads to a build-up of a filament with a radius which is limited by gravity. The periodic boundary prevents the filament from collapsing along its axis and prohibits the loss of turbulent motions. As the radius does not grow to large values, we can often optimize the resolution of our simulations and use a boxsize of 0.4 pc which is half as large as the standard boxsize used in paper I. We adjust the outer boundary density to set the mass accretion rate and for most of the simulations we use the same rate as in paper I of $\dot{M}/L = 16.8\,\mathrm{M_\odot\,pc^{-1}\,Myr^{-1}}$ by doubling the density in the inflow region to a value of $\rho_0 = 7.84 \cdot 10^{-22}\,\mathrm{g\,cm^{-3}}$, which corresponds to about $2 \cdot 10^2$ particles per cubic centimeters for a molecular weight of $\mu = 2.36$. For simulations where we show the equilibrium level of turbulence, we reduce the density in the inflow region in order to have enough time to allow the equilibrium to settle without the filament collapsing. We also use the density in the inflow region as a mean density inside of the box together with a random perturbation of 50%. The gas is set to be isothermal with a temperature of 10 K and the cells surrounding the inflow zone are given the same constant density and do not affect the simulation.

The minimum resolution is set to 256^3, which at this boxsize is equivalent to the minimum resolution used in paper I. We employ adaptive mesh refinement (AMR) in order to resolve higher densities. Over the evolution of the simulation the filament stays unrefined and AMR only plays a role in the high density cores. The maximum resolution is set to 512^3 and in such a way that we terminate the simulation as soon as we do not fulfill the Truelove criterion for the maximum density within a factor of 16 in all simulations (Truelove et al., 1997).

9.4 Simulations

As in paper I we study the velocity dispersion and radius of the filament. We show the typical evolution of a simulation in Figure 9.1 where we plot slices through the central axis of the filament. As the filament grows in mass it first expands, reaches a maximum in radius and decreases again in radius. Towards reaching the critical line-mass of $f_{\mathrm{cyl}} = 1.0$, usually one or more cores can be seen to condense inside the filament. Our simulation ends when we

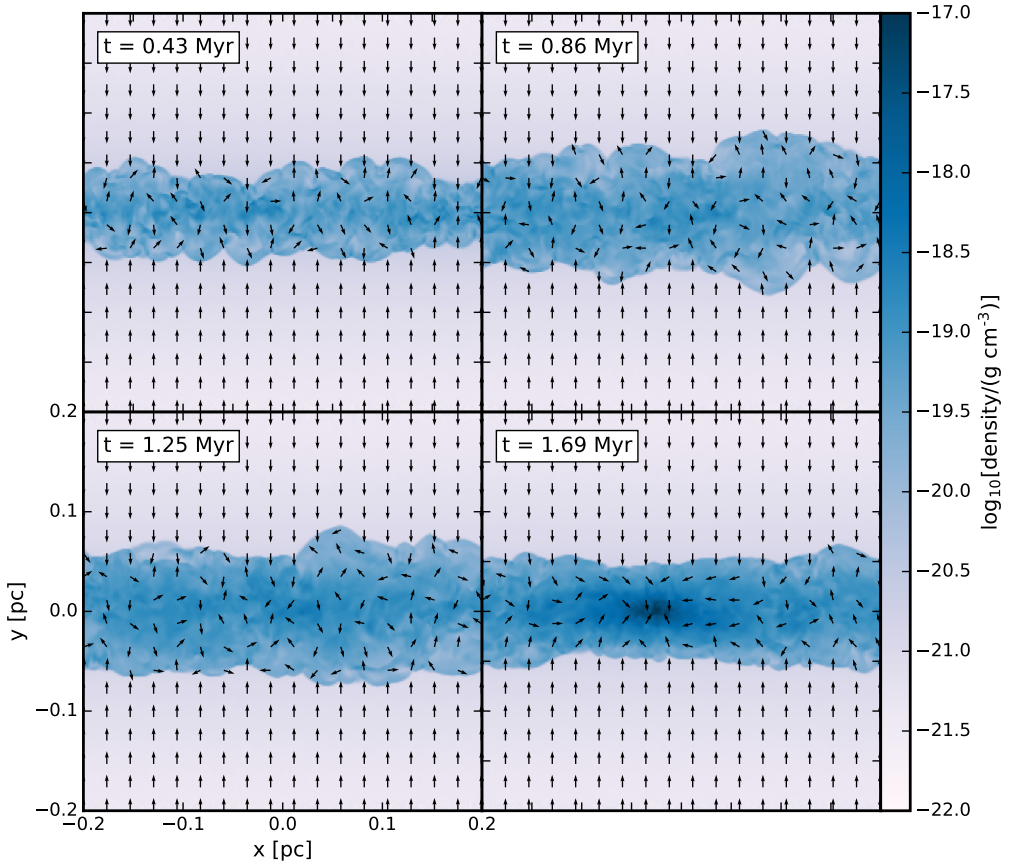

Figure 9.1: Evolution of an accreting filament with an inflow velocity of Mach 6.0 and an accretion rate of 8.4 $M_\odot$ pc^{-1} Myr^{-1}. The image shows four slices at different evolutionary times through the centre of the filament. The cylindrical accretion induces obvious turbulent motions until a core is formed where the dominant motions change to an accretion onto the core.

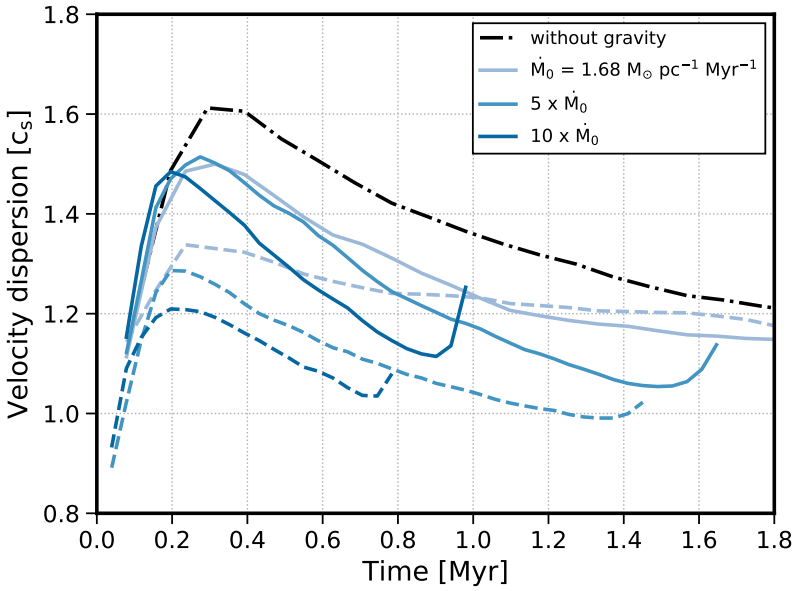

Figure 9.2: Evolution of the velocity dispersion for a Mach 6.0 inflow with varying accretion rate. We include a filament without gravity given by the dashed-dotted line as a reference case. The solid lines show filaments with different accretion rates. The dashed lines are the same initial values but with a pre-existing 1/r profile inside the box which smooths out the initial accretion shock.

reach the maximum allowed density due to the Truelove criterion of around 10^{-17} g cm^{-3} or 10^7 particles per cubic centimeter where we would need to insert a sink particle. As the subsequent core collapse happens on much shorter timescales than the evolution of the filament and we do not model expected feedback from protostellar outflows, we terminate our simulations as soon as we reach this threshold.

9.4.1 Evolution of the velocity dispersion

In order to calculate the velocity dispersion of the filament gas, we need to distinguish it from the accretion flow. Due to the formation of an accretion shock at the filament boundary, there is a clear jump in density and a drop in radial velocity of the material. As the density inside the filament still varies considerably, we use the change in radial velocity as an indicator of filament material.

For the determination of the velocity dispersion in paper I, we used the standard deviation of the density weighted velocity:

$$u_i = \frac{m_i v_i}{\langle m \rangle} = \frac{N m_i v_i}{\sum m_i} = \frac{N m_i v_i}{M} \tag{9.28}$$

where N is the total number of cells and $\langle\rangle$ indicates the mean of a distribution. A more common way of defining the velocity dispersion of gas with zero mean velocity is by calculating

the total kinetic energy in the gas:

$$\sigma = \sqrt{\frac{1}{M}\sum_i m_i v_i^2}. \tag{9.29}$$

In the limit that the density is constant, both ways of calculating the velocity dispersion are equivalent as the velocity mean is zero and the standard deviation then is given by

$$\sigma_u = \sqrt{\langle u^2\rangle - \langle u\rangle^2} = \sqrt{\frac{N^2\sum_i m_i^2 v_i^2}{NM^2}} = \sqrt{\frac{m_i\sum_i v_i^2}{M}} \tag{9.30}$$

where we use the definition of the total mass $M = Nm_i$. As the density inside a filament is not constant in our simulations, we expect different measured values of the velocity dispersions for the different methods. Especially for large values of turbulence the differences should increase as more and more shocks form inside the filament with larger density contrasts. For this study we use the method of the total kinetic energy (Equation 9.29).

In paper I we found that without self-gravity the velocity dispersion settles to a constant equilibrium value over time. This behavior was also found in a similar study by Clarke et al. (2017) which used the Smooth Particle Hydrodynamic code GANDALF (Hubber et al., 2018) and which included gravity but in addition also an initially perturbed velocity field. We want to test if it is possible to reproduce the transition to equilibrium in RAMSES if we include self-gravity. For very low mass accretion rates, there should be no difference to the non self-gravitational case as this would be just the limit of a zero mass accretion flow. This can be seen in Figure 9.2, where we show the evolution of the velocity dispersion for the same inflow velocity of Mach 6.0 but for different mass accretion rates. The black dashed-dotted line is the evolution of the velocity dispersion of the non-gravitational case and ends in the equilibrium value presented in paper I, where we also show that the equilibrium continues on for much longer timescales. The solid light blue curve shows a filament with an accretion rate which is ten times lower than that of the reference case. Its velocity dispersion ends at the same equilibrium value, within the usual spread of simulations, as the non-gravitational reference case. It's accretion rate is essentially so low that the total mass build-up in the filament is not enough for it to be affected by gravity.

This behavior changes for a filament with an accretion rate of five times the original rate, given by the medium blue line. It shows no such equilibrium value. At all times its velocity dispersion is less than the one for a low accretion rate and continually drops off until core formation sets in where it increases due to collapse motions onto the core. The same is true for even higher accretion rates shown by the solid dark blue line which we use as our fiducial case for further analysis. The filament accretes mass with ten times the original rate and therefore as fast as the non-gravitational case. Here, the velocity dispersion is even lower and core formation sets in earlier.

We also test if our initial condition influences the evolution of the velocity dispersion. Therefore, we change our initial density profile in the box from a flat distribution to a $1/r$ profile, consistent with Equation 9.13 as if the accretion flow has already been established. The corresponding lines are shown in Figure 9.2 by the dashed lines. We see that it does not

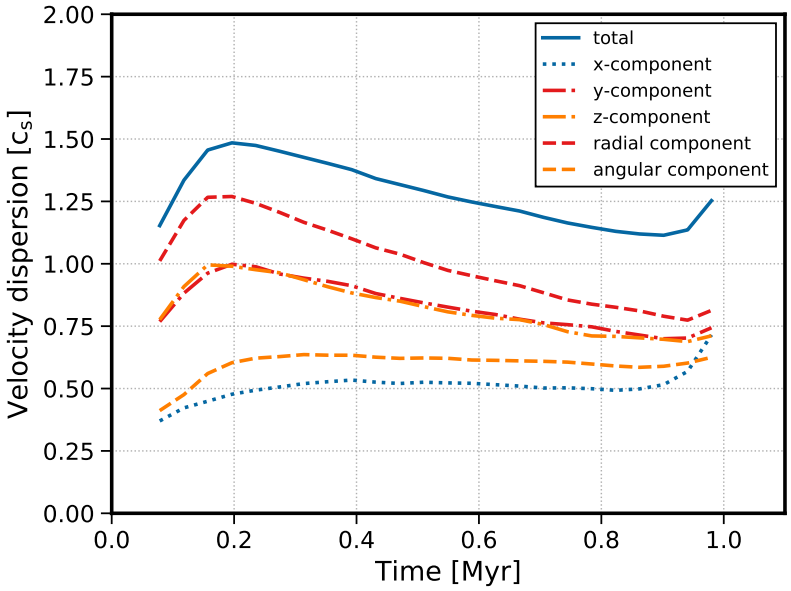

Figure 9.3: Evolution of the velocity dispersion of all components for a Mach 6.0 inflow with mass accretion rate of 16.8 $M_\odot$ pc^{-1} Myr^{-1}. The total velocity dispersion is shown by the blue solid line, the Cartesian components in y and z direction by the red and orange dashed-dotted lines and the cylindrical components in radial direction and in angular direction by the dashed red and orange lines respectively. The x-component, which is valid for both geometries is given by the blue dotted line.

influence the equilibrium level of the low accretion rate case but does remove the initial spike in velocity dispersion. For higher accretion rates the initial value from where the velocity dispersion decays is lower and therefore it drops off to lower values.

We also split up the velocity dispersions into its cylindrical components by splitting the respective velocities into the x-component along the filament axis, the azimuthal and the radial velocities. Their evolution is shown in Figure 9.3 together with the Cartesian y and z component of the velocity dispersion. One can see that the turbulent motions are dominated by the radial velocity component and also only decay in the radial component while the other two stay constant over time. This is due to the difference in crossing times. Not only is the initial radial dispersion more than twice as large as the other components but it has also the lowest driving scale, with the azimuthal driving scale being a factor π larger and the driving scale along the filament being the boxsize in theory.

Therefore, albeit the equilibrium velocity dispersion is robust for filaments which are not dominated by gravity, gravitational collapse does influence the velocity dispersion by reducing it over time until the point of core collapse where collapse motions increase it again. This result is in agreement with Equation 9.25, as for the non self-gravitational case, the radius evolves linearly, setting a constant dissipation rate and allowing for the velocity dispersion to settle to an equilibrium value. However, for self-gravitational filaments the radius has a maximum value and decreases again for large line-masses. This leads to a constant change in dissipation rate and thus no equilibrium can be achieved.

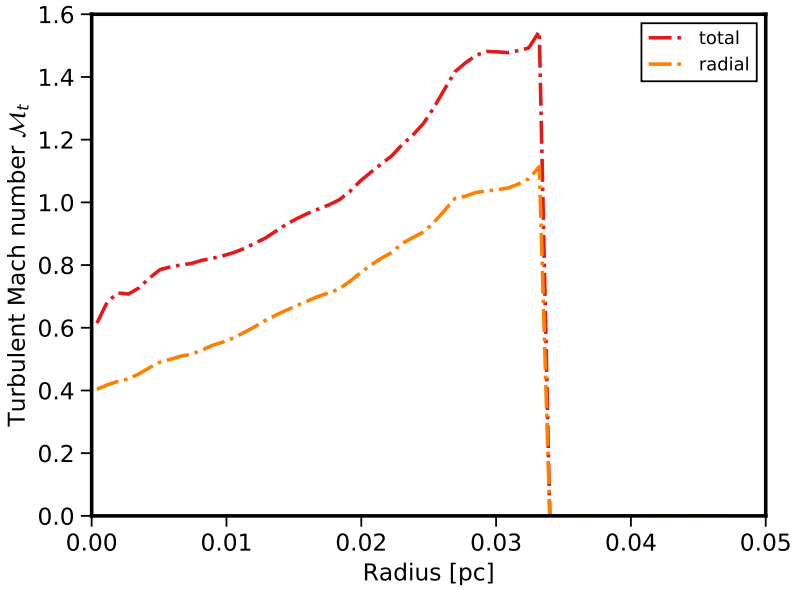

Figure 9.4: Turbulent Mach number averaged in radial bins of our fiducial filament with a Mach 6.0 accretion flow and an accretion rate of 16.8 $M_\odot$ pc^{-1} Myr^{-1} measured at 0.5 Myr which corresponds to time where the filament reaches its maximum radius. The total velocity dispersion is shown by the red dashed-dotted curve, the radial velocity dispersion by the orange dashed-dotted line.

9.4.2 Radial evolution

We showed that in the non self-gravitational case, the radius evolves linearly in time and is supported by the radial turbulent motions (see also Appendix A). According to Equation 9.7, the radial expansion is limited in the self-gravitational prediction, reaching a maximum at $f_{\rm cyl} = 0.5$, followed by a subsequent decrease. In order to assess the impact of turbulent motions on the radial extent, we compare Equation 9.17 to the measured radius. If turbulence has an impact on the scale height, one would see an off-set in the radius maximum. This off-set can be substantial, e.g. a factor of two in the case where the velocity dispersion is larger than the order of the sound speed. Thus, by measuring the radial evolution, we can not only test the impact of turbulence on the radius but also if it acts as additional pressure support.

Before we compare the measured radius to Equation 9.17, we have to determine the turbulent Mach number at the filament boundary, as $\mathcal{M}_t$ in the above equation is not the total Mach number, but the one determining hydrostatic equilibrium at the boundary. In order to do that, we show the radial profile of the turbulent Mach number in Figure 9.4. As the filament is very thin we increase the resolution by re-simulating our fiducial case with a four times smaller box with a size of 0.1 pc. In order to keep the accretion rate constant, we increase the inflow density by a factor of four. We take each slice of the filament, split the domain in radial bins with a width of 4 cells, subtract the mean velocity of the bin, determine the total kinetic energy in the bin and finally average over all slices along the filament. The Mach number of the total turbulence is shown in red and the Mach number of the radial turbulence in orange. As one can see, the velocity dispersion is not constant throughout the filament, but is minimal at

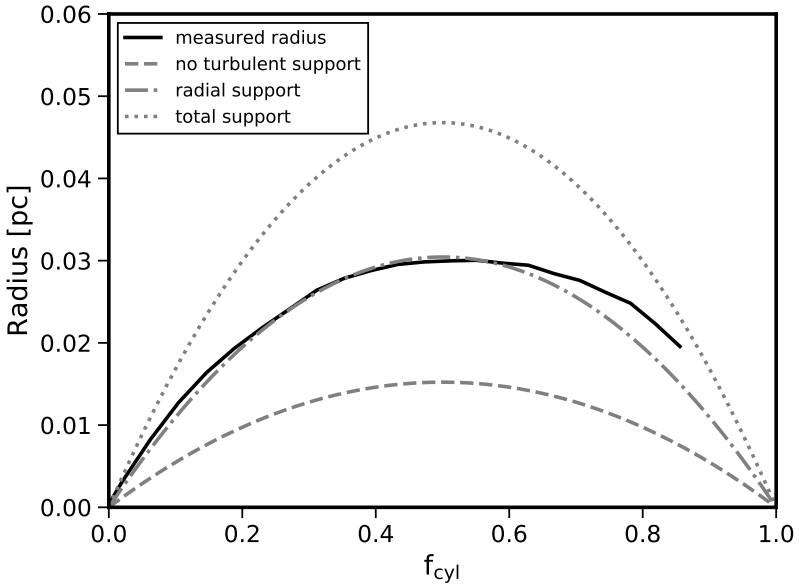

Figure 9.5: Evolution of the measured average radius of a filament with a Mach 6.0 accretion flow and an accretion rate of 16.8 $M_\odot$ pc^{-1} Myr^{-1} compared to the average line-mass. The curve ends as soon as the core reaches the critical line-mass and collapses. The analytical evolution of the radius (Equation 9.17) without turbulent pressure contribution is shown by the dashed line, with radial turbulence support as the black dashed-dotted line and with total turbulence support as the black dashed-dotted line.

the filament centre and has its maximum at the boundary. This shows how turbulent motions are stirred at the surface of the filament and dissipate in the higher density layers. In order to calculate the predicted radius we need to use the boundary value. In principle, one would need to determine this value at every time step but we do not see a significant change and it stays close to constant over time. We use both boundary values, the total and the radial Mach number, in Equation 9.17 and plot the predicted radius as well as the average measured radius against the average line-mass in Figure 9.5. The measured radial evolution is shown by the solid black line, the case of no turbulent support as the dashed curve, the case of radial turbulent pressure support as the dashed-dotted line and the case of total turbulent pressure support as the dotted curve. The measured radius follows closely the radial turbulent support model. Note that the same is true in the non self-gravity case in Figure 9.A.1. Only the radial motions contribute to the hydrostatic equilibrium. One can see that the curve reaches its maximum value at about $f_{\rm cyl} = 0.5$. It is important to note, that while turbulence does influence the maximum radius, it does not, or at most only marginally, affect the maximum line-mass and thus the point of where the radius reaches its maximum. According to Equation 9.27, we would expect a maximum line-mass of twice the isothermal maximum mass for an inflow velocity of Mach 6.0. Thus, the radial evolution should peak at a unadjusted value of about $f_{\rm cyl} = 1.0$. Therefore, there is no indication of radial pressure support against gravity by turbulence as is consistent with the radial collapse discussed in the next section.

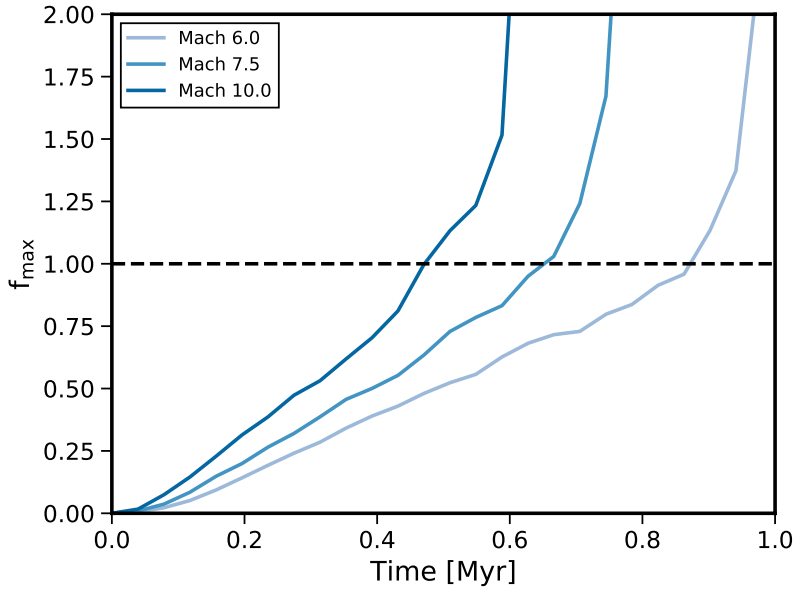

Figure 9.6: Time evolution of the maximum line-mass for different inflow Mach numbers. Due to the increasing mass in the filament, the maximum line-mass grows linearly. As soon as it reaches the unmodified critical line-mass at a value of 1.0, the core at this position collapses radially as can be seen in the non-linear evolution.

9.4.3 Core formation

We showed that turbulence does not have an effect on where the radial evolution has its maximum with respect to the filament line-mass. Therefore, we assume that there is no additional support against radial collapse which we test by analysing the growth of the forming core and whether or not it collapses at the critical line-mass. We plot the line-mass at the position of the core against time in Figure 9.6. In Heigl et al. (2016) we showed that the radial collapse of the core is visible in the non-linear evolution of the line-mass. If turbulence indeed plays a role for the stability of a filament, we expect an offset from $f_{\rm cyl} = 1.0$ with respect to the line-mass growth change from linear to non-linear. If we adapt Equation 9.27, we predict a shift in the critical line-mass to at least double the usual value for turbulent Mach numbers of the same order as the sound speed. As one can see from the form of the curves, a non-linear evolution sets in as soon as the local line-mass at the position of the core exceeds the critical line-mass determined without turbulent support. This shows again that turbulence in our simulations does not have a supporting effect on the line-mass, consistent with the findings of the radial evolution.

9.4.4 Why is there no pressure support?

In order to determine why there is no pressure support, we analyse the pressure profile of our high resolution fiducial filament as we did for the turbulent Mach number in Figure 9.4. We distinguish between cells that are part of the filament and others which trace the accretion flow by using the same method of determining the filament radius by the jump in radial

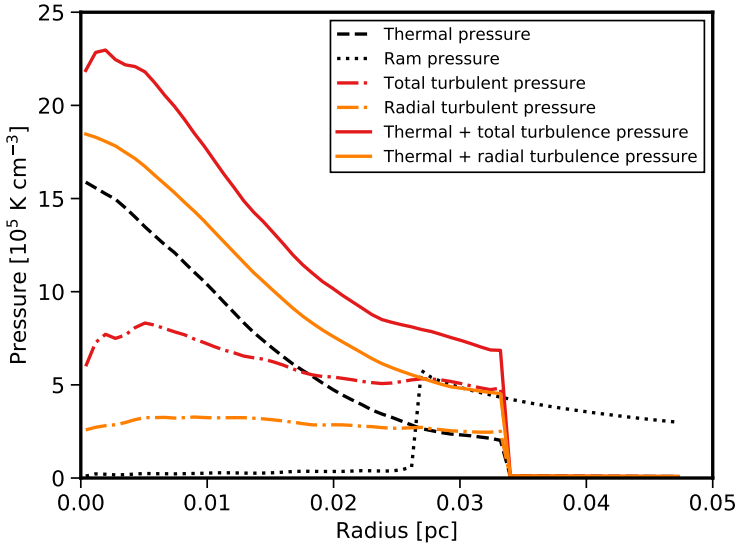

Figure 9.7: The different pressure contributions averaged in radial bins of our fiducial filament with an accretion flow of Mach 6.0 and an accretion rate of 16.8 $M_\odot$ pc^{-1} Myr^{-1} measured at 0.5 Myrs. The black dashed line shows the thermal pressure of the filament gas and the black dotted line the ram pressure in the accretion flow. The turbulent pressure is given by the dashed-dotted lines and the sum together with the thermal pressure to show the total filament pressure by the solid lines: for the total velocity dispersion in red and for the radial velocity dispersion in orange.

velocity as mentioned above. As the filament radius is not uniform, we get an overlap region where cells of both regions are present. We calculate the respective pressures with cells of the respective region. For the turbulent pressure we use only cells tracing the filament and determine the average density and kinetic energy in each bin i from which we calculate the pressure as $\langle \rho_i \rangle \sigma_i^2$ and then average over all slices. For the ram pressure we determine the average density and radial velocity in the accretion flow and calculate the ram pressure as $\langle \rho_i \rangle \left\langle v_i^{\rm rad} \right\rangle^2$ and then average over all slices. The resulting pressure components are shown in Figure 9.7. The thermal pressure is given by the black dashed line, the ram pressure by the black dotted line, the total and radial turbulent pressure by the red and orange dashed-dotted line respectively and the combined thermal plus turbulent pressure by the respective solid line. We already showed in the last subsection that the radial turbulent motions provide the hydrostatic equilibrium together with the ram pressure. This can be seen also in the pressure directly, where the combined thermal plus radial turbulent pressure given by the orange solid line exactly balance the ram pressure in the overlap region. In contrast, the total turbulent pressure provides a pressure which is too large for an equilibrium. Moreover, one can see that the accretion driven turbulence, given by the dashed-dotted lines, distributes itself over the filament in a way that the turbulent pressure component is constant throughout the filament. This leads to the fact that the pressure profile of the filament is only shifted to a larger pressure due to turbulence by a constant value. One can interpret this as a shift in the

isothermal equation of state to include a constant offset:

$$p = \rho c_s^2 + p_0, \tag{9.31}$$

which does not change the solution of the isothermal, cylindrical Lane-Emden equation, as the hydrostatic equilibrium depends only on the gradient of the pressure. The scaling of the profile does not change and thus the maximum line-mass remains the same. As the boundary pressure of the filament is larger, it extends further into the surrounding medium. Note that turbulence thus can influence the absolute value of the scale height by setting the central density, but it is not added as isotropic pressure contribution to the sound speed.

9.5 Implications for core formation

The radial velocity dispersion at the filament boundary amounts to about 0.85 times the total equilibrium velocity dispersion of the non self-gravitational case independent of the inflow Mach number. Thus, we can calculate the theoretical radius of the filament at every line-mass and therefore we can make predictions on the fragmentation length and time-scales of cores forming in an accreting filament. Small density perturbations in the linear regime along the filament axis of the form:

$$\rho(r, x, t) = \rho_0(r)\,(1 + \epsilon \exp(ikx - i\omega t)) \tag{9.32}$$

will grow for values of k where the dispersion relation $\omega^2(k)$ is negative. Here ρ_0 is the unperturbed initial density, $k = 2\pi/\lambda$ is the wave vector with λ being the perturbation length, x is the filament axis, $\omega = 1/\tau$ is the growth rate with τ being the growth timescale, t the time variable and ϵ the perturbation strength. The fastest growing, or dominant, fragmentation length scale $\lambda_{\rm dom}$ as well as the growth timescale of the dominant mode $\tau_{\rm dom}$ depend on the current line-mass of the filament and are given by the pre-calculated (Nagasawa, 1987) and interpolated values in Fischera and Martin (2012), shown by their table E.1. We use these values to determine the length scale of the fastest growing mode at every line-mass for the same mass accretion rate but for different inflow Mach numbers as shown in Figure 9.8. As one can see, the dominant fragmentation length changes over the evolution of the line-mass. At the boundary values it vanishes to zero and it has a maximum at about $f_{\rm cyl} = 0.4$. The figure is self-similar for different mass accretion rates, with a lower rate leading to a larger dominant fragmentation length. For a constant accretion rate, the fragmentation length does not vary much for different inflow Mach numbers. Only for large and for very low inflow Mach numbers, the fragmentation length is slightly larger. As the dominant fragmentation length constantly changes as $f_{\rm cyl}$ grows, it is hard to make predictions of what will be the final distance between forming cores. But the curves have a maximum which allows us to make a prediction about the minimum number of cores that will form. For instance, a filament with an inflow Mach number of 4.0 and a length of 0.2 pc will form at least one core. As soon as the first core forms, the further evolution of the filament is also influenced by the gravitational attraction of the core. This makes the formation of additional cores even more unpredictable.

We can get some further constrains by calculating the time a core needs to double its local line-mass and therefore clearly forms a visible over-density if it would continue to grow on

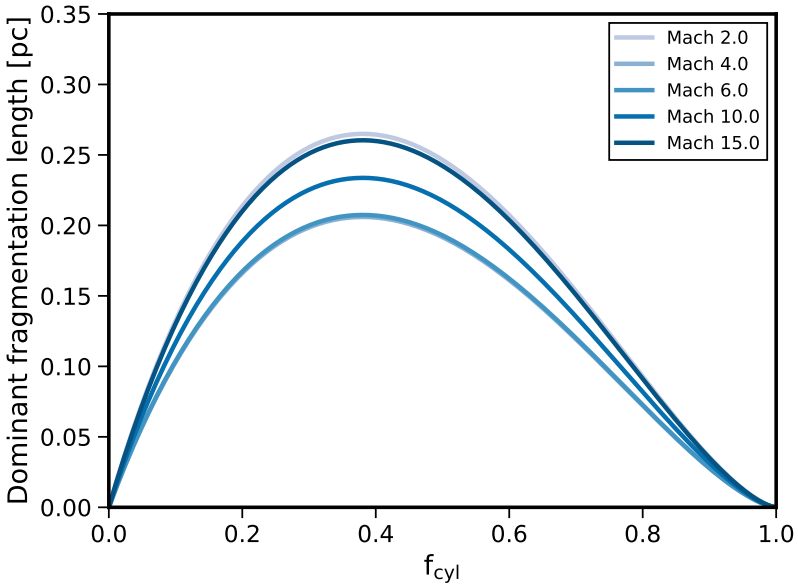

Figure 9.8: The dominant fragmentation length as a function of the line-mass for the same mass accretion rate of 16.8 $M_\odot$ pc^{-1} Myr^{-1} but for different inflow Mach numbers.

the fastest growing mode and compare it to the time, the overall filament needs to reach the critical line-mass and to collapse. As a core only condenses out of the filament if it can grow considerably in mass and the fastest growing mode is constantly changing, this time threshold gives the best case scenario of a core being able to form. If it takes longer to double the local line-mass than the filament takes time to collapse, the core will not have enough time to grow and either the fastest growing mode will change too fast or the filament will collapse before it can form. Note that this is the maximum limit in line-mass a core forming in a filament with a line-mass below 0.5 can reach in the non-linear phase as then all mass from the under-dense evacuating region has been transferred to the core. It only can reach larger local line-masses in the non-linear phase where it could accrete mass from all over the filament (Heigl et al., 2016). In filaments with line-masses larger than 0.5, the core collapses radially as soon as it reaches the critical line-mass locally and thus fixes the position of the core. Therefore, in reality the core formation timescales for large line-masses are shorter as they reach the critical line-mass before they double their local line-mass.

The result of this calculation is shown in Figure 9.9. The filament is accreting mass at a constant rate, thus the time for it to reach the maximum line-mass is decreasing linearly as shown by the black dashed line. To determine the time a core needs to double its local line-mass, one only has to solve for the time t where the dominant growth of the line-mass reaches a value of two times the initial line-mass:

$$f_{\rm cyl}^{\rm max}(t) = f_{\rm cyl}^{0}\left(1 + \epsilon \exp(t/\tau_{\rm dom})\right) = 2 f_{\rm cyl}^{0}, \tag{9.33}$$

where $f_{\rm cyl}^{0}$ is the unperturbed line-mass at the beginning of the growth of the respective fastest growing mode. One also has to assume a perturbation strength ϵ which we set to 5%, the

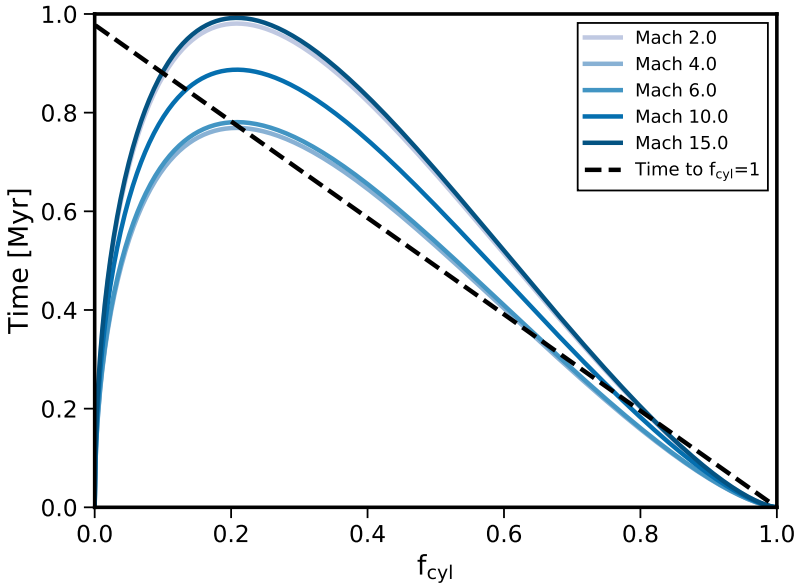

Figure 9.9: The dominant fragmentation time compared to the collapse time of a filament as a function of the line-mass. The dashed line shows the remaining time to reach a value of $f_{\mathrm{cyl}} = 1.0$ compared to the time it takes a growing core to reach the same value at each line-mass. Only at values of $f_{\mathrm{cyl}} \approx 0.7$ and above, cores have time to form before the filament collapses.

typical variation in the line-mass we measure along the filament in the simulations. As one can see, the growth timescale of a core is larger than the filament collapse time for the majority of its evolution. The dominant growth timescale is shorter for large central densities as is the case at very low and high values of f_{cyl} where the filament is centrally concentrated. The upper value of f_{cyl} where the growth time curves intersect the collapse timescale of the filament is approximately where we also typically observe core formation in our simulations. For lower values of f_{cyl} we never see any core formation occurring. We do see local overdensities on very small length scales similar to random noise but no real core forms. This is probably due to the fact that for line-mass values below 0.5, cores cannot collapse in the regime of linear perturbation and further growth is limited due to a limited mass reservoir. As the dominant length scale changes over time, any pre-existing overdensity is washed out. This changes for high line-masses as here the cores form local overdensities which large gravitational attraction suppresses the further change of the dominant mode. The timescale to reach the critical line-mass is very small and the collapse of the core is irreversible.

As in the case of the fragmentation length, the growth timescale is self-similar. A larger mass accretion rate only shortens the growth time as well as the time for the filament to reach the maximum line-mass in the same manner. Note that this relation therefore also holds true for an increasing inflow velocity due to a growing line-mass. This implies that if cores are observed in a filament it is more likely to have a line-mass closer to the maximum line-mass. From the results of Heigl et al. (2018b) which show that cores forming in high line-mass filaments lead to a reduced filament radius at the position of the core, we also expect the

cores to have a thinner morphology than the filament itself.

9.6 Discussion and conclusions

This work presents a numerical study on accretion driven turbulence in filaments. We have shown that accretion flows with expected inflow velocities and observed mass accretion rates can drive relatively fast supersonic motions. However, our model relies on several assumptions.

First of all, our simulations lack magnetic fields which could suppress turbulent motions. Although magnetic fields are thought of channelling accretion flows along striations, density enhancements perpendicular to the filament (Goldsmith et al., 2008; Palmeirim et al., 2013; Cox et al., 2016), they have been shown to stabilise filament against fragmentation depending on the field configuration (Stodólkiewicz, 1963; Nagasawa, 1987; Gehman et al., 1996b; Fiege and Pudritz, 2000b). They can act as an additional pressure support and also suppress motions perpendicular to the field lines. The effects of magnetic fields therefore will be explored in a future paper.

Furthermore, while we do include an initial density perturbation in order to break the symmetry, our accretion flow is very smooth. It could be that accretion is better treated by the infall of clumpy material or even with initial turbulent velocity distributions as in Clarke et al. (2017). Filaments do not form in isolation and driven turbulent box simulations show filaments forming as transient entities (Federrath, 2016). To that end, large scale simulations with realistic inflows in a molecular cloud environment are needed which are out of the scope of this work.

Observations of the massive filament DR21 show an increasing velocity dispersion toward the central axis of the filament (Schneider et al., 2010). While our model shows a decreasing velocity dispersion towards the centre of the filament, one has to take projection effects into account. In mock observations of our models we do not see an obvious increase. However, we do not see any systematic drop of velocity dispersion to the centre of the filament either.

Nevertheless, our simulations all show the lack of turbulent pressure support against radial collapse. This constitutes an interesting case where turbulence does not act as an additional pressure. We can summarise our findings as the following:

- A smooth radial accretion onto filaments drives turbulent motions which are radially dominated and decay over time.
- The turbulent pressure has a radial profile which is anti-correlated to the density as the low density outer layers are easier to stir.
- This leads to a constant turbulent pressure component which does not add radial stability as the stability relies on pressure gradients.
- We predict that cores usually form for higher line-mass in accreting filaments ($f_{\rm cyl} \geq 0.6$) as only then their growth is fast enough to outpace the collapse of the entire filament.

9.7 Acknowledgements

We thank Alvaro Hacar and the whole CAST group for helpful comments and discussions. AB, MG and SH have been supported by the priority programme 1573 "Physics of the Interstellar Medium" of the German Science Foundation and the Cluster of Excellence "Origin and Structure of the Universe". The simulations were run using resources of the Leibniz Rechenzentrum (LRZ, Munich; linux cluster CoolMUC2).

9.A Non self-gravitational radius evolution revisited

While we found a linear relation between the inflow velocity and the equilibrium velocity dispersion in paper I, we could not find a reasonable explanation for the offset of the linear fit. As we have refined our measurement techniques and updated our model, we want to discuss the implications of this study on our previous work.

9.A.1 Radial evolution without self-gravity

As the density inside the filament is constant in the non self-gravitational case, we formerly modeled the radius by the mass accretion rate (Equation 9.12) assuming that the mean density inside the filament is given by the exterior density times the square of the Mach number in an isothermal shock:

$$\langle\rho\rangle_{\rm fil} = \rho_{\rm ext}\mathcal{M}_a^2. \tag{9.34}$$

The mass accretion rate together with the total mass of the filament

$$M = \pi R^2 L \langle\rho\rangle_{\rm fil} = \pi R^2 L \rho_{\rm ext}\mathcal{M}_a^2 = \pi R L \rho_0 R_0 \mathcal{M}_a^2, \tag{9.35}$$

then leads to a radius evolution given by

$$R(t) = \frac{2c_s^2 t}{v_a}. \tag{9.36}$$

While we found a good agreement, this does not take into account the effect of turbulence on the radius. A better model is to consider the pressure equilibrium at the filament boundary, analogous to Equation 9.15, supported internally by the turbulent pressure $\langle\rho\rangle_{\rm fil}\,\sigma^2$ and by the ram pressure $\rho_{\rm ext}v_a^2$ on the outside:

$$\langle\rho\rangle_{\rm fil}\left(c_s^2 + \sigma^2\right) = \rho_{\rm ext}\left(c_s^2 + v_a^2\right). \tag{9.37}$$

This gives the internal mean density

$$\langle\rho\rangle_{\rm fil} = \rho_{\rm ext}\frac{\left(1+\mathcal{M}_a^2\right)}{\left(1+\mathcal{M}_t^2\right)} \tag{9.38}$$

which leads to the radius evolution of

$$R(t) = 2v_a t\frac{\left(1+\mathcal{M}_t^2\right)}{(1+\mathcal{M}_a^2)}. \tag{9.39}$$

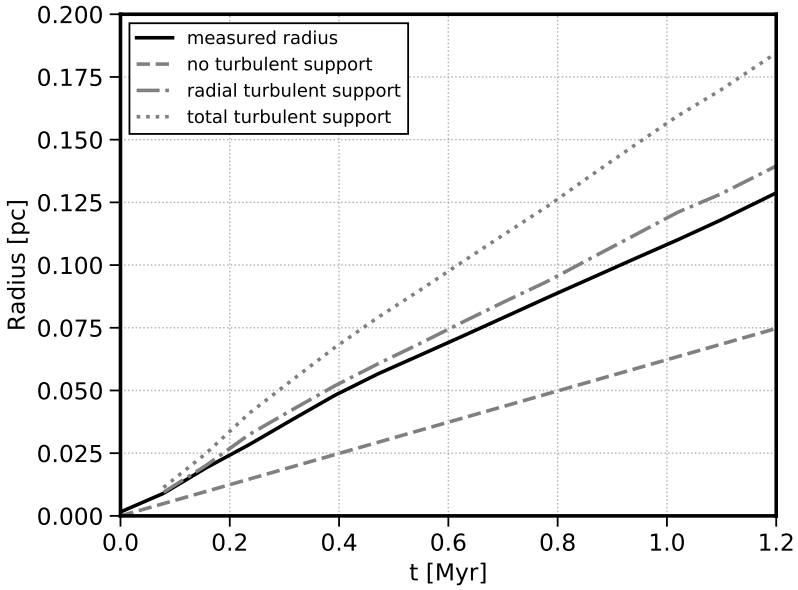

Figure 9.A.1: Radial evolution of a filament with a Mach 6 inflow without gravity. The solid black line is the measured radius at each time step. The theoretical predictions are given by Equation 9.39 with the full, radial and no turbulent support is given by the dotted, dashed-dotted and dashed line respectively.

As we have shown in Figure 9.3 the turbulence inside the filament is not isotropic. Thus, it is not necessarily the total velocity dispersion which supports the internal pressure. Furthermore, it is important to note that the hydrostatic equilibrium is given by the turbulent pressure at the boundary. As the non self-gravitating velocity dispersion has a similar radial profile as shown for the self-gravitating case in Figure 9.4, we would need to use the boundary velocity dispersion value in Equation 9.39. However, for the non self-gravitational case, the boundary velocity dispersion is very similar to the velocity dispersion calculated from the total filament as it does not have a density profile. Therefore, we do not see an anti-correlation between density and velocity dispersion and the latter is then dominated by the largest value which is at the boundary. We plot the radial evolution as solid line in Figure 9.A.1 together with the expected evolution including no turbulent support as dashed line, only radial support as dashed-dotted line and total turbulence support as dotted line. Compared to paper I, we improved our measurement method of the radius by not using the largest density jump but by using the same methodology as we do for the velocity dispersion which distinguishes filament material from the surrounding by using the drop in radial velocity. We found that the density inside the filament can vary substantially and the largest density jump does underestimate the filament radius. Moreover, sometimes the filament can be deformed, having an more elliptical formed cross-section. We reduce the impact of this effect by using the mean radius of two perpendicular cuts through the centre of the filament. The expected evolution follows from Equation 9.39 together with the measured velocity dispersion at every time-step. Note that the no turbulent support case is indistinguishable from the isothermal shock radial evolution of Equation 9.36 for large inflow Mach numbers.

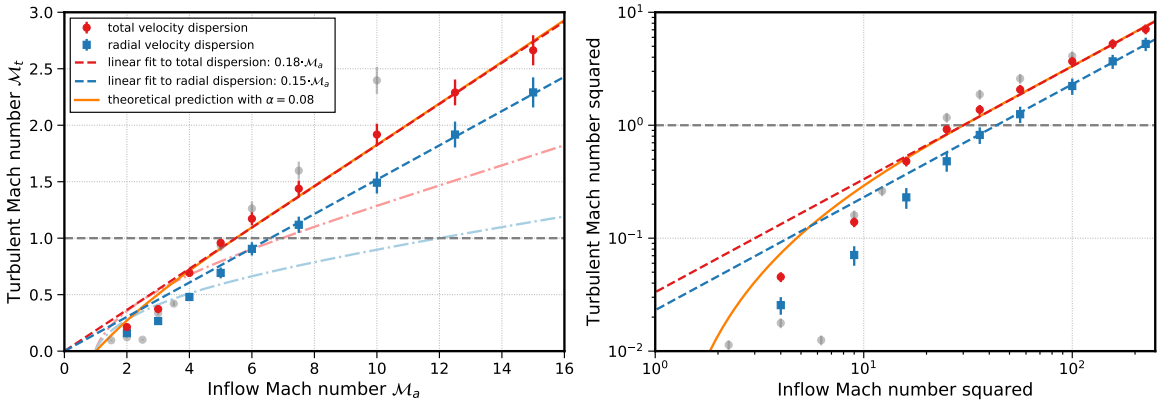

Figure 9.A.2: Equilibrium values of accretion driven turbulence in dependence of the inflow Mach number. Both plots show the same data points. On the left hand side we directly plot the values which we calculate from the kinetic energy. The gray data points are the values of the density weighted standard deviation we used in paper I. On the right hand side we show the same data points with squared values in log-log scale.

As one can see, the radius is best fitted by a support of the radial component of the velocity dispersion. This shows that only radial motions of the filament are important in setting the boundary pressure against the radial inflow.

9.A.2 Equilibrium velocity dispersion

We now want to use the information about the non self-gravitational radius evolution to explain the linear relationship we found in paper I between the inflow velocity and the created turbulence. We measure the equilibrium value which we plot as red data points in Figure 9.A.2. The left panel shows the direct relationship between the inflow velocity and the generated turbulence. On the right hand side we plot the same values but squared in order to compare the inflow energy to the turbulent energy. Additionally, we show the values of the radial turbulence as blue squares. The error bars indicate that different seeds in the random density distribution result in slightly different equilibrium values with a spread of about 10%. In gray, we also plot the data values of paper I which where calculated using the density weighted standard deviation. One can see that for low values the differences are not huge but they become increasingly larger for higher inflow Mach numbers, as discussed at the beginning of Section 9.4. Compared to paper I, we also extend the range of inflow velocities to Mach 15 which is already much greater than the expected values but serves as a good upper limit.

The reason why in general there is an equilibrium level in the velocity dispersion in the non-gravitational case is due to Equation 9.25. If the radius is growing linearly with time as shown in Equation 9.39 and if the equilibrium has been established, the dissipation rate is constant in time (Equation 9.20):

$$\dot{E}_d \approx \frac{1}{2}\frac{M(t)\sigma^3}{L_d(t)} = \frac{1}{2}\frac{\dot{M}t\sigma^3\left(1+\mathcal{M}_a^2\right)}{4v_a t\left(1+\mathcal{M}_t^2\right)} = \frac{\dot{M}\sigma^3\left(1+\mathcal{M}_a^2\right)}{8v_a\left(1+\mathcal{M}_t^2\right)}. \tag{9.40}$$

If the velocity dispersion is greater than the equilibrium value, the excess is dissipated away, if it is lower, less energy is dissipated. Thus it will settle at a value where the dissipation is constant.

In order to compare to theoretical models we first discuss the prediction by Heitsch (2013). It assumes that one can express the dissipation rate as a constant fraction of the constant energy inflow (Equation 9.22):

$$\epsilon = \left| \frac{\dot{E}_d}{\dot{E}_a} \right|. \tag{9.41}$$

Note that ϵ can only be constant in time for a constant mass accretion rate if the dissipation rate is constant in time. For a non-linear radial evolution this is not the case. Furthermore, the model assumes that ϵ is independent of the inflow velocity which is not necessarily true as the fraction of accreted energy converted to turbulent motions can change with the inflow velocity. Nevertheless, in the non-gravitational case Equation 9.23 transforms to

$$\frac{\mathcal{M}_t^3}{\left(1 + \mathcal{M}_t^2\right)} = \frac{4\epsilon \mathcal{M}_a^3}{(1 + \mathcal{M}_a^2)}. \tag{9.42}$$

As turbulence is generated in oblique shocks on the surface of the filament, we need supersonic inflow motions. Below an inflow velocity of Mach 1.0 we do not generate turbulent motions or even form a pressure bound filament. Therefore, we shift the zero point of Equation 9.42 to an inflow velocity of Mach 1.0 by effectively applying the transformation $\mathcal{M}'_a = \mathcal{M}_a - 1$. Note that this transformation only affects the energy accretion term and not to the evolution of the radius. Thus, the equation is now:

$$\frac{\mathcal{M}_t^3}{\left(1 + \mathcal{M}_t^2\right)} = \frac{4\epsilon \mathcal{M}_a'^2 \mathcal{M}_a}{(1 + \mathcal{M}_a^2)}. \tag{9.43}$$

A realistic estimate of ϵ is expected to lie between 5% and 10% (Klessen and Hennebelle, 2010) which we plot as the dashed-dotted light blue and red lines respectively. As one can see the curves do not fit the measured points and fit even worse if we do not apply the transformation. The shape of the curve cannot be matched to the data points even if we fit different values of ϵ. This leaves us with the conclusion that ϵ is only a constant in time for a certain inflow velocity but varies with the inflow velocity.

As we clearly cannot apply the model by Heitsch (2013), we try to fit Equation 9.25 directly. If we insert the evolution of the non self-gravitational radius, it transforms to

$$\mathcal{M}_t^2 = \alpha \mathcal{M}_a'^2 - \frac{\mathcal{M}_t^3 \left(1 + \mathcal{M}_a^2\right)}{4\mathcal{M}_a \left(1 + \mathcal{M}_t^2\right)}. \tag{9.44}$$

We fit this relation in Figure 9.A.2 as solid, orange line and get the best fitting value of $\alpha = 0.085$. As one can see it follows the data points well and has the same scaling for large $\mathcal{M}_a$. Only for low inflow Mach numbers there is some discrepancy where the data points lie not exactly on the relation. Therefore, our model seems to reasonably explain the connection of accretion driven turbulence an inflow Mach number.

Nevertheless, our simulations show that most of the inflow energy is lost and only about 3% is retained in turbulent motions at equilibrium for large inflow Mach numbers. Only 8,5% is kept in the shock phase and the remaining difference is dissipated continuously.

10 | Final remarks

As the thesis draws to a close, this final section gives a summary of our main findings and provides a direction for further investigations. Although the big questions of filament physics remain, such as the existence of a universal filament width and the creation of fibres, this thesis has contributed to and questioned our understanding of filaments. Many unresolved challenges remain and detailed studies on the various physical processes influencing filaments are important in order to and form a more comprehensive theory of star formation.

First, we investigated whether we can apply the idealised model of gravitational filament fragmentation to a real-world observation. Indeed, the L1517 region in Taurus seems to be an ideal candidate as two filaments are actively forming two cores respectively and show the consistent predicted velocity structure. Not only can we reproduce all observable quantities to a reasonable degree, our method also allows us to predict the inclination of filaments in the plane of the sky and to determine the local ambient pressure of the ISM. While many star-forming regions may not exhibit the same ideal conditions, our study is a proof of concept that shows the validity of the gravitational fragmentation mechanism.

Second, we demonstrated the importance of accretion flows with regard to generating turbulence in filaments. While this connection has always been assumed, we showed in a numerical study that expected gravitationally driven inflows with velocities consistent with observations can easily provide a source of turbulent motions similar to the observed non-thermal broadening. For non self-gravitating filaments we find that the velocity dispersion settles to an equilibrium value with a linear relation between inflow velocity and generated turbulence. However, only a fraction of the accreted energy is converted to turbulent motions. Furthermore, while the generated turbulence is non-isotropic and radially dominated, it does contribute to the hydrostatic equilibrium as a source of pressure. The driving of turbulence via accretion could be a viable alternative to the inheritance of non-thermal motions via a turbulent cascade and provides a source of turbulence which can be sustained over long timescales.

Third, we extend the model of the two different core formation modes discussed by Nagasawa (1987). Not only do we show that the effect of a broad or pinched morphology of the core with respect to the filament applies as soon as the initial line-mass of the filament is not exactly half the critical line-mass, but also that it should lead to an observable tracer in the column density. In principle, the difference in morphology should allow observers to determine the line-mass of a filament independent of inclination and perturbation length. Moreover, the timescales involved in the fragmentation at different line-masses for the same ambient pressure should lead to a predominant morphology being present in a particular re-

gion, as high line-mass filaments fragment and form stars much faster than their low line-mass counterparts.

Fourth, we include the effects of self-gravity in our model of accretion driven turbulence in filaments. In contrast to the non self-gravitating model, the velocity dispersion does not settle to an equilibrium but continuously dissipates. We show that the dissipation is connected to the evolution of the filament radius which is not only limited to a maximum value but also set by the level of turbulence inside the filament. As before, the turbulence is non-isotropic and radially dominated but shows an anti-correlation to the radial density profile of the filament. This leads to a constant pressure contribution of the turbulent pressure which does not change its scale height. Therefore, non-thermal motions do not increase the maximum line-mass of hydrostatic equilibrium but only affect the maximum value of the radius. As the filament is constantly accreting mass, its lifetime is limited to the time it takes to reach the maximum line-mass. We demonstrate how the radial evolution influences the core growth timescale and show that only cores which form in high line-mass filament grow fast enough to form significant overdensities. This constraint could be a possible explanation for the trend in *Herschel* observations which shows that cores tend to form only in high line-mass filaments.

There are several methods by which our model can be extended. In addition there are several open questions which arise naturally from this thesis:

- A major shortcoming of our simulations is the exclusion of magnetic fields. We know from observations and theoretical models that magnetic fields can be dynamically relevant. Not only can they change the fragmentation scales of filaments but also alter the flow of gas. A particularly interesting aspect would be the interplay of magnetic fields with the turbulent motions driven by accretion, as this could change the hydrostatic structure of the filament. Including magnetic fields would be a straightforward approach towards a more realistic model.

- Including a chemical and radiative model could prove to be useful in establishing the observational implications of our simulations. As different densities are followed by distinct tracers, features detected in observations could be influenced by the chemical structure of a filament. In the case of gravitational accretion especially one would expect a significant footprint of the accretion shock. Another interesting study could focus on the chemical and velocity structure of a forming core, as here freeze-out of CO is expected to influence the observed signal. This could not only have implications for the observed velocity dispersion but also on the observed morphology of cores.

- An interesting question is the effect of a finite length on the fragmentation of filaments. Over time a filament will collapse along its axis and the formation of two end-dominating cores is expected. However, we were able to show that this process can be prevented by including a radial accretion flow onto the filament. The accretion not only leads to a continuous increase in mass, but also pushes material along the filament from its centre to either end of the filament from where it is distributed into the surrounding medium. This effectively halts the longitudinal collapse and prevents the

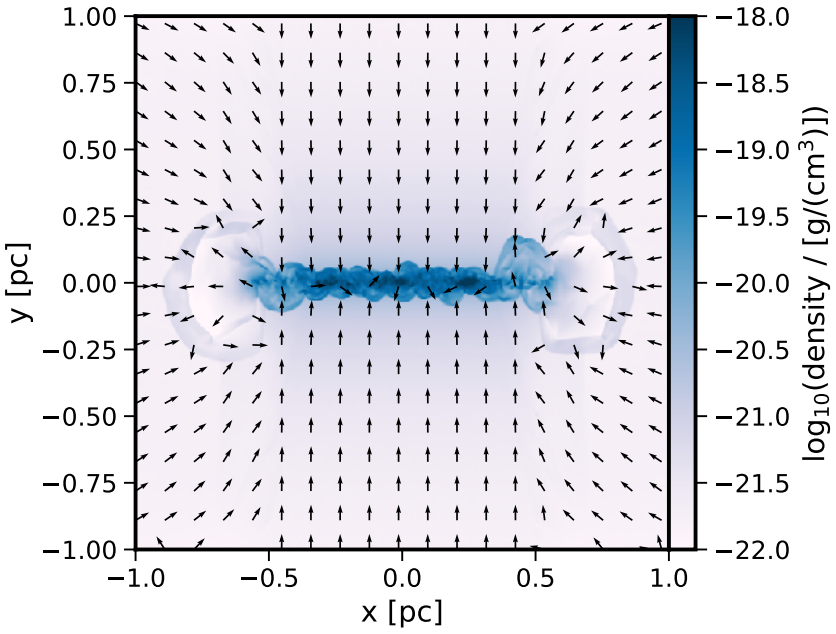

Figure 10.1: Density slice through the centre of a finite filament with an accretion flow. The accretion leads to an outflow at the ends of the filament which prevents its longitudinal collapse and the formation of end-dominating cores.

formation of cores at both ends of the filament. An example is shown in Figure 10.1. We will investigate this case in detail in a future numerical study.

- Finally, simulations with higher resolutions could provide a self-consistent model of protoplanetary disc formation inside cores which form out of a filamentary environment. Not only is it necessary to redistribute the accreted angular momentum in order to form a thin disc, but resolving the accretion flow onto the disc could enable us to assess whether discs are formed smoothly from a continuous accretion or whether clumpy accretion plays an important role. However, this requires our physical model to include feedback processes from the forming young star.

While small scale isolated simulations can provide an insight into different physical processes, a long-term goal would be to connect highly resolved filament models to large scale simulations of molecular clouds. This would not only provide more realistic initial conditions but also provide feedback from young stellar objects onto larger scales. The tasks of observational studies will be to gather even higher resolution data in order to explore the formation mechanisms and substructure of filaments, eventually connecting high density to low density star forming regions. Research in the field of star formation has never been as active as it is today and it will be the task of future studies to refine our theoretical model and collect additional observational data.

Bibliography

Abergel, A., F. Boulanger, A. Mizuno, and Y. Fukui
1994. Comparative Analysis of the Far-Infrared and 13CO (J = 0–1) Emissions of the Taurus Complex. *The Astrophysical Journal*, 423:L59.

Alves, J., C. J. Lada, E. A. Lada, S. J. Kenyon, and R. Phelps
1998. Dust Extinction and Molecular Cloud Structure: L977. *The Astrophysical Journal*, 506(1):292–305.

Alves, J., M. Lombardi, and C. J. Lada
2007. The mass function of dense molecular cores and the origin of the IMF. *Astronomy and Astrophysics*, 462(1):L17–L21.

Alves, J. F., C. J. Lada, and E. A. Lada
2001. Internal structure of a cold dark molecular cloud inferred from the extinction of background starlight. *Nature*, 409(6817):159–161.

Alves de Oliveira, C., N. Schneider, B. Merín, T. Prusti, Á. Ribas, N. L. J. Cox, R. Vavrek, V. Könyves, D. Arzoumanian, E. Puga, G. L. Pilbratt, Á. Kóspál, P. André, P. Didelon, A. Men'shchikov, P. Royer, C. Waelkens, S. Bontemps, E. Winston, and L. Spezzi
2014. Herschel view of the large-scale structure in the Chamaeleon dark clouds. *Astronomy and Astrophysics*, 568:A98.

Amenomori, M., S. Ayabe, X. J. Bi, D. Chen, S. W. Cui, Danzengluobu, L. K. Ding, X. H. Ding, C. F. Feng, and Z. Feng
2006. Anisotropy and Corotation of Galactic Cosmic Rays. *Science*, 314(5798):439–443.

André, P., D. Arzoumanian, V. Könyves, Y. Shimajiri, and P. Palmeirim
2019. The role of molecular filaments in the origin of the prestellar core mass function and stellar initial mass function. *Astronomy and Astrophysics*, 629:L4.

André, P., J. Di Francesco, D. Ward-Thompson, S.-I. Inutsuka, R. E. Pudritz, and J. E. Pineda
2014. From Filamentary Networks to Dense Cores in Molecular Clouds: Toward a New Paradigm for Star Formation. *Protostars and Planets VI*, Pp. 27–51.

André, P., A. Men'shchikov, S. Bontemps, V. Könyves, F. Motte, N. Schneider, P. Didelon, V. Minier, P. Saraceno, D. Ward-Thompson, J. di Francesco, G. White, S. Molinari, L. Testi, A. Abergel, M. Griffin, T. Henning, P. Royer, B. Merín, R. Vavrek, M. Attard,

D. Arzoumanian, C. D. Wilson, P. Ade, H. Aussel, J.-P. Baluteau, M. Benedettini, J.-P. Bernard, J. A. D. L. Blommaert, L. Cambrésy, P. Cox, A. di Giorgio, P. Hargrave, M. Hennemann, M. Huang, J. Kirk, O. Krause, R. Launhardt, S. Leeks, J. Le Pennec, J. Z. Li, P. G. Martin, A. Maury, G. Olofsson, A. Omont, N. Peretto, S. Pezzuto, T. Prusti, H. Roussel, D. Russeil, M. Sauvage, B. Sibthorpe, A. Sicilia-Aguilar, L. Spinoglio, C. Waelkens, A. Woodcraft, and A. Zavagno
2010. From filamentary clouds to prestellar cores to the stellar IMF: Initial highlights from the Herschel Gould Belt Survey. *Astronomy and Astrophysics*, 518:L102.

Arzoumanian, D., P. André, P. Didelon, V. Könyves, N. Schneider, A. Men'shchikov, T. Sousbie, A. Zavagno, S. Bontemps, J. di Francesco, M. Griffin, M. Hennemann, T. Hill, J. Kirk, P. Martin, V. Minier, S. Molinari, F. Motte, N. Peretto, S. Pezzuto, L. Spinoglio, D. Ward-Thompson, G. White, and C. D. Wilson
2011. Characterizing interstellar filaments with Herschel in IC 5146. *Astronomy and Astrophysics*, 529:L6.

Arzoumanian, D., P. André, V. Könyves, P. Palmeirim, A. Roy, N. Schneider, M. Benedettini, P. Didelon, J. Di Francesco, J. Kirk, and B. Ladjelate
2019. Characterizing the properties of nearby molecular filaments observed with Herschel. *Astronomy and Astrophysics*, 621:A42.

Arzoumanian, D., P. André, N. Peretto, and V. Könyves
2013. Formation and evolution of interstellar filaments. Hints from velocity dispersion measurements. *Astronomy and Astrophysics*, 553:A119.

Bakes, E. L. O. and A. G. G. M. Tielens
1994. The photoelectric heating mechanism for very small graphitic grains and polycyclic aromatic hydrocarbons. *The Astrophysical Journal*, 427:822–838.

Ballesteros-Paredes, J., L. Hartmann, and E. Vázquez-Semadeni
1999. Turbulent Flow-driven Molecular Cloud Formation: A Solution to the Post-T Tauri Problem? *The Astrophysical Journal*, 527(1):285–297.

Ballesteros-Paredes, J., R. S. Klessen, and E. Vázquez-Semadeni
2003. Dynamic Cores in Hydrostatic Disguise. *The Astrophysical Journal*, 592(1):188–202.

Ballesteros-Paredes, J., E. Vázquez-Semadeni, A. Gazol, L. W. Hartmann, F. Heitsch, and P. Colín
2011. Gravity or turbulence? - II. Evolving column density probability distribution functions in molecular clouds. *Monthly Notices of the Royal Astronomical Society*, 416(2):1436–1442.

Bally, J., W. D. Langer, A. A. Stark, and R. W. Wilson
1987. Filamentary Structure in the Orion Molecular Cloud. *The Astrophysical Journal*, 312:L45.

Bastian, N., K. R. Covey, and M. R. Meyer
2010. A Universal Stellar Initial Mass Function? A Critical Look at Variations. *Annual Review of Astronomy and Astrophysics*, 48:339–389.

Bastien, P.
1983. Gravitational collapse and fragmentation of isothermal, non-rotating, cylindrical clouds. *Astronomy and Astrophysics*, 119:109–116.

Bastien, P., J.-P. Arcoragi, W. Benz, I. Bonnell, and H. Martel
1991. Fragmentation of elongated cylindrical clouds. I - Isothermal clouds. *The Astrophysical Journal*, 378:255–265.

Batten, P., N. Clarke, C. Lambert, and D. Causon
1997. On the Choice of Wave Speeds for the HLLC Riemann Solver. *SIAM J. Sci. and Stat. Comp.*, 18:1553–1570.

Benson, P. J. and P. C. Myers
1989. A survey for dense cores in dark clouds. *Astrophysical Journal Supplement Series*, 71:89–108.

Berger, M. J. and P. Colella
1989. Local Adaptive Mesh Refinement for Shock Hydrodynamics. *Journal of Computational Physics*, 82(1):64–84.

Berger, M. J. and J. Oliger
1984. Adaptive Mesh Refinement for Hyperbolic Partial Differential Equations. *Journal of Computational Physics*, 53(3):484–512.

Bertoldi, F. and C. F. McKee
1992. Pressure-confined clumps in magnetized molecular clouds. *The Astrophysical Journal*, 395:140–157.

Beuther, H., S. E. Ragan, K. Johnston, T. Henning, A. Hacar, and J. T. Kainulainen
2015. Filament fragmentation in high-mass star formation. *Astronomy and Astrophysics*, 584:A67.

Bohlin, R. C., B. D. Savage, and J. F. Drake
1978. A survey of interstellar H I from Lalpha absorption measurements. II. *The Astrophysical Journal*, 224:132–142.

Bok, B. J.
1956. Palomar Schmidt star counts for two heavily obscured fields. *Astronomical Journal*, 61:309–316.

Bonnor, W. B.
1956. Boyle's Law and gravitational instability. *Monthly Notices of the Royal Astronomical Society*, 116:351.

Bontemps, S., P. André, V. Könyves, A. Men'shchikov, N. Schneider, A. Maury, N. Peretto, D. Arzoumanian, M. Attard, F. Motte, V. Minier, P. Didelon, P. Saraceno, A. Abergel, J. P. Baluteau, J. P. Bernard, L. Cambrésy, P. Cox, J. di Francesco, A. M. di Giorgo, M. Griffin, P. Hargrave, M. Huang, J. Kirk, J. Li, P. Martin, B. Merín, S. Molinari, G. Olofsson, S. Pezzuto, T. Prusti, H. Roussel, D. Russeil, M. Sauvage, B. Sibthorpe, L. Spinoglio, L. Testi, R. Vavrek, D. Ward-Thompson, G. White, C. Wilson, A. Woodcraft, and A. Zavagno
2010. The Herschel first look at protostars in the Aquila rift. *Astronomy and Astrophysics*, 518:L85.

Bourke, T. L., P. C. Myers, P. Caselli, J. Di Francesco, A. Belloche, R. Plume, and D. J. Wilner
2012. Initial Conditions for Star Formation in Clusters: Physical and Kinematical Structure of the Starless Core Oph A-N6. *The Astrophysical Journal*, 745(2):117.

Burgers, J.
1948. A mathematical model illustrating the theory of turbulence. *Advances in Applied Mechanics*, 1:171 – 199.

Burkert, A. and L. Hartmann
2004. Collapse and Fragmentation in Finite Sheets. *The Astrophysical Journal*, 616:288–300.

Burkert, A. and D. N. C. Lin
2000. Thermal Instability and the Formation of Clumpy Gas Clouds. *The Astrophysical Journal*, 537(1):270–282.

Busquet, G., Q. Zhang, A. Palau, H. B. Liu, Á. Sánchez-Monge, R. Estalella, P. T. P. Ho, I. de Gregorio-Monsalvo, T. Pillai, F. Wyrowski, J. M. Girart, F. P. Santos, and G. A. P. Franco
2013. Unveiling a Network of Parallel Filaments in the Infrared Dark Cloud G14.225-0.506. *The Astrophysical Journal*, 764(2):L26.

Caselli, P., C. M. Walmsley, M. Tafalla, L. Dore, and P. C. Myers
1999. CO Depletion in the Starless Cloud Core L1544. *The Astrophysical Journal*, 523(2):L165–L169.

Chandrasekhar, S. and E. Fermi
1953. Problems of Gravitational Stability in the Presence of a Magnetic Field. *The Astrophysical Journal*, 118:116.

Chapman, N. L., P. F. Goldsmith, J. L. Pineda, D. P. Clemens, D. Li, and M. Krčo
2011. The Magnetic Field in Taurus Probed by Infrared Polarization. *The Astrophysical Journal*, 741(1):21.

Chen, C.-Y. and E. C. Ostriker
2014. Formation of Magnetized Prestellar Cores with Ambipolar Diffusion and Turbulence. *The Astrophysical Journal*, 785(1):69.

Chini, R., B. Reipurth, D. Ward-Thompson, J. Bally, L. Å. Nyman, A. Sievers, and Y. Billawala
1997. Dust Filaments and Star Formation in OMC-2 and OMC-3. *The Astrophysical Journal*, 474(2):L135–L138.

Clark, P. C., S. C. O. Glover, R. S. Klessen, and I. A. Bonnell
2012. How long does it take to form a molecular cloud? *Monthly Notices of the Royal Astronomical Society*, 424:2599–2613.

Clarke, S. D. and A. P. Whitworth
2015. Investigating the global collapse of filaments using smoothed particle hydrodynamics. *Monthly Notices of the Royal Astronomical Society*, 449:1819–1825.

Clarke, S. D., A. P. Whitworth, A. Duarte-Cabral, and D. A. Hubber
2017. Filamentary fragmentation in a turbulent medium. *Monthly Notices of the Royal Astronomical Society*, 468:2489–2505.

Clarke, S. D., A. P. Whitworth, R. L. Spowage, A. Duarte-Cabral, S. T. Suri, S. E. Jaffa, S. Walch, and P. C. Clark
2018. Synthetic $C^{18}O$ observations of fibrous filaments: the problems of mapping from PPV to PPP. *Monthly Notices of the Royal Astronomical Society*, 479(2):1722–1746.

Contreras, Y., G. Garay, J. M. Rathborne, and P. Sanhueza
2016. Fragmentation in filamentary molecular clouds. *Monthly Notices of the Royal Astronomical Society*, 456(2):2041–2051.

Contreras, Y., J. Rathborne, and G. Garay
2013. Structure and radial equilibrium of filamentary molecular clouds. *Monthly Notices of the Royal Astronomical Society*, 433(1):251–258.

Courant, R., K. Friedrichs, and H. Lewy
1928. Über die partiellen Differenzengleichungen der mathematischen Physik. *Mathematische Annalen*, 100:32–74.

Cox, N. L. J., D. Arzoumanian, P. André, K. L. J. Rygl, T. Prusti, A. Men'shchikov, P. Royer, Á. Kóspál, P. Palmeirim, A. Ribas, V. Könyves, J.-P. Bernard, N. Schneider, S. Bontemps, B. Merin, R. Vavrek, C. Alves de Oliveira, P. Didelon, G. L. Pilbratt, and C. Waelkens
2016. Filamentary structure and magnetic field orientation in Musca. *Astronomy and Astrophysics*, 590:A110.

Crutcher, R. M.
2012. Magnetic Fields in Molecular Clouds. *Annual review of astronomy and Astrophysics*, 50:29–63.

Davis, Leverett, J. and J. L. Greenstein
1951. The Polarization of Starlight by Aligned Dust Grains. *The Astrophysical Journal*, 114:206.

Dhabal, A., L. G. Mundy, M. J. Rizzo, S. Storm, and P. Teuben
2018. Morphology and Kinematics of Filaments in the Serpens and Perseus Molecular Clouds. *The Astrophysical Journal*, 853(2):169.

di Francesco, J., N. J. Evans, II, P. Caselli, P. C. Myers, Y. Shirley, Y. Aikawa, and M. Tafalla
2007. An Observational Perspective of Low-Mass Dense Cores I: Internal Physical and Chemical Properties. *Protostars and Planets V*, Pp. 17–32.

Dobbs, C. L., J. E. Pringle, and A. Burkert
2012. Giant molecular clouds: what are they made from, and how do they get there? *Monthly Notices of the Royal Astronomical Society*, 425(3):2157–2168.

Draine, B. T.
2003. Interstellar Dust Grains. *Annual review of astronomy and Astrophysics*, 41:241–289.

Draine, B. T. and H. M. Lee
1984. Optical Properties of Interstellar Graphite and Silicate Grains. *The Astrophysical Journal*, 285:89.

Duvert, G., J. Cernicharo, and A. Baudry
1986. A molecular survey of three dark clouds in Taurus. *Astronomy and Astrophysics*, 164:349–357.

Ebert, R.
1955. Über die Verdichtung von H I-Gebieten. Mit 5 Textabbildungen. *Zeitschrift für Astrophysik*, 37:217.

Egan, M. P., R. F. Shipman, S. D. Price, S. J. Carey, F. O. Clark, and M. Cohen
1998. A Population of Cold Cores in the Galactic Plane. *The Astrophysical Journal*, 494(2):L199–L202.

Elmegreen, B. G. and A. Burkert
2010. Accretion-Driven Turbulence and the Transition to Global Instability in Young Galaxy Disks. *The Astrophysical Journal*, 712:294–302.

Elmegreen, B. G. and J. Scalo
2004. Interstellar Turbulence I: Observations and Processes. *Annual review of astronomy and Astrophysics*, 42:211–273.

Enoch, M. L., I. Evans, Neal J., A. I. Sargent, J. Glenn, E. Rosolowsky, and P. Myers
2008. The Mass Distribution and Lifetime of Prestellar Cores in Perseus, Serpens, and Ophiuchus. *The Astrophysical Journal*, 684(2):1240–1259.

Evans, II, N. J., M. M. Dunham, J. K. Jørgensen, M. L. Enoch, B. Merín, E. F. van Dishoeck, J. M. Alcalá, P. C. Myers, K. R. Stapelfeldt, T. L. Huard, L. E. Allen, P. M. Harvey, T. van Kempen, G. A. Blake, D. W. Koerner, L. G. Mundy, D. L. Padgett, and A. I. Sargent
2009. The Spitzer c2d Legacy Results: Star-Formation Rates and Efficiencies; Evolution and Lifetimes. *Astrophysical Journal Supplement Series*, 181:321–350.

Falgarone, E., J. Pety, and T. G. Phillips
2001. Filamentary Structure and Helical Magnetic Fields in the Environment of a Starless Dense Core. *The Astrophysical Journal*, 555(1):178–190.

Fatuzzo, M. and F. C. Adams
1993. Magnetohydrodynamic Wave Propagation in One-dimensional Nonhomogeneous, Self-gravitating Clouds. *The Astrophysical Journal*, 412:146.

Federrath, C.
2013. On the universality of supersonic turbulence. *Monthly Notices of the Royal Astronomical Society*, 436:1245–1257.

Federrath, C.
2016. On the universality of interstellar filaments: theory meets simulations and observations. *Monthly Notices of the Royal Astronomical Society*, 457:375–388.

Federrath, C., R. S. Klessen, and W. Schmidt
2008. The Density Probability Distribution in Compressible Isothermal Turbulence: Solenoidal versus Compressive Forcing. *The Astrophysical Journal*, 688:L79.

Federrath, C., J. Roman-Duval, R. S. Klessen, W. Schmidt, and M.-M. Mac Low
2010. Comparing the statistics of interstellar turbulence in simulations and observations. Solenoidal versus compressive turbulence forcing. *Astronomy and Astrophysics*, 512:A81.

Federrath, C., S. Sur, D. R. G. Schleicher, R. Banerjee, and R. S. Klessen
2011. A New Jeans Resolution Criterion for (M)HD Simulations of Self-gravitating Gas: Application to Magnetic Field Amplification by Gravity-driven Turbulence. *The Astrophysical Journal*, 731:62.

Fernández-López, M., H. G. Arce, L. Looney, L. G. Mundy, S. Storm, P. J. Teuben, K. Lee, D. Segura-Cox, A. Isella, J. J. Tobin, E. Rosolowsky, A. Plunkett, W. Kwon, J. Kauffmann, E. Ostriker, K. Tassis, Y. L. Shirley, and M. Pound
2014. CARMA Large Area Star Formation Survey: Observational Analysis of Filaments in the Serpens South Molecular Cloud. *The Astrophysical Journal*, 790(2):L19.

Fiege, J. D. and R. E. Pudritz
2000a. Helical fields and filamentary molecular clouds - I. *Monthly Notices of the Royal Astronomical Society*, 311(1):85–104.

Fiege, J. D. and R. E. Pudritz
2000b. Helical fields and filamentary molecular clouds - II. Axisymmetric stability and fragmentation. *Monthly Notices of the Royal Astronomical Society*, 311:105–119.

Field, G. B.
1965. Thermal Instability. *The Astrophysical Journal*, 142:531.

Fischera, J. and P. G. Martin
2012. Physical properties of interstellar filaments. *Astronomy and Astrophysics*, 542:A77.

Fryxell, B., K. Olson, P. Ricker, F. X. Timmes, M. Zingale, D. Q. Lamb, P. MacNeice, R. Rosner, J. W. Truran, and H. Tufo
2000. FLASH: An Adaptive Mesh Hydrodynamics Code for Modeling Astrophysical Thermonuclear Flashes. *Astrophysical Journal Supplement Series*, 131(1):273–334.

Gehman, C. S., F. C. Adams, M. Fatuzzo, and R. Watkins
1996a. Wave Motions in Molecular Clouds: Results in Two Dimensions. *The Astrophysical Journal*, 457:718.

Gehman, C. S., F. C. Adams, and R. Watkins
1996b. Linear Gravitational Instability of Filamentary and Sheetlike Molecular Clouds with Magnetic Fields. *The Astrophysical Journal*, 472:673.

Glassgold, A. E., D. Galli, and M. Padovani
2012. Cosmic-Ray and X-Ray Heating of Interstellar Clouds and Protoplanetary Disks. *The Astrophysical Journal*, 756:157.

Godunov, S. K.
1959. A difference method for numerical calculation of discontinuous solutions of the equations of hydrodynamics. *Matematicheskii Sbornik*, 47(89):3:271–306.

Goldsmith, P. F., M. Heyer, G. Narayanan, R. Snell, D. Li, and C. Brunt
2008. Large-Scale Structure of the Molecular Gas in Taurus Revealed by High Linear Dynamic Range Spectral Line Mapping. *The Astrophysical Journal*, 680(1):428–445.

Goldsmith, P. F. and W. D. Langer
1978. Molecular cooling and thermal balance of dense interstellar clouds. *The Astrophysical Journal*, 222:881–895.

Gómez, G. C. and E. Vázquez-Semadeni
2014. Filaments in Simulations of Molecular Cloud Formation. *The Astrophysical Journal*, 791(2):124.

Gómez, G. C., E. Vázquez-Semadeni, and M. Zamora-Avilés
2018. The magnetic field structure in molecular cloud filaments. *Monthly Notices of the Royal Astronomical Society*, 480(3):2939–2944.

Gong, H. and E. C. Ostriker
2011. Dense Core Formation in Supersonic Turbulent Converging Flows. *The Astrophysical Journal*, 729(2):120.

Goodman, A. A., J. A. Barranco, D. J. Wilner, and M. H. Heyer
1998. Coherence in Dense Cores. II. The Transition to Coherence. *The Astrophysical Journal*, 504(1):223–246.

Gould, R. J. and E. E. Salpeter
1963. The Interstellar Abundance of the Hydrogen Molecule. I. Basic Processes. *The Astrophysical Journal*, 138:393.

Gritschneder, M., S. Heigl, and A. Burkert
2017. Oscillating Filaments. I. Oscillation and Geometrical Fragmentation. *The Astrophysical Journal*, 834(2):202.

Gritschneder, M. and D. N. C. Lin
2012. The Role of θ Oph in the Formation and Evolution of the Pipe Nebula - Is Star Formation Ever Isolated? *The Astrophysical Journal*, 754:L13.

Hacar, A., J. Alves, A. Burkert, and P. Goldsmith
2016a. Opacity broadening and interpretation of suprathermal CO linewidths: Macroscopic turbulence and tangled molecular clouds. *Astronomy and Astrophysics*, 591:A104.

Hacar, A., J. Kainulainen, M. Tafalla, H. Beuther, and J. Alves
2016b. The Musca cloud: A 6 pc-long velocity-coherent, sonic filament. *Astronomy and Astrophysics*, 587:A97.

Hacar, A. and M. Tafalla
2011. Dense core formation by fragmentation of velocity-coherent filaments in L1517. *Astronomy and Astrophysics*, 533:A34.

Hacar, A., M. Tafalla, and J. Alves
2017. Fibers in the NGC 1333 proto-cluster. *Astronomy and Astrophysics*, 606:A123.

Hacar, A., M. Tafalla, J. Forbrich, J. Alves, S. Meingast, J. Grossschedl, and P. S. Teixeira
2018. An ALMA study of the Orion Integral Filament: I. Evidence for narrow fibers in a massive cloud. *ArXiv e-prints*.

Hacar, A., M. Tafalla, J. Kauffmann, and A. Kovács
2013. Cores, filaments, and bundles: hierarchical core formation in the L1495/B213 Taurus region. *Astronomy and Astrophysics*, 554:A55.

Hall, J. S.
1949. Observations of the Polarized Light from Stars. *Science*, 109(2825):166–167.

Hanawa, T., T. Kudoh, and K. Tomisaka
2017. Fragmentation of a Filamentary Cloud Permeated by a Perpendicular Magnetic Field. *The Astrophysical Journal*, 848(1):2.

Harten, A.
1983. High resolution schemes for hyperbolic conservation laws. *Journal of Computational Physics*, 49(3):357–393.

Harten, A., P. D. Lax, and B. Leer
1983. On upstream differencing and Godunov-type schemes for hyperbolic conservation laws. *SIAM J. Sci. and Stat. Comp.*, 25(1):35–61.

Hartmann, L.
2001. On Age Spreads in Star-forming Regions. *Astronomical Journal*, 121:1030–1039.

Hartmann, L.
2002. Flows, Fragmentation, and Star Formation. I. Low-Mass Stars in Taurus. *The Astrophysical Journal*, 578:914–924.

Heigl, S., A. Burkert, and M. Gritschneder
2018a. Accretion-driven turbulence in filaments - I. Non-gravitational accretion. *Monthly Notices of the Royal Astronomical Society*, 474(4):4881–4893.

Heigl, S., A. Burkert, and A. Hacar
2016. Non-linear dense core formation in the dark cloud L1517. *Monthly Notices of the Royal Astronomical Society*, 463:4301–4310.

Heigl, S., M. Gritschneder, and A. Burkert
2018b. Morphology of prestellar cores in pressure-confined filaments. *Monthly Notices of the Royal Astronomical Society*, 481(1):L1–L5.

Heiles, C. and T. H. Troland
2003. The Millennium Arecibo 21 Centimeter Absorption-Line Survey. II. Properties of the Warm and Cold Neutral Media. *The Astrophysical Journal*, 586(2):1067–1093.

Heitsch, F.
2013. Gravitational Infall onto Molecular Filaments. *The Astrophysical Journal*, 769:115.

Heitsch, F., J. Ballesteros-Paredes, and L. Hartmann
2009. Gravitational Collapse and Filament Formation: Comparison with the Pipe Nebula. *The Astrophysical Journal*, 704:1735–1742.

Heitsch, F., L. W. Hartmann, and A. Burkert
2008. Fragmentation of Shocked Flows: Gravity, Turbulence, and Cooling. *The Astrophysical Journal*, 683:786–795.

Heitsch, F., A. D. Slyz, J. E. G. Devriendt, L. W. Hartmann, and A. Burkert
2006. The Birth of Molecular Clouds: Formation of Atomic Precursors in Colliding Flows. *The Astrophysical Journal*, 648(2):1052–1065.

Hennebelle, P.
2013. On the origin of non-self-gravitating filaments in the ISM. *Astronomy and Astrophysics*, 556:A153.

Hennebelle, P. and M. Pérault
1999. Dynamical condensation in a thermally bistable flow. Application to interstellar cirrus. *Astronomy and Astrophysics*, 351:309–322.

Hennebelle, P. and M. Pérault
2000. Dynamical condensation in a magnetized and thermally bistable flow. Application to interstellar cirrus. *Astronomy and Astrophysics*, 359:1124–1138.

Hennebelle, P., M. Pérault, D. Teyssier, and S. Ganesh
2001. Infrared dark clouds from the ISOGAL survey. Constraints on the interstellar extinction curve. *Astronomy and Astrophysics*, 365:598–611.

Hennemann, M., F. Motte, N. Schneider, P. Didelon, T. Hill, D. Arzoumanian, S. Bontemps, T. Csengeri, P. André, V. Konyves, F. Louvet, A. Marston, A. Men'shchikov, V. Minier, Q. Nguyen Luong, P. Palmeirim, N. Peretto, M. Sauvage, A. Zavagno, L. D. Anderson, J. P. Bernard, J. Di Francesco, D. Elia, J. Z. Li, P. G. Martin, S. Molinari, S. Pezzuto, D. Russeil, K. L. J. Rygl, E. Schisano, L. Spinoglio, T. Sousbie, D. Ward-Thompson, and G. J. White
2012. The spine of the swan: a Herschel study of the DR21 ridge and filaments in Cygnus X. *Astronomy and Astrophysics*, 543:L3.

Henshaw, J. D., P. Caselli, F. Fontani, I. Jiménez-Serra, J. C. Tan, S. N. Longmore, J. E. Pineda, R. J. Parker, and A. T. Barnes
2016. Investigating the structure and fragmentation of a highly filamentary IRDC. *Monthly Notices of the Royal Astronomical Society*, 463(1):146–169.

Henshaw, J. D., I. Jiménez-Serra, S. N. Longmore, P. Caselli, J. E. Pineda, A. Avison, A. T. Barnes, J. C. Tan, and F. Fontani
2017. Unveiling the early-stage anatomy of a protocluster hub with ALMA. *Monthly Notices of the Royal Astronomical Society*, 464(1):L31–L35.

Heyer, M., H. Gong, E. Ostriker, and C. Brunt
2008. Magnetically Aligned Velocity Anisotropy in the Taurus Molecular Cloud. *The Astrophysical Journal*, 680(1):420–427.

Heyer, M. H., C. Brunt, R. L. Snell, J. E. Howe, F. P. Schloerb, and J. M. Carpenter
1998. The Five College Radio Astronomy Observatory CO Survey of the Outer Galaxy. *Astrophysical Journal Supplement Series*, 115(2):241–258.

Heyer, M. H., R. L. Snell, P. F. Goldsmith, and P. C. Myers
1987. A survey of IRAS point sources in Taurus for high-velocity molecular gas. *The Astrophysical Journal*, 321:370–382.

Hill, T., F. Motte, P. Didelon, S. Bontemps, V. Minier, M. Hennemann, N. Schneider, P. André, A. Men'shchikov, L. D. Anderson, D. Arzoumanian, J. P. Bernard, J. di Francesco, D. Elia, T. Giannini, M. J. Griffin, V. Könyves, J. Kirk, A. P. Marston, P. G. Martin, S. Molinari, Q. Nguyen Luong, N. Peretto, S. Pezzuto, H. Roussel, M. Sauvage, T. Sousbie, L. Testi, D. Ward-Thompson, G. J. White, C. D. Wilson, and A. Zavagno
2011. Filaments and ridges in Vela C revealed by Herschel: from low-mass to high-mass star-forming sites. *Astronomy and Astrophysics*, 533:A94.

Hiltner, W. A.
1949. On the Presence of Polarization in the Continuous Radiation of Stars. II. *The Astrophysical Journal*, 109:471.

Hily-Blant, P. and E. Falgarone
2007. Dissipative structures of diffuse molecular gas. II. The translucent environment of a dense core. *Astronomy and Astrophysics*, 469(1):173–187.

Hollenbach, D. and E. E. Salpeter
1971. Surface Recombination of Hydrogen Molecules. *The Astrophysical Journal*, 163:155.

Hosseinirad, M., S. Abbassi, M. Roshan, and K. Naficy
2018. Gravitational instability of filamentary molecular clouds, including ambipolar diffusion; non-isothermal filament. *Monthly Notices of the Royal Astronomical Society*, 475(2):2632–2641.

Hosseinirad, M., K. Naficy, S. Abbassi, and M. Roshan
2017. Gravitational instability of filamentary molecular clouds, including ambipolar diffusion. *Monthly Notices of the Royal Astronomical Society*, 465:1645–1653.

Howard, A. D. P., A. P. Whitworth, K. A. Marsh, S. D. Clarke, M. J. Griffin, M. W. L. Smith, and O. D. Lomax
2019. L1495 revisited: a PPMAP view of a star-forming filament. *Monthly Notices of the Royal Astronomical Society*, 489(1):962–976.

Hubber, D. A., G. P. Rosotti, and R. A. Booth
2018. GANDALF - Graphical Astrophysics code for N-body Dynamics And Lagrangian Fluids. *Monthly Notices of the Royal Astronomical Society*, 473:1603–1632.

Ibáñez-Mejía, J. C., M.-M. Mac Low, R. S. Klessen, and C. Baczynski
2016. Gravitational Contraction versus Supernova Driving and the Origin of the Velocity Dispersion-Size Relation in Molecular Clouds. *The Astrophysical Journal*, 824:41.

Indriolo, N. and B. J. McCall
2012. Investigating the Cosmic-Ray Ionization Rate in the Galactic Diffuse Interstellar Medium through Observations of H^+_3. *The Astrophysical Journal*, 745(1):91.

Inutsuka, S.-i.
2001. The Mass Function of Molecular Cloud Cores. *The Astrophysical Journal*, 559(2):L149–L152.

Inutsuka, S.-i., T. Inoue, K. Iwasaki, and T. Hosokawa
2015. The formation and destruction of molecular clouds and galactic star formation. An origin for the cloud mass function and star formation efficiency. *Astronomy and Astrophysics*, 580:A49.

Inutsuka, S.-I. and S. M. Miyama
1992. Self-similar solutions and the stability of collapsing isothermal filaments. *The Astrophysical Journal*, 388:392–399.

Inutsuka, S.-i. and S. M. Miyama
1997. A Production Mechanism for Clusters of Dense Cores. *The Astrophysical Journal*, 480:681–693.

Jackson, J. M., S. C. Finn, E. T. Chambers, J. M. Rathborne, and R. Simon
2010. The "Nessie" Nebula: Cluster Formation in a Filamentary Infrared Dark Cloud. *The Astrophysical Journal*, 719(2):L185–L189.

Jessop, N. E. and D. Ward-Thompson
2000. A far-infrared survey of molecular cloud cores. *Monthly Notices of the Royal Astronomical Society*, 311:63–74.

Johnstone, D. and J. Bally
1999. JCMT/SCUBA Submillimeter Wavelength Imaging of the Integral-shaped Filament in Orion. *The Astrophysical Journal*, 510(1):L49–L53.

Johnstone, D., C. D. Wilson, G. Moriarty-Schieven, G. Joncas, G. Smith, E. Gregersen, and M. Fich
2000. Large-Area Mapping at 850 Microns. II. Analysis of the Clump Distribution in the ρ Ophiuchi Molecular Cloud. *The Astrophysical Journal*, 545(1):327–339.

Joy, A. H.
1945. T Tauri Variable Stars. *The Astrophysical Journal*, 102:168.

Kainulainen, J., A. Hacar, J. Alves, H. Beuther, H. Bouy, and M. Tafalla
2016. Gravitational fragmentation caught in the act: the filamentary Musca molecular cloud. *Astronomy and Astrophysics*, 586:A27.

Kainulainen, J., S. E. Ragan, T. Henning, and A. Stutz
2013. High-fidelity view of the structure and fragmentation of the high-mass, filamentary IRDC G11.11-0.12. *Astronomy and Astrophysics*, 557:A120.

Kainulainen, J., A. M. Stutz, T. Stanke, J. Abreu-Vicente, H. Beuther, T. Henning, K. G. Johnston, and S. T. Megeath
2017. Resolving the fragmentation of high line-mass filaments with ALMA: the integral shaped filament in Orion A. *Astronomy and Astrophysics*, 600:A141.

Kalberla, P. M. W. and J. Kerp
2009. The Hi Distribution of the Milky Way. *Annual review of astronomy and Astrophysics*, 47(1):27–61.

Kawachi, T. and T. Hanawa
1998. Gravitational Collapse of Filamentary Clouds. *Publications of the Astronomical Society of Japan*, 50:577–586.

Kirk, H., M. Klassen, R. Pudritz, and S. Pillsworth
2015. The Role of Turbulence and Magnetic Fields in Simulated Filamentary Structure. *The Astrophysical Journal*, 802(2):75.

Kirk, J. M., D. Ward-Thompson, P. Palmeirim, P. André, M. J. Griffin, P. J. Hargrave, V. Könyves, J. P. Bernard, D. J. Nutter, B. Sibthorpe, J. Di Francesco, A. Abergel, D. Arzoumanian, M. Benedettini, S. Bontemps, D. Elia, M. Hennemann, T. Hill, A. Men'shchikov, F. Motte, Q. Nguyen-Luong, N. Peretto, S. Pezzuto, K. L. J. Rygl, S. I. Sadavoy, E. Schisano, N. Schneider, L. Testi, and G. White
2013. First results from the Herschel Gould Belt Survey in Taurus. *Monthly Notices of the Royal Astronomical Society*, 432(2):1424–1433.

Kitsionas, S., C. Federrath, R. S. Klessen, W. Schmidt, D. J. Price, L. J. Dursi, M. Gritschneder, S. Walch, R. Piontek, J. Kim, A. K. Jappsen, P. Ciecielag, and M. M. Mac Low
2009. Algorithmic comparisons of decaying, isothermal, supersonic turbulence. *Astronomy and Astrophysics*, 508(1):541–560.

Klessen, R. S., J. Ballesteros-Paredes, E. Vázquez-Semadeni, and C. Durán-Rojas
2005. Quiescent and Coherent Cores from Gravoturbulent Fragmentation. *The Astrophysical Journal*, 620:786–794.

Klessen, R. S. and A. Burkert
2000. The Formation of Stellar Clusters: Gaussian Cloud Conditions. I. *Astrophysical Journal Supplement Series*, 128(1):287–319.

Klessen, R. S., A. Burkert, and M. R. Bate
1998. Fragmentation of Molecular Clouds: The Initial Phase of a Stellar Cluster. *The Astrophysical Journal*, 501:L205–L208.

Klessen, R. S. and S. C. O. Glover
2016. Physical Processes in the Interstellar Medium. *Saas-Fee Advanced Course*, 43:85.

Klessen, R. S. and P. Hennebelle
2010. Accretion-driven turbulence as universal process: galaxies, molecular clouds, and protostellar disks. *Astronomy and Astrophysics*, 520:A17.

Koch, E. W. and E. W. Rosolowsky
2015. Filament identification through mathematical morphology. *Monthly Notices of the Royal Astronomical Society*, 452:3435–3450.

Kolmogorov, A.
1941. The Local Structure of Turbulence in Incompressible Viscous Fluid for Very Large Reynolds' Numbers. *Akademiia Nauk SSSR Doklady*, 30:301–305.

Könyves, V., P. André, A. Men'shchikov, P. Palmeirim, D. Arzoumanian, N. Schneider, A. Roy, P. Didelon, A. Maury, Y. Shimajiri, J. Di Francesco, S. Bontemps, N. Peretto, M. Benedettini, J.-P. Bernard, D. Elia, M. J. Griffin, T. Hill, J. Kirk, B. Ladjelate, K. Marsh, P. G. Martin, F. Motte, Q. Nguyên Luong, S. Pezzuto, H. Roussel, K. L. J. Rygl, S. I. Sadavoy, E. Schisano, L. Spinoglio, D. Ward-Thompson, and G. J. White
2015. A census of dense cores in the Aquila cloud complex: SPIRE/PACS observations from the Herschel Gould Belt survey. *Astronomy and Astrophysics*, 584:A91.

Könyves, V., P. André, A. Men'shchikov, N. Schneider, D. Arzoumanian, S. Bontemps, M. Attard, F. Motte, P. Didelon, A. Maury, A. Abergel, B. Ali, J.-P. Baluteau, J.-P. Bernard, L. Cambrésy, P. Cox, J. di Francesco, A. M. di Giorgio, M. J. Griffin, P. Hargrave, M. Huang, J. Kirk, J. Z. Li, P. Martin, V. Minier, S. Molinari, G. Olofsson, S. Pezzuto, D. Russeil, H. Roussel, P. Saraceno, M. Sauvage, B. Sibthorpe, L. Spinoglio, L. Testi, D. Ward-Thompson, G. White, C. D. Wilson, A. Woodcraft, and A. Zavagno
2010. The Aquila prestellar core population revealed by Herschel. *Astronomy and Astrophysics*, 518:L106.

Körtgen, B., C. Federrath, and R. Banerjee
2019. On the shape and completeness of the column density probability distribution function of molecular clouds. *Monthly Notices of the Royal Astronomical Society*, 482(4):5233–5240.

Koyama, H. and S.-i. Inutsuka
2002. An Origin of Supersonic Motions in Interstellar Clouds. *The Astrophysical Journal*, 564:L97–L100.

Koyama, H. and S.-i. Inutsuka
2004. The Field Condition: A New Constraint on Spatial Resolution in Simulations of the Nonlinear Development of Thermal Instability. *The Astrophysical Journal*, 602(1):L25–L28.

Kritsuk, A. G., C. T. Lee, and M. L. Norman
2013. A supersonic turbulence origin of Larson's laws. *Monthly Notices of the Royal Astronomical Society*, 436:3247–3261.

Kritsuk, A. G. and M. L. Norman
2002. Thermal Instability-induced Interstellar Turbulence. *The Astrophysical Journal*, 569:L127–L131.

Kritsuk, A. G., M. L. Norman, P. Padoan, and R. Wagner
2007. The Statistics of Supersonic Isothermal Turbulence. *The Astrophysical Journal*, 665:416–431.

Kuiper, T. B. H., W. D. Langer, and T. Velusamy
1996. Evolutionary Status of the Pre-protostellar Core L1498. *The Astrophysical Journal*, 468:761.

Lada, C. J., J. Alves, and E. A. Lada
1999. Infrared Extinction and the Structure of the IC 5146 Dark Cloud. *The Astrophysical Journal*, 512(1):250–259.

Lada, C. J., E. A. Lada, D. P. Clemens, and J. Bally
1994. Dust Extinction and Molecular Gas in the Dark Cloud IC 5146. *The Astrophysical Journal*, 429:694.

Ladd, E. F. and P. C. Myers
1991. The Anomaly of AB Aurigae: Big Star in a Land of Small Cores. In *Atoms, Ions and Molecules: New Results in Spectral Line Astrophysics*, A. D. Haschick and P. T. P. Ho, eds., volume 16 of *Astronomical Society of the Pacific Conference Series*, P. 241.

Larson, R. B.
1981. Turbulence and star formation in molecular clouds. *Monthly Notices of the Royal Astronomical Society*, 194:809–826.

Larson, R. B.
1985. Cloud fragmentation and stellar masses. *Monthly Notices of the Royal Astronomical Society*, 214:379–398.

Lee, C. W. and P. C. Myers
1999. A Catalog of Optically Selected Cores. *Astrophysical Journal Supplement Series*, 123:233–250.

Lee, K. I., M. Fernández-López, S. Storm, L. W. Looney, L. G. Mundy, D. Segura-Cox, P. Teuben, E. Rosolowsky, H. G. Arce, E. C. Ostriker, Y. L. Shirley, W. Kwon, J. Kauffmann, J. J. Tobin, A. L. Plunkett, M. W. Pound, D. M. Salter, N. H. Volgenau, C.-Y. Chen, K. Tassis, A. Isella, R. M. Crutcher, C. F. Gammie, and L. Testi
2014. CARMA Large Area Star Formation Survey: Structure and Kinematics of Dense Gas in Serpens Main. *The Astrophysical Journal*, 797(2):76.

Li, H. B., A. Goodman, T. K. Sridharan, M. Houde, Z. Y. Li, G. Novak, and K. S. Tang
2014. The Link Between Magnetic Fields and Cloud/Star Formation. In *Protostars and Planets VI*, H. Beuther, R. S. Klessen, C. P. Dullemond, and T. Henning, eds., P. 101.

Lizano, S. and F. H. Shu
1989. Molecular Cloud Cores and Bimodal Star Formation. *The Astrophysical Journal*, 342:834.

Lombardi, M. and J. Alves
2001. Mapping the interstellar dust with near-infrared observations: An optimized multiband technique. *Astronomy and Astrophysics*, 377:1023–1034.

Lombardi, M., J. Alves, and C. J. Lada
2006. 2MASS wide field extinction maps. I. The Pipe nebula. *Astronomy and Astrophysics*, 454:781–796.

Lu, X., Q. Zhang, H. B. Liu, P. Sanhueza, K. Tatematsu, S. Feng, H. A. Smith, P. C. Myers, T. K. Sridharan, and Q. Gu
2018. Filamentary Fragmentation and Accretion in High-mass Star-forming Molecular Clouds. *The Astrophysical Journal*, 855(1):9.

Lu, X., Q. Zhang, H. B. Liu, J. Wang, and Q. Gu
2014. Very Large Array Observations of Ammonia in High-mass Star Formation Regions. *The Astrophysical Journal*, 790(2):84.

Lynn, W. T.
1887. First discovery of the great nebula in Orion. *The Observatory*, 10:232–233.

Mac Low, M.-M.
1999. The Energy Dissipation Rate of Supersonic, Magnetohydrodynamic Turbulence in Molecular Clouds. *The Astrophysical Journal*, 524:169–178.

Mac Low, M.-M. and R. S. Klessen
2004. Control of star formation by supersonic turbulence. *Reviews of Modern Physics*, 76:125–194.

Mac Low, M.-M., R. S. Klessen, A. Burkert, and M. D. Smith
1998. Kinetic Energy Decay Rates of Supersonic and Super-Alfvénic Turbulence in Star-Forming Clouds. *Physical Review Letters*, 80:2754–2757.

Maloney, P.
1988. The turbulent interstellar medium and pressure-bounded molecular clouds. *The Astrophysical Journal*, 334:761–770.

Marsh, K. A., M. J. Griffin, P. Palmeirim, P. André, J. Kirk, D. Stamatellos, D. Ward-Thompson, A. Roy, S. Bontemps, J. di Francesco, D. Elia, T. Hill, V. Könyves, F. Motte, Q. Nguyen-Luong, N. Peretto, S. Pezzuto, A. Rivera-Ingraham, N. Schneider, L. Spinoglio, and G. White
2014. Properties of starless and prestellar cores in Taurus revealed by Herschel: SPIRE/PACS imaging. *Monthly Notices of the Royal Astronomical Society*, 439:3683–3693.

Marsh, K. A., J. M. Kirk, P. André, M. J. Griffin, V. Könyves, P. Palmeirim, A. Men'shchikov, D. Ward-Thompson, M. Benedettini, D. W. Bresnahan, J. di Francesco, D. Elia, F. Motte, N. Peretto, S. Pezzuto, A. Roy, S. Sadavoy, N. Schneider, L. Spinoglio, and G. J. White
2016. A census of dense cores in the Taurus L1495 cloud from the Herschel Gould Belt Survey. *Monthly Notices of the Royal Astronomical Society*, 459(1):342–356.

Mathis, J. S., W. Rumpl, and K. H. Nordsieck
1977. The size distribution of interstellar grains. *The Astrophysical Journal*, 217:425–433.

Matzner, C. D. and C. F. McKee
2000. Efficiencies of Low-Mass Star and Star Cluster Formation. *The Astrophysical Journal*, 545(1):364–378.

McCrea, W. H.
1957. The formation of Population I Stars. Part I. Gravitational contraction. *Monthly Notices of the Royal Astronomical Society*, 117:562.

McKee, C. F. and I. Holliman, John H.
1999. Multipressure Polytropes as Models for the Structure and Stability of Molecular Clouds. I. Theory. *The Astrophysical Journal*, 522(1):313–337.

McKee, C. F. and E. C. Ostriker
2007. Theory of Star Formation. *Annual review of astronomy and Astrophysics*, 45:565–687.

McKee, C. F. and J. P. Ostriker
1977. A theory of the interstellar medium: three components regulated by supernova explosions in an inhomogeneous substrate. *The Astrophysical Journal*, 218:148–169.

McKee, C. F. and E. G. Zweibel
1995. Alfven Waves in Interstellar Gasdynamics. *The Astrophysical Journal*, 440:686.

McLaughlin, D. E. and R. E. Pudritz
1997. Gravitational Collapse and Star Formation in Logotropic and Nonisothermal Spheres. *The Astrophysical Journal*, 476(2):750–765.

Men'shchikov, A.
2013. A multi-scale filament extraction method: getfilaments. *Astronomy and Astrophysics*, 560:A63.

Men'shchikov, A., P. André, P. Didelon, V. Könyves, N. Schneider, F. Motte, S. Bontemps, D. Arzoumanian, M. Attard, A. Abergel, J.-P. Baluteau, J.-P. Bernard, L. Cambrésy, P. Cox, J. di Francesco, A. M. di Giorgio, M. Griffin, P. Hargrave, M. Huang, J. Kirk, J. Z. Li, P. Martin, V. Minier, M.-A. Miville-Deschênes, S. Molinari, G. Olofsson, S. Pezzuto, H. Roussel, D. Russeil, P. Saraceno, M. Sauvage, B. Sibthorpe, L. Spinoglio, L. Testi, D. Ward-Thompson, G. White, C. D. Wilson, A. Woodcraft, and A. Zavagno
2010. Filamentary structures and compact objects in the Aquila and Polaris clouds observed by Herschel. *Astronomy and Astrophysics*, 518:L103.

Mierkiewicz, E. J., R. J. Reynolds, F. L. Roesler, J. M. Harlander, and K. P. Jaehnig
2006. Detection of Diffuse Interstellar [O II] Emission from the Milky Way Using Spatial Heterodyne Spectroscopy. *The Astrophysical Journal*, 650(1):L63–L66.

Miettinen, O.
2012. A molecular line study of the filamentary infrared dark cloud G304.74+01.32. *Astronomy and Astrophysics*, 540:A104.

Miettinen, O. and J. Harju
2010. LABOCA mapping of the infrared dark cloud MSXDC G304.74+01.32. *Astronomy and Astrophysics*, 520:A102.

Mignone, A., G. Bodo, S. Massaglia, T. Matsakos, O. Tesileanu, C. Zanni, and A. Ferrari
2007. PLUTO: A Numerical Code for Computational Astrophysics. *Astrophysical Journal Supplement Series*, 170(1):228–242.

Miville-Deschênes, M.-A., P. G. Martin, A. Abergel, J.-P. Bernard, F. Boulanger, G. Lagache, L. D. Anderson, P. André, H. Arab, J.-P. Baluteau, K. Blagrave, S. Bontemps, M. Cohen, M. Compiegne, P. Cox, E. Dartois, G. Davis, R. Emery, T. Fulton, C. Gry, E. Habart, M. Huang, C. Joblin, S. C. Jones, J. Kirk, T. Lim, S. Madden, G. Makiwa, A. Menshchikov,

S. Molinari, H. Moseley, F. Motte, D. A. Naylor, K. Okumura, D. Pinheiro Gonçalves, E. Polehampton, J. A. Rodón, D. Russeil, P. Saraceno, N. Schneider, S. Sidher, L. Spencer, B. Swinyard, D. Ward-Thompson, G. J. White, and A. Zavagno
2010. Herschel-SPIRE observations of the Polaris flare: Structure of the diffuse interstellar medium at the sub-parsec scale. *Astronomy and Astrophysics*, 518:L104.

Mizuno, A., T. Onishi, Y. Yonekura, T. Nagahama, H. Ogawa, and Y. Fukui
1995. Overall Distribution of Dense Molecular Gas and Star Formation in the Taurus Cloud Complex. *The Astrophysical Journal*, 445:L161.

Moeckel, N. and A. Burkert
2015. The Formation of Filamentary Bundles in Turbulent Molecular Clouds. *The Astrophysical Journal*, 807:67.

Molinari, S., B. Swinyard, J. Bally, M. Barlow, J.-P. Bernard, P. Martin, T. Moore, A. Noriega-Crespo, R. Plume, L. Testi, A. Zavagno, A. Abergel, B. Ali, L. Anderson, P. André, J.-P. Baluteau, C. Battersby, M. T. Beltrán, M. Benedettini, N. Billot, J. Blommaert, S. Bontemps, F. Boulanger, J. Brand, C. Brunt, M. Burton, L. Calzoletti, S. Carey, P. Caselli, R. Cesaroni, J. Cernicharo, S. Chakrabarti, A. Chrysostomou, M. Cohen, M. Compiegne, P. de Bernardis, G. de Gasperis, A. M. di Giorgio, D. Elia, F. Faustini, N. Flagey, Y. Fukui, G. A. Fuller, K. Ganga, P. Garcia-Lario, J. Glenn, P. F. Goldsmith, M. Griffin, M. Hoare, M. Huang, D. Ikhenaode, C. Joblin, G. Joncas, M. Juvela, J. M. Kirk, G. Lagache, J. Z. Li, T. L. Lim, S. D. Lord, M. Marengo, D. J. Marshall, S. Masi, F. Massi, M. Matsuura, V. Minier, M.-A. Miville-Deschênes, L. A. Montier, L. Morgan, F. Motte, J. C. Mottram, T. G. Müller, P. Natoli, J. Neves, L. Olmi, R. Paladini, D. Paradis, H. Parsons, N. Peretto, M. Pestalozzi, S. Pezzuto, F. Piacentini, L. Piazzo, D. Polychroni, M. Pomarès, C. C. Popescu, W. T. Reach, I. Ristorcelli, J.-F. Robitaille, T. Robitaille, J. A. Rodón, A. Roy, P. Royer, D. Russeil, P. Saraceno, M. Sauvage, P. Schilke, E. Schisano, N. Schneider, F. Schuller, B. Schulz, B. Sibthorpe, H. A. Smith, M. D. Smith, L. Spinoglio, D. Stamatellos, F. Strafella, G. S. Stringfellow, E. Sturm, R. Taylor, M. A. Thompson, A. Traficante, R. J. Tuffs, G. Umana, L. Valenziano, R. Vavrek, M. Veneziani, S. Viti, C. Waelkens, D. Ward-Thompson, G. White, L. A. Wilcock, F. Wyrowski, H. W. Yorke, and Q. Zhang
2010. Clouds, filaments, and protostars: The Herschel Hi-GAL Milky Way. *Astronomy and Astrophysics*, 518:L100.

Morris, M. and E. Serabyn
1996. The Galactic Center Environment. *Annual review of astronomy and Astrophysics*, 34:645–702.

Motte, F., P. Andre, and R. Neri
1998. The initial conditions of star formation in the rho Ophiuchi main cloud: wide-field millimeter continuum mapping. *Astronomy and Astrophysics*, 336:150–172.

Myers, P. C.
1983. Dense cores in dark clouds. III - Subsonic turbulence. *The Astrophysical Journal*, 270:105–118.

Myers, P. C.
2009. Filamentary Structure of Star-forming Complexes. *The Astrophysical Journal*, 700:1609–1625.

Nachman, P.
1979. Molecular line studies of dark clouds with associated young stellar objects. *Astrophysical Journal Supplement Series*, 39:103–133.

Nagasawa, M.
1987. Gravitational Instability of the Isothermal Gas Cylinder with an Axial magnetic Field. *Progress of Theoretical Physics*, 77:635–652.

Nakamura, F., T. Hanawa, and T. Nakano
1993. Fragmentation of filamentary molecular clouds with longitudinal and helical magnetic fields. *Publications of the Astronomical Society of Japan*, 45:551–566.

Nakamura, F. and Z.-Y. Li
2005. Quiescent Cores and the Efficiency of Turbulence-accelerated, Magnetically Regulated Star Formation. *The Astrophysical Journal*, 631:411–428.

Nakamura, F. and M. Umemura
1999. On the Mass of Population III Stars. *The Astrophysical Journal*, 515(1):239–248.

Narayanan, G., M. H. Heyer, C. Brunt, P. F. Goldsmith, R. Snell, and D. Li
2008. The Five College Radio Astronomy Observatory CO Mapping Survey of the Taurus Molecular Cloud. *Astrophysical Journal Supplement Series*, 177(1):341–361.

Ntormousi, E., A. Burkert, K. Fierlinger, and F. Heitsch
2011. Formation of Cold Filamentary Structure from Wind-blown Superbubbles. *The Astrophysical Journal*, 731(1):13.

Nutter, D., J. M. Kirk, D. Stamatellos, and D. Ward-Thompson
2008. SCUBA and Spitzer observations of the Taurus molecular cloud - pulling the bull's tail. *Monthly Notices of the Royal Astronomical Society*, 384(2):755–763.

Ostriker, E. C., C. F. Gammie, and J. M. Stone
1999. Kinetic and Structural Evolution of Self-gravitating, Magnetized Clouds: 2.5-dimensional Simulations of Decaying Turbulence. *The Astrophysical Journal*, 513(1):259–274.

Ostriker, J.
1964. The Equilibrium of Polytropic and Isothermal Cylinders. *The Astrophysical Journal*, 140:1056.

Padoan, P., M. Juvela, A. A. Goodman, and Å. Nordlund
2001. The Turbulent Shock Origin of Proto-Stellar Cores. *The Astrophysical Journal*, 553:227–234.

Padoan, P. and Å. Nordlund
1999. A Super-Alfvénic Model of Dark Clouds. *The Astrophysical Journal*, 526:279–294.

Padoan, P., A. Nordlund, and B. J. T. Jones
1997. The universality of the stellar initial mass function. *Monthly Notices of the Royal Astronomical Society*, 288:145–152.

Padoan, P., L. Pan, T. Haugbølle, and Å. Nordlund
2016. Supernova Driving. I. The Origin of Molecular Cloud Turbulence. *The Astrophysical Journal*, 822:11.

Pagani, L., C. Lefèvre, M. Juvela, V. M. Pelkonen, and F. Schuller
2015. Can we trace very cold dust from its emission alone? *Astronomy and Astrophysics*, 574:L5.

Palau, A., L. A. Zapata, C. G. Román-Zúñiga, Á. Sánchez-Monge, R. Estalella, G. Busquet, J. M. Girart, A. Fuente, and B. Commerçon
2018. Thermal Jeans Fragmentation within ÌČ1000 au in OMC-1S. *The Astrophysical Journal*, 855(1):24.

Palla, F. and S. W. Stahler
2000. Accelerating Star Formation in Clusters and Associations. *The Astrophysical Journal*, 540:255–270.

Palmeirim, P., P. André, J. Kirk, D. Ward-Thompson, D. Arzoumanian, V. Könyves, P. Didelon, N. Schneider, M. Benedettini, S. Bontemps, J. Di Francesco, D. Elia, M. Griffin, M. Hennemann, T. Hill, P. G. Martin, A. Men'shchikov, S. Molinari, F. Motte, Q. Nguyen Luong, D. Nutter, N. Peretto, S. Pezzuto, A. Roy, K. L. J. Rygl, L. Spinoglio, and G. L. White
2013. Herschel view of the Taurus B211/3 filament and striations: evidence of filamentary growth? *Astronomy and Astrophysics*, 550:A38.

Panopoulou, G. V., I. Psaradaki, R. Skalidis, K. Tassis, and J. J. Andrews
2017. A closer look at the 'characteristic' width of molecular cloud filaments. *Monthly Notices of the Royal Astronomical Society*, 466(3):2529–2541.

Panopoulou, G. V., K. Tassis, P. F. Goldsmith, and M. H. Heyer
2014. ^{13}CO filaments in the Taurus molecular cloud. *Monthly Notices of the Royal Astronomical Society*, 444(3):2507–2524.

Passot, T. and E. Vázquez-Semadeni
1998. Density probability distribution in one-dimensional polytropic gas dynamics. *Physical Review E*, 58:4501–4510.

Perault, M., A. Omont, G. Simon, P. Seguin, D. Ojha, J. Blommaert, M. Felli, G. Gilmore, F. Guglielmo, H. Habing, S. Price, A. Robin, B. de Batz, C. Cesarsky, D. Elbaz, N. Epchtein, P. Fouque, S. Guest, D. Levine, A. Pollock, T. Prusti, R. Siebenmorgen,

L. Testi, and D. Tiphene
1996. First ISOCAM images of the Milky Way. *Astronomy and Astrophysics*, 315:L165–L168.

Peretto, N., P. André, V. Könyves, N. Schneider, D. Arzoumanian, P. Palmeirim, P. Didelon, M. Attard, J. P. Bernard, J. Di Francesco, D. Elia, M. Hennemann, T. Hill, J. Kirk, A. Men'shchikov, F. Motte, Q. Nguyen Luong, H. Roussel, T. Sousbie, L. Testi, D. Ward-Thompson, G. J. White, and A. Zavagno
2012. The Pipe Nebula as seen with Herschel: formation of filamentary structures by large-scale compression? *Astronomy and Astrophysics*, 541:A63.

Peretto, N. and G. A. Fuller
2009. The initial conditions of stellar protocluster formation. I. A catalogue of Spitzer dark clouds. *Astronomy and Astrophysics*, 505(1):405–415.

Pilbratt, G. L., J. R. Riedinger, T. Passvogel, G. Crone, D. Doyle, U. Gageur, A. M. Heras, C. Jewell, L. Metcalfe, S. Ott, and M. Schmidt
2010. Herschel Space Observatory. An ESA facility for far-infrared and submillimetre astronomy. *Astronomy and Astrophysics*, 518:L1.

Pineda, J. E., A. A. Goodman, H. G. Arce, P. Caselli, J. B. Foster, P. C. Myers, and E. W. Rosolowsky
2010. Direct Observation of a Sharp Transition to Coherence in Dense Cores. *The Astrophysical Journal*, 712(1):L116–L121.

Pineda, J. E., A. A. Goodman, H. G. Arce, P. Caselli, S. Longmore, and S. Corder
2011. Expanded Very Large Array Observations of the Barnard 5 Star-forming Core: Embedded Filaments Revealed. *The Astrophysical Journal*, 739(1):L2.

Planck Collaboration, P. A. R. Ade, N. Aghanim, M. I. R. Alves, M. Arnaud, D. Arzoumanian, M. Ashdown, J. Aumont, C. Baccigalupi, A. J. Banday, R. B. Barreiro, N. Bartolo, E. Battaner, K. Benabed, A. Benoît, A. Benoit-Lévy, J.-P. Bernard, M. Bersanelli, P. Bielewicz, J. J. Bock, L. Bonavera, J. R. Bond, J. Borrill, F. R. Bouchet, F. Boulanger, A. Bracco, C. Burigana, E. Calabrese, J.-F. Cardoso, A. Catalano, H. C. Chiang, P. R. Christensen, L. P. L. Colombo, C. Combet, F. Couchot, B. P. Crill, A. Curto, F. Cuttaia, L. Danese, R. D. Davies, R. J. Davis, P. de Bernardis, A. de Rosa, G. de Zotti, J. Delabrouille, C. Dickinson, J. M. Diego, H. Dole, S. Donzelli, O. Doré, M. Douspis, A. Ducout, X. Dupac, G. Efstathiou, F. Elsner, T. A. Enßlin, H. K. Eriksen, D. Falceta-Gonçalves, E. Falgarone, K. Ferrière, F. Finelli, O. Forni, M. Frailis, A. A. Fraisse, E. Franceschi, A. Frejsel, S. Galeotta, S. Galli, K. Ganga, T. Ghosh, M. Giard, E. Gjerløw, J. González-Nuevo, K. M. Górski, A. Gregorio, A. Gruppuso, J. E. Gudmundsson, V. Guillet, D. L. Harrison, G. Helou, P. Hennebelle, S. Henrot-Versillé, C. Hernández-Monteagudo, D. Herranz, S. R. Hildebrandt, E. Hivon, W. A. Holmes, A. Hornstrup, K. M. Huffenberger, G. Hurier, A. H. Jaffe, T. R. Jaffe, W. C. Jones, M. Juvela, E. Keihänen, R. Keskitalo, T. S. Kisner, J. Knoche, M. Kunz, H. Kurki-Suonio, G. Lagache, J.-M. Lamarre, A. Lasenby, M. Lattanzi, C. R. Lawrence, R. Leonardi, F. Levrier, M. Liguori,

P. B. Lilje, M. Linden-Vørnle, M. López-Caniego, P. M. Lubin, J. F. Macías-Pérez, D. Maino, N. Mandolesi, A. Mangilli, M. Maris, P. G. Martin, E. Martínez-González, S. Masi, S. Matarrese, A. Melchiorri, L. Mendes, A. Mennella, M. Migliaccio, M.-A. Miville-Deschênes, A. Moneti, L. Montier, G. Morgante, D. Mortlock, D. Munshi, J. A. Murphy, P. Naselsky, F. Nati, C. B. Netterfield, F. Noviello, D. Novikov, I. Novikov, N. Oppermann, C. A. Oxborrow, L. Pagano, F. Pajot, R. Paladini, D. Paoletti, F. Pasian, L. Perotto, V. Pettorino, F. Piacentini, M. Piat, E. Pierpaoli, D. Pietrobon, S. Plaszczynski, E. Pointecouteau, G. Polenta, N. Ponthieu, G. W. Pratt, S. Prunet, J.-L. Puget, J. P. Rachen, M. Reinecke, M. Remazeilles, C. Renault, A. Renzi, I. Ristorcelli, G. Rocha, M. Rossetti, G. Roudier, J. A. Rubiño-Martín, B. Rusholme, M. Sandri, D. Santos, M. Savelainen, G. Savini, D. Scott, J. D. Soler, V. Stolyarov, R. Sudiwala, D. Sutton, A.-S. Suur-Uski, J.-F. Sygnet, J. A. Tauber, L. Terenzi, L. Toffolatti, M. Tomasi, M. Tristram, M. Tucci, G. Umana, L. Valenziano, J. Valiviita, B. Van Tent, P. Vielva, F. Villa, L. A. Wade, B. D. Wandelt, I. K. Wehus, N. Ysard, D. Yvon, and A. Zonca
2016. Planck intermediate results. XXXV. Probing the role of the magnetic field in the formation of structure in molecular clouds. *Astronomy and Astrophysics*, 586:A138.

Plummer, H. C.
1911. On the problem of distribution in globular star clusters. *Monthly Notices of the Royal Astronomical Society*, 71:460–470.

Pon, A., D. Johnstone, and F. Heitsch
2011. Modes of Star Formation in Finite Molecular Clouds. *The Astrophysical Journal*, 740(2):88.

Pon, A., J. A. Toalá, D. Johnstone, E. Vázquez-Semadeni, F. Heitsch, and G. C. Gómez
2012. Aspect Ratio Dependence of the Free-fall Time for Non-spherical Symmetries. *The Astrophysical Journal*, 756:145.

Porter, D. H., A. Pouquet, and P. R. Woodward
1994. Kolmogorov-like spectra in decaying three-dimensional supersonic flows. *Physics of Fluids*, 6:2133–2142.

Predehl, P. and J. H. M. M. Schmitt
1995. X-raying the interstellar medium: ROSAT observations of dust scattering halos. *Astronomy and Astrophysics*, 500:459–475.

Press, W. H. and P. Schechter
1974. Formation of Galaxies and Clusters of Galaxies by Self-Similar Gravitational Condensation. *The Astrophysical Journal*, 187:425–438.

Recchi, S., A. Hacar, and A. Palestini
2013. Nonisothermal filaments in equilibrium. *Astronomy and Astrophysics*, 558:A27.

Reynolds, R. J., F. Scherb, and F. L. Roesler
1973. Observations of Diffuse Galactic HA and [n II] Emission. *The Astrophysical Journal*, 185:869–876.

Roe, P. L.
1981. Approximate Riemann Solvers, Parameter Vectors, and Difference Schemes. *Journal of Computational Physics*, 43:357–372.

Roy, A., P. André, D. Arzoumanian, M. A. Miville-Deschênes, V. Könyves, N. Schneider, S. Pezzuto, P. Palmeirim, and J. M. Kirk
2019. How the power spectrum of dust continuum images may hide the presence of a characteristic filament width. *Astronomy and Astrophysics*, 626:A76.

Roy, A., P. André, D. Arzoumanian, N. Peretto, P. Palmeirim, V. Könyves, N. Schneider, M. Benedettini, J. Di Francesco, D. Elia, T. Hill, B. Ladjelate, F. Louvet, F. Motte, S. Pezzuto, E. Schisano, Y. Shimajiri, L. Spinoglio, D. Ward-Thompson, and G. White
2015. Possible link between the power spectrum of interstellar filaments and the origin of the prestellar core mass function. *Astronomy and Astrophysics*, 584:A111.

Roy, A., P. André, P. Palmeirim, M. Attard, V. Könyves, N. Schneider, N. Peretto, A. Men'shchikov, D. Ward-Thompson, J. Kirk, M. Griffin, K. Marsh, A. Abergel, D. Arzoumanian, M. Benedettini, T. Hill, F. Motte, Q. Nguyen Luong, S. Pezzuto, A. Rivera-Ingraham, H. Roussel, K. L. J. Rygl, L. Spinoglio, D. Stamatellos, and G. White
2014. Reconstructing the density and temperature structure of prestellar cores from Herschel data: A case study for B68 and L1689B. *Astronomy and Astrophysics*, 562:A138.

Roy, N., N. Kanekar, and J. N. Chengalur
2013. The temperature of the diffuse H I in the Milky Way - II. Gaussian decomposition of the H I-21 cm absorption spectra. *Monthly Notices of the Royal Astronomical Society*, 436(3):2366–2385.

Salpeter, E. E.
1955. The Luminosity Function and Stellar Evolution. *The Astrophysical Journal*, 121:161.

Schaap, W. E. and R. van de Weygaert
2000. Continuous fields and discrete samples: reconstruction through Delaunay tessellations. *Astronomy and Astrophysics*, 363:L29–L32.

Schisano, E., K. L. J. Rygl, S. Molinari, G. Busquet, D. Elia, M. Pestalozzi, D. Polychroni, N. Billot, S. Carey, R. Paladini, A. Noriega-Crespo, T. J. T. Moore, R. Plume, S. C. O. Glover, and E. Vázquez-Semadeni
2014. The Identification of Filaments on Far-infrared and Submillimiter Images: Morphology, Physical Conditions and Relation with Star Formation of Filamentary Structure. *The Astrophysical Journal*, 791(1):27.

Schneider, N., P. André, V. Könyves, S. Bontemps, F. Motte, C. Federrath, D. Ward-Thompson, D. Arzoumanian, M. Benedettini, E. Bressert, P. Didelon, J. Di Francesco, M. Griffin, M. Hennemann, T. Hill, P. Palmeirim, S. Pezzuto, N. Peretto, A. Roy, K. L. J. Rygl, L. Spinoglio, and G. White
2013. What Determines the Density Structure of Molecular Clouds? A Case Study of Orion B with Herschel. *The Astrophysical Journal*, 766:L17.

Schneider, N., T. Csengeri, S. Bontemps, F. Motte, R. Simon, P. Hennebelle, C. Federrath, and R. Klessen
2010. Dynamic star formation in the massive DR21 filament. *Astronomy and Astrophysics*, 520:A49.

Schneider, N., T. Csengeri, M. Hennemann, F. Motte, P. Didelon, C. Federrath, S. Bontemps, J. Di Francesco, D. Arzoumanian, V. Minier, P. André, T. Hill, A. Zavagno, Q. Nguyen-Luong, M. Attard, J.-P. Bernard, D. Elia, C. Fallscheer, M. Griffin, J. Kirk, R. Klessen, V. Könyves, P. Martin, A. Men'shchikov, P. Palmeirim, N. Peretto, M. Pestalozzi, D. Russeil, S. Sadavoy, T. Sousbie, L. Testi, P. Tremblin, D. Ward-Thompson, and G. White
2012. Cluster-formation in the Rosette molecular cloud at the junctions of filaments. *Astronomy and Astrophysics*, 540:L11.

Schneider, S. and B. G. Elmegreen
1979. A catalog of dark globular filaments. *Astrophysical Journal Supplement Series*, 41:87–95.

Seifried, D. and S. Walch
2015. The impact of turbulence and magnetic field orientation on star-forming filaments. *Monthly Notices of the Royal Astronomical Society*, 452(3):2410–2422.

Seifried, D., S. Walch, P. Girichidis, T. Naab, R. Wünsch, R. S. Klessen, S. C. O. Glover, T. Peters, and P. Clark
2017. SILCC-Zoom: the dynamic and chemical evolution of molecular clouds. *Monthly Notices of the Royal Astronomical Society*, 472(4):4797–4818.

Shimajiri, Y., P. André, P. Palmeirim, D. Arzoumanian, A. Bracco, V. Könyves, E. Ntormousi, and B. Ladjelate
2019. Probing accretion of ambient cloud material into the Taurus B211/B213 filament. *Astronomy and Astrophysics*, 623:A16.

Shu, F. H., F. C. Adams, and S. Lizano
1987. Star formation in molecular clouds - Observation and theory. *Annual review of astronomy and Astrophysics*, 25:23–81.

Shu, H. F.
1992. *The Physics of Astrophysics - Gas Dynamics*, volume 2. Sausalito, United States of America: University Science Books.

Smith, R. J., S. C. O. Glover, and R. S. Klessen
2014. On the nature of star-forming filaments - I. Filament morphologies. *Monthly Notices of the Royal Astronomical Society*, 445:2900–2917.

Smith, R. J., S. C. O. Glover, R. S. Klessen, and G. A. Fuller
2016. On the nature of star-forming filaments - II. Subfilaments and velocities. *Monthly Notices of the Royal Astronomical Society*, 455:3640–3655.

Soler, J. D., P. Hennebelle, P. G. Martin, M. A. Miville-Deschênes, C. B. Netterfield, and L. M. Fissel
2013. An Imprint of Molecular Cloud Magnetization in the Morphology of the Dust Polarized Emission. *The Astrophysical Journal*, 774(2):128.

Sousbie, T.
2011. The persistent cosmic web and its filamentary structure - I. Theory and implementation. *Monthly Notices of the Royal Astronomical Society*, 414(1):350–383.

Springel, V.
2010. E pur si muove: Galilean-invariant cosmological hydrodynamical simulations on a moving mesh. *Monthly Notices of the Royal Astronomical Society*, 401(2):791–851.

Stanke, T., M. D. Smith, R. Gredel, and T. Khanzadyan
2006. An unbiased search for the signatures of protostars in the ρ Ophiuchi molecular cloud . II. Millimetre continuum observations. *Astronomy and Astrophysics*, 447(2):609–622.

Starck, J. L., D. L. Donoho, and E. J. Candès
2003. Astronomical image representation by the curvelet transform. *Astronomy and Astrophysics*, 398:785–800.

Steinacker, J., A. Bacmann, T. Henning, and S. Heigl
2016. Prestellar core modeling in the presence of a filament. The dense heart of L1689B. *Astronomy and Astrophysics*, 593:A6.

Stodólkiewicz, J. S.
1963. On the Gravitational Instability of Some Magneto-Hydrodynamical Systems of Astrophysical Interest. Part III. *Acta Astronomica*, 13:30–54.

Stone, J. M., T. A. Gardiner, P. Teuben, J. F. Hawley, and J. B. Simon
2008. Athena: A New Code for Astrophysical MHD. *Astrophysical Journal Supplement Series*, 178(1):137–177.

Stone, J. M. and M. L. Norman
1992. ZEUS-2D: A Radiation Magnetohydrodynamics Code for Astrophysical Flows in Two Space Dimensions. I. The Hydrodynamic Algorithms and Tests. *Astrophysical Journal Supplement Series*, 80:753.

Stone, J. M., E. C. Ostriker, and C. F. Gammie
1998. Dissipation in Compressible Magnetohydrodynamic Turbulence. *The Astrophysical Journal*, 508:L99–L102.

Suri, S., Á. Sánchez-Monge, P. Schilke, S. D. Clarke, R. J. Smith, V. Ossenkopf-Okada, R. Klessen, P. Padoan, P. Goldsmith, H. G. Arce, J. Bally, J. M. Carpenter, A. Ginsburg, D. Johnstone, J. Kauffmann, S. Kong, D. C. Lis, S. Mairs, T. Pillai, J. E. Pineda, and A. Duarte-Cabral
2019. The CARMA-NRO Orion Survey. Filamentary structure as seen in $C^{18}O$ emission. *Astronomy and Astrophysics*, 623:A142.

Tafalla, M. and A. Hacar
2015. Chains of dense cores in the Taurus L1495/B213 complex. *Astronomy and Astrophysics*, 574:A104.

Tafalla, M., P. C. Myers, P. Caselli, and C. M. Walmsley
2004. On the internal structure of starless cores. I. Physical conditions and the distribution of CO, CS, N_2H^+, and NH_3 in L1498 and L1517B. *Astronomy and Astrophysics*, 416:191–212.

Tafalla, M., J. Santiago-García, P. C. Myers, P. Caselli, C. M. Walmsley, and A. Crapsi
2006. On the internal structure of starless cores. II. A molecular survey of L1498 and L1517B. *Astronomy and Astrophysics*, 455:577–593.

Takahashi, S., P. T. P. Ho, P. S. Teixeira, L. A. Zapata, and Y.-N. Su
2013. Hierarchical Fragmentation of the Orion Molecular Filaments. *The Astrophysical Journal*, 763(1):57.

Tanaka, T., F. Nakamura, Y. Awazu, Y. Shimajiri, K. Sugitani, T. Onishi, R. Kawabe, H. Yoshida, and A. E. Higuchi
2013. The Dynamical State of the Serpens South Filamentary Infrared Dark Cloud. *The Astrophysical Journal*, 778:34.

Teixeira, P. S., S. Takahashi, L. A. Zapata, and P. T. P. Ho
2016. Two-level hierarchical fragmentation in the northern filament of the Orion Molecular Cloud 1. *Astronomy and Astrophysics*, 587:A47.

Teyssier, R.
2002. Cosmological hydrodynamics with adaptive mesh refinement. A new high resolution code called RAMSES. *Astronomy and Astrophysics*, 385:337–364.

Tilley, D. A. and R. E. Pudritz
2004. The formation of star clusters - I. Three-dimensional simulations of hydrodynamic turbulence. *Monthly Notices of the Royal Astronomical Society*, 353(3):769–788.

Toalá, J. A., E. Vázquez-Semadeni, and G. C. Gómez
2012. The Free-fall Time of Finite Sheets and Filaments. *The Astrophysical Journal*, 744(2):190.

Toci, C. and D. Galli
2015a. Polytropic models of filamentary interstellar clouds - I. Structure and stability. *Monthly Notices of the Royal Astronomical Society*, 446:2110–2117.

Toci, C. and D. Galli
2015b. Polytropic models of filamentary interstellar clouds - II. Helical magnetic fields. *Monthly Notices of the Royal Astronomical Society*, 446(2):2118–2124.

Toro, E., M. Spruce, and W. Speares
1994. Restoration of the contact surface in the hll-riemann solver. *Shock Waves*, 4(1):25–34.

Toro, E. F.
1999. *Riemann Solvers and Numerical Methods for Fluid Dynamics*, second edition. Berlin, Germany: Springer-Verlag.

Tritsis, A., C. Federrath, N. Schneider, and K. Tassis
2018. A new method for probing magnetic field strengths from striations in the interstellar medium. *Monthly Notices of the Royal Astronomical Society*, 481(4):5275–5285.

Tritsis, A. and K. Tassis
2016. Striations in molecular clouds: streamers or MHD waves? *Monthly Notices of the Royal Astronomical Society*, 462(4):3602–3615.

Tritsis, A. and K. Tassis
2018. Magnetic seismology of interstellar gas clouds: Unveiling a hidden dimension. *Science*, 360(6389):635–638.

Truelove, J. K., R. I. Klein, C. F. McKee, J. H. Holliman, II, L. H. Howell, and J. A. Greenough
1997. The Jeans Condition: A New Constraint on Spatial Resolution in Simulations of Isothermal Self-gravitational Hydrodynamics. *The Astrophysical Journal*, 489:L179–L183.

van den Ancker, M. E., D. de Winter, and H. R. E. Tjin A Djie
1998. HIPPARCOS photometry of Herbig Ae/Be stars. *Astronomy and Astrophysics*, 330:145–154.

van Leer, B.
1976. MUSCL, a new approach to numerical gas dynamics. In *Computing in Plasma Physics and Astrophysics*, D. Biskamp, ed., P. 1.

van Leer, B.
1977. Towards the Ultimate Conservative Difference Scheme. IV. A New Approach to Numerical Convection. *Journal of Computational Physics*, 23:276.

van Leer, B.
1979. Towards the ultimate conservative difference scheme. V. A second-order sequel to Godunov's method. *Journal of Computational Physics*, 32(1):101 – 136.

van Leer, B.
1984. On the Relation Between the Upwind-Differencing Schemes of Godunov, Engquist-Osher and Roe. *SIAM J. Sci. and Stat. Comp.*, 5(1):1–20.

Vazquez-Semadeni, E.
1994. Hierarchical Structure in Nearly Pressureless Flows as a Consequence of Self-similar Statistics. *The Astrophysical Journal*, 423:681.

Vázquez-Semadeni, E., J. Ballesteros-Paredes, and R. S. Klessen
2003. A Holistic Scenario of Turbulent Molecular Cloud Evolution and Control of the Star Formation Efficiency: First Tests. *The Astrophysical Journal*, 585(2):L131–L134.

Vázquez-Semadeni, E., A. Gazol, and J. Scalo
2000. Is Thermal Instability Significant in Turbulent Galactic Gas? *The Astrophysical Journal*, 540(1):271–285.

Vázquez-Semadeni, E., J. Kim, M. Shadmehri, and J. Ballesteros-Paredes
2005. The Lifetimes and Evolution of Molecular Cloud Cores. *The Astrophysical Journal*, 618:344–359.

Vázquez-Semadeni, E., D. Ryu, T. Passot, R. F. González, and A. Gazol
2006. Molecular Cloud Evolution. I. Molecular Cloud and Thin Cold Neutral Medium Sheet Formation. *The Astrophysical Journal*, 643:245–259.

Viala, Y. P. and G. Horedt
1974. Polytropic Sheets, Cylinders and Spheres with Negative Index. *Astronomy and Astrophysics*, 33:195.

Wang, K., Q. Zhang, L. Testi, F. van der Tak, Y. Wu, H. Zhang, T. Pillai, F. Wyrowski, S. Carey, S. E. Ragan, and T. Henning
2014. Hierarchical fragmentation and differential star formation in the Galactic 'Snake': infrared dark cloud G11.11-0.12. *Monthly Notices of the Royal Astronomical Society*, 439(4):3275–3293.

Ward-Thompson, D., J. M. Kirk, P. André, P. Saraceno, P. Didelon, V. Könyves, N. Schneider, A. Abergel, J.-P. Baluteau, J.-P. Bernard, S. Bontemps, L. Cambrésy, P. Cox, J. di Francesco, A. M. di Giorgio, M. Griffin, P. Hargrave, M. Huang, J. Z. Li, P. Martin, A. Men'shchikov, V. Minier, S. Molinari, F. Motte, G. Olofsson, S. Pezzuto, D. Russeil, M. Sauvage, B. Sibthorpe, L. Spinoglio, L. Testi, G. White, C. Wilson, A. Woodcraft, and A. Zavagno
2010. A Herschel study of the properties of starless cores in the Polaris Flare dark cloud region using PACS and SPIRE. *Astronomy and Astrophysics*, 518:L92.

Wardle, M.
2007. Magnetic fields in protoplanetary disks. *Astrophysics and Space Science*, 311:35–45.

Weingartner, J. C. and B. T. Draine
2001. Dust Grain-Size Distributions and Extinction in the Milky Way, Large Magellanic Cloud, and Small Magellanic Cloud. *The Astrophysical Journal*, 548(1):296–309.

White, R. J. and A. M. Ghez
2001. Observational Constraints on the Formation and Evolution of Binary Stars. *The Astrophysical Journal*, 556:265–295.

Williams, G. M., N. Peretto, A. Avison, A. Duarte-Cabral, and G. A. Fuller
2018. Gravity drives the evolution of infrared dark hubs: JVLA observations of SDC13. *Astronomy and Astrophysics*, 613:A11.

Wolf, M.
1923. Über den dunklen Nebel NGC 6960. *Astronomische Nachrichten*, 219(7):109.

Zamora-Avilés, M., J. Ballesteros-Paredes, and L. W. Hartmann
2017. Are fibres in molecular cloud filaments real objects? *Monthly Notices of the Royal Astronomical Society*, 472(1):647–656.

Zhou, C., M. Zhu, J. Yuan, Y. Wu, L. Yuan, T. J. T. Moore, and D. J. Eden
2019. Star formation in IRDC G31.97+0.07. *Monthly Notices of the Royal Astronomical Society*, 485(3):3334–3351.

List of scientific publications

Refereed publications

- **S. Heigl**, A. Burkert, A. Hacar, 'Non-linear dense core formation in the dark cloud L1517', 2016, *Monthly Notices of the Royal Astronomical Society*, 463, 4301-4310
- J. Steinacker, A. Bacmann, Th. Henning, **S. Heigl**, 'Prestellar core modeling in the presence of a filament. The dense heart of L1689B', *Astronomy and Astrophysics*, 593, A6
- M, Gritschneder, **S. Heigl**, A. Burkert, 'Oscillating Filaments. I. Oscillation and Geometrical Fragmentation', 2017, *The Astrophysical Journal*, 834(2), 202
- **S. Heigl**, A. Burkert, M. Gritschneder, 'Accretion-driven turbulence in filaments - I. Non-gravitational accretion', 2018, *Monthly Notices of the Royal Astronomical Society*, 474, 4881-4893
- **S. Heigl**, M. Gritschneder, A. Burkert, 'Morphology of prestellar cores in pressure-confined filaments', 2018, *Monthly Notices of the Royal Astronomical Society*, 481, L1-L5

Submitted publications

- **S. Heigl**, A. Burkert, M. Gritschneder, 'Accretion-driven turbulence in filaments - II. Effects of self-gravity', 2019, submitted to *Monthly Notices of the Royal Astronomical Society*

Acknowledgments

First and foremost, I am deeply grateful to my supervisor Andreas Burkert for having me as a student. Your truly inspiring and enthusiastic personality has taught me more than physics: the true love for science.

Second, I thank my friends and family for always encouraging me even when times where difficult. The impact of you on the accomplishments and happiness of my life cannot be overstated.

Third, in all honesty I have to acknowledge the impact of coffee. Well, not only coffee but also the supplier Klaus Dolag, who keeps the group together and whose office is the central hub of the USM universe.

Furthermore, I thank my colleagues as without you I could not have finished. Matthias for always having an open door and being an overall source of positivity, Alvaro and Paola for all the scientific input and discussions, Tadziu for fixing everything which breaks and always being helpful, David for the development sessions (which are not a pyramid scheme), Rhea for everything she does for the group and for supporting me throughout my studies, the secretaries Nicola, Sabine and Gudrun for making everything easier at the USM, my co-PhD students for being the best colleagues and friends one can wish for: Alex for being an awesome office mate, Adelheid, Felix, Joe, Johann, Manuel, Marcel, Uli, Kristina, all participants of the star/planet formation lunch for keeping it alive and all the people who have accompanied me during my studies.